INVESTIGATION OF MG-ZN-AL METAL ALLOYS AS NEW PCMS FOR LATENT HEAT ENERGY STORAGE APPLICATIONS

ELENA RISUEÑO VILCHES

Index

Index of figures

Index of tables

Objective

The main objective of this thesis is to investigate new classes of materials, metal alloys, as phase change materials (PCMs) for thermal energy storage (TES) application. In particular, this work consists to analyze and characterize a set of binary and ternary metal alloys based on different compositions of Mg-Al-Zn mixtures, in order to identify new eutectic and peritectic compositions with adequate melting temperatures combined with appropriate thermophysical properties for their use as PCM storage media at high temperature for concentrated solar power (CSP) and industrial waste heat recovery applications among others.

The first stage of this experimental work consists of synthesis of the selected eutectic and peritectic binary and ternary metal alloys by using different routes of preparation. When the materials are synthesized a complete structural analysis is conducted by combining different techniques such as X-ray diffraction (XRD) and scanning electron microscopy (SEM) in order to confirm or to correct the theoretical compositions of the synthesised metal alloys. The second stage of this work is to determine the most relevant thermophysical properties of these materials in this field such as the melting temperature, the heat capacity, the latent heat, the thermal diffusivity and conductivity, among others. The third stage is to investigate the long term thermal stability of the studied PCM by implementing two kind of cycling methodologies, the first one based on the thermal cycling of the material by means of differential scanning calorimeter (DSC) to determine its short term stability; and the second one based on the use of a high temperature furnace to determine the long term stability behaviour of the selected materials. The final stage of this work consists to investigate the compatibility study between the selected alloys and different containment materials in order to identify the most suitable stainless steels that can be used in the construction of thermal energy storage unit for each specific composition of the investigated metal alloys.

1. State of the art and introduction

1.1. Background

The current society is facing an unprecedented challenge: the advances in combating the pollution and increasing the efficiency on natural resources use are not enough to balance the pressure on the environment produced by the current world socioeconomic trend. Within this context and in the frame of energy sector, the largest participation of renewable energies in the global energy model and the increasing energy efficiency play key role to mitigate the CO_2 emissions and alleviate the remarkable growing energy demand.

World Energy Outlook 2014 (WEO'14) released by International Energy Agency (IEA) [1] estimates a growing of energy demand nearly of 37% between 2013 and 2040. The population growth and rising living standards are the key drivers behind the growing demand of energy. According to The Global Demographic Study released by United Nations (UN) in 2014 [2] the current population of 7200 millions of person will be of 8100 millions on 2025 and will rise 9600 millions on 2050. This represents around 40% more than in 2000. On the other hand, according to the WEO'15 the economy will growth one 150% for 2040 [3], which will imply an increasing demand for energy. The Organization for Economic Co-operation and Development (OECD) [4] in its report on environmental predictions due to inaction estimated that in 2050 will use 80% more energy that nowadays, of which an 85% will be based on fossil fuels due to the lack of more effective energetic policies. This report anticipated that global greenhouse gas (GHG) emissions to rise by 50% in 2050, mainly due to 70% increase in CO_2 emissions related to power generation, which would imply an increase of average global temperature of between 3 – 6 °C by the end of the century.

Regarding this increasing in energy demand, a growing concern about the environmental sustainability on the global energy model has been produced. The World Energy Council (WEC) [5] has developed the concept of "energy trilemma" to define the triple challenge of obtaining energy in a safe, affordable and respectful with the environment as is shown in Figure 1. Currently,

the agents responsible for energy policies and energy producers have to face a huge challenge: Energy must be accessible and affordable at all levels of society, but the impact of energy production and energy use on the environment must be minimized.

Numerous sustainable energy scenarios for climate change mitigation are proposed by different international organizations and institutions, such as Current Policies Scenario (CPS), New Policies Scenario (NPS) and 450 Scenario (450S) of International Energy Agency (IEA). CPS takes in consideration the real energetic policies adopted until 2010; NPS is based on the accomplishment of the current committed energy policies even if they are not still implemented, and 450S is the desired scenario to limit the average global temperature rise up to 2ºC at the end of the century. These scenarios differ on the severity or permissiveness of the proposed measures to reduce in more or less degree GHG emissions. However, all of them show a combination of the same action measures, among which the largest participation of renewable energy in the global energy model and the increasing energy efficiency are fundamental [6,7].

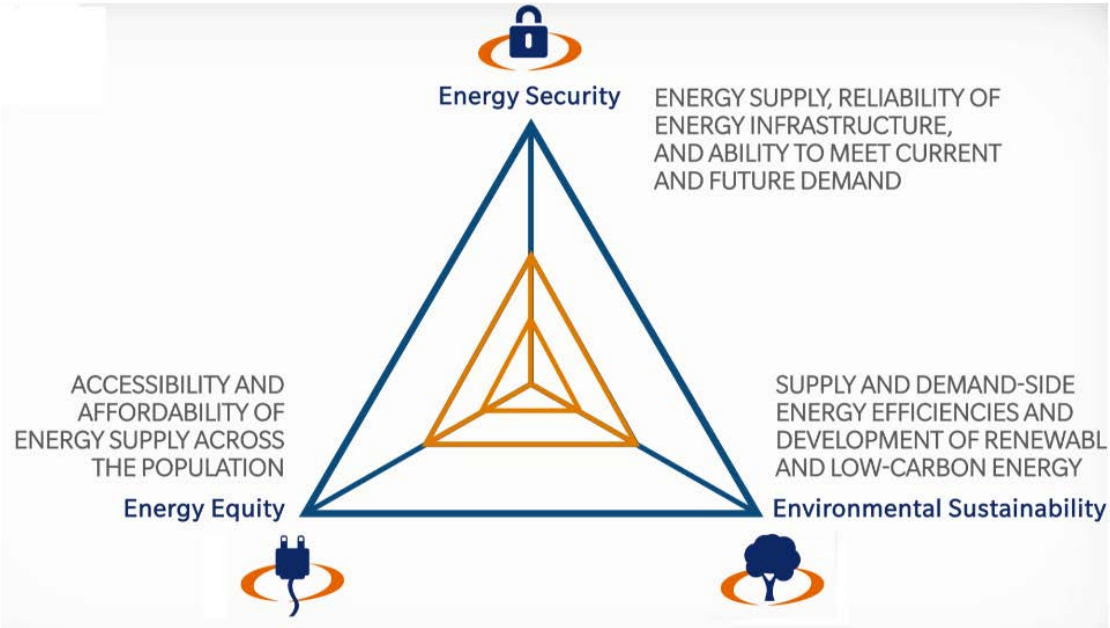

Figure 1. Balancing of three core dimensions of the concept of "energy trilemma" defined by the World Energy Council (WEC) [5].

Figure 2 and Figure 3 shows, respectively, a comparison of the CO_2 emissions trend between 450S-CPS and 450S-NPS in base of the technologies to be applied. As it may be observed from the figures, in both cases energetic efficiency and renewable energies represent the largest percentage of CO_2 emissions reduction.

As it is know the renewable energy is defined as energy that is collected from theoretically inexhaustible natural source such as sunlight, wind, rain, tides, waves, and geothermal heat. In this way, different renewable energy technologies exist such as bioenergy, wind power, solar energy, hydropower or geothermal energy. Traditionally the sustainable development model is composed of three pillars; the economy, ecology and society. The interest of renewable energy sources is based on the fact that it contributes to the achievement of important objectives in the three pillars, allowing: The social and economic development, access to energy, energy security and mitigation of climate change and reducing its effects on the environment and health [6]. In other words, renewable energies can reduce on large scale GHG emissions without thereby being a threat to the lifestyle and economic growth. For the success of strategies against climate change through a largest use of renewable energies the innovation and technological advancement are fundamental, inasmuch as these technologies must become economically and technically viable alternatives to fossil energy sources.

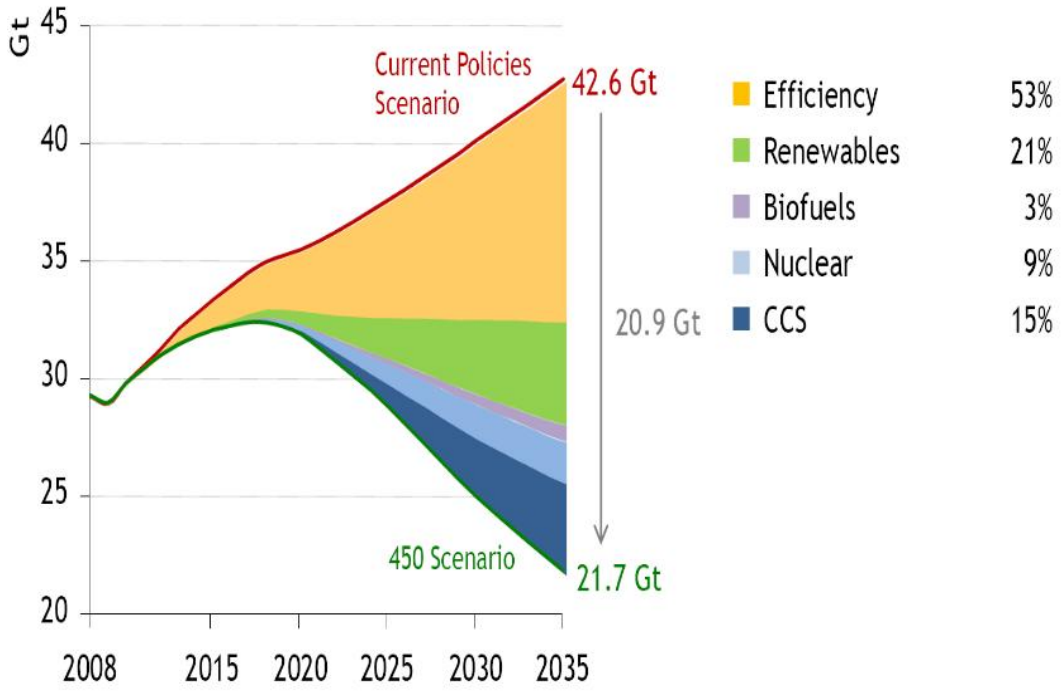

Figure 2. Comparison of the CO_2 emissions between 450S and CPS in base of the technologies to be applied [8].

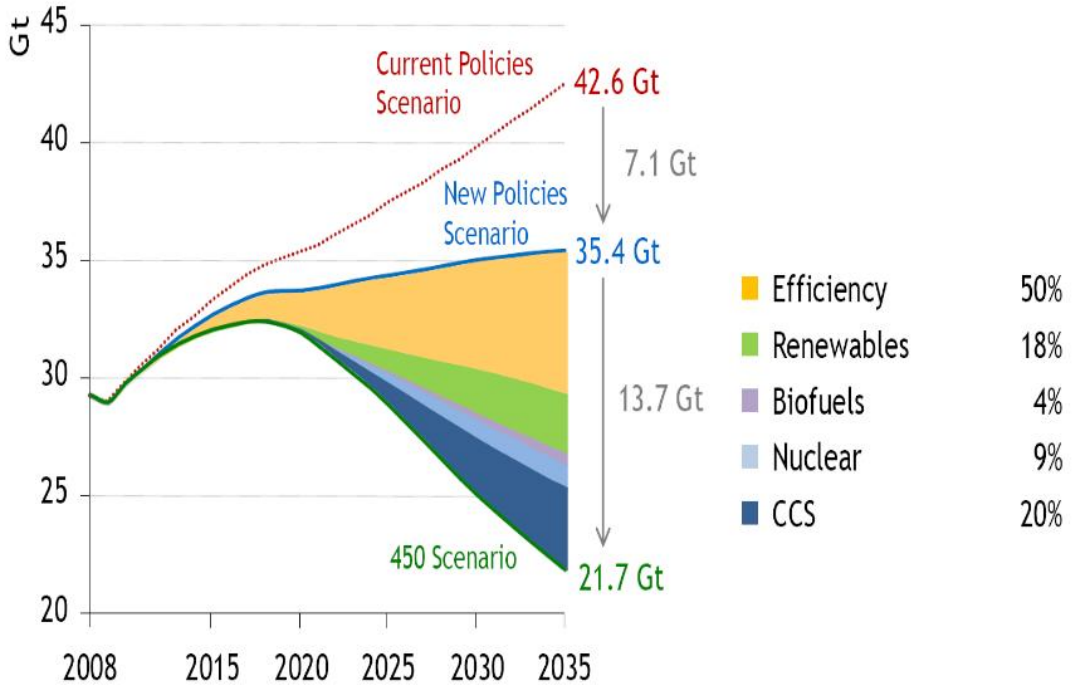

Figure 3. Comparison of the CO_2 emissions between 450S and NPS in base of the technologies to be applied [8].

One of the drawbacks of renewable energies is the intermittency of its production, which have directly repercussions on the competitiveness against conventional energy sources. In order to overcome this limitation and increase its global efficiency, energy storage (ES) strategies are a key issue.

All forms of energy are potentially storable with an appropriate method or technology. The Figure 4 shows energy storage systems under development [9], among which is found the thermal energy storage (TES).

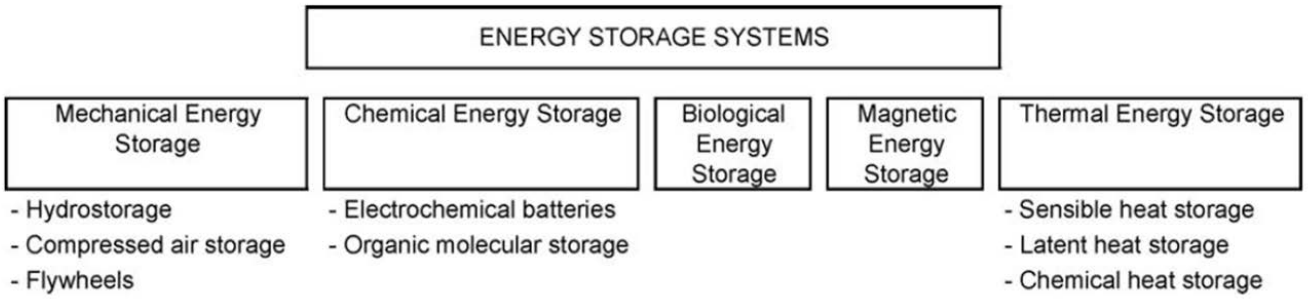

Figure 4. Classification of energy storage systems under development [9].

1.2. Thermal energy storage (TES)

The thermal energy storage (TES) includes different technologies that encompass a wide range of needs. It allows storage the excess of thermal energy for its posterior use, which can be given after hours, days or months. As examples, the stored energy of daytime can be used in nighttime, the summer heat can be stored for winter or the cold of winter can be used to provide air conditioning in summer, being the first example the most deployed one. In particular, daily TES technology has shown a very high potential in order to increase the global efficiency in concentrated solar power (CSP) plants [10,11], industrial waste heat recovery [12,13], industrial processes [14] or building applications [15,16] among others.

TES can be carried out by technologies based on sensible heat storage (SHS), latent heat storage (LHS), and thermochemical energy storage (TcES):

- In SHS technologies the thermal energy is stored when material temperature increases and is released when material temperature decreases. In these systems the working temperature range of the system and the specific heat capacity of the storage material determine the thermal energy storage density. As SHS materials water, heat transfer oils, molten salts and liquid sodium among others are commonly used [17].
- In LHS technologies the thermal energy storage is based on phase change transition of a given material, which is called phase change material (PCM). The thermal energy storage/release takes place when PCMs adsorb/release heat during their phase transition process. LHS shows advantages addressing to SHS due to its higher energy storage density and quasi-isothermal nature of thermal energy charge/discharge process. The phase transitions can be classified into solid–solid, solid–liquid and liquid-gas types:
    - Solid–solid transition adsorbs/releases heat during the crystal transition, where, the typical materials used as PCMs include polyalcohols, macromolecules and inorganic salts [18,19].
    - Solid–liquid transition is more extended than solid-solid transition due to its higher energy involved in its phase change. The commonly used PCMs in this case can be divided into organic and inorganic materials, where mainly, organic solid–liquid PCMs include paraffin and fatty acids [20] and inorganic materials include salt hydrates, metals, and inorganic salts [21,22].
    - Liquid-gas transition has even higher entropy changes and, as a consequence, higher latent heat value. However, phase transitions involving the gas state are

usually impractical due to the large volume change between the two involved phases.

- In TcES technologies are based on endothermic/exothermic chemical reaction heat for thermal energy storage/release. Among the most promising materials are calcium and iron carbonates, hydroxides and sulphates [23]. The main advantage of these thermochemical materials is their highest energy densities. However, currently, more research is required before commercial implementation can occur.

Early 80s SHS systems started to work in the field of solar energy by implementation of the two-tank molten salt technology [24], which since to present is extensively used in many concentrated solar power (CSP) plants. As a consequence, this storage system has become a developed and mature technology.

Then, the interest of PCMs growth due to their high storage densities and isothermal natures of the storage processes. Since the lasts four decades, many types of low temperature PCMs, with mainly melting temperature below 100ºC, were extensively studied for a wide range of applications [17,21,25-28].

However, since the last decade the latent heat energy storage (LHES) in high-temperature (HT) (>300ºC) [22] has become an interest focus due to its utilization can improved significantly the thermal efficiency of CSP plants and numerous industrial processes. As a consequence, in the last years numerous researches have been carried out in this scope [29-39].

HT-PCMs under study are inorganic salts, eutectic and non-eutectic inorganic salt mixtures, metals and eutectic and non-eutectic metallic alloys. The inorganic salts and their mixtures include fluorides, chlorides, bromides, hydroxides, sulphates, nitrates, carbonates and other salts [40]. The metals and their alloys are based on Pb, Al, Zn, Cu, Si, Mg metals and on Ca, Sb and P alloying elements [22]. However, inorganic salts have been more extensively investigated than metals, where chlorides, hydroxides, and nitrates have aroused the greatest interest.

According to A. Sharma et al. [17] materials to be used for LHES should satisfy following requirements:

- Thermal properties: Suitable phase-transition temperature, high latent heat of fusion and high thermal conductivity.
- Physical properties: Congruent phase-transition, stable phase equilibrium, high density, small volume change and low vapour pressure.

- Kinetic properties: No sub-cooling and sufficient crystallization rate.
- Chemical properties: Long-term chemical stability, compatibility with containments materials, no toxic and no fire hazard.
- Economics: Abundant, available and low cost.

However, any material satisfies completely all the requirements. In this way, the principal limitation of inorganic salts are their poor thermal conductivity, followed of other common limitation such as incongruent phase-transition, considerable thermal hysteresis, corrosion problems, high volume change during the melting and high cost of some salts [22]. Regarding metals their main limitation is the high cost, which led to a not serious consideration as PCMs in last decades. However, M. M. Kenisarin et al. [40] concluded that the use of metals as PCMs have being underestimated by researchers although their properties such as high thermal conductivity, small volume change and no thermal hysteresis overcome the set of drawbacks of the salts. In fact, metals despite their lower heat of fusion per weight unit, in some cases can compete with salts as it has been demonstrated by several investigations:

J. Yagi et al. [41] investigated inorganic salts (NaCl, KNO_3-47$NaNO_3$) and metals (Pb, Al, Al-12.6Si, Al-25.1Si) as high-temperature phase change materials (HT-PCM) with melting temperatures in the range of 220-750 ºC and in a single encapsulated configuration for waste heat recovery above 220 ºC from iron and steel-making industries. After the fundamental studies of heat transfer, it was found that metals are more profitable than salts due to their almost uniform temperature distribution addressing the large temperature gradient observed in salts.

S. Khare et al. [42] used a materials selection software to identify potential PCMs for solar energy high temperature application (>420 ºC). It was found that metals such as Al, Mg, Si and Zn and their eutectics are highly suitable PCMs than conventional molten salts.

As shown Figure 5 M. Liu et al. [22] compared the heat capacity and media cost against the melting point of PCMs (NaOH, $NaNO_3$, KNO_3, KOH, LiCl, Pb and Zn) with melting temperature in the range of 300-550 ºC for solar power generation application. The results of this analysis demonstrated that KOH and Zn are the most cost effective materials.

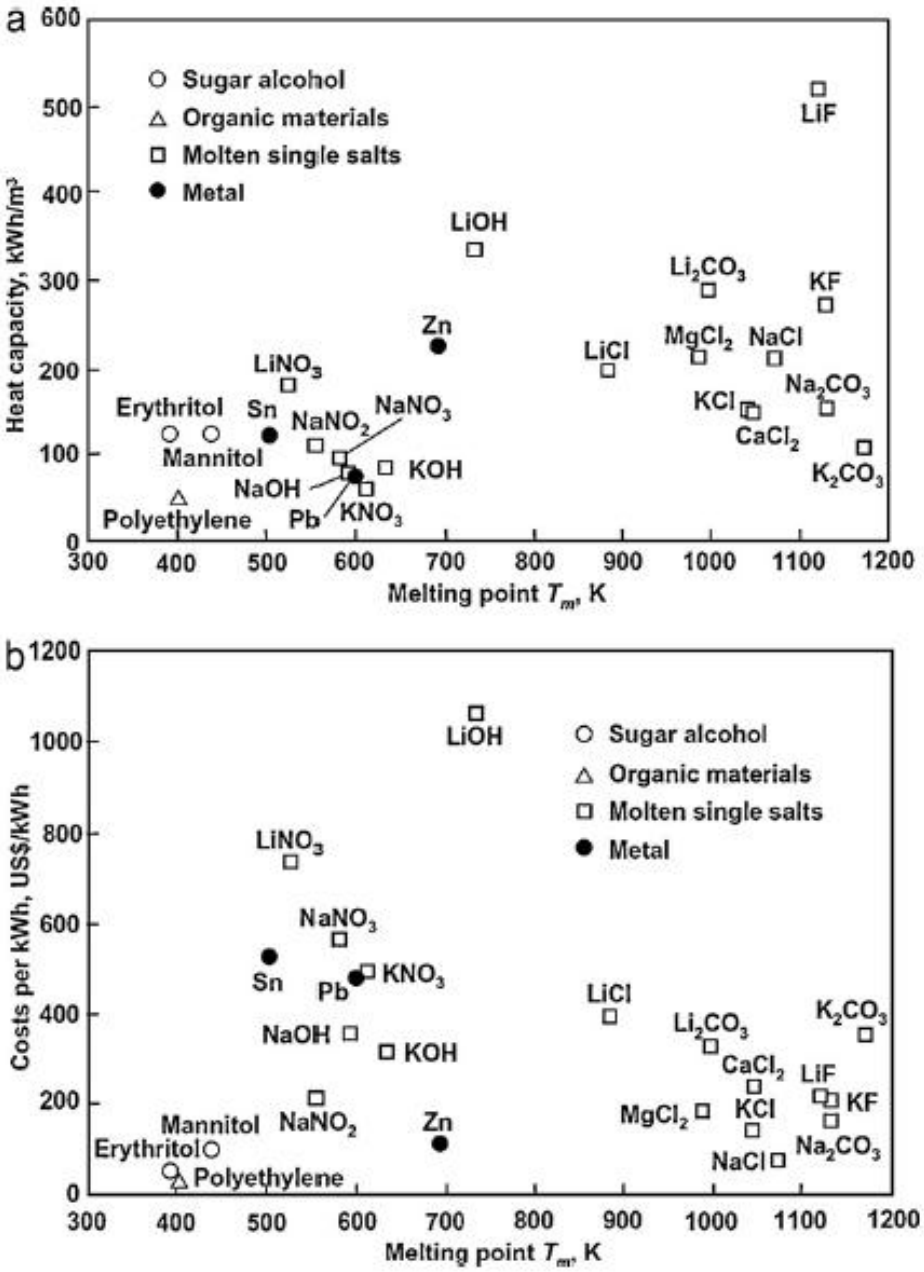

Figure 5. Heat capacity (a) and media cost (b) of HT-PCMs [22].

A. Hoshi et al. [43] investigated the suitability of HT-PCMs for use in large scale solar thermal electricity plants. Among their conclusions, it was indicated that Zn may be a cost effective option for parabolic trough systems using higher boiler temperatures.

The most important shortcomings of inorganic salts are their low thermal conductivity values, between 0.4 and 5 W/mK [28,40]. These low thermal conductivities limit dramatically the heat transfer in the storage material and make difficult their use in thermal storage applications which

usually require a high release ratio of the stored energy. Many attempts have been done to enhance the heat transfer coefficient in TES systems based on HT-PCMs as is shown in Figure 6 [22].

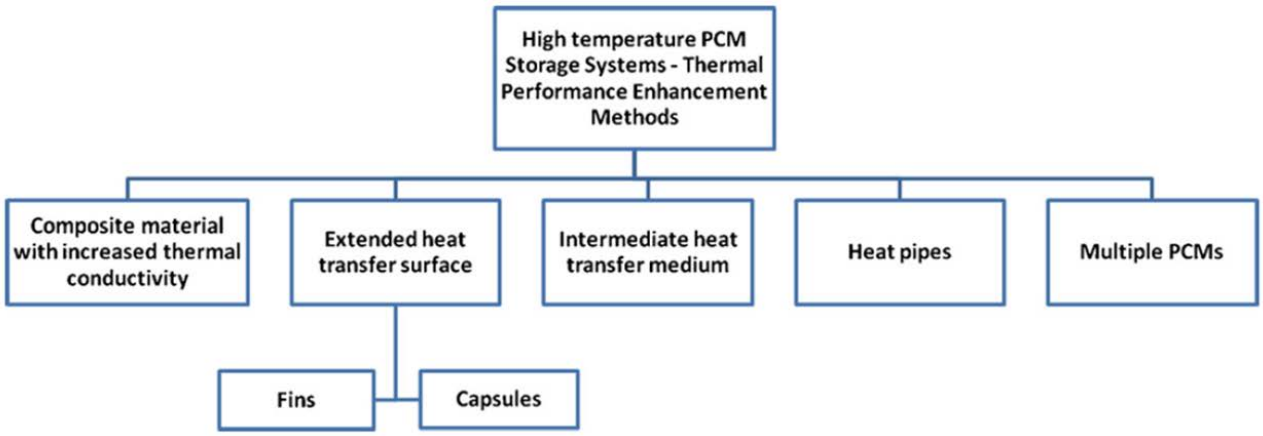

Figure 6. Investigated heat transfer enhancement methods for HT-PCM storage systems [22].

Another alternative to improve the thermal conductivity is the use of metals as PCMs instead of inorganic salts. In fact, the thermal conductivity values of metals, around two orders of magnitude higher than the one of materials commonly used, inorganic salts, on TES applications.

On the other hand, the high thermal conductivity of metals allows reaching higher power ratio and consequently opens the range of applications in both solar and industrial fields. As examples:

- In the industrial sector:
    - The use of high-power TES systems is the only storage possibility when very high power levels and very fast thermal response are required.
- In solar power plants, it could:
    - Reduce the complexity, size and cost of the heat exchanger.
    - Provide appropriate protection against thermal shocks on different components of the plant mainly the receiver.
    - Reduce the impact of solar fluctuations on the production turbine work regime, which it is currently done by burning natural gas, which its use depends on the regulation of each country where CSP plant is constructed. This solution implies

the elimination of back-up fuel consumption include the gas fired back-up boiler integration into the CSP plant

- Reduce the start-up times in the morning in order to shorter the time to arrive to the base load turbine production.

1.3. Metal alloys as phase change materials

In this thesis the use of eutectic metal alloys as LHES materials is proposed as an innovative solution addressing the limitations of inorganic salts as mentioned previously.

Metal alloys as PCMs by means of binary and ternary eutectic alloy systems of Al, Mg, Zn, Cu, Si P and Ca elements were proposed more than three decades ago [44-46]. However, during last decades several experimental studies about the use of metals and metal alloys as PCMs were performed, where Al-Si alloys [34,47,48], Al-Mg-Zn [49], Cu-based encapsulated PCMs [50,51], isolated metals [35] or miscibility gap alloys [52] have been mainly investigated. Nevertheless, a deep effort is still needed in order to demonstrate the potentiality of metal alloys in heat energy storage frame.

Within the metallic material family, the main criteria to select a competitive PCM are a high fusion entropy, availability and low cost [44,45]. On the other hand, [43] indicated the high suitability of Al, Mg and Zn metals as PCM and [22,42] pointed the Zn metal as a cost effective option as PCM. According to these conclusions Zn, Al and Mg metal alloys have being selected as potential LHS materials to be investigated by our group. The Zn-Al-Mg, Zn-Al and Zn-Mg phase diagrams are shown in Figures 7, 8 and 9, respectively [53-55]. Few references about Mg-Zn-Al binary and ternary alloys systems as potential PCMs have been found in the literature [46,49,56]. In addition, none of these publications present a complete study to cover the main relevant criteria to select the most suitable PCM materials to be used in the TES field. As it is very known (see Figure 10), to identify potential PCMs the study of thermophysical properties such as phase change temperatures, phase-transition latent heats or the thermal conductivity among other, are essential. However, the selection must be also performed in basis to the long-term thermal stability of thermophysical properties. In addition, the realization of compatibility study between the potential PCMs and containment materials are also required in order to select the adequate materials for containment unit constructions and ensure long term stability of the storage materials and containers.

In this way, in this thesis, a complete research study of the selected metal alloys as PCMs has been carried out from the synthesis of samples to pilot plant scale testing. The experimental results

obtained in this work for each aspect are presented in separated chapters according to the following scheme. The selection of the candidates, as well as, the experimental procedure followed to synthesis the metal alloys are described in Chapter 3. The structural characterization and thermophysical properties determination of the obtained metal alloys are presented in Chapter 4.1. The evaluation of the accelerated thermal cycling tests to evaluate the long-term thermal stability of the investigated PCMs is discussed in Chapter 4.2. Some results regarding the development of a semi-empirical mathematical model to predict specific heat of metals and the testing of one of the studied eutectic alloys in a laboratory scale TES unit, obtained in collaboration with other CIC Energigune groups, are described in Chapter 5. Finally, the work developed during the research stay at I2M – CNRS – TREFLE, University of Bordeaux (France) is described in Chapter 7.4.

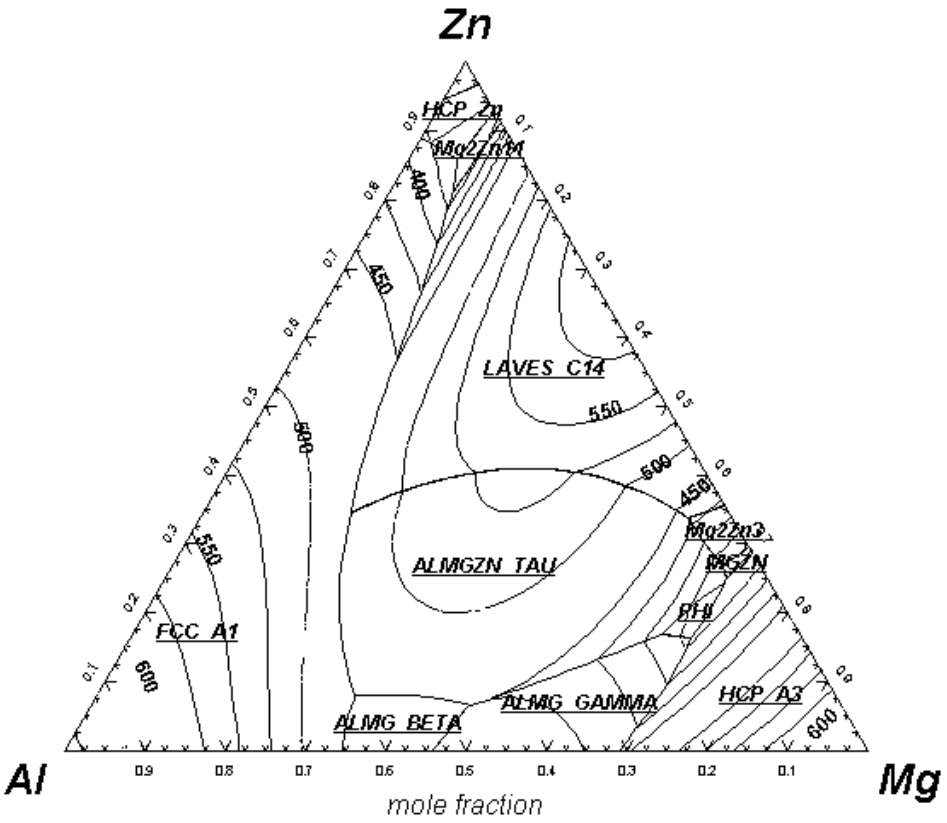

Figure 7. Mg-Zn-Al ternary liquidus projection [53].

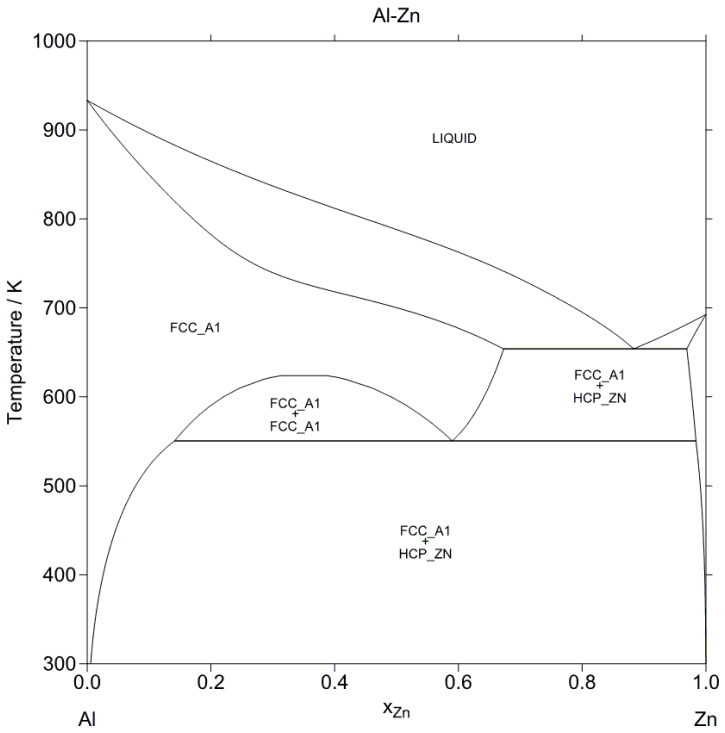

Figure 8. Al-Zn binary phase diagram [54].

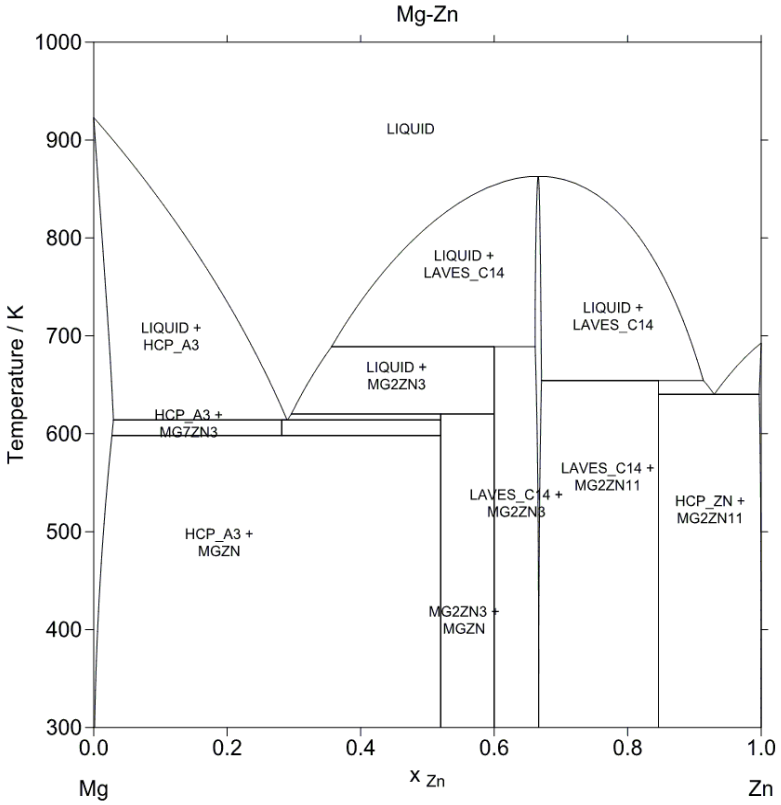

Figure 9. Mg-Zn binary phase diagram [55].

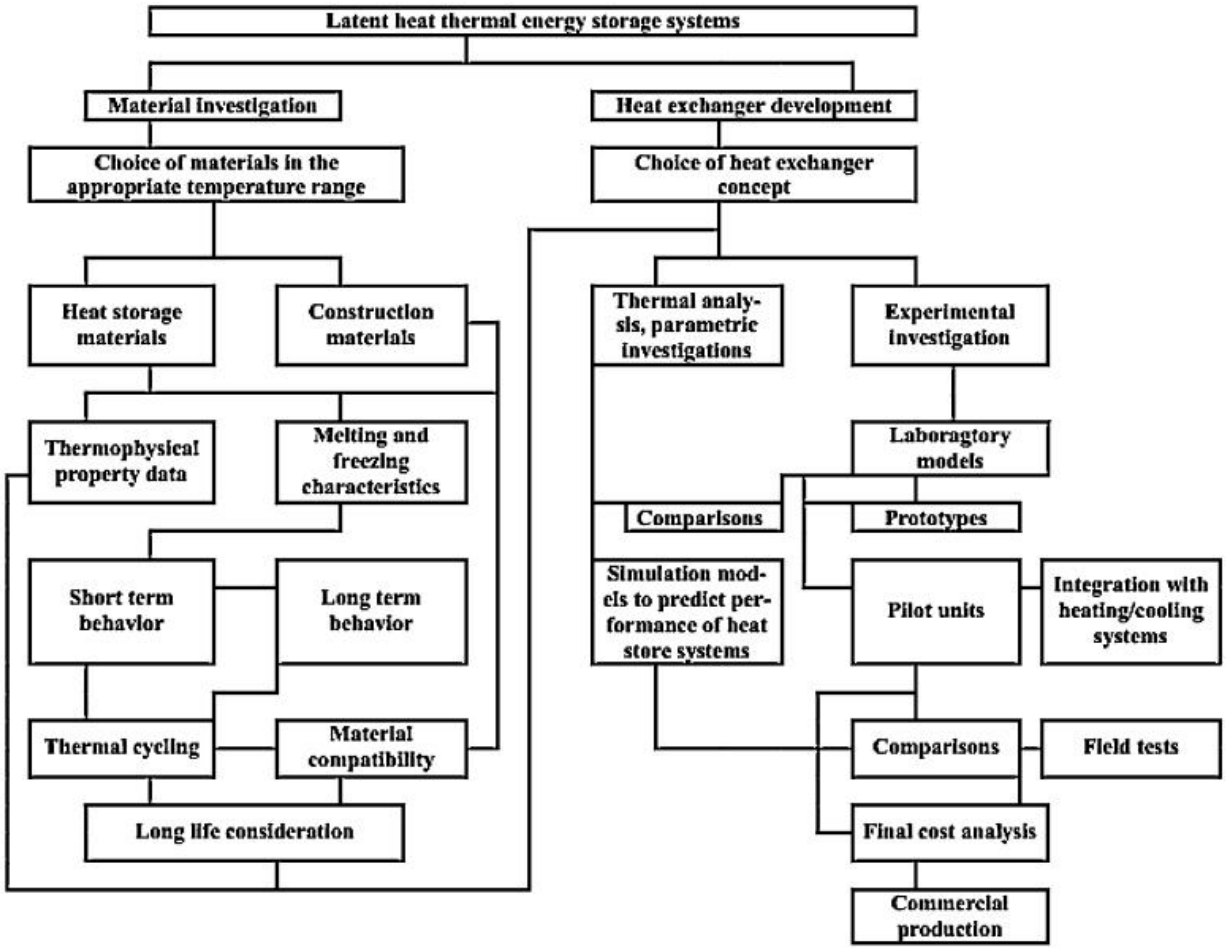

Figure 10. The steps in the development of a latent heat storage system [40].

1.4. Scientific publications as result of this thesis work:

As result of the research work carried out in this thesis several scientific papers were published and under review in high impact factor journal. It has to be noted that the sections of chapter (4) are based on papers resulting of this thesis and the sections of chapter (5) are based on collaboration papers, related but not resulting of this thesis.

- **Chapter 4: Papers resulting of this thesis**

  - Section (4.1.1): **E. Risueño**, S. Doppiu, J. Rodríguez-Aseguinolaza, P. Blanco, A. Gil, M. J. Tello, A. Faik and B. D'Aguanno, "Experimental investigation of Mg-Zn-Al metal alloys for latent heat storage application". Journal of Alloys and Compounds, 685 (2016)724-732.

    Published

- Section (4.1.2): **E. Risueño**, A. Faik, A. Gil, J. Rodríguez-Aseguinolaza, M. J. Tello and B. D'Aguanno "Zinc-rich eutectic alloys for high energy density latent heat storage applications".

  Submitted to Journal of Alloy and Compound

- Section (4.2.1): **E. Risueño**, A. Gil, J. Rodríguez-Aseguinolaza, M. J. Tello, A. Faik and B. D'Aguanno "Thermal cycling testing of Zn-Mg-Al eutectic metal alloys as potential high-temperature phase change materials for latent heat storage".

  Submitted to Journal of Thermal Analysis and Calorimetry

- Section (4.3.1): **E. Risueño**, A. Faik, J. Rodríguez-Aseguinolaza, A. Gil, M. J. Tello, and B. D'Aguanno "Corrosion behaviour of stainless steels in Mg-Zn-Al molten metal alloys for latent heat storage application".

  Submitted to Journal of Solar Energy

- **Chapter 5: Collaboration papers, not resulting of this thesis**

  - Section 5.1: J. Rodríguez-Aseguinolaza, P. Blanco-Rodríguez, **E. Risueño**, M. J. Tello and S. Doppiu , "Thermodynamic study of the eutectic Mg49-Zn51 alloy used for thermal energy storage", Journal of Thermal Analysis and Calorimetry, 117 (1) (2014) 93-99.

    Published

  - Section 5.2: P. Blanco-Rodríguez, J. Rodríguez-Aseguinolaza, **E. Risueño** and M. J. Tello, "Thermophysical characterization of Mg-51%Zn eutectic metal alloy: A phase change material for thermal energy storage in direct steam generation applications". Energy, 72 (2014) 414-420. [Corrigendum: Energy 75 (2014) 630].

    Published

- Section 5.3: P. Blanco-Rodríguez, J. Rodríguez-Aseguinolaza, A. Gil, **E. Risueño**, B. D'Aguanno, I. Loroño and L Martín "Experiments on a Lab Scale TES Unit using Eutectic Metal Alloy as PCM", Energy Procedia, 69 (2015) 769-778.

  Published

- **Other related papers but not included in this thesis**

  - **E. Risueño**, A. Faik, J. Rodríguez-Aseguinolaza, P. Blanco-Rodríguez, A. Gil, M. J. Tello and B. D'Aguanno, "Mg-Zn-Al Eutectic Alloys as Phase Change Material for Latent Heat Thermal Energy Storage", Energy Procedia, 69 (2015) 1006-1013.

    Published

  - T. Echániz, R.B. Pérez-Sáez, **E. Risueño**, L. González-Fernández, A. Faik, J. Rodríguez-Aseguinolaza, P. Blanco-Rodríguez, S. Doppiu and M. J. Tello "Thermal emissivity spectra and structural phase transitions of the eutectic Mg-51%Zn alloy: A candidate for thermal energy storage", Journal of Alloys and Compounds 684 (2016) 62-67.

    Published

2. Experimental equipment

2.1. Scanning Electron Microscopy (SEM) and Energy Dispersive X-Ray Spectroscopy (EDS)

Scanning Electron Microscopy (SEM)

The alloys microstructure and morphology investigations were performed using a Quanta FEG 250 Scanning electron microscopy (SEM). The scanning electron microscope (SEM) is a type of electron microscope that produces high-resolution images of a sample by scanning a focused beam of accelerated electrons. When the electron beam strikes the sample are produced several interactions with the sample that result in the emission of electrons or photons. These emitted particles are collected with the appropriate detector to provide information about the microstructure, topography and composition of sample surface.

The optical resolution can be approximated as wavelength λ/2NA (NA is the numerical aperture of the lens, typically ~ 1.0). By accelerating electrons by a high voltage, its wavelength is reduced. The acceleration takes place in the microscope column by a potential range from 1000 to 30000 V. These voltages reduce the wavelength of the electrons from approximately 4 nm to 0.7 nm for voltages 1000 V and 30000 V, respectively. Thus, by SEM higher resolutions of the order of 1 nm can be obtained to observe details of the sample surface that are in this order of size. Samples can be observed in a wide range of conditions; from high vacuum or humid conditions or cryogenic.

The accelerated electron beam from electron gun is focused and reduces along the column by condenser lenses and objective, respectively. By deflector coils, the electron beam on the sample is scanned point by point and line by line. The electrons interact with the atoms at various depths within the sample. As a consequence of this interaction different types of signals are produced secondary electrons (SE), reflected or back-scattered electrons (BSE) or photons of characteristic X-rays among others.

Secondary electrons are electrons stripped from the surface of the sample due to a process ionization produced by the interaction with electron of beam (primary radiation). They occur when an electron beam passes close to the nucleus of an atom in the sample, providing enough energy to one or more of the inner electrons to jump out of the sample. These electrons are very close to the surface and therefore, they provide topographical information displays at very high resolution (less than 1 nm). It is the most common detection mode in SEM.

Back-scattered electrons (BSE) are beam electrons that are reflected from the sample by elastic scattering due to a collision with the nucleus of an atom. Because the intensity of the BSE signal is proportional to the atomic number (Z) of the atoms, their images can provide information about the distribution of different elements in the sample. Back-scattered electrons emerge from deeper locations of the sample than secondary electrons and consequently the resolution of BSE images is usually poorer (5 to 10 nm). In analytical SEM, the BSE are often along used with the spectra made from the characteristic X-rays.

Characteristic X-rays are produced when a secondary electron is removes from an inner shell from the atom and another outermost electron can jump inside to fill this gap. In this way, the excess energy of the electron that migrates to an inner shell to fill the newly created hole is emitted as X-ray. The X-rays are characteristic of each element of the sample, which are used to obtain information on the composition of the sample.

Energy Dispersive X-Ray Spectroscopy (EDS)

Energy Dispersive X-Ray Spectroscopy (EDS or EDX) is an analytical technique used for the elemental analysis or chemical characterization, which it is used in conjunction with SEM. The EDS is used to analysis characteristic X-ray spectra. The number and energy of characteristic X-rays emitted from the sample are detected by an energy-dispersive spectrometer. The EDS X-ray detector measures the relative abundance of emitted X-rays versus their energy. The EDS detector converts X-ray energy into voltage signals. Then this information is sent to a pulse processor, which measures the signals and passes them onto an analyzer for their display and analysis.

As the energies of the X-rays are characteristic of the difference in energy between the two shells and of the atomic structure of the emitting element, EDS allows know the elemental composition of the sample. The qualitative analysis involves the identification of the lines in the X-ray spectrum and the quantitative analysis. Quantitative analysis (determination of the

concentrations of the elements present) entails measuring line intensities for each element and for each element in a calibration Standard of known composition.

X-ray intensities are measured by counting photons and the precision obtainable is limited by statistical error. The overall analytical accuracy is commonly ± 2%, owing to factors such as uncertainties in the compositions of the standards and errors in the various corrections which need to be applied to the raw data. On the other hand, together with the characteristic X-ray lines, a continuous X-ray spectrum is also emitted by the sample. This continuous spectrum gives rise to the presence of "background" which limits the observation of small peaks. This effect can be reduced by using long counting times.

2.2. X-Ray Power Diffraction (XRPD)

The phase and cell parameter determination on alloy samples has been performed by X-ray powder diffraction (XRPD) technique using a Bruker D-8 Advance Diffractometer. XRPD is based on the study of X-rays diffracted by the sample (powder or bulk) where their geometry is strongly linked to the geometry of the crystal structure.

Crystalline materials are characterized by the orderly periodic arrangements of atoms. The unit cell is the basic repeating unit that defines a crystal and its possible shapes are defined by 7 crystal systems, which are based on the relationship among *a,b,c* (unit cell dimensions along *x, y, z,* respectively) and α, β, γ (angles between *b,c* (α); *a,c* (β); *a,b* (γ)). Parallel planes of atoms intersecting the unit cell are defined by Miller index (*hkl*).

When the electromagnetic waves of an X-ray beam impact on atoms of the crystalline material, the waves are scattered in all directions creating constructive or destructive interferences. When a coherent dispersion occurs, the accuracy of the periodicity of the incident wave is preserved. Due to the regular arrangement of crystals, their atoms are a periodic serie of coherent dispersers which can diffract X-rays, where there is a strong geometrical relationship between the directions of the diffracted waves and the crystal structure of material.

An X-ray diffracted beam is composed of a large number of scattered rays of different parallel planes. The diffracted X-rays comply the following conditions: (i) The plane normal must be parallel to the diffraction vector (the vector that bisects the angle between the incident and diffracted beam). (ii) The angle of incidence (θ) on a plane's atom is equal to the scattering angle (θ). (iii) The angle of diffraction (2θ) is the sum of incidence and scattering angles. (iv) The

difference in length of paths ($2d \sin \theta$) between two rays diffracted by atoms in two different parallel planes is equal to an integer multiple (n) of the wavelength (λ) of the incident beam. These conditions are included in Bragg's law by the equation (1):

$$n\lambda = 2d \cdot \sin\theta \quad (1)$$

Where d is the distance between parallel planes. For parallel planes of atoms, with a distance d between the planes, constructive interference only occurs when Bragg's law is satisfied. In a diffractometer, the wavelength of X-rays is known and fixed. The sample is rotated so that the angle of diffraction changes. Consequently, a family of planes produces a diffraction peak only when a specific angle (θ) is reached. Thereby, the space interplaner d is known. At the same time, a relationship between d-value and the miller index and lattice constants of each crystallographic system exists.

The diffracted rays produce dark dots on a detector plate. In a powder sample, due to the random orientations of many crystals cone of diffraction, called Debye cone, are obtained. A detector transforms these cones in a discrete diffraction peaks. A diffraction pattern shows the position (2θ) and intensity of these peaks, where each one of which corresponds to a set of planes of crystal, where the space d_{hkl} between the planes determines peak positions and the peak intensity (I) is determined by the amount of atoms presents in set of planes. By the study of diffraction patterns can be obtained extensive information about the crystalline structure; qualitative and quantitative information, unit cell lattice parameters, crystallite size or microstrain among another.

Powder diffractometers typically use the Bragg-Brentano geometry. The incident angle (θ) is defined between the X-ray source and the sample. The diffracted angle (θ) is defined between the incident beam and the detector angle. The X-ray tube is fixed whereas the sample rotates at θ°/min and the detector at 2θ°/min.

The X-ray tube is the source of the incident X-ray. The production of X-ray involves bombarding a metallic target (anode) with electrons from a hot filament (catode), which are strongly accelerated by a high potential. When electrons collide with the target can eject electrons from the inner layers of its atoms. These vacancies are filled by electrons falling from higher levels, with higher energy. That energy difference between levels (characteristic of the atom) is released by the emission of a photon of X-ray with a wavelength (energy) determined. When the electron is ejected from the K shell (n = 1) and the transition occurs from the level n = 2 to n = 1 the X-ray is

called Kα, when produced from n = 3 to n = 1 is called K_β, and so on. In XPRD, K_α X-rays are normally used, from molybdenum or copper metal target.

Phase identification and unit cell parameter determination

Diffraction directions depend on crystal system and network parameters of the crystal, i.e., on the shape and size of the unit cell. So, a given crystalline phase always produces a characteristic diffraction pattern. In this made, the identification of crystalline phases is based. To qualitative analysis the diffraction pattern is compared with established patterns of crystalline phases. Diffraction patterns of each phase may be obtained from databases such as International Center Diffraction Data (ICDD) database.

The unit cell parameters determination is performed by refinement. The refinement consists in minimize the difference between the experimental diffractogram and a calculated diffractogram. The function to minimize, S_y, is given in the equation (2):

$$S_y = \sum_i w_i \cdot \left| y_i(o) - y_i(c) \right|^2 \tag{2}$$

Where $y_i(o)$ and $y_i(c)$ are the observed and calculated intensity, respectively, of the i-th point of the data set, and w_i is the weight assigned to each data. The experimental profile contains two types of contributions those caused by the physical and geometric aberrations of the diffractometer and the corresponding to real profile. In this way, two types of data are needed to obtain the calculated intensities, $y_i(c)$. The data that allow calculate the intensities of the different reflections, called "atomic parameters" and a group of parameters that affect the entire diffractogram, called "global parameters". When you do not have an adequate structural model (set of atomic positions) you can make a preliminary step of refinement called the "whole pattern fitting or matching profile." In this case the calculated intensity, $y_i(c)$, is modelled as shown in the equation (3):

$$y_i(c) = y_{bi} + \sum_{k=k_1}^{k_2} I_k \cdot \Omega_k \left(2\theta_i - 2\theta_k \right) \tag{3}$$

Where y_{bi} is the background continuous intensity in measurement step *i*, $\Omega(2\theta_i - 2\theta_k)$ describe the shape of *k* peak in the Bragg angle $2\theta_i$ (the most common functions to define the peak shape are Gaussian, Lorentzian, pseudo-Voigt among others.), I_k is the integrated intensity of the k-th peak of the diffractogram that contributing to step of measured *i*.

To minimize this expression should be obtained the derivatives with respect to the parameters, p_j, that depends the structural model, and equalize to zero, as is known in the equation (4):

$$\frac{\partial S_Y}{\partial p_j} = \sum_i w_i \cdot \Delta|y_i| \cdot \frac{\partial y_i(c)}{\partial p_j} = 0 \qquad (4)$$
$$j = 1,2,...n$$

In the refinement the function is approximated around a parameter, p_j, value. In each cycle of refinement is obtained a new set of parameters that described better the model and that they are the starting point for a new cycle refinement. Refinement is continued until convergence is reached, i.e. until no variation of parameters. The quality of the fit is measured by indices of disagreement [57].

2.3. Gas pycnometry

A gas pycnometer measures the volume and density of solid materials employing the volume/pressure relationship known as Boyle's Law, which affirms that the absolute pressure exerted by a given mass of an ideal gas is inversely proportional to the volume it occupies if the temperature and amount of gas remain unchanged within a closed system as is shown by equation (5) and (6):

$$P \propto \frac{1}{V} \qquad (5)$$

or

$$P \cdot V = k \qquad (6)$$

Where P is gas pressure, V is gas volume and k is a constant. The equation states that product of pressure and volume is a constant for a given mass of confined gas as long as the temperature is constant. For comparing the same substance under two different sets of condition, the law can be usefully expressed as the equation (7):

$$P_1V_1 = P_2V_2 \qquad (7)$$

The equation shows that, as volume increases, the pressure of the gas decreases in proportion. Similarly, as volume decreases, the pressure of the gas increases.

A gas pycnometer operates by detecting the pressure change resulting from displacement of gas by a solid object. Expanding a quantity of gas at known pressure into an empty chamber and measuring the pressure establishes a baseline. Then a sample is placed in the chamber and the

chamber is resealed. The same quantity of gas at the same pressure is again expanded into the sample chamber, and the pressure is measured. The difference in the two pressure combined with the known volume of the empty sample chamber allows the volume of the sample to be determined by way of the gas law. The accuracy and precision of the gas pycnometer in determining density is good, but the method relies greatly on the cleanliness of the sample material and purity of the analysis gas. Gas pycnometry is recognized as one of the most accurate and reproducible techniques for obtaining true, absolute, skeletal, and apparent volume and density. Inert gases, such as helium or nitrogen, are used as the displacement medium.

2.4. Dilatometry (DIL)

The linear coefficients of thermal expansion (CTE) of the alloys were determined by push-rod dilatometer Netzsch Model 402C. Dilatometry (DIL) is a thermo-analytical technique for the measurement of expansion or shrinkage of a material as a function of temperature when subjected to a controlled temperature/time program in a specified atmosphere. Dilatometers can be used to different application [58] where one the most common is the coefficient of thermal expansion (CTE) determination, in which two physical quantities i.e. displacement and temperature are measured on a sample, as it is shown in the equation (8):

$$\beta = \frac{1}{V}\left(\frac{\partial V}{\partial T}\right)_P \tag{8}$$

Where β is thermal expansion coefficient, V_0 is the sample volume at initial T_0 temperature (usually room temperature), ΔV is the volume increase between T_0 and T_1 temperatures and ΔT is the temperature increasing. The volume change of crystalline materials during heating happens for two reasons [59]: The thermal expansion due to asymmetric thermal vibrations of the ions in the crystalline lattice and the phase transformation connected with their rearrangement in the lattice. For an isotropic material with cubic form, the material volume at the temperature T is $V = V_0(1+\beta\cdot\Delta t) = l_0^3(1+\alpha\cdot\Delta t) \cong l_0^3(1+3\alpha\cdot\Delta t)$, where α is the linear CTE. So, $\beta = 3\alpha$ relationship is given. Consequently, it is sufficient to measure the change in length of a sample and calculate the linear CTE by the follow equation (8):

$$\alpha = \frac{1}{L_0}\cdot\frac{\Delta L}{\Delta T} \tag{9}$$

Where L_0 is the sample length at initial T_0 temperature and ΔL is the length increase between room T_0 and T_1 temperatures.

There are different dilatometer types; capacitance, connecting rod, high resolution – laser and optical dilatometer, where connecting rod (push rod) dilatometer is the most commonly used. In connecting rod (push rod) dilatometer a specimen is heated in a furnace and displacements of the ends of the specimen are transmitted to a sensor by means of push rods. It employs the differential principle, where the dilatometric cell which is parallel with the measured sample plays the role of the reference sample. The dilatometric cell is usually alumina or silica, where their length changes as function of temperature are known. The push-rod dilatometers use linear variable differential transducer (LVDT) as linear displacement sensor. Due to they are differential systems, calibration with a reference sample are needed. The push-rod dilatometers need 25 to 50 mm length samples. The length samples contribute to the measurability and reliability of the data and, as a consequence, to the overall accuracy of the measured value of $\Delta L/L_0$. The position of the sample in the dilatometric cell can be different, where most push-rod dilatometers employ horizontal position of the sample.

2.5. Differential Scanning Calorimetry (DSC)

Differential scanning calorimetry (DSC) measurements were performed by using a TA Q2000 calorimeter to determine the melting/solidification temperatures, latent heat and specific heat of the alloys. DSC is a thermo analytical technique in which difference in the heat flow rate (q) to a sample and to a reference sample are measured while they are subjected to a controlled temperature program. DSC analysis is usually performed under a temperature increase as a function of time, where the sample and reference are maintained at same temperature throughout the experiment and the reference sample has a well-defined heat capacity over the range of temperatures. When the sample experiments a physical transformation such as phase transition, a higher (or lower) heat flow rate through the sample will be needed, compared to the reference, in order to maintain the temperature constant on both. In this way, when endothermic phase transition occurs a higher heat flow is required, as well as the sample undergoes exothermic processes less heat is required to raise the sample temperature. The ΔT signal is converted to a heat flow rate using a temperature dependent proportionality factor, as shown in the equation (10):

$$\dot{q} = E(T) \cdot \Delta T \tag{10}$$

The proportionality factor *E(T)* depends upon the geometry and materials of construction of the differential temperature sensor, which is determined by the manufacturer and is common to all instruments of a given type. By the determination of the difference in heat flow, DSC is able to measure the amount of heat absorbed or released during the phase transitions. In DSC experiment a

curve of heat flux versus temperature or versus time is given. By the area of this curve the enthalpies of transitions can be calculated using the following equation (11):

$$\Delta H = K \cdot A \tag{11}$$

Where ΔH is the enthalpy of transition, K is the calorimetric constant determined by instrument, and A is the area under the curve.

The specific heat of the alloys was measured by quasi-isothermal modulated DSC technique (QiMTDSC). This technique involves the holding and modulation of a sample at a specific temperature for extended periods of time. The temperature can be increased or decreased through a transition, which eliminates the influence of scanning rate, while also allowing investigation of time dependent processes. The quasi-isothermal method uses a heating rate of zero, hence the heat capacity is measured as a function of time at any temperature. The general temperature program, $T(t)$, is given by the equation (12):

$$T(t) = T_0 + \beta_0 \cdot t + A_T \cdot \sin \omega \cdot t \tag{12}$$

Where T_o is the initial temperature, β_0 is the underlying (average) heating rate, t is the time, A_T is temperature amplitude and ω is angular frequency, defined as $2\pi/P$, where P is the period of the sine wave.

The measured heat flow in response to this temperature program is also periodic. Using the dynamic definition of the heat capacity, C_p, of the equation (13):

$$C_p = \frac{\partial Q}{\partial t} \cdot \frac{1}{m \cdot \beta_0} \tag{13}$$

Where, $\partial Q/\partial t$ is the heat flow and m is the sample mass. In this way, the complex heat capacity, C_p^*, is calculated according to the equation (14):

$$\left|C_p^*\right| = \frac{A_q}{A_\beta} \cdot \frac{1}{m} \tag{14}$$

Where, A_q and A_β denote the amplitudes of the modulated heat flow and heating rate.

2.6. Laser Flash Apparatus (LFA)

The laser flash Apparatus (LFA) (LFA 457 MicroFlashTM NETZSCH) is used to measure thermal diffusivity (capacity to conducted the thermal energy) of the alloy samples. The procedure

consists on the determination of the superficial temperature change of a plane solid sample heated up from the opposite parallel surface by a high intensity and short duration laser pulse. Based on this measurement, depending on the laser pulse time duration, sample thickness and heat diffusion time through the sample, different mathematical models implemented in the experimental setup provide accurate values of the thermal diffusivity. In a one-dimensional, adiabatic case the thermal diffusivity, is calculated from this temperature rise as follow in the equation (15):

$$a = 0.1388 \cdot \frac{d^2}{t_{1/2}} \tag{15}$$

Where a is the thermal diffusivity, d is the thickness of the sample and $t_{1/2}$ is the time to the half maximum.

3. Experimental processes

3.1. Synthesis process

High purity ingots of Mg, Zn and Al metals were used as primary materials (99.94 mass%, 99.995 mass% and 99.7 mass% purity, respectively) for the alloys synthesis process. The Mg and Zn were supplied by Alealsa S.A and Al was supplied by Sigma-Aldrich. The $Zn_{84}Al_{8.7}Mg_{7.3}$, $Zn_{88.7}Al_{11.3,}$ $Zn_{92.2}Mg_{7.8,}$ $Zn_{72}Mg_{28}$ and $Mg_{70}Zn_{24.9}Al_{5.1}$ eutectic alloys and the $Mg_{71}Zn_{28.9}Al_{0.1}$ and $Mg_{70}Zn_{24.4}Al_{5.6}$ quasi-peritectic alloys, were prepared by the stoichiometric proportion of the primary metals. Then, the pre-alloys, with around 60 g of weight, were placed into alumina conical crucibles. To avoid the possible oxidation during the synthesis process the alumina crucibles were hermetically closed inside AISI 316 stainless steel reactors in a glove box under argon inert atmosphere as can be observed in Figure 11.

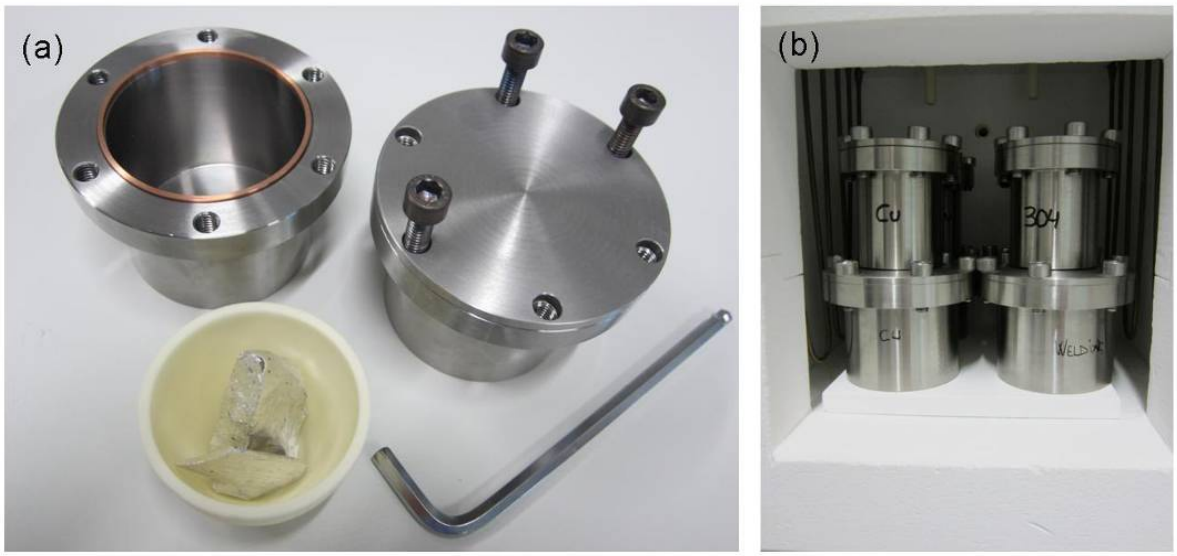

Figure 11. (a) Primary metals placed into alumina conical crucibles and stainless steel reactors. (b) Reactor places on the furnace.

The reactors were introduced in a muffle electrical furnace and were heated with a heating rate of 10 K/min up to 450-500ºC for 4-6 hours. Once the Zn was melted, Mg and Al were gradually dissolved on it. During the synthesis process an external mechanical movement was applied every 30 minutes in order to ensure the homogeneity of the alloys. After cooling down to room temperature, the solid samples were turned upside down and were melted again. This process was repeated three times in order to ensure the homogeneity of the samples. The final cooling down of five eutectic alloys was conducted at 10 K/min rate to ensure their correct crystallisations without the presence of any metastable phases. In the case of the $Mg_{70}Zn_{24.9}Al_{5.1}$ eutectic alloy and the $Mg_{71}Zn_{28.9}Al_{0.1}$, and $Mg_{70}Zn_{24.4}Al_{5.6}$ quasi-peritectic compositions cooling rates of 10 K/min and 0.1 K/min were applied to study the effect of this parameter on the microstructure of the obtained samples. Table 1 summarizes the experimental conditions of the synthesis of the materials studied in this thesis.

Alloy	Alloying temperature	Time	Numbers of consecutive synthesis processes	Cooling rate
	(ºC)	(h)	-	(K/min)
$Zn_{84}Al_{8.7}Mg_{7.3}$ eutectic	450	4	3	10
$Zn_{88.7}Al_{11.3}$ eutectic	450	4	3	10
$Zn_{92.2}Mg_{7.8}$ eutectic	450	4	3	10
$Zn_{72}Mg_{28}$ eutectic	450	4	1	10
$Mg_{70}Zn_{24.9}Al_{5.1}$ eutectic	500	6	1	0.1, 10
$Mg_{71}Zn_{28.9}Al_{0.1}$ quasi-peritectic	500	6	1	0.1, 10
$Mg_{70}Zn_{24.4}Al_{5.6}$ quasi-peritectic	500	6	1	0.1, 10

Table 1. Summary of alloys synthesis process parameters.

Finally, to conduct the characterization of the alloys, different geometries (rectangular, cylinder, tablet, etc.) of the samples were mechanized by different techniques. In this way, the turning and grinding mechanizing processes were performed in Armeria Eskola whereas that the cut and polished processes were carried out in CIC energiGUNE by a diamond saw (IsoMet 4000 BUEHLER) and a disc grinder (Saphir 520 ATA), respectively. Figure 12 shows samples with tablet and cylinder shapes for LFA and DIL measurements, respectively.

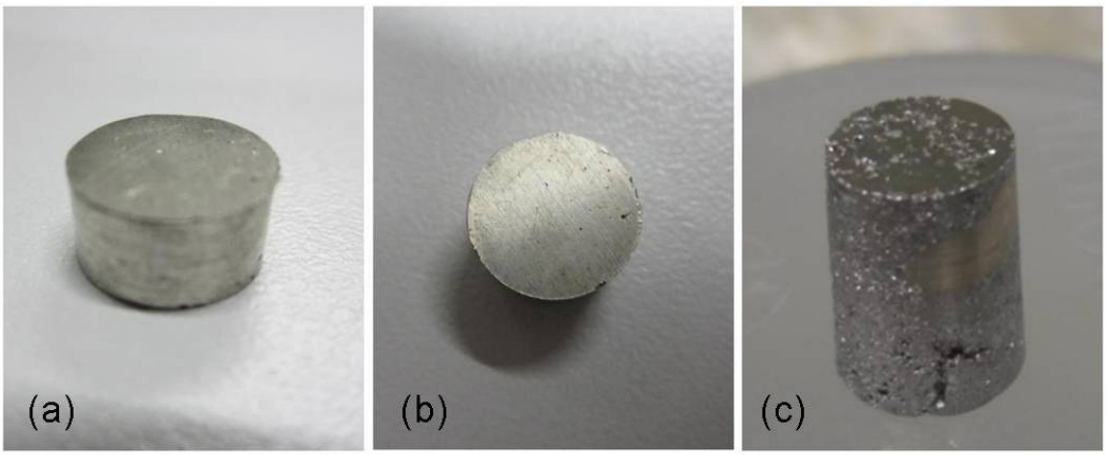

Figure 12. (a) and (b) tablet shape sample. (c) Cylinder shape sample.

3.2. Accelerated thermal cycling tests protocol

3.2.1. Short term thermal stability tests

For short term thermal stability determination alloy pieces of around 100 mg of weight were subjected to consecutive melting/solidification cycles by DSC. The samples were introduced in open alumina holders and heating/cooling rates of 10 K/min were applied under a 100 ml/min flow of protective argon atmosphere. The alloys were subjected to 100 melting/solidification cycles from 300ºC to 450ºC. The phase change temperatures and the latent heat of fusion of each cycle were continuously recorded with an experimental error of ±0.01ºC and ±0.1 %, respectively.

3.2.2. Long term thermal stability test

The long term thermal stability tests were performed for the $Zn_{72}Mg_{28}$ and $Mg_{70}Zn_{24.9}Al_{5.1}$ alloys by a tubular muffle electrical furnace as it is shown in Figure 13. Samples around 100 g were put in alumina crucibles inside of hermetically closed quartz tube under a protective argon flux (100 ml/min) in order to avoid any oxidation process. In each melting/solidification cycle, heating/cooling rate of 10 K/min was applied between 300 and 450 ºC with isothermal steps at minimum and maximum temperatures (300 and 450ºC) for 10 min. The samples of each material were subjected to a 500 melting/solidification cycles. During the test small alloy pieces of around 20 g were cut after 50, 100, 300 and 500 cycles to detect any changes in the thermophysical properties and the microstructure of the materials.

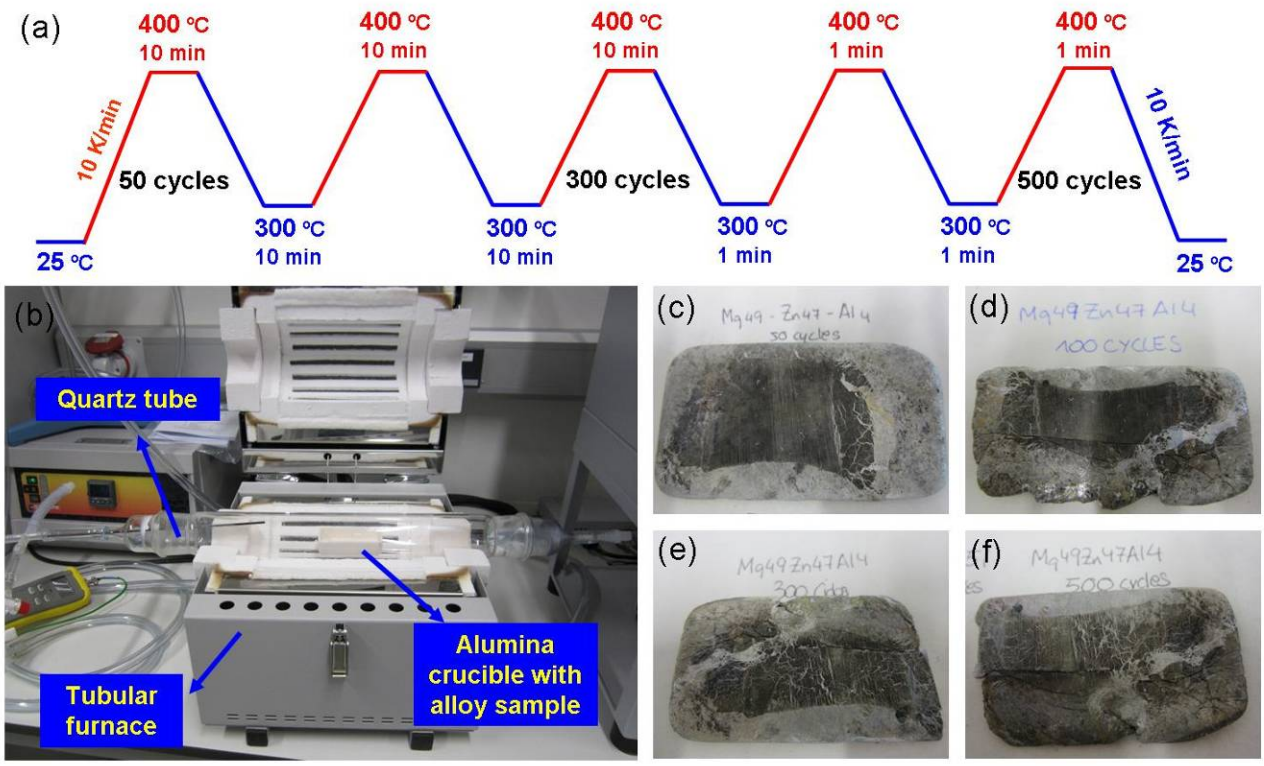

Figure 13. (a) Accelerated thermal cycling parameters. (b) Experimental setup. (c-f) $Mg_{70}Zn_{24.9}Al_{5.1}$ alloy sample after 50, 100, 300 and 500 cycles, respectively.

In this way, the phase change temperature and heat of fusion were determined by DSC analysis. Samples of around 100 mg were cycled 3 times in alumina open holders between 200ºC and 450ºC, with heating/cooling rate of 10 K/min and under argon flow of 100 ml/min.

On the other hand, the microstructure investigation of the alloy pieces was performed by SEM. For this propose, smooth surfaces of samples were prepared by using SiC papers and diamond pastes down to 3 µm grain size.

3.3. Compatibility tests protocol

The compatibility of the investigated eutectic metallic alloys with stainless steels was performed in two stages. In the first stage, the common stainless steels, i.e. AISI 304, 304L, 316 and 316L, were selected to perform the corrosion tests. In the case that the four selected stainless steels are not fully compatible with the metal alloys, in the second stage, special stainless steels, i.e. 321, 316Ti and 430, were investigated to identify the highest corrosion resistant steel to the molten alloys. The chemical compositions of the investigated stainless steels are shown in Table 2.

Stainless steels	Chemical composition (wt.%)								
AISI	C	Mn	Si	Cr	Ni	P	S	Mo	Ti
304	0.08	2	1	18-20	8.00-12.00	0.045	0.03	-	-
304L	0.03	2	1	18-20	8.00-12.00	0.045	0.03	-	-
316	0.08	2	1	16-18	10.00-14.00	0.045	0.03	2.00-3.00	-
316L	0.03	2	1	16-18	10.00-14.00	0.045	0.03	2.00-3.00	-
316Ti	0.08	2	1	16-18	10.00-14.00	0.045	0.03	2.00-3.00	(5 x C)-0.07
321	0.08	2	1	17-19	9.00-12.00	0.045	0.03	-	5 x C min
430	0.12	1	1	16-18	-	0.04	0.03	-	-

Table 2. Chemical composition of selected stainless steels in weight percentage.

For this purpose, rectangular sheets of stainless steels of around 10 mm of width, 20 mm of height and 2 mm of thickness were cut. In parallel, alloy samples of around 5 g were placed in alumina conical open crucibles. The alloys inside open crucibles were introduced in an electrical chamber furnace and were heated up to 400ºC under argon protective flow of 200 ml/min. Once the temperature was stabilized the alloy samples was maintained at 400ºC for 15 min in order to melt them. In the next step, the molten alloys were removed consecutively from the furnace and sheets of stainless steels were vertically immersed and were hold for few seconds up to the melted alloy solidified. Then, the alloy-steel samples inside alumina crucibles were hermetically closed inside stainless steels reactors in a glove box under argon inert atmosphere as can be observed in Figure 14 (a). Finally, the reactors were put in a chamber furnace and were heated at isothermal temperature of 400ºC for 360 hours and 720 hours. In this way, the $Zn_{84}Al_{8.7}Mg_{7.3}$, $Zn_{88.7}Al_{11.3}$ and $Mg_{70}Zn_{24.9}Al_{5.1}$ alloys were tested with AISI 304, 304L, 316 and 316L steels for 720 hours and $Zn_{84}Al_{8.7}Mg_{7.3}$ and $Zn_{88.7}Al_{11.3}$ alloys with 321, 316Ti and 430 steels for 360 hours. The conditions of the compatibility tests performed in this work are summarized in Table 3.

Metallic alloy (at%)	Stainless steels (AISI)	Temperature (ºC)	Time (h)
$Mg_{70}Zn_{24.9}Al_{5.1}$	304 - 304L - 316 - 316L	400	720
$Zn_{88.7}Al_{11.3}$	304 - 304L - 316 - 316L	400	720
	321 - 316Ti - 430	400	360
$Zn_{84}Al_{8.7}Mg_{7.3}$	304 - 304L - 316 - 316L	400	720
	321 - 316Ti - 430	400	360

Table 3. Summary of the performed compatibility tests conditions.

By metallographic investigations (SEM-EDX) the compatibility test results were analysed. So, previously of this analysis the alloy-steel samples were transversely cut and smooth surfaces of

alloy-steel samples were prepared by using SiC papers and diamond pastes down to 3 µm grain size as can be observed in Figures 14 (b) and (c).

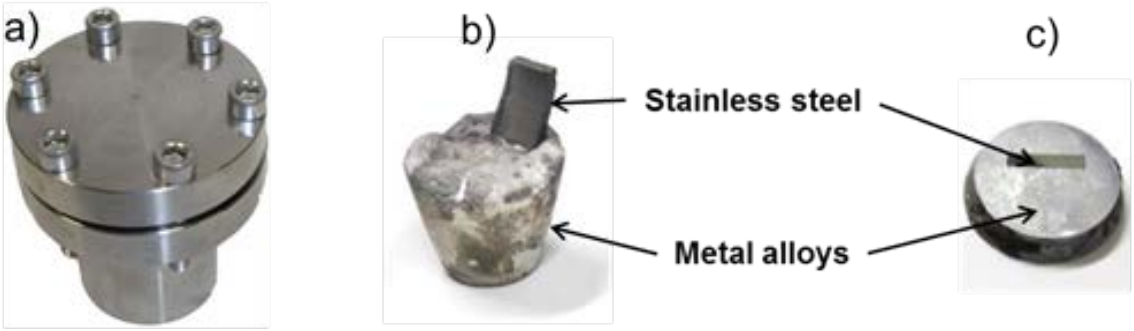

Figure 14. (a) The hermetically closed stainless steel reactor, (b) small piece of stainless steels immersed in the metal alloys after the compatibility test; and (c) sample cut and polished for SEM analysis.

3.4. Characterization methodology

3.4.1. Scanning Electron Microscopy (SEM)

The alloys microstructure and morphology investigations were performed using a Quanta FEG 250 SEM operated in high vacuum mode at 30 kV and with a back-scattered electron detector (BSED). In addition, an Apollo 10 SSD energy-dispersive X-ray spectrometer (EDX) equipped to microscope was used for elemental analysis in order to obtain chemical composition maps of the different observed sample zones. The error for quantitative standard less EDX analyses is estimated around 5%. For this propose, smooth surfaces of alloy samples were prepared by using SiC papers and diamond pastes down to 1 µm grain size.

3.4.2. X-Ray Power Diffraction (XRPD) and data analysis

X-ray powder diffraction technique was used for the structural analysis by means of a Bruker D-8 Advance Diffractometer in Bragg-Brentano geometry (θ-θ), using $CuK_{\alpha 1,2}$ radiation. The data were collected between 20° and 80° in 2θ with a step size of 0.02° and counting time of 8 second per step. To XRPD samples preparation alloy pieces were crushed until obtaining powder with a mortar.

The refinement of the diffractograms to determine the phases present in the alloys, as well as, their lattice parameters was performed using the WinPlotr/FullProf package [60,61]. The peak

shape was described by a Thompson-Cox-Hastings pseudo-Voigt function convoluted with axial divergence asymmetry function, and the background level was fixed. The refined parameters were: zero shift, lattice constants, peak profile and asymmetry parameters.

3.4.3. Gas pycnometry

To determine the density of the alloys a helium pycnometer AccuPyc II 1340 from Micromeritics was used. The densities at room temperature were measured using piece of samples of around 5 g of weight.

3.4.4. Dilatometry (DIL)

The determination of linear coefficient of thermal expansion (α) of the alloys was conducted on a push-rod dilatometer Netzsch Model 402C under inert argon atmosphere. For this proposed cylindrical samples with 10 mm of diameter and between 10-25 mm of length were mechanized through a lathe. Before the measurements, a calibration of the apparatus was done by using an alumina rod of 6 mm diameter and 15 mm of length. Instrument control and data acquisition as well as evaluation are carried out by a standard computer software package. The dilatometer used for this work was equipped with an alumina sample holder and push rod. The temperature measurement was done with a calibrated type S-thermocouple. The experiments were run in solid phase, from room temperature up to around 50ºC below to melting temperatures of the alloys with heating rate of 1 K/min and under argon flow.

3.4.5. Differential Scanning Calorimetry (DSC)

Differential scanning calorimetry (DSC) measurements were performed by using a TA Q2000 calorimeter to determine the melting/solidification temperatures, latent heat and specific heat of the alloys. For melting and solidification temperatures and latent heats determination, piece of samples of around 50 mg were measured inside open alumina sample holders and under argon flow of 100 ml/min. In order to check the reproducibility of the results three cycles between approximately 200ºC and 500ºC with heating and cooling rates of 10 K/min have been carried out. The experimental error in this technique for the phase transition temperature and latent heat are ±0.01ºC and ±0.1%, respectively.

The specific heat of the alloys was measured by modulated quasi-isothermal DSC technique. In the experiments, the modulation amplitude and period have been fixed to ±1 K and 120 seconds, respectively. Before measurements the instrument was calibrated using sapphire as standard

material. Alloy sample pieces of approximately 20 mg were placed inside aluminium hermetic pans in a glove box under argon inert atmosphere. Finally, under argon controlled atmosphere, the specific heat was measured from -80ºC to 200ºC with a step of 25 ºC. In order to avoid possible corrosion mechanisms between the alloy and the aluminium crucibles at high temperatures the maximum measuring temperature was maintained to below melting temperature of the alloys. The experimental error of this technique is below 3%.

3.4.6. Laser Flash Apparatus (LFA)

The thermal conductivity values are obtained in an indirect way from the thermal diffusivity, density and specific heat, according to the equation (16):

$$\lambda = \alpha \cdot \rho \cdot C_p \tag{16}$$

Where, λ is the thermal conductivity (W/m·K), α is the thermal diffusivity (mm^2/s), ρ is the density (kg/m^3) and C_p is the specific heat (J/g·K). The thermal diffusivity of the studied materials was obtained by using the laser flash apparatus (LFA).

For all the measurements carried out with the Laser Flash Apparatus, disc shaped samples with a side length of 10 mm and a thickness of around 1.5 mm were used. The sample machining by turning warranted parallel faces and smooth surfaces. In order to minimize the experimental error, a graphite film prime was added over the alloy samples. In other to ensure the reproducibility of the thermal diffusivity values three cycles from 50ºC to around 450ºC were carried out under argon flow (50 ml/min). The measurements were performed each 50ºC in the solid phase and each 20ºC in the liquid phase. The estimated experimental error of this technique is lower than 5% [62,63].

4. Experimental results

4.1. Structural and thermophysical characterization

4.1.1. Experimental investigation of Mg-Zn-Al metal alloys for LHS application

Introduction

In this study, three different alloys, with different Al content, have been selected from the Mg-rich corner of Mg-Zn-Al ternary phase diagram with general formulas $Mg_{71}Zn_{28.9}Al_{0.1}$, $Mg_{70}Zn_{24.9}Al_{5.1}$ and $Mg_{70}Zn_{24.4}Al_{5.6}$. Table 4 summarizes the general formula, atomic and weight compositions and the theoretical melting temperature of the investigated alloys. The first and third materials correspond to quasi-peritectic compositions and the second material corresponds to a eutectic composition. The eutectic composition is considered more suitable as PCMs for TES application due to its constant phase transition temperature. The two quasi-peritectic compositions have been selected to investigate the influence of the chemical composition changes on the thermophysical properties and consequently to study their potentiality regarding the energy storage density factor. For this propose a complete structural and thermophysical characterization of the selected metal alloys has been carried out in this section.

Alloy	Atomic percentage (%)			Weight percentage (%)			T_m *(theoretical)* (°C)	Reference
	Mg	Zn	Al	Mg	Zn	Al		
$Mg_{71}Zn_{28.9}Al_{0.1}$	71	28.9	0.1	47.7	52.2	0.1	340.48	[53]
$Mg_{70}Zn_{24.9}Al_{5.1}$	70	24.9	5.1	49.0	47.1	3.9	338.36	[53]
$Mg_{70}Zn_{24.4}Al_{5.6}$	70	24.4	5.7	49.4	46.2	4.4	340.07	[53]

Table 4.The compositions in atomic and weight portions, and the theoretical melting temperatures of $Mg_{71}Zn_{28.9}Al_{0.1}$, $Mg_{70}Zn_{24.9}Al_{5.1}$ and $Mg_{70}Zn_{24.4}Al_{5.6}$ alloys.

Results and Discussion

Structural analysis

Figure 15 shows the X-ray diffractograms of $Mg_{71}Zn_{28.9}Al_{0.1}$, $Mg_{70}Zn_{24.9}Al_{5.1}$ and $Mg_{70}Zn_{24.4}Al_{5.6}$ alloys synthesized using a cooling rate of 10 ºC/min. The results of the refinements show the presence of two phases in different proportions. The first one is an isostructural composition of the trigonal $Mg_{21}Zn_{25}$ intermetallic phase [64], and the second one is an isostructural composition of the hexagonal Mg phase [65]. According Mg-Zn-Al phase diagram [66], $Mg_{70}Zn_{24.9}Al_{5.1}$ and $Mg_{70}Zn_{24.4}Al_{5.6}$ alloys should present the cubic $Mg_{32}(Al,Zn)_{49}$ intermetallic compound as a third phase [67-69]. Ren et al. [70] suggested that $Mg_{32}(Al,Zn)_{49}$ is a metastable phase and its presence depends on the preparation conditions. Therefore, in order to study the effect of the cooling rate on the phases formation other materials have been prepared under slow cooling rate of 0.1 ºC/min. The analysis of the diffractograms shows the presence of the same phases established under the previous cooling rate of 10 ºC/min. From the one hand, this results shows that the $Mg_{32}(Al,Zn)_{49}$ has not been established under various cooling rates which is aligned with the result in [70]. From the other hand, this analysis demonstrates the stable behaviour of these ternary alloys independently of the applied cooling rates which is different to the metastable behaviour obtained for the $Mg_{72}Zn_{28}$ binary eutectic alloy where a random formation of two intermetallic phases (stable and metastable) was obtained [71]. The addition of Al metal (even a small amount of 0.1 at.%) to the Mg-Zn binary system leads to stabilise the system forming stable $Mg_{21}Zn_{25}$ intermetallic phase and Mg solid solution at room temperature.

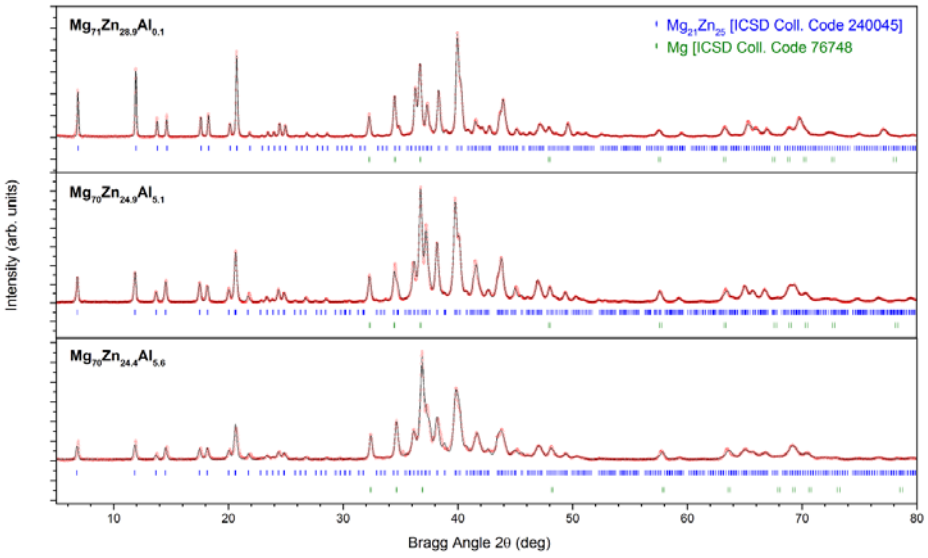

Figure 15. Experimental (--) and calculated (oo) X-ray diffraction patterns for the refinements of $Mg_{71}Zn_{28.9}Al_{0.1}$, $Mg_{70}Zn_{24.9}Al_{5.1}$ and $Mg_{70}Zn_{24.4}Al_{5.6}$ alloy samples. The bars in the lower part of the graphics represent the Bragg peak positions that correspond to Mg (bottom) and $Mg_{21}Zn_{25}$ (top) isotropic phases.

Table 5 shows the lattice parameters of the $Mg_{21}Zn_{25}$ and Mg isostructural phases obtained from the refinements in comparison to the lattice parameters of the pure phases obtained from ICSD database [64,65]. The refined lattice parameters are different to the ones of the pure $Mg_{21}Zn_{25}$ and Mg phases and these variations are related to the Zn and Al solubility in both structures.

In the case of $Mg_{71}Zn_{28.9}Al_{0.1}$ alloy, the calculated lattice parameters of both phases, $Mg_{21}Zn_{25}$ and Mg, are smaller than the ones of the pure reference phases. Considering the atomic radius of Mg (1.60 Å), Zn (1.42 Å) and Al (1.43 Å), the decrease of the lattice parameters indicates the substitution of the Mg atoms in both isostructural phases by the Zn and Al atoms which have smaller atomic radius.

Alloy	Mg lattice parameters(Å)			$Mg_{21}Zn_{25}$ lattice parameters (Å)		
	a(Å)	c(Å)	V(Å^3)	a(Å)	c(Å)	V(Å^3)
Mg	3.2093	5.2103	46.47	-	-	-
$Mg_{21}Zn_{25}$	-	-	-	25.7758	8.7624	5041.72
$Mg_{71}Zn_{28.9}Al_{0.1}$	3.2014	5.2004	46.16	25.7092	8.7281	4996.03
$Mg_{70}Zn_{24.9}Al_{5.1}$	3.1972	5.1901	45.95	25.8318	8.7296	5044.7
$Mg_{70}Zn_{24.4}Al_{5.6}$	3.1948	5.1909	45.9	25.877	8.7302	5061.77

Table 5. The refined lattice parameters of the $Mg_{21}Zn_{25}$ and Mg isotopic phases obtained from the refinements of the X-ray diffractograms of $Mg_{71}Zn_{28.9}Al_{0.1}$, $Mg_{70}Zn_{24.9}A_{l5.1}$ and $Mg_{70}Zn_{24.4}Al_{5.6}$ alloys. The lattice parameters of the pure phases are given for comparison.

In the case of $Mg_{70}Zn_{24.9}Al_{5.1}$ and $Mg_{70}Zn_{24.4}Al_{5.6}$ alloys two different effects in the lattice parameters are observed. As in $Mg_{71}Zn_{28.9}Al_{0.1}$ alloy, the lattice parameters of Mg solid solution decrease with the addition of Al due to the substitution of Mg by smaller Zn and Al atoms. However, the $Mg_{21}Zn_{25}$ phase lattice parameters increase with the addition of Al. This result suggests that the Al, present in these alloys, could be contained in the $Mg_{21}Zn_{25}$ intermetallic phase deforming its cell unit.

To confirm the results observed by XRD measurements, scanning electron microscopy (SEM) experiments were performed. The images of three alloys are shown in Figure 16 where each row of images corresponds to an alloy composition. In general, the observed structures by SEM confirm the eutectic and quasi-peritectic nature of the investigated alloys [72-74]. It can be observed that the crystal size of the phases increases with higher Al content in the material. However, in the case of the $Mg_{71}Zn_{28.9}Al_{0.1}$ alloy (Figures 16 a, b and c), the small amount of the Al which actuates as an impurity, increases the number of germination nucleus. As a consequence, the crystal size is smaller and the structure is more refined. In the first column of Figure 16, images at low magnification of the three samples cooled at 10 ºC/min confirm the homogeneity of the prepared samples. Finally, in

the second and third columns, images at high magnification of the samples cooled at 10 K/min and 0.1 K/min demonstrate that the decreasing of the cooling rate leads to larger crystal sizes.

Additionally, the images provide a strong experimental confirmation of the existence of only two phases after the solidification processes. The black coloured microstructures correspond to the Mg isostructural phase and the white coloured ones to the $Mg_{21}Zn_{25}$ isostructural phase. An exhaustive microstructural inspection of the sample surfaces also confirms the absence of the cubic $Mg_{32}(Al,Zn)_{49}$ intermetallic phase in $Mg_{70}Zn_{24.9}Al_{5.1}$ and $Mg_{70}Zn_{24.4}Al_{5.6}$ alloys.

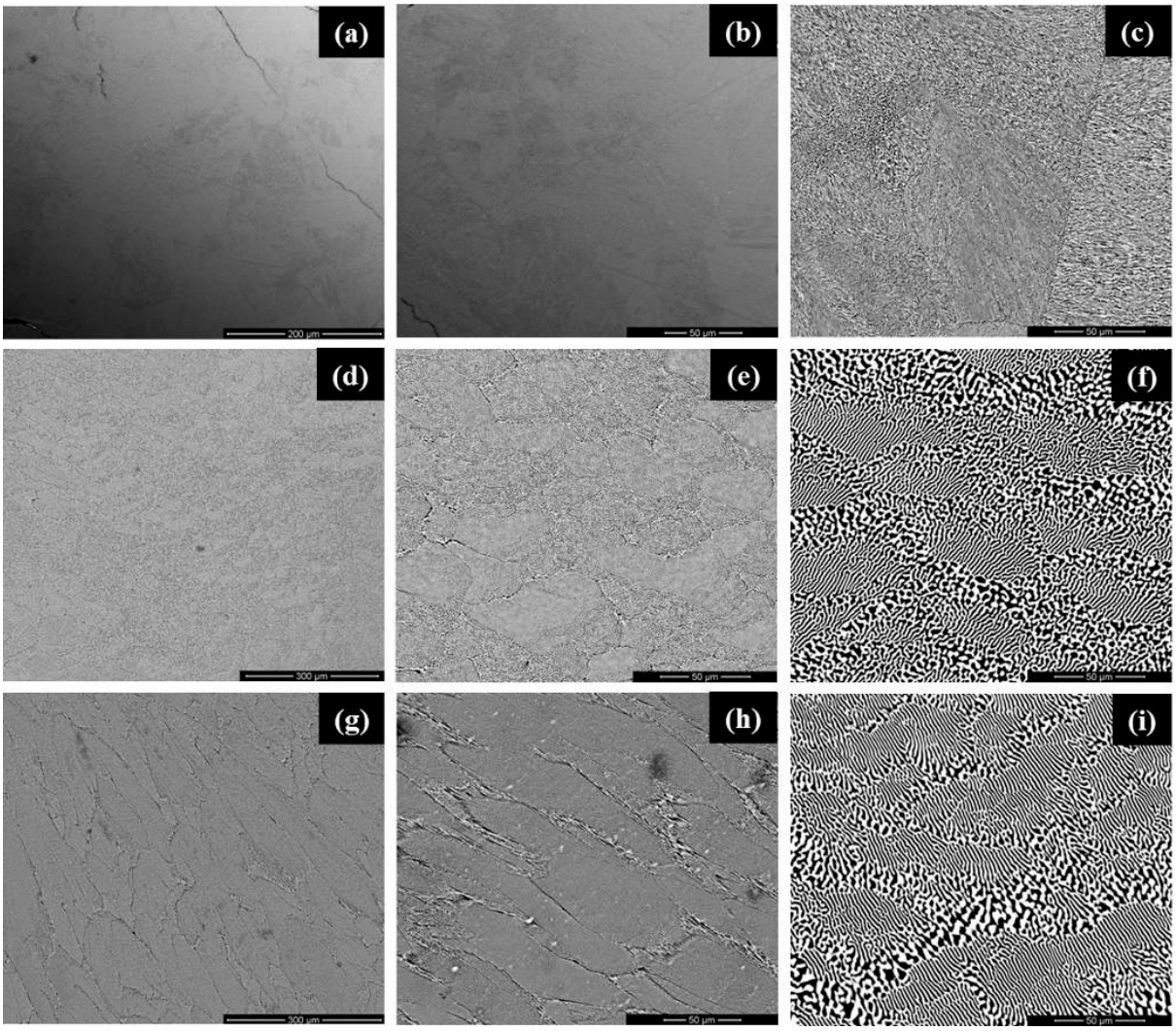

Figure 16. SEM images of $Mg_{71}Zn_{28.9}Al_{0.1}$ (a, b and c), $Mg_{70}Zn_{24.9}Al_{5.1}$ (d, e and f) and $Mg_{70}Zn_{24.4}Al_{5.6}$ (g, h and i) alloys. In the first column (a, d and g), low magnification (×400) images of the alloys cooled at 10ºC/min rate are showed. In the second (b, e and h) and third columns (c, f and i), high magnification (×1200) images of samples cooled at 10 K/min and 0.1K/min rate are showed, respectively.

In order to determine the experimental compositions of the intermetallic phases present in each alloy EDX analysis was performed. Table 6 summarizes the observed phase compositions and their proportions compared to the theoretical ones obtained from the ternary phase diagram at room temperature [65]. Regarding the Mg isotopic phase compositions, it can be observed that Mg is substituted by Zn and Al. Moreover, it can be noted that increasing the Al proportion in the alloys, the Zn solubility in Mg phase also increases. It can also be remarked that the increasing of the Al proportion in the alloy leads to an increase of the Zn solubility in the composition of Mg phase, as Ren et al. observed in [75]. For the case of the experimental $Mg_{21}Zn_{25}$ isostructural phase composition of, around 8 at.% and 10 at.% Al solution have been found in $Mg_{70}Zn_{24.9}Al_{5.1}$ and $Mg_{70}Zn_{24.4}Al_{5.6}$ alloys, respectively. The Mg-Zn-Al phase diagram at room temperature indicates a maximum Al solubility around 2.5 at.% in $Mg_{21}Zn_{25}$ phase [66]. This discrepancy between experimental and theoretical values might be related to the absence of the $Mg_{32}(Al,Zn)_{49}$ phase in these alloys. As a consequence, the Al amount associated to the ternary phase was dissolved mainly in the $Mg_{21}Zn_{25}$ phase. Another consequence, of this anomalous Al distribution in this intermetallic phase, is the increase of the lattice parameter values, as indicated by the experimental XRD analysis. So, the extension of the Al solubility in the $Mg_{21}Zn_{25}$ phase causes some deformation in its structure and gets bigger its lattice parameters. Similar extension solubility results were observed in previous study of Sn-Bi alloy system with an extension of solid solubility up to 35 at.% Bi content [76,77]. Overall, the SEM-EDX results are in agreement with the XRD analysis and confirm the presence of only two phases $Mg_{21}Zn_{25}$ and Mg in the studied materials.

Material	Composition of expected phases	Proportion of expected phases (at.%)	Composition of observed phases by EDX analysis	Proportion of observed phases (at.%)
$Mg_{71}Zn_{28.9}Al_{0.1}$	Mg	46	$Mg_{0.95}Zn_{0.04}Al_{0.01}$	43
	$Mg_{21}Zn_{25}$	54	$Mg_{21.6}Zn_{24.4}$	57
$Mg_{70}Zn_{24.9}Al_{5.1}$	Mg	46	$Mg_{0.91}Zn_{0.08}Al_{0.01}$	52
	$Mg_{21}Zn_{25}$	36	$Mg_{21.6}Zn_{20.7}Al_{3.7}$	48
	$Mg_{32}(Al, Zn)_{49}$	18	-	
$Mg_{70}Zn_{24.4}Al_{5.6}$	Mg	46	$Mg_{0.89}Zn_{0.09}Al_{0.02}$	56
	$Mg_{21}Zn_{25}$	32	$Mg_{21.2}Zn_{20.2}Al_{4.6}$	44
	$Mg_{32}(Al, Zn)_{49}$	22	-	

Table 6. Results of the phase compositions and their proportions for $Mg_{71}Zn_{28.9}Al_{0.1}$, $Mg_{70}Zn_{24.9}Al_{5.1}$ and $Mg_{70}Zn_{24.4}Al_{5.6}$ alloys.

Thermophysical characterization

Density

The determination of the density (ρ) is an important data not only to determine compaction of obtained samples but also to calculate the storage energy density of TES materials. Two techniques are used to determine the density of the materials: Archimedes technique and helium pycnometer (AccuPyc-II 1340 from Micromeritics), which is an accurate technique for measuring the density of alloys [78]. Table 7 summarizes different density values for each alloy, the theoretical value calculated from the pure expected phases obtained from the ternary phase diagram, and the experimental values obtained by helium pycnometer and Archimedes techniques measurements. As it can be observed, the density decreases with the decrease of Zn proportion in the alloys. This effect is due to the higher Zn density compared to Mg and Al ones. In the investigated alloys, the experimental density values measured by the Archimedes technique are smaller than the ones obtained by helium pycnometer. The deviation is less than 4% and corresponds to the open pores in the materials. The experimental helium pycnometer densities are smaller than the calculated ones and the difference is less than 3% which corresponds to the closed pores in the samples. So, this slight reduction in density values confirms the compactness of the materials. The total amounts of the open and close pores are less than 6%.

Alloy	Density (g/cm^3)		
	Theoretical	Experimental (pycnometer)	Experimental (Archimedes method)
$Mg_{71}Zn_{28.9}Al_{0.1}$	3.09	3	2.89
$Mg_{70}Zn_{24.9}Al_{5.1}$	3.02	2.82	2.76
$Mg_{70}Zn_{24.4}Al_{5.6}$	3.01	2.79	2.73

Table 7. Theoretical, calculated and experimental density values at room temperature of $Mg_{71}Zn_{28.9}Al_{0.1}$, $Mg_{70}Zn_{24.9}Al_{5.1}$ and $Mg_{70}Zn_{24.4}Al_{5.6}$ alloys.

Calorimetric analysis

Figure 17 shows the heating and cooling curves of DSC measurements for $Mg_{71}Zn_{28.9}Al_{0.1}$, $Mg_{70}Zn_{24.9}Al_{5.1}$ and $Mg_{70}Zn_{24.4}Al_{5.6}$ alloys. The three alloys show similar behaviour with similar melting and solidification temperatures and enthalpies. Hysteresis values between 8 ºC and 11 ºC are observed. However, the slight compositional differences between the investigated alloys lead to different phase transition mechanisms.

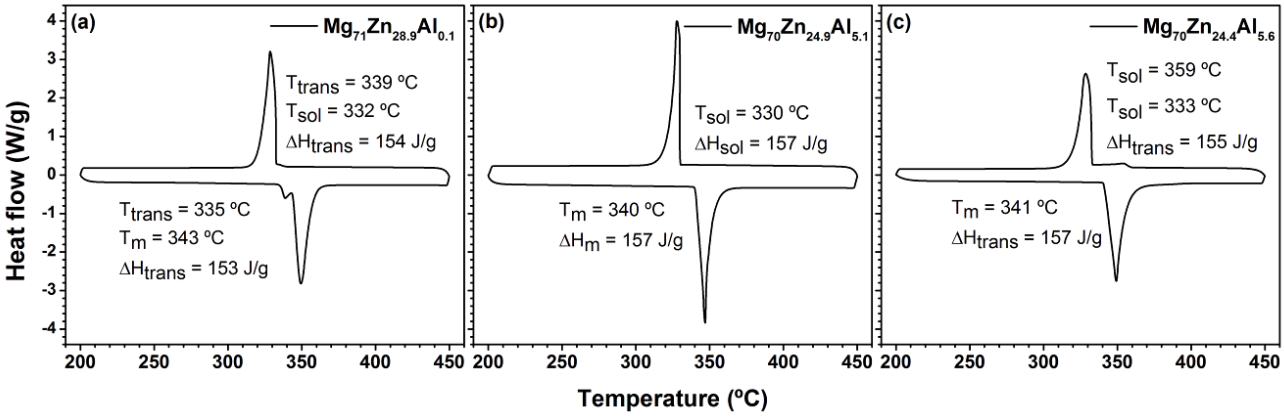

Figure 17. Melting and solidification temperatures and enthalpies obtained from DSC results at 10 °C/min heating/cooling rates. In (a) the values for Mg71Zn28.9Al0.1 quasi-peritectic alloy, in (b) the values for Mg70Zn24.9Al5.1 eutectic alloy and (c) the values for Mg70Zn24.4Al5.6 quasi-peritectic alloy.

Figure 17 (a) shows the heating and cooling curves of $Mg_{71}Zn_{28.9}Al_{0.1}$ quasi-peritectic alloy. Its behaviour is similar to the binary eutectic $Mg_{72}Zn_{28}$ alloy due to their close compositions. On the heating run, two partially overlapped transformation processes are found. The first peak at 335 ºC corresponds to the eutectoid solid-solid phase transformation $Mg_{0.95}Zn_{0.04}Al_{0.01}$ + $Mg_{24.4}Zn_{21.6}$ → ($Mg_{51}Zn_{20}$). The second one at 343 ºC is associated to the solid-liquid phase transition ($Mg_{51}Zn_{20}$) + $Mg_{24.4}Zn_{21.6}$ → L. Due to the overlapping between both transformation processes it is difficult to obtain accurate individual transformation enthalpy values. However, the overall enthalpy associated to both transitions is 153 J/g. On the cooling run, both transformation processes are totally overlapped and a single calorimetric peak is obtained at 332 ºC with a transition enthalpy of 154 J/g. Figure 17 (b) displays the heating and cooling curves of $Mg_{70}Zn_{24.9}Al_{5.1}$ eutectic alloy. On the heating $Mg_{0.91}Zn_{0.08}Al_{0.01}$ + $Mg_{21.6}Zn_{20.7}Al_{3.7}$ ↔ L eutectic phase transition occurs at 340 ºC with an enthalpy value of 157 J/g. On the cooling run the solidification process occurs at 330 ºC with an enthalpy of 157 J/g. Figure 17 (c) displays the heating and cooling curves of $Mg_{70}Zn_{24.4}Al_{5.6}$ quasi-peritectic alloy. According to phase diagram, two transformation processes are expected; the first one corresponds to eutectic phase transition and the second one, due to quasi-peritectic nature of the alloy, is associated to the melting of primary crystal. As it can be seen from the curve, only a single large peak is obtained at 341 ºC and is related to the overlapping of both transformations with an overall enthalpy of 157 J/g. During the cooling run two partially overlapped transformation processes are found. A first peak at 359 ºC corresponds to solidification of the mentioned primary crystals and the second one corresponds to L → $Mg_{0.89}Zn_{0.09}Al_{0.02}$ + $Mg_{21.2}Zn_{20.2}Al_{4.6}$ eutectic phase transition at 333 ºC.

It has to be noted that the three alloys show stable phase transitions unlike observed metastable nature in the $Mg_{72}Zn_{28}$ binary eutectic alloy [81]. On the other hand, the absence of $Mg_{32}(Al, Zn)_{49}$ intermetallic compound does not affect the phase transition behaviour of the $Mg_{70}Zn_{24.9}Al_{5.1}$ eutectic alloy, which shows a single and narrow peak in phase transition process, which ensures the eutectic and homogeneous nature of alloy sample. In contrast, the other two investigated alloys show the contribution of secondary peaks due to their chemical composition. In this way, a eutectoid reaction in $Mg_{71}Zn_{28.9}Al_{0.1}$ quasi-peritectic composition and primary crystals melting and solidification processes in $Mg_{70}Zn_{24.4}Al_{5.6}$ quasi-peritectic alloy have been observed.

The observed behaviours of DSC curves of the investigated alloys are in agreement with the expected reactions sequences and also with the theoretical and experimental melting temperatures and transition enthalpies values reported by several authors [79-81].

Specific heat

The specific heat (C_p) of the alloys has been measured by means of the modulated DSC method from -80 ºC to 200 ºC for $Mg_{71}Zn_{28.9}Al_{0.1}$ and $Mg_{70}Zn_{24.4}Al_{5.6}$ alloys. The specific heat data of $Mg_{70}Zn_{24.4}Al_{5.6}$ alloy are not presented due to their similarity of Cp values of $Mg_{70}Zn_{24.8}Al_{5.1}$. As it was explained recently in Ref. [71] the C_p of metal alloys can be calculated in the complete temperature range through a theoretical approach. This thermodynamic calculation has been used to determine the C_p of the three investigated alloys. The experimental and calculated data show good agreements as can be clearly observed in Figure 18. Then, three alloys show similar C_p values with a difference around 1 to 4% at 300 ºC. On the other hand, $Mg_{71}Zn_{28.9}Al_{0.1}$ alloy presents the lower C_p values due to its lower content of Al. The obtained values at 25 ºC is around 0.70 J/g·K, 0.72 J/g·K and 0.73 J/g·K for $Mg_{71}Zn_{28.9}Al_{0.1}$, $Mg_{70}Zn_{24.9}Al_{5.1}$ and $Mg_{70}Zn_{24.4}Al_{5.6}$ alloys, respectively.

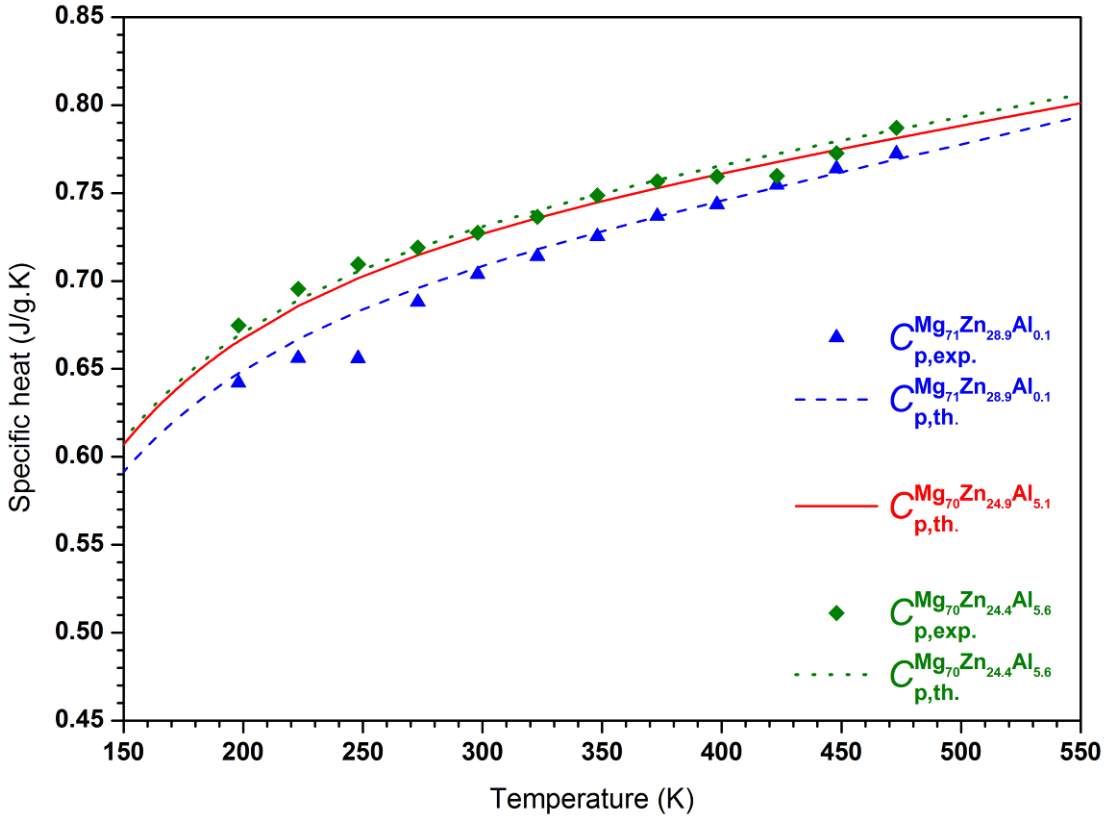

Figure 18. The experimental and calculated Cp data for (blue) $Mg_{71}Zn_{28.9}Al_{0.1}$ and (green) $Mg_{70}Zn_{24.4}Al_{5.6}$ alloys. The calculated Cp data for (red) $Mg_{70}Zn_{24.9}Al_{5.1}$ alloy.

Thermal diffusivity and thermal conductivity

The high thermal conductivity (λ) of metals and alloys is the main advantage when compared with current heat storage materials, such as molten salts. Figure 19 shows the thermal diffusivity (α) curves of the three investigated materials obtained by means of the laser flash technique. The measurements are obtained in the temperature range from 50 ºC to 400 ºC covering the solid and liquid phases. The obtained thermal diffusivities at room temperature of $Mg_{71}Zn_{28.9}Al_{0.1}$, $Mg_{70}Zn_{24.9}Al_{5.1}$ and $Mg_{70}Zn_{24.4}Al_{5.6}$ materials are 26.2 mm^2/s, 22.5 mm^2/s and 20.4 mm^2/s, respectively. In the solid phase range, up to around 320 ºC, the curves are approximately constant and then, after the melting process, the measured values decrease around the half, 11.0 mm^2/s, 14.9 mm^2/s and 11.4 mm^2/s at 350 ºC for $Mg_{71}Zn_{28.9}Al_{0.1}$, $Mg_{70}Zn_{24.9}Al_{5.1}$ and $Mg_{70}Zn_{24.4}Al_{5.6}$ alloys, respectively.

According to equation (16), the thermal conductivity (λ) was calculated in a temperature range from 50 ºC to 400 ºC using the following parameters: (i) The experimental thermal diffusivity (ii) the density, which has been approximated to a constant value equal to the one measured at room temperature (iii) the calculated C_p values due to the lack of experimental data in the complete

temperature range. Figure 19 shows the obtained λ values for the investigated alloys. The thermal conductivities at 50 ºC are 56.5 W/m·K, 46.8 W/m·K and 40.8 W/m·K for the $Mg_{71}Zn_{28.9}Al_{0.1}$, $Mg_{70}Zn_{24.9}Al_{5.1}$ and $Mg_{70}Zn_{24.4}Al_{5.6}$ alloys, respectively. Similar behaviour to the thermal diffusivity curves is observed due to the quasi linear behaviour of the specific heat and the constant value of the density in this range of temperature. Thereby, the thermal conductivity curves are approximately constant in the solid phase and decrease up to half in liquid phase. However, the three investigated alloys present high thermal conductivity values, being the lowest value in liquid phase 26.6 W/m·K, 34.7 W/m·K and 25.7 W/m·K for $Mg_{71}Zn_{28.9}Al_{0.1}$, $Mg_{70}Zn_{24.9}Al_{5.1}$ and $Mg_{70}Zn_{24.4}Al_{5.6}$ alloys, respectively.

The obtained thermal conductivity values for the three alloys are smaller than the obtained for the $Mg_{72}Zn_{28}$ binary eutectic alloy [82]. This result is due to the periodicity reduction of unit cells of Mg and $Mg_{21}Zn_{25}$ phases due to Al presence in them, As an example, the $Mg_{70}Zn_{24.9}Al_{5.1}$ eutectic alloy with around 5 at.% of the Al content shows a value of thermal conductivity 30 % lower than the obtained for the $Mg_{72}Zn_{28}$ alloy at 50 ºC and the $Mg_{71}Zn_{28.9}Al_{0.1}$ alloy with a small amount of 0.1 at.% Al shows 15.6 % lower thermal conductivity than the eutectic Mg-Zn binary alloy.

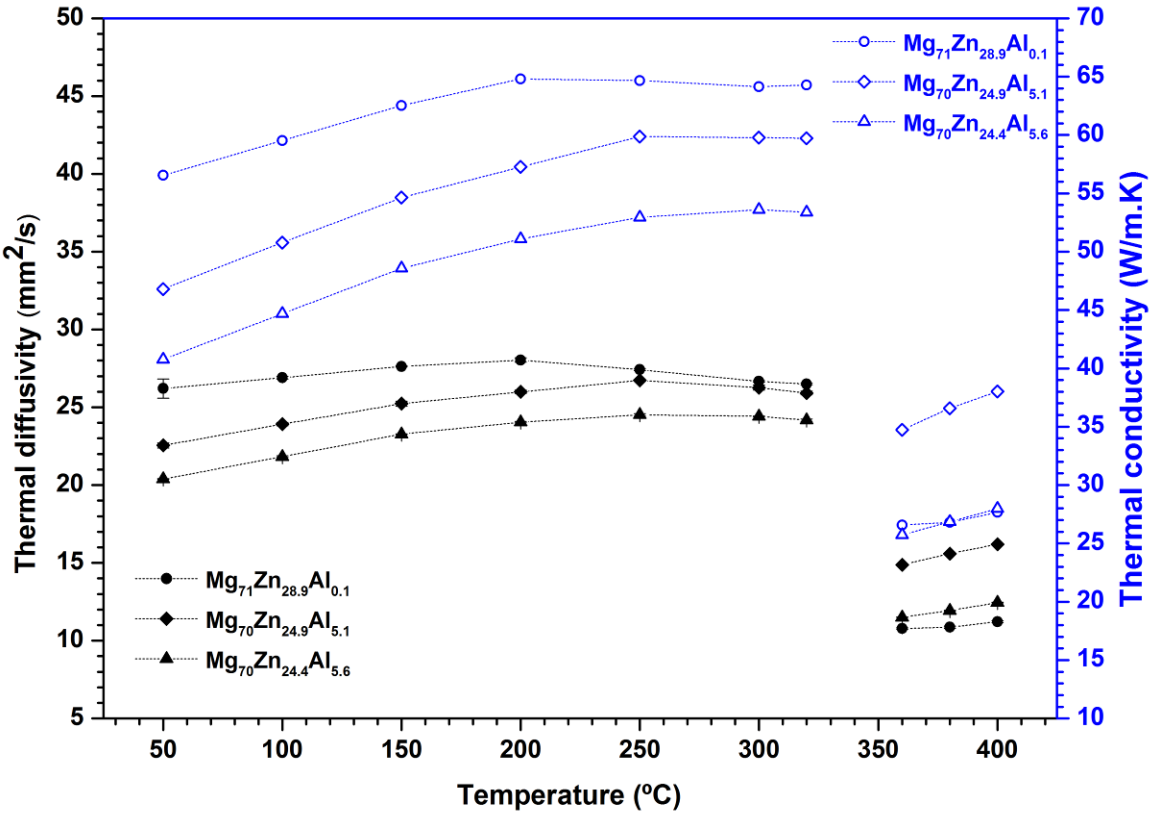

Figure 19. Thermal diffusivity and conductivity of (circle) $Mg_{71}Zn_{28.9}Al_{0.1}$, (diamond) $Mg_{70}Zn_{24.9}Al_{5.1}$ and (triangle) $Mg_{70}Zn_{24.4}Al_{5.6}$ alloy compositions. The thermal diffusivity is indicated by open symbols and the thermal conductivity by solid symbols. Dotted line is a guide for the eyes.

Conclusions

In this work, $Mg_{71}Zn_{28.9}Al_{0.1}$ (quasi-peritectic), $Mg_{70}Zn_{24.9}Al_{5.1}$ (eutectic) and $Mg_{70}Zn_{24.4}Al_{5.6}$ (quasi-peritectic) alloys have been selected as potential PCMs. The structural and thermophysical characterization of the selected alloys confirms that the three compositions are suitable to be used as high thermal conductivity phase change materials for thermal energy storage applications. The studied metal alloys have shown high structural stabilities in comparison to the binary eutectic $Mg_{72}Zn_{28}$ metal alloy which has shown a random formation of stable and metastable phases. In this work, independently of the cooling rate only the stable phase compositions, even in $Mg_{71}Zn_{28.9}Al_{0.1}$ metal alloy where a small amount 0.1 at.% of Al content is present, have been established at room temperature. The experimental values of the thermophysical properties obtained for $Mg_{71}Zn_{28.9}Al_{0.1}$, $Mg_{70}Zn_{24.9}Al_{5.1}$ and $Mg_{70}Zn_{24.4}Al_{5.6}$ alloys are similar. A large difference was obtained for the thermal diffusivity and conductivity properties. In this regard, a small variation of around 5 % in the Al content in the alloy lead to a difference of around 29 % in the measured thermal conductivity. Their thermal conductivity values are also smaller than the obtained for the $Mg_{72}Zn_{28}$ binary eutectic alloy. These thermal conductivity reductions are due to Al presence in Mg and $Mg_{21}Zn_{25}$ phases, which reduces the periodicity of their unit cells and as consequence the mean free path of electrons in the crystalline structures of phases. However, the obtained thermal conductivity values for the studied alloys are still high, being the lower value around 26 W/m·K in liquid phase. The high thermal conductivity of the investigated metallic PCMs will allow the design and construction of TES devices with extremely fast charging/discharging rates.

In general, this investigation has shown the high potential of Mg-Zn-Al ternary system in thermal energy storage area. Within the studied compositions, the $Mg_{70}Zn_{24.9}Al_{5.1}$ eutectic alloy could be the best candidate for this kind of application due to its eutectic nature which will display better its long term thermal stability.

4.1.2. Zinc-rich eutectic alloys for latent heat storage applications

Introduction

In this section, the complete characterization of Zn-rich eutectic alloys as LHS materials is carried out. In particular, $Zn_{84}Al_{8.7}Mg_{7.3}$, $Zn_{84.7}Al_{11.3}$ and $Zn_{92.2}Mg_{7.8}$ (at.%) eutectic alloys, with melting point between 340 – 380 ºC, have been evaluated. The calculated liquidus projection of Zn-Al-Mg ternary phase diagram is shown in Figure 20 [81]. The main goal is to determine their relevant thermophysical properties in the field of thermal energy storage in order to demonstrate their suitability as storage media. Once the correct eutectic compositions of the synthesized alloys are confirmed, the melting/solidification temperatures, phase transition latent heat, specific heat and thermal conductivity have been carried out. On the other hand, several of current investigations about high temperature phase change material for solar TES have been shown and discussed.

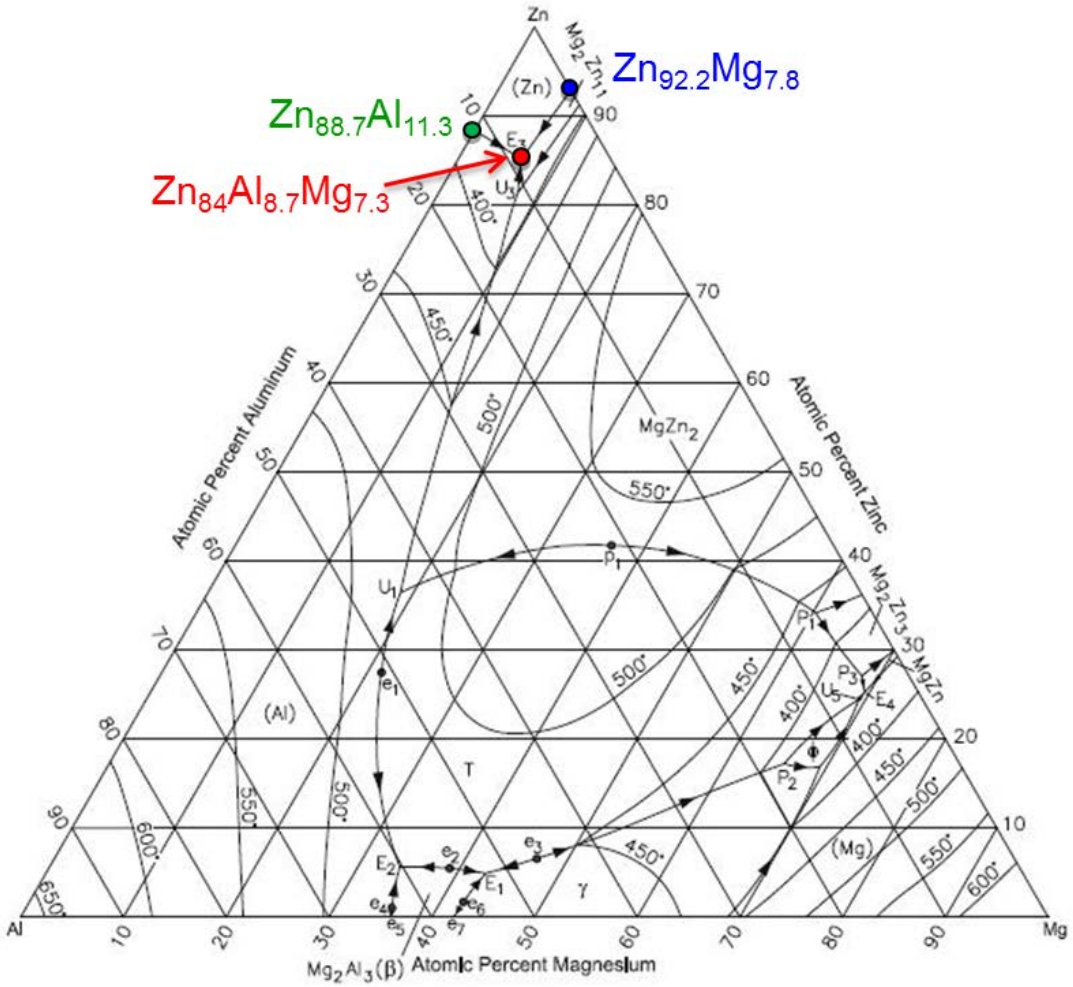

Figure 20. Mg-Zn-Al calculated liquidus projection [81].

Results and discussion

Structural analysis

After the synthesis processes described above, the correct eutectic compositions of $Zn_{84}Al_{8.7}Mg_{7.6}$, $Zn_{88.7}Al_{11.3}$ and $Zn_{92.2}Al_{7.8}$ alloy samples have been checked by means of XRD and SEM analysis. The identification of the phases present in each sample has been obtained by XRD analysis and the results are shown in Figure 21. As can be seen, the diffractogram of $Zn_{84}Al_{8.7}Mg_{7.6}$ sample exhibits a combination of the Mg_2Zn_{11}-Al-Zn ternary eutectic structure. The diffractogram of $Zn_{88.7}Al_{11.3}$ sample presents Al-Zn binary eutectic structure. And the $Zn_{92.2}Mg_{7.8}$ sample shows Zn-$MgZn_2$ binary eutectic structure with traces of Mg_2Zn_{11} intermetallic phase. The observed phase combination in first and second samples are in agreement with equilibrium phase diagrams whereas on the third sample the Zn-$MgZn_2$ metastable eutectic structure with traces of Mg_2Zn_{11} phase is observed instead of Zn-Mg_2Zn_{11} stable eutectic structure. However, as M. V Akdepniz et al. [83] indicate the $Zn_{92.2}Mg_{7.8}$ eutectic alloy exhibit competitive growth between these metastable and stable eutectic systems, where the metastable Zn-$MgZn_2$ eutectic mixture are observed under normal solidification conditions and the stable Zn-Mg_2Zn_{11} eutectic mixtures after rapid solidification. On the other hand, the $MgZn_2$ primary phase is involved in the subsequent Mg_2Zn_{11} phase formation through $MgZn_2 + L \rightarrow Mg_2Zn_{11}$ peritectic reaction. So, the observation of Mg_2Zn_{11} phase traces in this sample is due to the incomplete peritectic transformation, which is consequence of the metastable nature of $MgZn_2$ phase.

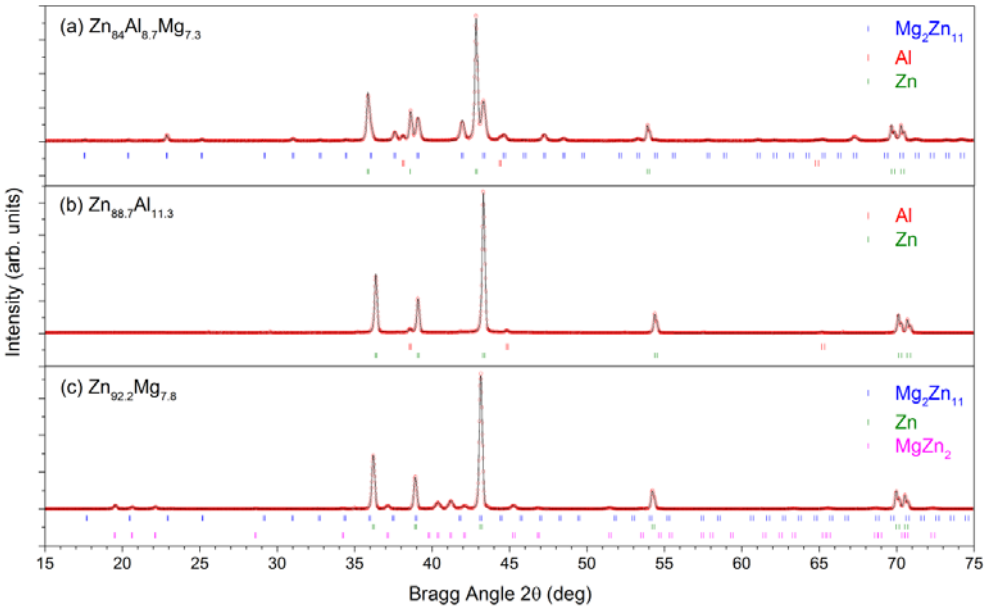

Figure 21. X-ray diffraction patterns of the (a) $Zn_{84}Al_{8.7}Mg_{7.6}$, (b) $Zn_{88.7}Al_{11.3}$ and (c) $Zn_{92.2}Al_{7.8}$ alloys. The bars in the lower part of the graphics represent the Bragg peak positions that correspond to each detected phase.

The lattice parameters, of phases presented in each alloy, have been obtained by profile machine refinements. The Table 8 shows their values in comparison the lattice parameters of the pure phases obtained from ICSD database.

Alloy	Lattice parameters			
	Phases	a (Å)	c (Å)	V (Å^3)
$Zn_{84}Al_{8.7}Mg_{7.3}$	Al	4.041	-	66.01
	Zn	2.661	4.945	30.32
	Mg_2Zn_{11}	8.525	-	619.55
$Zn_{88.7}Al_{11.3}$	Zn	2.665	4.95	30.46
	Al	4.05	-	66.44
$Zn_{92.2}Mg_{7.8}$	Zn	2.664	4.946	30.39
	Mg_2Zn_{11}	8.624	-	641.46
	$MgZn_2$	5.218	8.563	201.92
Lattice parameters from ICSD data base	Al	4.05	-	66.41
	Zn	2.664	4.957	30.39
	Mg_2Zn_{11}	8.552	-	625.47
	$MgZn_2$	5.223	8.566	202.37

Table 8. The lattice parameters of the phases in alloy samples in comparison with their values from the ICSD database. [ICSD codes: Al (10216), Zn (421014), Mg_2Zn_{11} (104898) and $MgZn_2$ (150576)].

In the $Zn_{84}Al_{8.7}Mg_{7.3}$ alloy, the Al and Zn solid solution lattice parameters are similar to those of Al and Zn pure phases, which indicate a high level of purity in the crystalline structures of these phases. However, the Mg_2Zn_{11} intermetallic phase shows a slight reduction, from 8.552 to 8.525. Considering the atomic radius of Mg (1.60 Å), Zn (1.42 Å) and Al (1.43 Å), this decreasing indicates the substitution of the Mg by the Zn and Al atoms. In the $Zn_{88.7}Al_{11.3}$ alloy, the Zn and Al solid solution lattice parameters do not show any changes respect Al and Zn pure phase parameters. This result notes the very high purity of Zn and Al solid solution. In the $Zn_{92.2}Mg_{7.8}$ alloy, the Zn solid solution lattice parameters are similar to ones of Zn pure phases, confirming its high purity. However, The $MgZn_2$ phase parameters are slightly lower than their values in $MgZn_2$ pure phase, showing a reduction from 5.223 to 5.218. This reduction indicated the substitution of the Mg by the Zn atoms. Conversely, the Mg_2Zn_{11} phase lattice parameters are higher than those of pure Mg_2Zn_{11} phases. They increase markedly from 8.552 to 8.624, which indicated the substitution of the Zn by the Mg atoms in the crystalline structure of this intermetallic phase.

Sample surfaces have been analysed by SEM to ensure the homogeneity and the correct eutectic microstructure of studied metal alloys. Figure 22 shows SEM images of the samples at three different magnifications for each one. In general, the three samples show the expected lamellar eutectic microstructures, where images at low magnification confirm the homogeneity of eutectic structures on samples. Thereby, the microstructure of the eutectic $Zn_{84}Al_{8.7}Mg_{7.6}$ alloy is composed

of Mg_2Zn_{11}, (α-Al + η-Zn)$_{eutectoid}$ and η-Zn three phases, which are observed in grey, dark-grey and light-grey, respectively. The regular Al-Zn lamellar structure of the eutectic $Zn_{88.7}Al_{11.3}$ alloy can be clearly distinguished in Figure 22, where α-Al is in black colour and η-Zn in white. Finally, $MgZn_2$ and η-Zn phases that composed the metastable eutectic microstructure of $Zn_{92.2}Al_{7.8}$ alloy are in grey and black, respectively. The traces of Mg_2Zn_{11} phase identified in this sample form Mg_2Zn_{11}-Zn stable eutectic structure; however this microstructure has not been distinguished from the metastable one due to the low amount of Mg_2Zn_{11}.

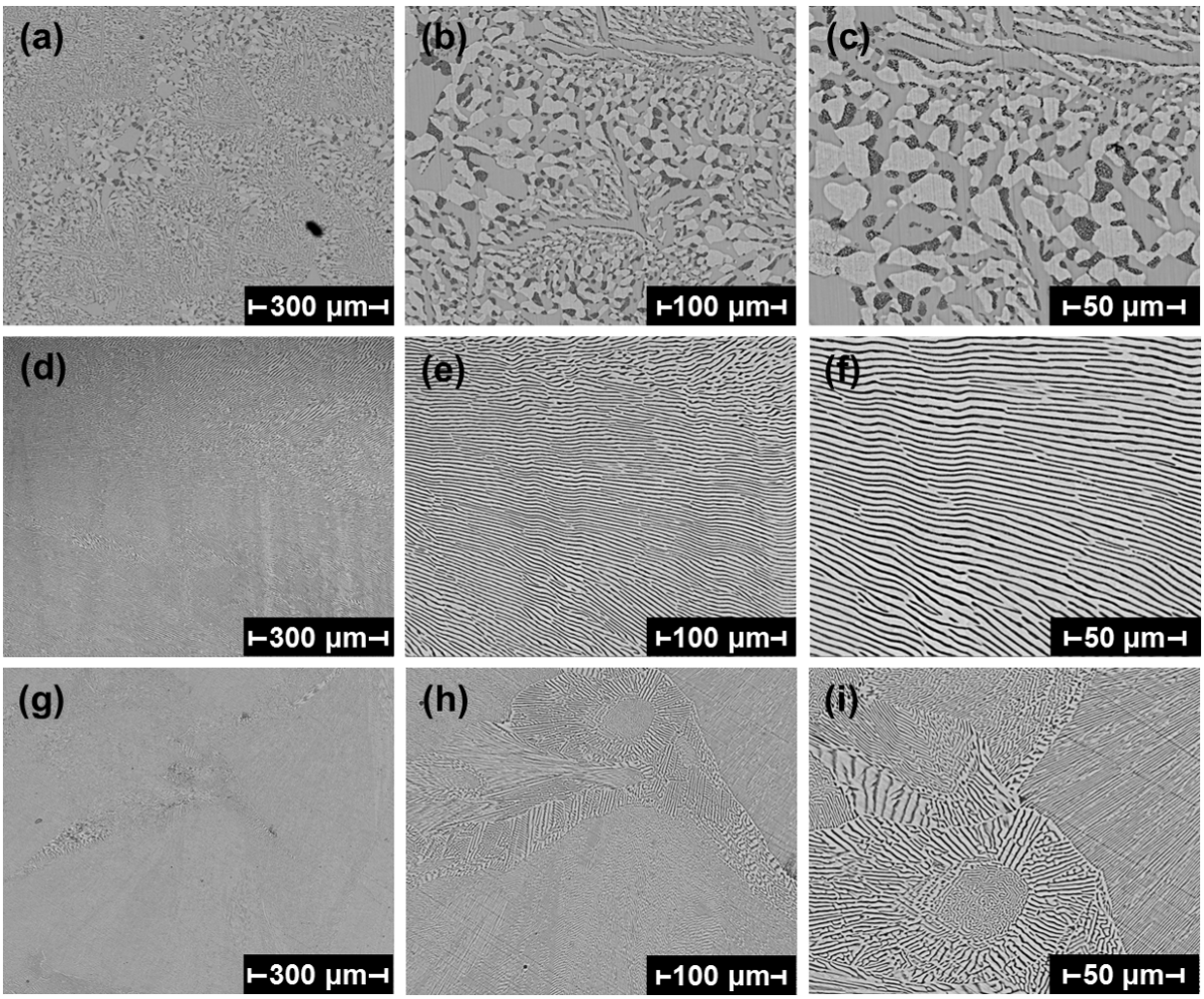

Figure 22. SEM images of $Zn_{84}Al_{8.7}Mg_{7.6}$ (a-c), $Zn_{88.7}Al_{11.3}$ (d-f) and $Zn_{92.2}Mg_{7.8}$ (g-i) eutectic alloys at 300X (300 µm), 800X (100 µm) and 1500X (50 µm) magnifications.

Thermophysical characterization

Calorimetric analysis

Phase transition latent heats and melting/solidification temperatures were measured by calorimetric analysis (DSC). After measurements, no weight variation was observed in alloy

samples, confirming the absence of oxidation and evaporation reaction during measurements. The stable phase equilibrium of three eutectic alloys was confirmed by the reproducibility of DSC curves at different cycle's number as shown in Figure 23. In general, three alloys show their melting and solidification eutectic phase transition processes by narrow peaks on the bottom and top part of each curve, respectively, whereas, the $Zn_{84}Al_{8.7}Mg_{7.6}$ and $Zn_{88.7}Al_{11.3}$ show also a second peak corresponding to a eutectoid reaction. The observed reaction sequence and melting temperatures are in agreement with the theoretical ones of the equilibrium phase diagrams [53-55].

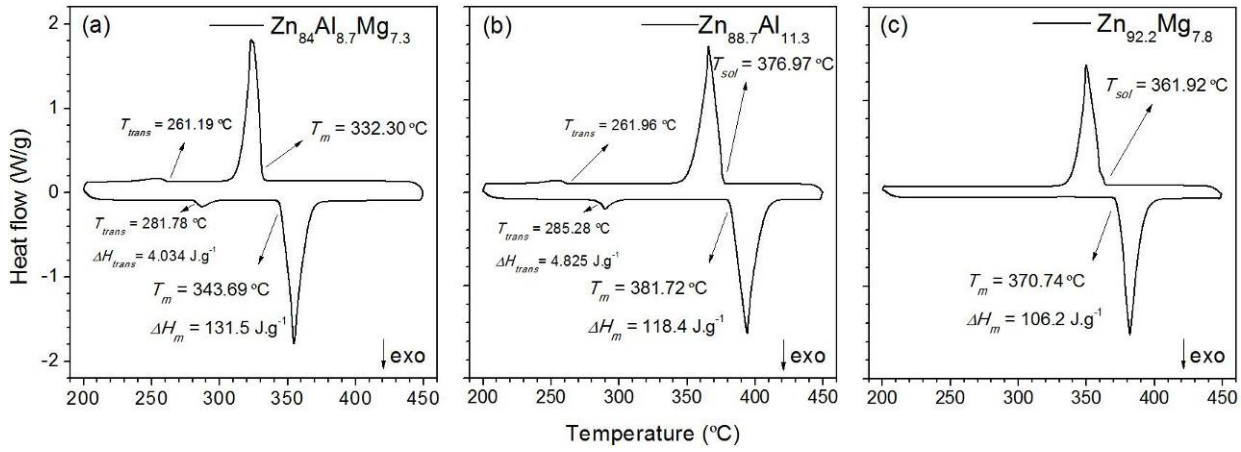

Figure 23. DSC curves of (a) $Zn_{84}Al_{8.7}Mg_{7.6}$, (b) $Zn_{88.7}Al_{11.3}$ and (c) $Zn_{92.2}Al_{7.8}$ eutectic alloys.

On the heating run of $Zn_{84}Al_{8.7}Mg_{7.6}$ alloy two exothermic peaks can be observed in Figure 23 (a). The first peak at 281.78 ºC corresponds to the transformation predicted in the phase diagram of α-Al + η-Zn → β-Al (Zn-rich Al solid solution) solid → solid phase transition (eutectoid reaction). The enthalpy value of this phase transition is around 4.03 $J \cdot g^{-1}$. Then, the β-Al + η-Zn + Mg_2Zn_{11} → L eutectic melting process occurs at temperature of 343.69 ºC and with fusion heat of 131.5 $J \cdot g^{-1}$. On the cooling run, same phase transition occurs with temperatures of 332.30 ºC. Moreover, the phase transition temperatures show 11.39 ºC of hysteresis. The $Zn_{88.7}Al_{11.3}$ alloy in Figure 23 (b) shows the same solid → solid phase transition α-Al + η-Zn ↔ β-Al reaction, with melting temperature and fusion heat of 285.28 ºC and 4.82 $J \cdot g^{-1}$, respectively. In this case, the melting and solidification temperatures are 381.72 and 376.97 ºC, respectively, in the β-Al + η-Zn ↔ L phase transition, with heat of fusion of 118.4 $J \cdot g^{-1}$ And a small hysteresis of 4.75 ºC. Regarding the $Zn_{92.2}Mg_{7.8}$ alloy in Figure 23 (c), the η-Zn + $MgZn_2$ → L metastable eutectic phase transition process occurs at intermediate melting and solidification temperatures of 370.74 and 361.92 ºC, respectively. On the other hand, this alloy shows the lowest latent heat of 106.2 $J \cdot g^{-1}$ and a hysteresis of 8.82 ºC.

Three alloys shows their eutectic meting temperatures in a narrow temperature range, as well as, similar heats of fusion values, where $Zn_{84}Al_{8.7}Mg_{7.6}$, $Zn_{88.7}Al_{11.3}$ and $Zn_{92.2}Mg_{7.8}$ alloy, melt at 343.69, 381.72 and 370.74 ºC with 131.5, 118.4 and 106.2 $J \cdot g^{-1}$, respectively, where, a slightly hysteresis less than 12 ºC has been observed. According to [56] the composition of Zn-Al eutectic alloy is $Zn_{90.8}Al_{9.2}$, which is slight different from $Zn_{88.7}Al_{11.3}$ composition. On the other hand, melting point of 381 ºC and heat of fusion of 138 $J \cdot g^{-1}$ are indicated for this eutectic binary alloy, which are in agreement with obtained results in this work. In a previous work by E. Risueño et al. [84], $Zn_{85.8}Al_{8.2}Mg_6$ composition was characterized as Zn-Al-Mg ternary eutectic alloy, where 344ºC of melting point and 104 $J \cdot g^{-1}$ of heat of fusion were observed. In this study, the eutectic composition of this ternary alloy has been corrected and the new composition ($Zn_{84}Al_{8.7}Mg_{7.6}$) has been characterized. The $Zn_{84}Al_{8.7}Mg_{7.6}$ alloy shows similar melting temperature and higher latent heat than $Zn_{85.8}Al_{8.2}Mg_6$ alloy. No other publications on proposed metal alloys as PCM have been found.

Specific heat

The specific heat (C_p) was only measured in the solid phase by ramp modulated DSC method in the temperature range between RT and 300ºC. Besides, the experimental results are also compared with a semi-empirical specific heat model in order to understand the underlying physical mechanisms leading to the obtained experimental specific heat data. This theoretical model takes into account the harmonic, electronic and anharmonic specific heat contribution of the individual metals and is amply described in [71]. The experimental and calculated specific heats together the standard deviations (SD) between them are shown in Table 9.

	$Zn_{84}Al_{8.7}Mg_{7.6}$			$Zn_{88.7}Al_{11.3}$			$Zn_{92.2}Mg_{7.8}$		
T (ºC)	Cp_{exp} ($J \cdot kg^{-1} \cdot K^{-1}$)	Cp_{model}	*SD* %	Cp_{exp} ($J \cdot kg^{-1} \cdot K^{-1}$)	Cp_{model}	*SD* %	Cp_{exp} ($J \cdot kg^{-1} \cdot K^{-1}$)	Cp_{model}	*SD* %
40	457.01	443.51	3.0	449.24	427.86	5.0	466.23	421.30	10.7
60	465.91	447.87	4.0	455.93	431.84	5.6	467.82	424.94	10.1
80	473.21	452.03	4.7	462.40	435.75	6.1	477.69	428.52	11.5
100	476.90	456.04	4.6	467.00	439.50	6.3	495.90	431.99	14.8
120	483.27	459.95	5.1	474.99	443.15	7.2	516.17	435.37	18.6
140	488.75	463.80	5.4	482.82	446.73	8.1	521.50	438.69	18.9
160	494.74	467.59	5.8	490.61	450.26	9.0	519.63	441.97	17.6
180	498.73	471.35	5.8	497.40	453.76	9.6	510.08	445.23	14.6
200	503.46	475.12	6.0	503.75	457.25	10.2	504.92	448.49	12.6
220	510.81	478.89	6.7	513.37	460.73	11.4	501.91	451.76	11.1
240	517.33	482.69	7.2	528.14	464.24	13.8	506.22	455.04	11.2
260	528.82	486.52	8.7	547.36	467.77	17.0	507.18	458.36	10.7
280	502.37	490.41	2.4	563.41	471.34	19.5	524.77	465.11	12.8
300	532.11	494.35	7.6	535.29	474.96	12.7	521.82	468.56	11.4

Table 9. Experimental and calculated specific heats of eutectic $Zn_{84}Al_{8.7}Mg_{7.6}$, $Zn_{88.7}Al_{11.3}$ and $Zn_{92.2}Mg_{7.8}$ alloys and standard deviations between both values.

In general, C_p increases with temperature and three alloys display similar C_p values in all temperature range. In this way, the experimental specific heats at 40 and 300 ºC are 457.01 – 532.11 $J \cdot kg^{-1} \cdot K^{-1}$ for $Zn_{84}Al_{8.7}Mg_{7.3}$ alloy, 449.24 – 535.29 $J \cdot kg^{-1} \cdot K^{-1}$ for $Zn_{88.7}Al_{11.3}$ and 466.23 – 521.82 $J \cdot kg^{-1} \cdot K^{-1}$ for $Zn_{92.2}Mg_{7.8}$. The C_p increases as Mg and Al concentration increases, where the $Zn_{84}Al_{8.7}Mg_{7.6}$ alloy shows the highest value, followed successively by $Zn_{88.7}Al_{11.3}$ and $Zn_{92.2}Mg_{7.8}$ alloys. The obtained specific heats are higher than the one of pure Zn (390 $J \cdot kg^{-1} \cdot K^{-1}$) due to the specific heat contribution of Mg (1023 $J \cdot kg^{-1} \cdot K^{-1}$) and Al (897 $J \cdot kg^{-1} \cdot K^{-1}$) metals. The calculated and experimental C_p present a good agreement where average standard deviations are 5.5, 10.1 and 13.3 % for $Zn_{84}Al_{8.7}Mg_{7.3,}$ $Zn_{84.7}Al_{11.3}$ and $Zn_{92.2}Mg_{7.8}$, respectively. In the $Zn_{84}Al_{8.7}Mg_{7.3}$ and $Zn_{84.7}Al_{11.3}$ alloys, maximum SD is observed between 260 and 380 ºC due to the α-Al + η-Zn ↔ β-Al eutectoid reaction in this temperature range.

Thermal conductivity

Thermal conductivities of investigated alloys were indirectly calculated in a temperature range between 50 and 450 ºC as a product of the thermal diffusivity, density and specific heat. For this propose, thermal diffusivities of the alloys were measured in the liquid and solid state by LFA apparatus. Experimental specific heats were taken into account, where their values in the liquid state were calculated by the extrapolation of the obtained curves. Finally, densities of alloys were measured at room temperature and were approximated to a constant value in the interest temperature range. Thereby, density measurements showed high values, around 6546, 6752 and 6763 $kg \cdot m^{-3}$ for the $Zn_{84}Al_{8.7}Mg_{7.3,}$ $Zn_{88.7}Al_{11.3}$ and $Zn_{92.2}Mg_{7.8}$ alloys, respectively, due to their high Zn content. Thermal conductivities of investigated alloys are shown in Figure 24. In general, three alloys show approximately constant thermal conductivities in the solid state, which slightly decrease with the increasing of temperature. Then, after the melting process the thermal conductivity, which also includes the convective effect, decreases around to the half.

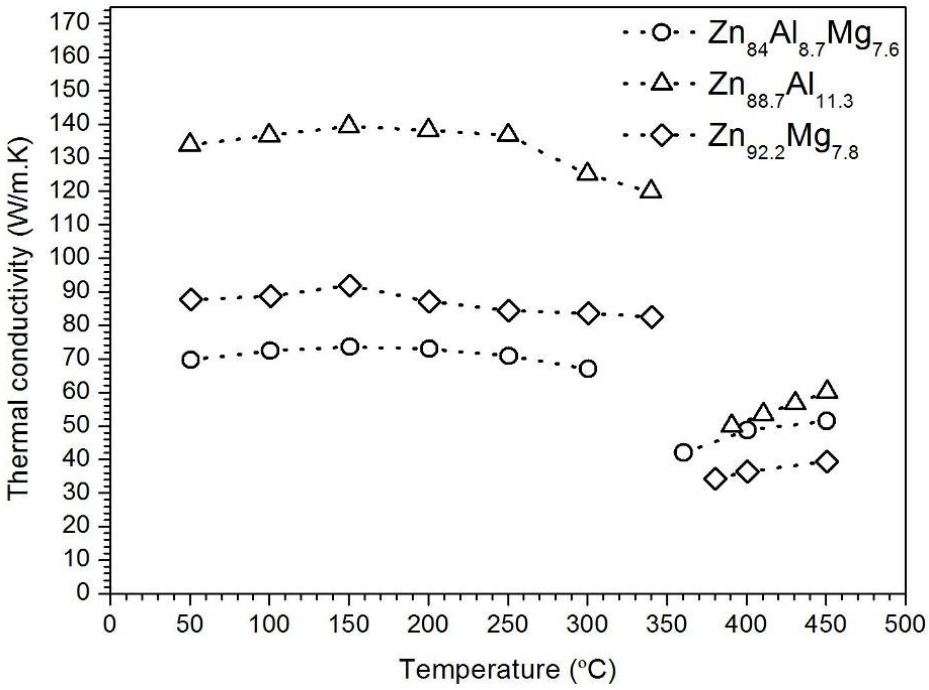

Figure 24. The thermal conductivity in solid and liquid states of $Zn_{84}Al_{8.7}Mg_{7.6}$, $Zn_{88.7}Al_{11.3}$ and $Zn_{92.2}Mg_{7.8}$ eutectic alloys.

The average conductivities in solid and liquid phases are 71.10 – 44.44 $W \cdot m^{-1} \cdot K^{-1}$ for $Zn_{84}Al_{8.7}Mg_{7.3}$ alloy, 132.81 – 55.07 $W \cdot m^{-1} \cdot K^{-1}$ for $Zn_{88.7}Al_{11.3}$ and 86.57 – 36.73 $W \cdot m^{-1} \cdot K^{-1}$ for $Zn_{92.2}Mg_{7.8}$. Thus, the $Zn_{88.7}Al_{11.3}$ alloy shows the highest conductivity followed successively by $Zn_{92.2}Mg_{7.8}$ and $Zn_{84}Al_{8.7}Mg_{7.3}$ alloy. Taken into account the thermal conductivities of isolated metals, 132.57, 133.74 and 119.12 $W \cdot m^{-1} \cdot K^{-1}$ theoretical values are estimated at room temperature, where λ increase as Al concentration increase for $Zn_{84}Al_{8.7}Mg_{7.3,}$ $Zn_{88.7}Al_{11.3}$ and $Zn_{92.2}Mg_{7.8}$ alloys, respectively. The $Zn_{88.7}Al_{11.3}$ alloy, with highest Al content, shows the highest λ in agreement with expected results. On the other hand, its average conductivity value in solid phase is very similar to the theoretically calculated one due to high purity and periodicity of crystalline unit cells of Al and Zn phases in this alloy. In the same way, the $Zn_{84}Al_{8.7}Mg_{7.3}$ and $Zn_{92.2}Mg_{7.8}$ average thermal conductivities in solid phases present substantial reduction respect estimated theoretical values due to the atomic substitutions in the crystalline unit cells of their Mg_2Zn_{11} and $MgZn_2$ intermetallic phases, which reduce the cells periodicity and as a consequence the thermal conductivity.

Short review on potential high temperature PCM (HT-PCM) for TES application

Several up to date research publications focused on potential high temperature phase change materials (HT-PCM) for solar TES applications are reported in Tables 10, 11 and 12. The tables

show the reported thermophysical properties, as well as, the performed thermal cycling and compatibility tests.

In Table 10 listed several research publications [31-33,85] focused on salts as HT-PCMs for their use in cascaded latent heat storage (CLHS):

H. Michels et al. [85] investigated several nitrated salts with melting point between 300 – 400 ºC. Among their conclusions $NaNO_3$ (306 ºC, 172 $J \cdot g^{-1}$) was identified as proper PCM with respect to its heat of fusion and corrosiveness. On the other hand, the necessity of further PCMs identification with sufficient heat of fusion and satisfying corrosiveness was indicated. Finally, it was found that the low thermal conductivity of proposed PCMs limited the use of this storage technology.

G. C. Glatzmaier et al. [32] evaluated several salts with melting temperature near to 320, 350 and 380 ºC. Among proposed candidates, KNO_3/KCl (95.5/4.5) (wt.%) (~320 ºC, ~82 $J \cdot g^{-1}$) was identified as the best candidate for 320 ºC PCM. However, among the evaluated salts for 350 and 380 ºC PCM no good candidate was found due to the corrosiveness and the high vapour pressure of the chlorides. It was indicated the necessity of other candidate consideration, where, the finding a salt for 350 ºC PCM is extremely difficult due to that all the possible candidates are mixtures of chlorides and fluorides, which are corrosive.

Finally, M .Liu et al. [31] and X. Wei et al. [33] identified CA1 (~397 ºC, ~279 $J \cdot g^{-1}$) and CH1 (~439 ºC, ~204 $J \cdot g^{-1}$), as well as, SYSU-4 (424 ºC, 190 $J \cdot g^{-1}$) as promising HTPCM, respectively.

Research publications focused on salts composites with enhanced thermal conductivities are summarized in Table 11, where it should be noted the high thermal conductivities of the composites developed in [88,89]:

S. Pincemin et al. [88] evaluated graphite/salt composites with melting point around 200 ºC for parabolic trough systems. In this study, the thermophysical properties were deeply evaluated as a function of amount, type and size of the graphite. Among their results, it was found a decreasing of latent heat after 200 thermal cycling due to type and size of the graphite, as well as, a significant dependence of the thermal conductivity on these parameters. One of the targets of this work was to elaborate new materials with a thermal conductivity of at least 8 $W \cdot m^{-1} \cdot K^{-1}$ in order to match with the operational conditions of the solar application. However, a strong decreasing of the thermal conductivity is found with the temperature increasing, where in all cases, the thermal conductivity was less than 8 $W \cdot m^{-1} \cdot K^{-1}$ near to 200 ºC. Bases on these results, it was indicated that the enhanced

thermal conductivity are still too low for the operational requirements of CSP plants. Finally, according to experimental and simulated results, a sandwich design by combination of composite like NG/400/30 or GFG/500/21 and radial graphite fins was proposed.

Z. Huang et al. [89] reported thermophysical properties characterization and stored analysis of $LiNO_3/KCl_{eu.}$/expanded graphite (EG) composites for solar TES at ~200 ºC. The eutectic $LiNO_3$/KCl system was characterized as a function of mass fraction of EG, where, a decreasing on latent heat with increasing of EG mass fraction was observed, whereas that no changes on melting temperature was recorded. On the other hand, a notable increasing on thermal conductivity was observed with EG mass content and apparent density of composites. Finally, the heat storage performance showed an improvement due to thermal conductivity enhancement whereas the storage duration was increased with apparent density of the composite materials.

H. Tian et al. [90] performed the thermophysical properties characterization of eutectic chloride-EG composites as HT-PCM for solar TES. These properties are evaluated as function of mass fraction of EG, where, no changes in melting temperature, decreasing on latent heat and enhancement of thermal conductivity were found with the increasing of EG proportion. On the other hand a deeper analysis of specific heat was performed, which showed a decreasing with EG content and temperature.

Compound	Melting point	Heat of fusion	Thermal hysteresis	Density	Heat storage capacity		Energy density	Specific heat		Thermal conductivity		Thermal stability	Thermal cycling test	Compatibility test
	(ºC)	(kJ·kg^{-1})	(ºC)	(kg·m^{-3})	(kJ·kg^{-1})	(kJ·cm^{-3})	(kW·h·m^{-3})	(kJ·kg^{-1}·K^{-1})		(W·m^{-1}·K^{-1})		(ºC)	(cycles#)	
								Solid	Liquid	Solid	Liquid			Compatible material
H. Michels et al. [85]:	Nitrate salts experimental investigation by vertical shell and tube type heat exchanger and simulated numerical results are reported to identified potential HT-PCMs for cascaded latent heat storages (CLHS) in parabolic though based solar power plants with													
$NaNO_3$	306	172	-	2261	-	-	~108	1.1	-	0.5	-	-	-	-
KNO_3/KCl (95.5/4.5) eu.	320	74	-	2100	-	-	~43	1.21	-	0.5	-	-	-	-
KNO_3	335	95	-	2019	-	-	~53	0.953	-	0.5	-	-	-	-
KOH	360	134	-	2040	-	-	~76	1.34	-	0.5		-	-	-
$MgCl_2$/KCl/NaCl (60/20.4/19.6) eu.	380	400	-	1800	-	-	~200	0.96	-	-		-	-	-
G. C. Glatzmaier et al. [32]:	Thermal and chemical chacterization of salts with melting point near to 320, 350 and 380 ºC are performed to identified potential HT-PCMs for three-PCM CLHS for parabolic though based solar power plants with 300 to 400ºC operational temperature.													
KNO_3/KCl (97/3)	320.67	87.62	3.73	-	-	-	n/a	0.94 - 1.24(1)	1.20 - 1.21(1)	-	-	-	-	-
KNO_3/KCl (95.5/4.5) eu.	319.69	82.05	0	-	-	-	n/a	1.4	1.31	-	-	-	-	-
KNO_3/KCl/KBr (89.98/2.95/7.06)	327.72	75.29	4.1	-	-	-	n/a	1.07 - 1.30(1)	1.27 - 1.25(1)	-	-		-	316/Al1100/Al3003/Al_2O_3
NaCl/KCl/LiCl (7.87/50.88/41.25)	344	-	-	-	-	-	n/a	-	-	-	-	Unstable	-	Al3003/Al_2O_3
NaCl/KCl/LiCl (34.81/32.29/32.90)	352.37	138	2.18	-	-	-	n/a	-	-	-	-	Unstable	-	Al3003/Al_2O_3
$MgCl_2$/KCl/NaCl (60/20.4/19.60) eu.	387.6	199	10.9	-	-	-	n/a	-	-	-	-	Unstable	-	Al_2O_3
M .Liu et al. [31]:	Thermophysical properties characterization and thermal stability testing of salts HT-PCMs for CLHS in solar power applications are carried out.													
Li_2CO_3/K_2CO_3/$3Na_2CO_3$ (32/35/33) (CA1)	396.7	278.9	22.7	-	-	-	n/a	1.42	1.68	-	-	-	-	-
Li_2CO_3/K_2CO_3/$3Na_2CO_3$ (22/62/16) (CA4)	425.5	274.7	12.7	-	-	-	n/a	1.25	1.56	-	-	-	100	-
$MgCl_2$/NaCl (52/48) (CH1)	439.1	204.2	8.4	-	-	-	n/a	1.07	-	-	-	-	40	-
$MgCl_2$/KCl (64/36) (CH2)	459.1	210.2	8.4	-	-	-	n/a	0.73	-	-	-	-	40	-
Li_2CO_3/K_2CO_3 (28.5/71.5) (CA2)	479.9	298.2	58.6	-	-	-	n/a	1.29	1.66	-	-	-	100	-
Li_2CO_3/K_2CO_3 (35/65) (CA3)	503.7	295.2	58.6	-	-	-	n/a	1.43	1.73	-	-	-	100	-
X. Wei et al. [33]:	New ternary eutectic salt HT-PCM development and termophysical properties characterization for solar TES are carried out.													
SYSU-C4 (NaCl/$CaCl_2$/$MgCl_2$) eu.	424	190	-	2500	-	-	~132	0.83	1.19	-	-	700	50	-

(1): Estimated from Fig. 1 of [32] reference.

Table 10. Several of current investigations about salts as for their use potential high temperature phase change material (HT-PCM) in solar power generation technologies.

Compound	Melting point	Heat of fusion	Thermal hysteresis	Density	Heat storage capacity		Energy density	Specific heat		Thermal conductivity		Thermal stability	Thermal cycling test	Compatibility test
	(ºC)	(kJ·kg^{-1})	(ºC)	(kg·m^{-3})	(kJ·kg^{-1})	(kJ·cm^{-3})	(kW·h·m^{-3})	(kJ·kg^{-1}·K^{-1})		(W·m^{-1}·K^{-1})		(ºC)	(cycles#)	
								Solid	Liquid	Solid	Liquid			Compatible material
S. Pincemin et al. [88]:	Graphite/salt composite thermophysical properties characterization, simulated results according to different possible TES unit designs and the synergy between the composite and the interfacial area with HTF are presented and discussed for parabolic trough based solar power plants.													
NG/400/22 - $NaNO_3/KNO_3$ (50/50) eu.	218	73	-	-	-	-	n/a	-	-	7.68 - 4.18[(1)]	-	350	200	-
NG/400/30 - $NaNO_3/KNO_3$ (50/50) eu.	219	67	-	-	-	-	n/a	-	-	8.5[(1)]	-	350	200	-
GFG/50/20 - $NaNO_3/KNO_3$ (50/50) eu.	212	68	-	-	-	-	n/a	-	-	7.3[(1)]	-	350	200	-
GFG/500/21 - $NaNO_3/KNO_3$ (50/50) eu.	214	77	-	-	-	-	n/a	-	-	9.41 - 6.09[(1)]	-	350	200	-
Z. Huang et al. [89]:	Thermophysical properties characterization and stored analysis of proposed $LiNO_3$/KCl - expanded graphite (EG) composite is reported for solar TES.													
$LiNO_3$/KCl(50/50) eu.	165.6	204.7	-	-	-	-	n/a	-	-	1.749	-	-	-	-
EG(10) - $LiNO_3$/KCl(50/50) eu.	165.55	178.1	-	-	-	-	n/a	-	-	5.00	-	-	-	-
EG(15) - $LiNO_3$/KCl(50/50) eu.	165.87	170.69	-	-	-	-	n/a	-	-	7.01	-	-	-	-
EG(20) - $LiNO_3$/KCl(50/50) eu.	165.57	164.5	-	-	-	-	n/a	-	-	9.21	-	-	-	-
EG(25) - $LiNO_3$/KCl(50/50) eu.	165.55	150.96	-	-	-	-	n/a	-	-	11.32	-	-	-	-
EG(30) - $LiNO_3$/KCl(50/50) eu.	165.58	142.41	-	-	-	-	n/a	-	-	13.43	-	-	-	-
H.Tian et al. [90]:	Preparation and thermophysical properties characterization of eutectic chloride/EG composites as HT-PCM for solar TES are carried out.													
NaCl/$CaCl_2$/$MgCl_2$ (53.44/14.95/31.61) eu.	431.61	206.2	-	-	-	-	n/a	1.623 - 2.026	2.20 - 2.83[(2)]	1.174	-	-	45	-
EG(0.5) - NaCl/$CaCl_2$/$MgCl_2$ eu.	430.48	204.1	-	-	-	-	n/a	0.804 - 1.466	1.42 - 2.91[(2)]	1.58	-	-	-	-
EG(1) - NaCl/$CaCl_2$/$MgCl_2$ eu.	431.22	191.2	-	-	-	-	n/a	0.536 - 1.42	1.27 - 3.97[(2)]	1.64	-	-	-	-
EG(3) - NaCl/$CaCl_2$/$MgCl_2$ eu.	430.79	179.9	-	-	-	-	n/a	0.519 - 1.227	1.38 - 3.33[(2)]	1.68	-	-	-	-
EG(5) - NaCl/$CaCl_2$/$MgCl_2$ eu.	432.49	170.2	-	-	-	-	n/a	0.196 - 1.015	1.06 - 2.53[(2)]	2.08	-	-	-	-

(1): Estimated from Fig. 8 of [88] reference; (2): Estimated from Fig. 3 of [90] reference.

Table 11. Several of current investigations about salts with enhanced thermal conductivities for their use as potential HT-PCM in solar power generation technologies.

Table 12 shows current investigations, where, metals are proposed as HT-PCMs for solar power applications. In this frame, [47,34,48] proposed Al-Si alloys, [52] miscibility gap binary metal alloy systems and [46,82,84] together with present work Al-Mg-Zn alloy system:

Z. Wang et al. [47] identified several Al-Si alloys as potential HT-PCM, which show a decreasing in their specific heats and thermal conductivities with the increasing of Si content. On the other hand, the combination of Al-Si binary system with investigated ternary systems is proposed in order to cover application temperature from 580 to 1100 ºC. N. Gokon et al. [34] compared the calculated thermal storage capacities of investigated hypereutectic Al-Si alloys as sensible and latent heat storage media with Na_2CO_3 molten salt. The results indicate that the hyperecteutic Al-Si alloys are available to use in the solar reforming natural gas, as well as, the Na_2CO_3. Meanwhile, R. Fukahori et al. [48] determines the good compatibility of Al-Si alloys with ceramic materials after corrosion tests at 1000 ºC for 100 hours.

H. Sugo et al. [52] proposed miscibility gap alloys as innovative solution to overcome the current problems of conventional PCMs. The system is based on a metal PCM dispersed in a thermodynamically stable metal matrix, where the PCM presents lower melting temperature than the matrix. Several matrix/fusible material systems are discussed and proposed for a wide temperature range and applications.

On the other hand [46,82,84] investigations and in present work Al-Mg-Zn alloys are identified as potential HT-PCM, where a good long term thermal stability and low corrosiveness had observed in [46,84] references.

The present study proposed Zn-rich alloys as potential PCM, where it is remarkable the highest densities of these metal alloys. By the comparison of their properties and salts properties listed in Tables 10, 11 and 12, it can be seen that the main advantages of these metal alloys compared with inorganic salts are their high densities, between two and three times higher, together with their thermal conductivities, which are two and even three orders of magnitude higher. On the other hand, heats of fusion of investigated alloys are lower than those values in some salts. However, the high density of alloys leads to similar values of energy density. Finally, the specific heat values are around a half of those of inorganic salts. Anyway, this is not a driving thermophysical parameter for LHS.

Compound	Melting point	Heat of fusion	Thermal hysteresis	Density	Heat storage capacity		Energy density	Specific heat		Thermal conductivity		Thermal stability	Thermal cycling test	Compatibility test
	(ºC)	(kJ·kg^{-1})	(ºC)	(kg·m^{-3})	(kJ·kg^{-1})	(kJ·cm^{-3})	(kW·h·m^{-3})	(kJ·kg^{-1}·K^{-1})		(W·m^{-1}·K^{-1})		(ºC)	(cycles#)	
								Solid	Liquid	Solid	Liquid			Compatible material
Z.Wang et al. [47]:	Thermophysical properties characterization of Al-Si alloys for their use as HT-PCM in solar TES are carried out.													
Al-Si (87.8/12.2) eu.	~580	499.2	-	2620	-	-	~363	0.87 - 1.19[(1)]	-	165 - 158	-	-	-	-
Al-Si (80/20)	~580	552.6	-	2580	-	-	~396	0.86 - 1.16[(1)]	-	154 - 145	-	-	-	-
Al-Si (70/30)	~580	644.3	-	2540	-	-	~455	0.86 - 1.09[(1)]	-	142 - 118	-	-	-	-
Al-Si (60/40)	~580	721.2	-	2510	-	-	~503	0.87 - 1.07[(1)]	-	119 - 84	-	-	-	-
Al-Si-Fe (45/40/15)	869.4	562.2	-	3360	-	-	~525	0.81 - 1.05[(1)]	-	12.8 - 8.6	-	-	-	-
Al-Si-Ni (17/53/30)	1079.2	960.3	-	4290	-	-	~1144	0.65 - 0.79[(1)]	-	51.7 - 47.5	-	-	-	-
N. Gokon et al. [34]:	Al-Si hyperectectic alloys for sensible and latent heat storage are proposed as solar receiver tube with air as heat tranfer fluid (HTF) and as solar reformed, with methanol + air as HTF, for the production of thermochemical fuels in tower-type solar concentrating systems.													
Na_2CO_3	858	-	-	-	1534[(2)]	3.04[(2)]	n/a	-	-	-	-	-	-	-
Al-Si (87.4/12.6) eu.	577	483	-	-	1030[(2)]	3.03[(2)]	n/a	-	-	-	-	-	-	-
Al-Si (80/20) hypereu.	577	462	-	-	1100[(2)]	2.43[(2)]	n/a	-	-	-	-	-	20	Graphite
Al-Si (75/25) hypereu.	577	434	-	-	1151[(2)]	2.59[(2)]	n/a	-	-	-	-	-	20	Graphite
Al-Si (70/30) hypereu.	577	405	-	-	1207[(2)]	2.73[(2)]	n/a	-	-	-	-	-	20	Graphite
Al-Si (65/35) hypereu.	577	376	-	-	1270[(2)]	2.88[(2)]	n/a	-	-	-	-	-	20	Graphite
R. Fukahori et al. [48]:	Thermophysical properties characterization and corrosion tests of Al-Si alloys for their use as HT-PCM in solar TES are carried out.													
Al	661	391	-	-	-	-	n/a	-	-	-	-	-	-	Al_2O_3/AlN/Si_3N_4
ADC12 (Si 9.6–12%) standarized alloy	572	441	-	-	-	-	n/a	-	-	-	-	-	-	Al_2O_3/AlN/Si_3N_4
AC9A (Si 23.4%) standarized alloy	575	395	-	-	-	-	n/a	-	-	-	-	-	-	Al_2O_3/AlN/Si_3N_4
Al–Si (75/25)	576	429	-	-	-	-	n/a	-	-	-	-	-	-	Al_2O_3/AlN/Si_3N_4
H. Sugo et al. [52]:	Miscibility gap binary metal alloy systems are proposed to operate through the latent heat of fusion of one component dispersed in a thermodynamically stable matrix for several applications such as solar TES.													
Al-Sn (Sn fusible phase)	232	59	4	-	-	-	n/a	-	-	237	-	-	30	-
Al-Bi (Bi fusible phase)	271	52	-	-	-	-	n/a	-	-	237	-	-	-	-
Fe-Mg (Mg fusible phase)	650	346	-	-	-	-	n/a	-	-	80	-	-	-	-
Fe-Cu (Cu fusible phase)	1085	205	-	-	-	-	n/a	-	-	80	-	-	30	-
SiC-Si (Si fusible phase)	1414	1926	-	-	-	-	n/a	-	-	200	-	-	-	-

Sun et al. [49]:	Thermal reliability test and corrosion tests in function of thermal cycling of Al-Mg-Zn alloy are performed for its use as HT-PCM in solar TES.													
Al-Mg-Zn (59.36/34.02/6.62)	450.01	329.1	-	-	-	-	n/a	-	-	-	-	-	1000	304L
P. Blanco-Rodríguez et al. [82]:	Thermophysical properties characterization of Mg-Zn eutectic alloy for its use as HT-PCM for TES in direct steam generation applications is carried out.													
Mg-Zn (49/51) eu.	342	155	13	2850	-	-	~123	0.73 - 0.84	-	67 - 75	-	-	20	-
E. Risueño et al. [84]:	Thermophysical properties characterization of Mg-Zn-Al eutectic alloys for their use as HT-PCM in solar TES is carried out.													
$Mg_{70}Zn_{24.9}Al_{5.1}$ (49/47/4) eu.	340	157	-	2820	-	-	~123	0.69 - 0.83	-	47 - 59	38	-	700	304/304L/316/316L
$Zn_{85.8}Al_{8.2}Mg_6$ (93.9/3.7/2.4) eu.	344	104	-	6190	-	-	~179	0.41 - 0.53	-	59 - 55	31	-	100	-
This work:	Thermophysical properties characterization of Zn-rich Zn-Al-Mg eutectic alloys is performed for their use as HT-PCM in solar TES.													
$Zn_{84}Al_{8.7}Mg_{7.6}$ (93/4/3) eu.	343.69	131.5	11.39	6546	-	-	~239	0.46 - 0.53	-	~ 70 - 67	~ 42 - 52	-	-	-
$Zn_{88.7}Al_{11.3}$ (95/5) eu.	381.72	118.4	4.75	6752	-	-	~222	0.45 - 0.54	-	~ 134 - 120	~ 50 - 61	-	-	-
$Zn_{92.2}Mg_{7.8}$(97/3) eut.	370.74	106.2	8.82	6763	-	-	~200	0.47 - 0.52	-	~ 88- 83	~ 34 - 40	-	-	-

(1): Estimated from Fig. 2 of [47] reference; (2): Latent + sensible heat at 550-1000ºC.

Table 12. Several of current investigations about metal alloys for their use as potential HT-PCM in solar power generation technologies.

The comparison among the summarized materials (in Table 10, 11 and 12) shows the advantage of use metal alloys as PCMs for solar power generation technologies. On the other hand, G. C. Glatzmaier et al. [32] reported the difficult to find PCMs with fusion temperature near to 350 and 380 ºC. In this frame, the $Zn_{84}Al_{8.7}Mg_{7.3}$ (~344 ºC) and $Zn_{88.7}Al_{11.3}$ (~382 ºC) eutectic alloys are a good PCM option for these operational temperatures. According with this conclusion, three-PCM cascade latent heat storage (CLHS) system with KNO_3/KCl (95.5/4.5) (~320 ºC, ~82 $J \cdot g^{-1}$), $Zn_{84}Al_{8.7}Mg_{7.3}$ (~344 ºC, ~132 $J \cdot g^{-1}$) and $Zn_{88.7}Al_{11.3}$ (~382 ºC, ~138 $J \cdot g^{-1}$) PCMs is proposed for parabolic though solar plants in order to overcome the limitations exposed by H. Michels et al. [85] and G. C. Glatzmaier et al. [32].for this promising technology.

Conclusions

The current study presents thermophysical properties characterization of Zn-rich ($Zn_{84}Al_{8.7}Mg_{7.3,}$ $Zn_{88.7}Al_{11.3}$ and $Zn_{92.2}Mg_{7.8}$) eutectic alloys in order to be used as potential PCMs. From the structural study the correct eutectic composition of alloys has been proved. The calorimetric analysis has shown heats of fusion around 106.2 – 131.5 $J \cdot g^{-1}$ and melting onset temperatures around 343.69 – 381.72 ºC, which are in agreement with equilibrium phase diagrams. It was also observed the hysteresis values ranging from 4.75 to 11.39 ºC. A good agreement between experimentally and theoretically calculated values of specific heat was demonstrated, where, the experimental measured values of the specific heat are in range of 449.24 – 563.41 $J \cdot kg^{-1} \cdot K^{-1}$. Finally, Tte average thermal conductivity values in solid state are in the range of 132.81 - 71.10 $W \cdot m^{-1} \cdot K^{-1}$, whereas, in liquid state are in the range of 55.07 to 36.73 $W \cdot m^{-1} \cdot K^{-1}$.

Several up to date research publications focused on different types of PCMs have been shown and discussed. This sort review shows the high potentiality of metals as PCMs. A comparison between the investigated alloys and some inorganic salts reported in literature has been also performed. The results shown similar energy densities, where, lower heats of fusion of alloys compared with salts are balanced by higher density values due to the high Zn concentration in the alloys.

It is worth to mention the higher thermal conductivity values of the alloys in front of salt, being between 10 and 100 order of magnitude higher. These high thermal conductivities represent one of the main advantages of use of a metal alloys as PCM, which might simplify the design of TES systems and consequently reduce their size and cost.

Finally the $Zn_{84}Al_{8.7}Mg_{7.3}$ (~344 ºC) and $Zn_{88.7}Al_{11.3}$ (~382 ºC) alloys are proposed for cascade latent heat storage (CLHS) systems in order to overcome the limitation in CLHS technology exposed by other authors.

4.2. Accelerated thermal cycling tests

4.2.1. Thermal cycling testing of Zn-Mg-Al eutectic metal alloys as potential high-temperature phase change materials for latent heat storage

Introduction

To identify a potential PCM the study of its thermophysical properties is essential. However, the selection of a PCM must be also performed in basis of its long term thermal stability, i.e., the long term performance of a PCM should be thermally, chemically, and physically stable. In this way, no phase segregation or chemical degradation should be happen, the phase change temperatures should not present great changes and the phase transition heats should be constants without presenting any decreases of their values.

To evaluate the long-term performance of storage unit, the changes in the thermophysical properties should be analysed after repeated number of thermal cycles. In this frame, repeated thermal cycles process performed under controlled conditions in the laboratory is aimed to understand the behaviour of the material under real conditions [91]. Although there are numerous studies of thermal stability for low temperature phase change materials [20,91-99] the researches for high temperature PCMs are scarce [49,100-103].

In this context, accelerated thermal cycling tests of $Zn_{84}Al_{8.7}Mg_{7.3}$, $Zn_{88.7}Al_{11.3}$, $Zn_{92.2}Mg_{7.8}$, $Zn_{72}Mg_{28}$ and $Mg_{70}Zn_{24.9}Al_{5.1}$ eutectic alloys have been performed in this section. The Table 13 shows their theoretical melting temperature and composition, in atomic and weight percentages. The changes on theirs melting temperatures and heat of fusion values have been analysed after large number of melting/solidification thermal cycles. The main objective is determining the long term thermal behaviour of these eutectic alloys to determine their potentiality in real application, in where, a long life service of the storage material is required.

Candidate	Theoretical melting temperature	Eutectic composition	
	(ºC)	(at.%)	(wt.%)
A	345	$Zn_{84}Al_{8.7}Mg_{7.3}$	93.9Zn - 3.7Al - 2.4Mg
B	380	$Zn_{88.7}Al_{11.3}$	95Zn - 5Al
C	370	$Zn_{92.2}Mg_{7.8}$	97Zn - 3Mg
D	340	$Mg_{72}Zn_{28}$	49Mg - 51Zn
E	338	$Mg_{70}Zn_{24.9}Al_{5.1}$	49Mg - 47Zn - 4Al

Table 13. Theoretical melting temperature and composition, in atomic and weight percentages, of the selected PCM candidates.

Results and discussion

Short term thermal stability tests

The five alloys have been cycled for 100 times, and their phase change temperatures and heat of fusion have been continuously recorded. The phase change temperatures, heat of fusion and their relative percentage difference (RPD) respect to first reference cycle of $Zn_{84}Al_{8.7}Mg_{7.3}$ (A), $Zn_{88.7}Al_{11.3}$ (B), $Zn_{92.2}Mg_{7.8}$ (C), $Zn_{72}Mg_{28}$ (D) and $Mg_{70}Zn_{24.9}Al_{5.1}$ (E) are shown in Tables 14-18, respectively. In order to resume the results only one set after each 10 successive cycles was presented. The RPD between each property *i* of the material at any number of cycle *n* and the 1st cycle can be defined as it is indicated in equation (17):

$$RPD = \frac{x_{n,i} - x_{1,i}}{x_{1,i}} \times 100(\%) \quad (17)$$

Where $x_{n,i}$ is the value of the given property after *n* cycles and $x_{1,i}$ is the value of this property at 1st cycle.

The first column of the tables shows the number of the cycle. The second and third columns show the melting onset temperature and its RPD (%) respect to the 1st cycle. The fourth and fifth columns present the melting peak temperature with its RPD (%) value. The sixth column indicates the melting range temperature from which has been used as limits to calculate the heat of fusion. It has to be noted that this range from DSC comes from the dynamic nature of the experiment. Due to the eutectic nature of the alloys the melting process happens at isothermal temperature, where any range is expected in isothermal measurements. The seventh and eighth columns show the calculated heat of fusion and its RPD (%) value. Finally, the last column presents the thermal hysteresis observed in the solidification process.

The results obtained after analysis of sample A are presented in Table 14, from which it can be seen that the first cycle has a melting onset temperature of 343.69 ºC, and no remarkable variations were observed after 100 cycles of testing. Thereby, the maximum RPD value calculated was 0.16% for the 10th cycle, which it can be evaluated as negligible in the frame of a possible application of this alloy as latent heat storage material. Regarding the peak temperature no relevant variations can be observed up to cycle 90th, where the peak temperature is reduced in a 0.6%.

The average melting temperature range has been taken from 336.40 and 384.61 ºC. On the other hand, the heat of fusion for sample A was calculated for the melting temperature ranges obtained in each cycle, being 131.5 J·g^{-1} as it is indicated in the 1st cycle. Regarding the RPD, its value gradually decreases with the thermal cycling from 0.15% in the 20th cycle to 1.90 in the 100th cycle. So, the heat of fusion of the eutectic phase transition in sample A decreases 2.5 J·g^{-1} after 100 cycles. Finally, thermal hysteresis values are almost constant and present an average value of 12.45 ºC.

No. of cycles	Onset temperature (ºC)		Peak temperature (ºC)		Melting range (ºC)	Heat of fusion (J/g)		Thermal hysteresis (ºC)
		RPD (%)		RPD (%)			RPD (%)	
1	343.69	-	354.72	-	336.91 – 379.88	131.5	-	11.39
10	344.25	0.16	354.93	0.06	335.79 – 387.45	131.5	0	12.97
20	343.84	0.04	355.04	0.09	338.69 – 380.10	131.3	-0.15	12.41
30	343.87	0.05	354.98	0.07	336.68 – 390.34	131.6	0.08	12.57
40	343.82	0.04	354.74	0.01	337.80 – 383.22	131.2	-0.23	12.38
50	343.86	0.05	354.78	0.02	334.01 – 384.78	130.8	-0.53	12.57
60	343.85	0.05	354.76	0.01	335.13 – 382.55	130.8	-0.53	12.41
70	343.89	0.06	354.78	0.02	336.02 – 387.23	130.2	-0.99	12.54
80	343.91	0.06	354.79	0.02	336.24 – 385.67	129.5	-1.52	12.60
90	343.89	0.06	352.66	-0.58	334.22 – 386.72	129.3	-1.67	12.66
100	343.88	0.06	352.62	-0.59	338.91 – 382.77	129.0	-1.90	12.41

Table 14. Latent heat of fusion, melting onset temperature and subcooling degrees of candidate A ($Zn_{84}Al_{8.7}Mg_{7.3}$) at different numbers of thermal cycles measured by DSC.

Sample B presented similar results than sample A after thermal cycling, as may be observed in Table 15. The melting onset temperature and peak temperature were measured before cycling, obtaining values of 381.71 ºC and 394.64 ºC, respectively. After 100 cycles, RPD values calculated were under 0.01% for onset temperature and under 0.76% for peak temperature, which can be considered an almost negligible variation when the material is evaluated as PCM candidate in a TES application.

No. of cycles	Onset temperature (ºC)		Peak temperature (ºC)		Melting range (ºC)	Heat of fusion (J/g)		Thermal hysteresis (ºC)
		RPD (%)		RPD (%)			RPD (%)	
1	381.72	-	394.64	-	374.49 – 420.89	118.4	-	4.75
10	381.69	-0.01	394.89	-0.69	376.88 – 415.17	119.2	0.68	4.68
20	381.70	-0.01	394.84	-0.70	376.28 – 416.05	119.1	0.59	4.75
30	381.71	0.00	394.74	-0.73	377.01 – 416.05	119.5	0.93	5.24
40	381.71	0.00	394.71	-0.74	377.01 – 417.79	119.5	0.93	4.96
50	381.71	0.00	394.70	-0.74	376.76 – 417.66	119.7	1.10	4.93
60	381.73	0.003	394.68	-0.74	376.51 – 420.77	119.9	1.27	4.85
70	381.72	0.00	394.64	-0.75	376.39 – 415.42	119.7	1.10	4.91
80	381.70	-0.01	394.63	-0.76	377.26 – 414.80	119.7	1.10	4.89
90	381.73	0.00	394.62	-0.76	377.63 – 415.05	119.7	1.10	5.84
100	381.72	0.00	394.60	-0.76	376.14 – 415.30	119.9	1.27	6.52

Table 15. Latent heat of fusion, melting onset temperature and subcooling degrees of candidate B ($Zn_{88.7}Al_{11.3}$) at different numbers of thermal cycles measured by DSC.

The average melting range to calculate the heat of fusion is 376.07 - 416.12 ºC. In this case, a heat of fusion for the 1st cycle is 118.4 $J \cdot g^{-1}$ and increases up to 119.9 $J \cdot g^{-1}$ after 100 cycles, Finally, the thermal hysteresis, which is apparently very small, experiences almost negligible variations during the thermal cycling, being in a range between 4.68 ºC and 6.52 ºC, taking an average value of 5.12 ºC.

Thermal cycling results of the sample C are shown in Table 16. The melting onset temperature of 370.36 ºC and the peak temperature of 382.52 ºC are obtained and maintained constants during the thermal cycling, where the maximum RPD value are 0.21 % and 0.80 %, respectively. For the average melting range of 362.88 and 411.40 ºC with RPD values less than 0.63 and 0.63 ºC, respectively. The heat of fusion of sample C decreases from 106.4 $J \cdot g^{-1}$ to 85.39 $J \cdot g^{-1}$ after 100 thermal cycles. The heat of fusion shows a progressive decrease with the thermal cycling and RDP value of around 19.75% after 100 thermal cycles. On the other hand, the sub-cooling increases from 4.53 ºC in the 1st cycle up to 9.53 ºC in the 10th cycle and then, its value is constant with an average value of 9.30 ºC.

No. of cycles	Onset temperature (ºC)		Peak temperature (ºC)		Melting range (ºC)	Heat of fusion (J/g)		Thermal hysteresis (ºC)
		RPD (%)		RPD (%)			RPD (%)	
1	370.36	-	382.52	-	362.94 – 418.44	106.4	-	4.53
10	370.74	0.10	382.51	0.00	362.73 – 409.67	105.3	-1.03	9.17
20	370.50	0.04	382.50	-0.01	365.73 – 408.92	102.3	-3.85	9.07
30	370.94	0.16	381.13	-0.36	364.21 – 409.05	101.7	-4.42	9.53
40	370.54	0.05	379.47	-0.80	362.65 – 410.16	98.51	-7.42	9.17
50	370.59	0.06	379.59	-0.77	362.65 – 411.27	96.39	-9.41	9.19
60	370.65	0.08	381.10	-0.37	365.09 – 410.16	93.99	-11.66	9.15
70	371.14	0.21	381.14	-0.36	362.21 – 411.27	91.59	-13.92	9.71
80	371.05	0.19	381.32	-0.31	360.65 – 409.49	89.61	-15.78	9.58
90	370.52	0.04	381.43	-0.28	362.65 – 411.03	87.03	-18.20	9.07
100	370.48	0.03	380.01	-0.66	362.87 – 411.71	85.39	-19.75	8.98

Table 16. Latent heat of fusion, melting onset temperature and subcooling degrees of candidate C ($Zn_{92.2}Mg_{7.8}$) at different numbers of thermal cycles measured by DSC.

The results of sample D are shown in Table 17 and this material presents similar behaviour as sample A. The melting onset temperature of 341.07 ºC and the peak temperature of 349.57 ºC are constant during the thermal cycling, where the RPD values are less than 0.28% and 1.15%, respectively. The heat of fusion has been calculated in the average melting range of 337.63 -381.19 ºC. Its values slightly decrease from 152.7 $J \cdot g^{-1}$ to 150.1 $J \cdot g^{-1}$ which represents a progressive decreasing with the thermal cycling of around 1.70 % after 100 thermal cycles. On the other hand, the thermal hysteresis increases from 7.17 ºC in the 1st cycle up to 9.01 ºC in the 30th cycle and then, its value remains approximately constant after 100 cycles, with an average value of 9.30 ºC.

Finally, the results of sample E are presented in Table 18 show a constant onset melting and peak temperatures of around 339.98 ºC and 348.30 ºC with RPD values less than 0.11% and 0.40%, respectively. Similar to the results of samples A and D, it can be observed a slightly and progressive decrease of the heat of fusion with cycling. Regarding the enthalpy, sample E shows a slight decreasing from 159.6 $J \cdot g^{-1}$ to 158.9 $J \cdot g^{-1}$, which corresponds to a reduction of 0.44% after 100 cycles, which can be considered negligible. The thermal hysteresis degrees are approximately constant with an average value of 9.05 ºC.

No. of cycles	Onset temperature (ºC)		Peak temperature (ºC)		Melting range (ºC)	Heat of fusion (J/g)		Thermal hysteresis (ºC)
		RPD (%)		RPD (%)			RPD (%)	
1	341.07	-	349.57	-	337.48 – 380.11	152.7	-	7.17
10	341.84	0.23	351.34	0.51	336.95 – 384.80	152.8	0.07	7.75
20	341.93	0.25	352.98	0.98	338.65 – 382.98	152.5	-0.13	7.64
30	341.97	0.26	353.14	1.02	337.08 – 381.49	151.8	-0.59	9.01
40	342.00	0.27	353.31	1.07	337.70 – 382.88	151.5	-0.79	9.04
50	341.98	0.27	353.37	1.09	336.84 – 383.62	151.5	-0.79	9.04
60	341.98	0.27	353.59	1.15	337.91 – 381.60	151.3	-0.92	9.05
70	342.03	0.28	353.44	1.11	338.12 – 380.32	151.2	-0.98	9.17
80	342.00	0.27	353.42	1.10	337.38 – 378.83	150.8	-1.24	9.15
90	341.24	0.05	353.32	1.07	337.70 – 379.25	150.5	-1.44	8.42
100	341.22	0.04	353.28	1.06	338.12 – 377.55	150.1	-1.70	8.38

Table 17. Latent heat of fusion, melting onset temperature and subcooling degrees of candidate D ($Mg_{72}Zn_{28}$) at different numbers of thermal cycles measured by DSC.

No. of cycles	Onset temperature (ºC)		Peak temperature (ºC)		Melting range (ºC)	Heat of fusion (J/g)		Thermal hysteresis (ºC)
		RPD (%)		RPD (%)			RPD (%)	
1	339.98	-	348.30	-	337.48 – 379.66	159.6	-	8.79
10	340.00	0.01	348.98	0.20	336.31 – 379.87	159.5	-0.06	8.61
20	340.34	0.11	348.38	0.02	337.27 – 379.56	159.4	-0.13	8.19
30	340.32	0.10	349.00	0.20	336.18 – 379.88	159.0	-0.38	9.11
40	340.13	0.04	348.51	0.06	336.95 – 379.57	159.2	-0.25	8.71
50	340.31	0.10	349.03	0.21	336.10 – 379.34	158.8	-0.50	9.65
60	340.10	0.04	349.09	0.23	335.78 – 379.45	158.8	-0.50	9.38
70	340.21	0.07	349.06	0.22	337.27 – 380.30	158.9	-0.44	8.81
80	340.20	0.06	349.12	0.24	337.59 – 380.30	158.8	-0.50	9.28
90	340.26	0.08	349.08	0.22	336.42 – 380.73	158.8	-0.50	9.44
100	340.37	0.11	349.69	0.40	337.16 – 380.41	158.9	-0.44	9.54

Table 18. Latent heat of fusion, melting onset temperature and subcooling degrees of candidate E ($Mg_{70}Zn_{24.9}Al_{5.1}$) at different numbers of thermal cycles measured by DSC.

Figures 25 and 26 display the melting and solidification curves obtained by DSC corresponding to the 1st, 25th, 50th 75th and 100th cycles of samples B and C. As it may be observed, the form of 1st cycle curve in each sample differs of the rest of the cycles, which can be attributed to the change of the surface contact between the sample and the bottom of the alumina crucible. However, the sample B shows consistent repeatability, whereas in the case of sample C it can be clearly observed a progressive formation of a secondary peak before the main peak, indicated by arrow in the solidification curves, for the 50th, 75th and 100th cycles, which corresponds to a solidification of another phase. However, this fact may be explained by the competitive growth between a Zn-$MgZn_2$ metastable phase and Zn-Mg_2Zn_{11} stable phase observed for this material $Zn_{92.2}Mg_{7.8}$ by M. V. Akdepniz et al. [83]. However, further investigations are on-going in our laboratory to confirm this hypothesis.

In summary, all the studied materials show some changes in melting and solidification temperatures accompanied with some changes of the heat of fusion. In this way, A, B, D and E candidates show negligible changes in their heat of fusion of 1.90%, 1.27%, 1.70% and 0.44%, respectively. In the case of sample C is a substantial fusion heat reduction of 19.75% and a secondary peak progressive formation with cycling. It can be concluded that A, B, D and E alloys show a good thermal stability after 100 cycles despite the slight enthalpy reduction, which can be attributed to slight oxidations produced during the experiments.

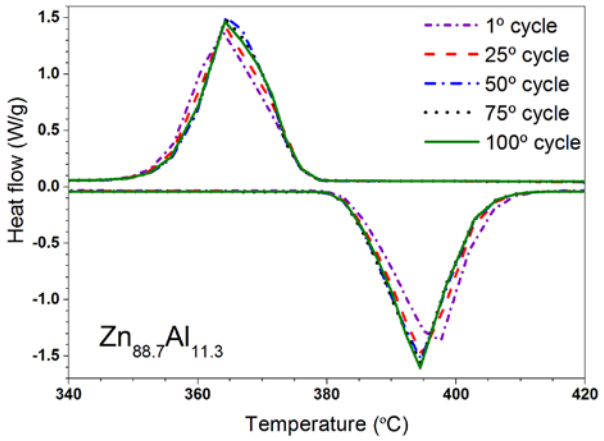

Figure 25. Melting and solidification DSC curves after 1, 25, 75 and 100 thermal cycles of the candidate B ($Zn_{88.7}Al_{11.3}$).

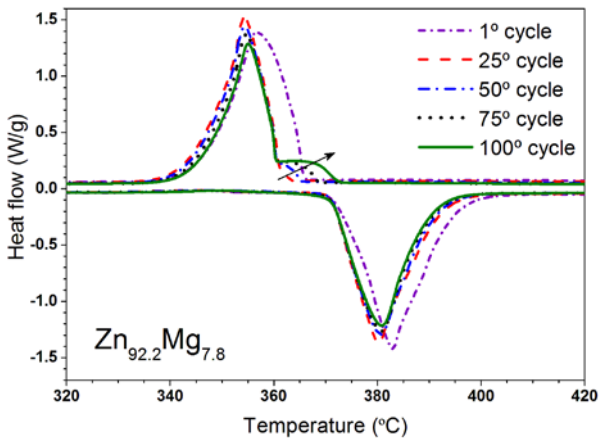

Figure 26. Melting and solidification DSC curves after 1, 25, 75 and 100 thermal cycles of candidate C ($Zn_{92.2}Mg_{7.8}$).

Long term thermal stability tests

The melting/solidification DSC curves of samples D and E after 1, 50, 100, 300 and 500 thermal cycles are shown in Figures 27 and 28. By simple comparison of the curves of each sample a good thermal stability of the materials can be observed. The melting peaks of sample D in Figure 27 show a secondary peak before the eutectic melting process. This peak corresponds to a solid → solid phase transition (Mgt_7Zn_3 + Mg → $Mg_{21}Zn_{25}$). This phase transition is predicted by Mg-Zn phase diagram and has been experimentally confirmed in [71,81]. Due to the overlapping of the secondary and the melting peaks the heat of fusion listed in Table 19 has been calculated from both transformations.

Table 19 shows the long term thermal stability results of sample D. No changes are observed in the melting onset temperature of 340.38 ºC and peak temperature of 347.22 ºC after the 500 thermal cycles, where their RPD values are less than 0.21% and 1.79%, respectively. The thermal hysteresis changes between 7.82 and 9.59 ºC, where its average value is 8.55 ºC. The heat of fusion for untreated sample, i.e. no cycled sample, is around 154.9 $J \cdot g^{-1}$. This value oscillates during the thermal cycle. However, no decreasing trend with the increase of the number of cycles is observed. Thereby, this oscillation may be due to the experimental error coming from the use of different pieces of the sample. On the other hand, the observed RPD value of 0.39% after 500 cycles can be considered negligible. So it can be considered that alloy D presents a good thermal stability after 500 thermal cycles, where its phase change temperature and heat of fusion are practically maintained constant.

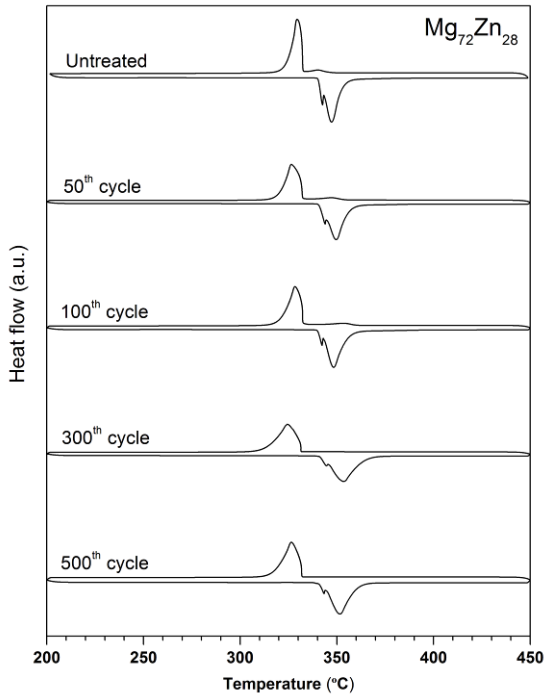

Figure 27. Melting and solidification DSC curves of candidate D ($Mg_{72}Zn_{28}$) for after 0, 50, 100, 300 and 500 thermal cycles.

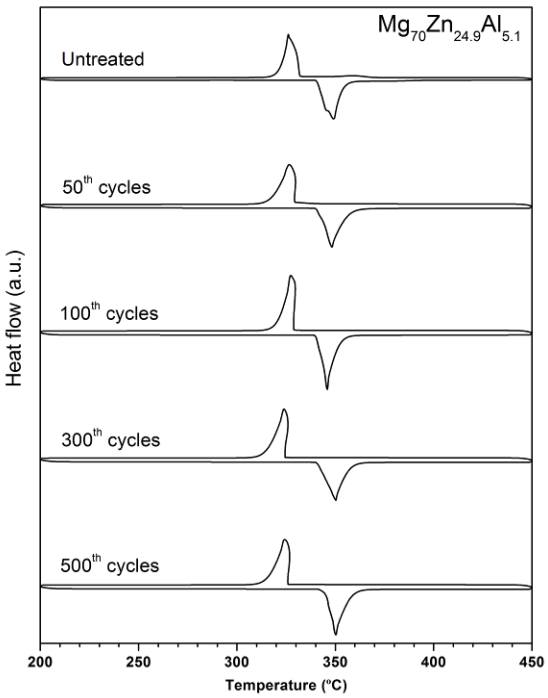

Figure 28. Melting and solidification DSC curves of candidate E ($Mg_{70}Zn_{24.9}Al_{5.1}$) after 0, 50, 100, 300 and 500 thermal cycles.

No. of cycles	Onset temperature (ºC)		Peak temperature (ºC)		Melting range (ºC)	Heat of fusion (J/g)		Thermal hysteresis (ºC)
		RPD (%)		RPD (%)			RPD (%)	
1	340.38	-	347.22	-	337.38 – 381.70	154.9	-	7.98
50	340.84	0.14	349.59	0.68	336.99 – 386.47	153.3	-1.03	8.60
100	340.15	-0.07	348.32	0.32	337.61 – 386.48	155.4	0.32	7.82
300	341.09	0.21	353.43	1.79	336.50 – 380.38	153.6	-0.84	9.59
500	340.64	0.08	351.54	1.24	336.99 – 374.41	154.3	-0.39	8.78

Table 19. Latent heat of fusion, melting onset temperature and subcooling degrees of candidate D ($Mg_{72}Zn_{28}$) cycled in electrical furnace.

Finally, Table 20 shows the long term thermal stability results of candidate E. In the untreated sample, the meting onset temperature is 341.09 ºC. This temperature is reproducible during the thermal cycling, where the RPD values for onset and peak temperatures do not exceeded 0.53% and 1.10%, respectively. In this case, thermal hysteresis temperatures show higher differences than in short term thermal cycling and fluctuate between 6.73 ºC and 16.01 ºC without detecting any continuous increasing trend on theirs values with the increase of the cycle number. The average melting range, taken for the heat of fusion calculation, is between 336.64 ºC and 383.06 ºC. After the 1st cycle the heat of fusion increases its value from 152.9 $J \cdot g^{-1}$ in the 1st cycle to 155.2 $J \cdot g^{-1}$ in 50th cycle and then, it remains practically constant up to 500 cycles. So, it can be concluded that the alloy E also presents a good thermal stability after 500 cycles.

No. of cycles	Onset temperature (ºC)		Peak temperature (ºC)		Melting range (ºC)	Heat of fusion (J/g)		Thermal hysteresis (ºC)
		RPD (%)		RPD (%)			RPD (%)	
1	341.09	-	349.38	-	336.88 – 386.50	152.9	-	8.18
50	340.28	-0.24	348.12	-0.36	337.74 – 382.35	155.2	0.84	11.97
100	339.29	-0.53	345.55	-1.10	336.85 – 387.96	156.8	1.88	10.80
300	340.80	-0.09	350.21	0.24	336.30 – 380.97	154.9	0.65	16.01
500	340.62	-0.14	348.60	-0.22	335.41 – 377.52	156.1	1.43	6.73

Table 20. Latent heat of fusion, melting onset temperature and subcooling degrees of candidate E ($Mg_{70}Zn_{24.9}Al_{5.1}$) cycled in electrical furnace.

In order to analyse the microstructure evolution of the candidate E, SEM analysis has been carried out for the untreated sample and after 50, 100, 300 and 500 cycles. Figure 29 shows at different magnifications the microstructure of untreated sample and after 300 and 500 cycles. The microstructure of untreated sample is displayed in Figures 29 (a-c). The eutectic microstructure where $Mg_{21}Zn_{25}$ intermetallic phase is in light grey colour and the Mg solid solution is in dark grey colour can be observed. The eutectic microstructure of samples after 300 and 500 cycles is displayed in Figures 29 (d-i), where the stability of their microstructures can be clearly observed. So, from these results it can be concluded that no chemical degradation or segregation in candidate E after 500 cycles has been detected.

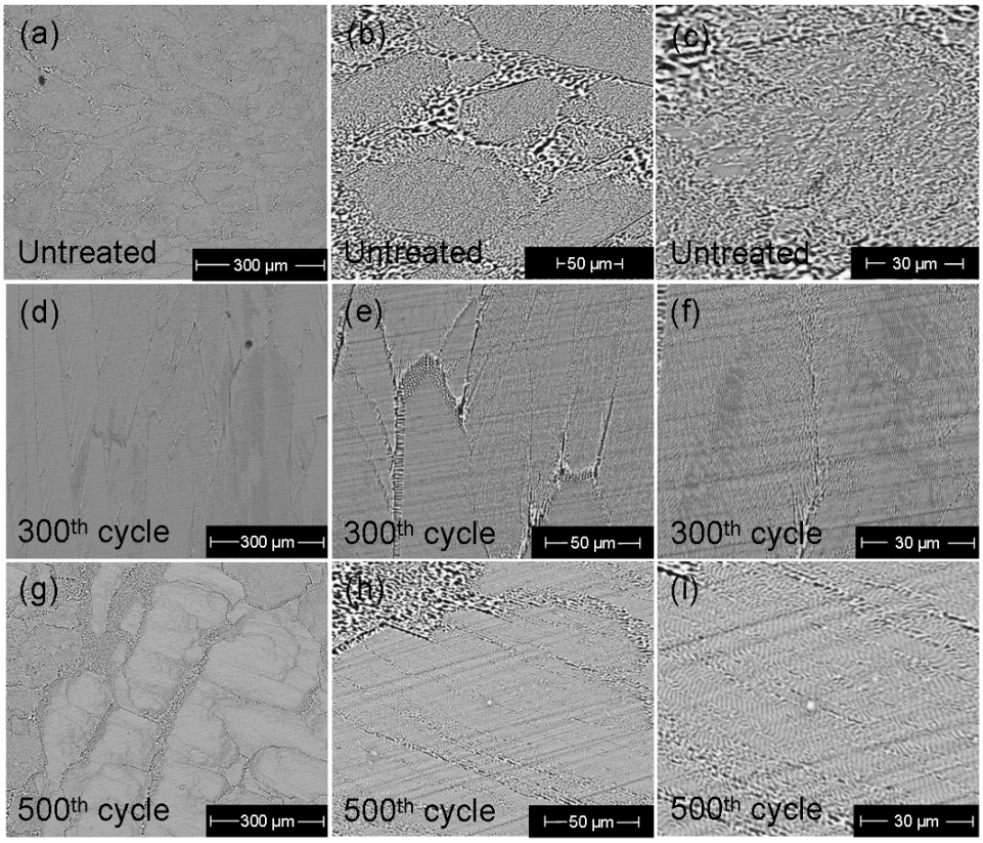

Figure 29. SEM images of candidate E ($Mg_{70}Zn_{24.9}Al_{5.1}$), untreated and after 300 and 500 thermal cycles at 300X (300 µm), 1500X (50 µm) and 3000X (30 µm) magnifications.

Conclusion

The thermal stability of five eutectic metal alloys as potential high-temperature PCMs has been evaluated in this work. Short term thermal cycling tests of 100 cycles have been carried out for the all candidates and long term cycling tests of 500 cycles for candidates D and E have been performed. The changes on melting temperatures, heat of fusion and thermal hysteresis have been analysed using the DSC technique in all cases. The changes in eutectic microstructure have been analysed by SEM for candidate E.

Thereby, after short term cycling tests of 100 cycles, no variations on the onset melting and solidification temperatures of the five materials have been obtained. The heat of fusion shows negligible changes in some cases may due to the small oxidation of the samples. An enthalpy reduction accompanied with a progressive formation of a secondary peak before solidification peak is observed for sample C. This behaviour might be explained by the random stable and meta-stable phase transition process observed for this eutectic alloy by M. V. Akdepniz et al. [83] and in this thesis work, however, further investigations are needed to confirm this hypothesis.

After long term thermal cycling tests of 500 cycles, alloy D ($Mg_{72}Zn_{28}$) does not show changes in its meting temperature of 340.38 ºC. The heat of fusion value of 154.9 $J \cdot g^{-1}$ oscillated during the thermal cycles, however, no decreasing trend with the increase of the cycle number is observed, where the RPD of 0.39% after 500 cycles can be considered negligible. In the same way, candidate E ($Mg_{70}Zn_{24.9}Al_{5.1}$) presents no changes in its melting temperature of 341.09 ºC. The heat of fusion value of 152.9 $J \cdot g^{-1}$ increases from 1^{st} to 10^{th} cycles and then fluctuates, showing an increasing of 1.43% after 500 cycles. Besides, the SEM analysis preformed in sample E after 300 and 500 cycles shows stable eutectic microstructure without any chemical degradation or segregation of the phases. So, in based of these results good thermal stability can be considered for samples D and E after 500 cycles.

Based on results of the performed thermal cycling tests, it can be concluded that the A ($Zn_{84}Al_{8.7}Mg_{7.3}$), B ($Zn_{88.7}Al_{11.3}$), D ($Mg_{72}Zn_{28}$) and E ($Mg_{70}Zn_{24.9}Al_{5.1}$) eutectic alloys are thermally stable after 100 and 500 cycles and can be considered as promising PCMs for thermal energy storage systems. However, according the literature already available, further analysis of at least 1000 cycles are recommended to guarantee the thermal reliability of presented materials.

4.3. Compatibility tests between alloys and containment materials

4.3.1. Corrosion behaviour of stainless steels in Mg-Zn-Al molten metal alloys for latent heat storage application

Introduction

In prior sections of chapter 4, the complete structural and thermophysical characterization and long term thermal stability behaviour analysis have been carried out, where $Mg_{70}Zn_{24.9}Al_{5.1}$, $Zn_{88.7}Al_{11.3}$ and $Zn_{84}Al_{8.7}Mg_{7.3}$ alloy potentiality as LHSMs has been demonstrated.

However, the investigation of metallic alloys used as PCM in the heat storage frame is still a growing topic which needs to be completed. One of the main issues to be investigated in order to deploy this technology in the large scale is the compatibility of the metallic PCM with the containment materials. Recently, Q. Sun et al. [49] investigated the corrosion of the Al–34%Mg–6%Zn metal alloy with the stainless steel SS304L and carbon steel C20. The result showed that SS304L may be considered more suitable containing materials than C20 in long term thermal storage applications. R. Fukahori et al. [48] investigated the corrosion of Al-Si alloys with ceramic materials for their use as high temperature PCMs in solar power plants, where they identified Al_2O_3, AlN and Si_3N_4 as suitable container materials for the investigated metal alloys.

In this section, compatibility tests of the $Mg_{70}Zn_{24.9}Al_{5.1}$, $Zn_{88.7}Al_{11.3}$ and $Zn_{84}Al_{8.7}Mg_{7.3}$ alloys with AISI 304, 304L, 316, 316L, 321, 316Ti and 430 stainless steels have been carried. To the best of our knowledge, this is the first time that the compatibility of the above cited alloys with these stainless steels is evaluated. As it has been explained in chapter 3, thee corrosion tests have been done at isothermal temperature for long contact period and by static immersions of steel sheets in molten metallic baths.

By metallographic investigations, the corrosion behaviours of stainless steels in molten metal alloys have been analysed, where the influence of the molten alloys and stainless steels chemical composition in corrosion reaction have been discussed, as well as, the control mechanism on corrosion reactions and the element diffusion through the interface layers.

Experimental results

$Mg_{70}Zn_{24.9}Al_{5.1}$ eutectic alloy

Compatibility tests with AISI 304, 304L and 316, 316L common stainless steels

Figure 30 shows SEM images of the interfaces between AISI 304, 304L, 316 and 316L stainless steels and $Mg_{70}Zn_{24.9}Al_{5.1}$ eutectic alloy after compatibility tests at 400 ºC for 720 hours. The images show stainless steels surfaces on the right side and alloy surface on the left side. As can be clearly seen, neither intermetallic layer no particles formation are observed in the interface between the stainless steels and the metal alloys.

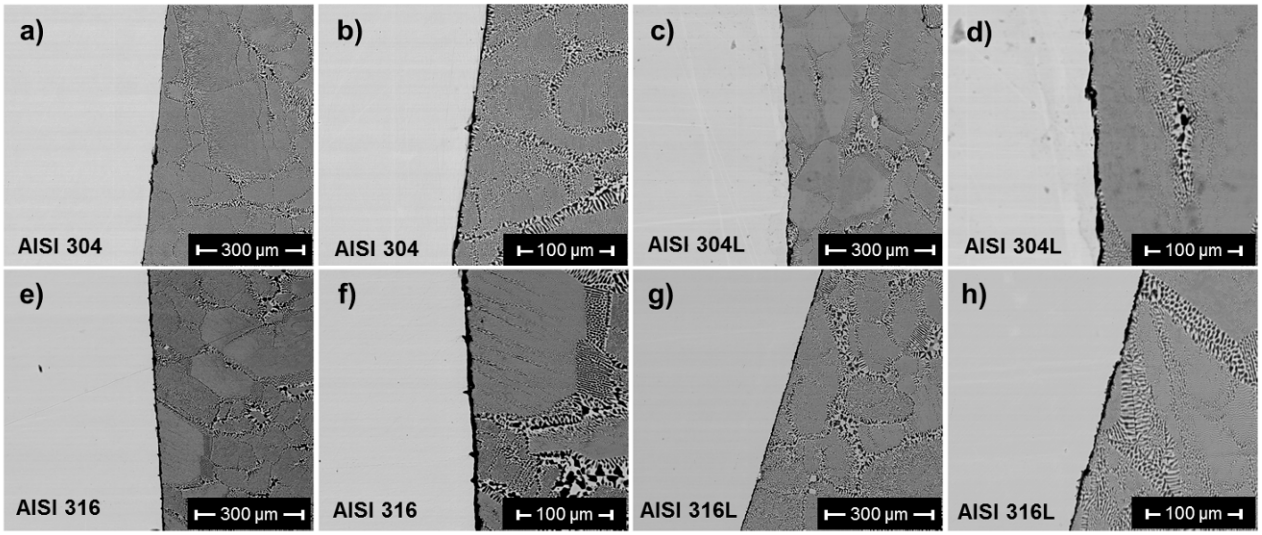

Figure 30. Back scattered-electron cross-section images (SEM) of (a-b) 304, (c-d) 304L, (e-f) 316 and (g-h) 316L stainless steels in the $Mg_{70}Zn_{24.9}Al_{5.1}$ eutectic molten alloy after 720 hours at isothermal temperature of 400 ºC.

Figure 31 presents the EDX maps of the most representative elements of each material: Mg and Zn from the metal alloy and Fe and Cr from the stainless steels. The EDX analyses confirm the absence of corrosion reaction in four cases, where no overlapping of the elements of the metal alloy and the ones of the stainless steels is observed. In addition, the analysis of the displayed EDX maps gives clear evidence that no diffusion or migration of metal alloy elements to the stainless steels, or vice versa. The four stainless steels present high corrosion resistance to the $Mg_{70}Zn_{24.9}Al_{5.1}$ molten

alloy, where in all cases no corrosion reaction is observed and a clear separation between both materials is obtained. This separation may be result of the high surface tension of the $Mg_{70}Zn_{24.9}Al_{5.1}$ molten alloy. As it is known, the corrosion reaction can be influenced by the adhesion level between the steel and molten alloy. The low ratio of adhesion between the studied materials, favored by the high surface tension of the molten metal, is the most important reason of the absence of the corrosion reaction. As conclusion, the investigated metal alloy is fully compatible with the four common AISI stainless steels: 304, 304L, 316 and 316L.

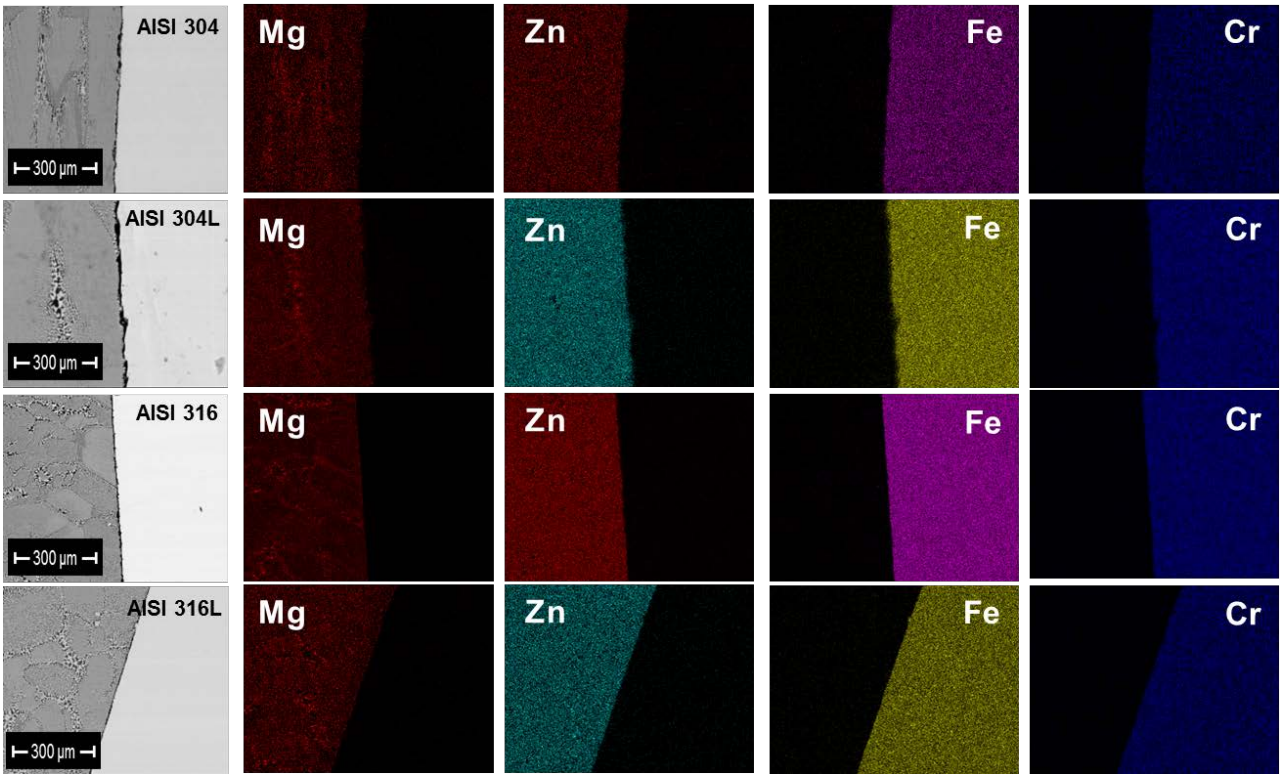

Figure 31. Back scattered-electron cross-section images (SEM) (left panel) and corresponding EDX maps of the compatibility experiments between 304, 304L, 316 and 316L stainless steels in the $Mg_{70}Zn_{24.9}Al_{5.1}$ eutectic molten alloy after 720 hours at isothermal temperature of 400 ºC.

$Zn_{88.7}Al_{11.3}$ eutectic alloy

Compatibility tests with AISI 304, 304L, 316, 316L common stainless steels

Back scattered-electron cross-section micrographs (SEM) of the interface between 304, 304L, 316 and 316L steels and $Zn_{88.7}Al_{11.3}$ metal alloy after compatibility tests are show in Figure 32. The images show stainless steels surfaces on the right side and alloy surface on the left side. The interfaces between steels and the molten alloy reveal to formation of corrosion layers. Two different

behaviours are obtained depending on the stainless steel composition. On the one hand, a strong corrosion behaviour is observed in the case of 304 and 304L. On the other hand, a slight corrosion behaviour is obtained in the case of 316 and 316L, where 316L stainless steel shows the highest corrosion resistant after 720 hours at 400 ºC.

Corrosion tests carried out with 304 and 304L show, on one hand, good adhesions between steels and corrosion layers, and, on the other hand, between corrosion layers and the molten alloy (see Figures 32 (a,b)). In both cases, corrosion layers are composed by an intermetallic layer adjacent to the steels and by a diffusion of small intermetallic particles from corrosion layers toward the molten metal. The corrosion layer thicknesses are similar in both steels. Intermetallic layers adjacent to the steels reach 3.2 µm and 33.1 µm thickness and the particles diffusion about 38.5 µm and 31.5 µm thickness for 304 and 304L steels, respectively. The identified intermetallic phase on layers adjacent to both steels is θ-Al_3Fe, with low Cr and Ni content dissolved in its matric. The identification of intermetallic particles has not been possible due to theirs small sizes.

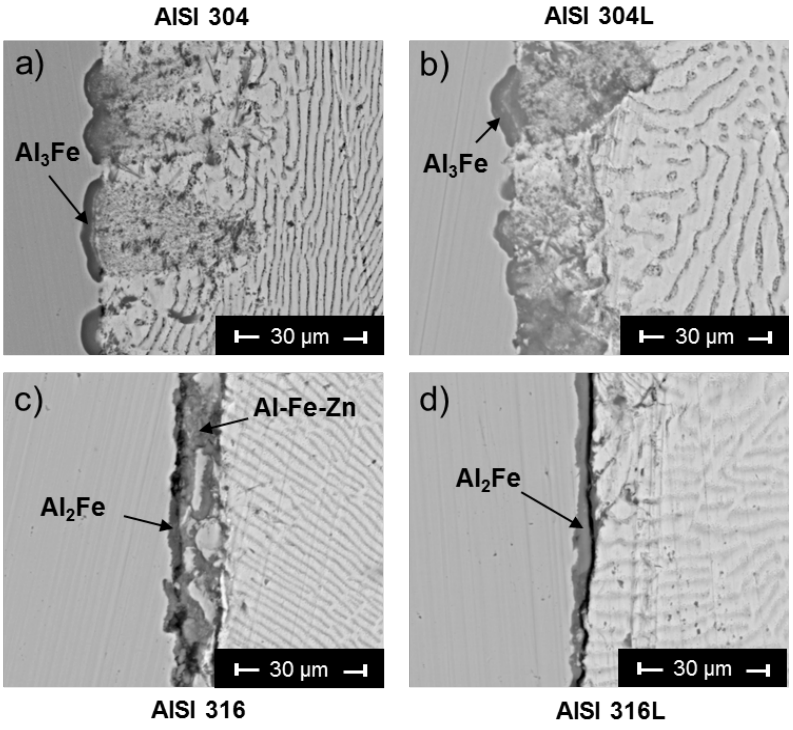

Figure 32. Back scattered-electron cross-section images (SEM) of (a) 304, (b) 304L, (c) 316 and (d) 316L stainless steels in the $Zn_{88.7}Al_{11.3}$ eutectic molten alloy after 720 hours at isothermal temperature of 400 ºC.

Similar corrosion behaviour between 316 and 316L steels can be seen in Figures 32 (c,d). In this case, uniform corrosion layers, without intermetallic particles diffusion are observed. These layers have regular and continuous structures. However, the corrosion layer in the 316 steel (see Figure 32 (c)) presents several big particles from molten alloy. The thicknesses of intermetallic layers are

approximately 10.3 μm and 2.8 μm for 316 and 316L steels, respectively. The EDX analysis shows two different intermetallic phases in the corrosion layer of the 316 steels. The first intermetallic phase, a thin layer adhered to steels, has been identified as Al_2Fe and the second or principal phase as an intermetallic phase of Al-Fe-Zn. On the other hand, the corrosion layer in the 316L steel has been identified as Al_2Fe intermetallic phase. The three intermetallic phases present low Cr and Ni content dissolved in their matrices. The adhesion of corrosion layers with steels and the molten alloy is different in both cases. The Al-Fe-Zn intermetallic layer in the 316 steel present fissures in its interface with Al_2Fe phase, adhered to the steel, and with the molten metal**.** However, the Al_2Fe intermetallic layer in 316L steel is adhered to the steel and presents a fissure in its interface with the molten alloy. Fissures are formed during the cooling process due to the different coefficients of thermal expansion (CTE) between the molten alloy and corrosion layers and between the Al-Zn-Fe and the Al_2Fe intermetallic phases. However, it can be concluded that the investigated $Zn_{88.7}Al_{11.3}$ metal alloy is not fully compatible with 304, 304L, 316 and 316L common stainless steels, where the last one presents the highest resistance to the corrosion reaction compared to the others. In general, the stainless steel 316L can be used as container material in direct contact with this metal alloy but in any case further investigation is required to analyse the evolution of this corrosion layer with time.

Compatibility tests with 321, 316Ti and 430 special stainless steels

In order to identify full compatible stainless steels with the investigated $Zn_{88.7}Al_{11.3}$ metal alloy other special stainless steels, i.e. 321, 316Ti and 430, have been selected. In Figure 33, cross-section images of the interface between $Zn_{88.7}Al_{11.3}$ eutectic alloy and 316Ti, 321 y 430 steels after being in contact 360 hours at 400 ºC are shown. In general, as it can be clearly seen, the corrosion layer is only present in the case of 321Ti steel while 321 and 430 steels show high corrosion resistance and no evidence of corrosion reaction products was detected.

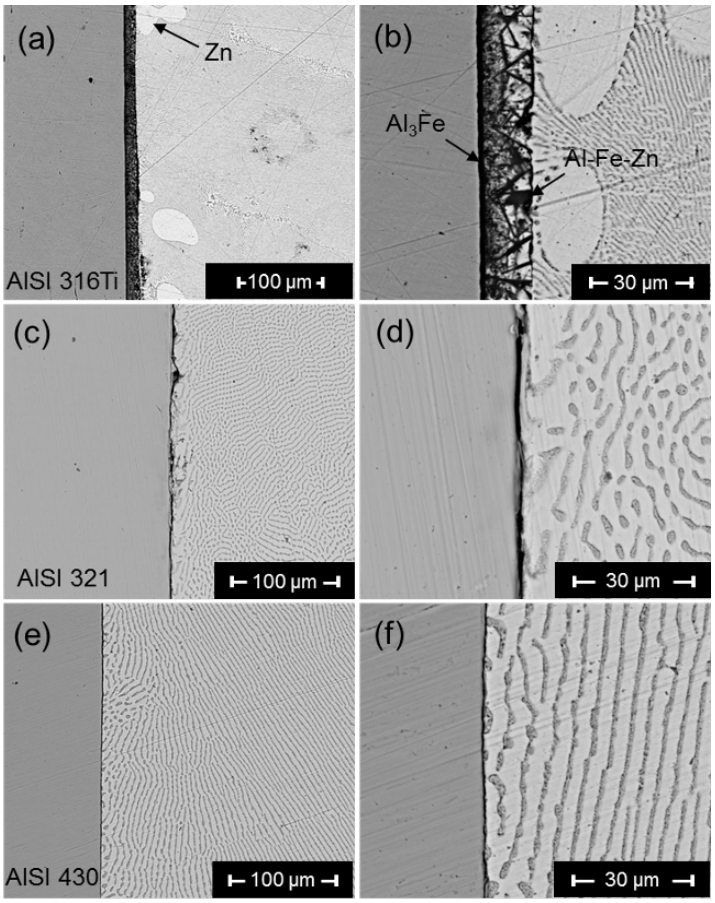

Figure 33. Back scattered-electron cross-section micrograph (SEM) of: (a-b) 316Ti, (c-d) 321, and (e-f) 430 stainless steels in the $Zn_{88.7}Al_{11.3}$ eutectic molten alloy after 360 hours at isothermal temperature of 400 ºC.

On the one hand, Figures 33 (a,b) displays the formed corrosion layer between $Zn_{88.7}Al_{11.3}$ alloy and 316Ti steel, which is totally adhered to both materials. This corrosion layer is formed by a regular and continuous intermetallic layer of 6.8 µm thickness and by a diffusion of intermetallic particles of 14.2 µm thickness from the layer toward the alloy. By means of EDX analysis the intermetallic layer adjacent to steel has been identified as θ-Al_3Fe phase and intermetallic particles as Al-Fe-Zn intermetallic phase. Both phases present low concentration of dissolved Cr and Ni atoms. It has to be noted the presence of solid solution of Zn dendrites in the interface between the 316Ti steel and metal alloy, which demonstrates an interaction in the intermediate region between them. On the second hand, Figure 33 (c,d) and Figure 33 (e,f) show cross-section micrographs of the $Zn_{88.7}Al_{11.3}$ alloy with 321 and 430 steels, respectively. As can be clearly seen, both steels present high corrosion resistance without showing formation of corrosion layers or intermetallic phases in the interfaces between both materials. These results give clear evidence that these two stainless steels 321 and 430 are fully compatible with $Zn_{88.7}Al_{11.3}$ eutectic alloy.

$Zn_{84}Al_{8.7}Mg_{7.3}$ eutectic alloy

Compatibility test with AISI 304, 304L, 316 and 316L common stainless steels

The interfaces between 304, 304L, 316 and 316L steels and the $Zn_{84}Al_{8.7}Mg_{7.3}$ eutectic alloy after compatibility tests at isothermal temperature of 400 ºC for 720 hours are shown in Figure 34.

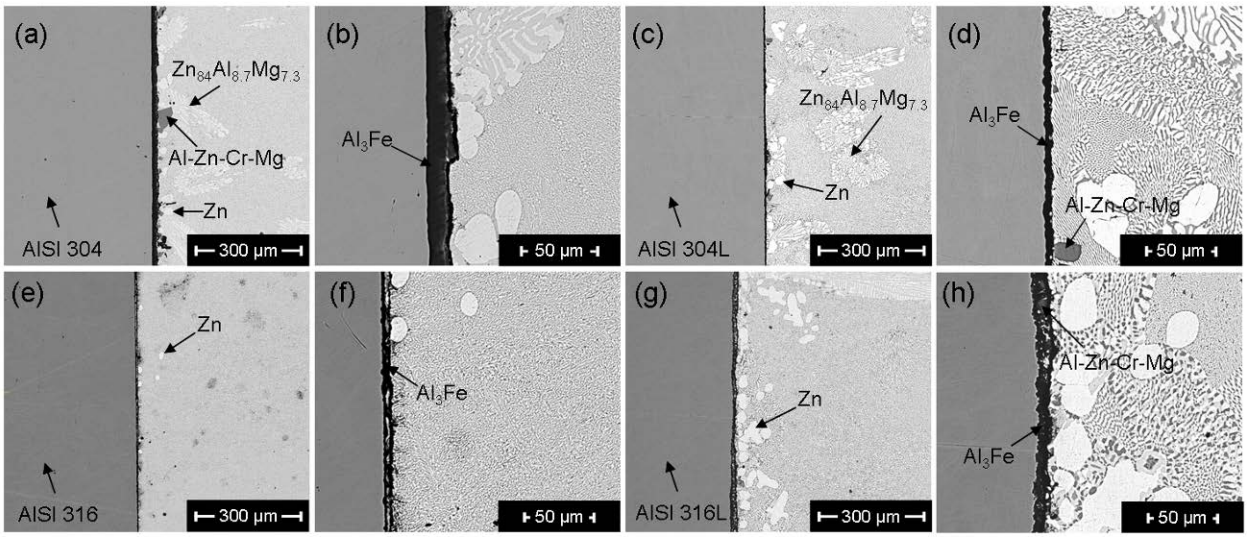

Figure 34. Back scattered-electron cross-section micrograph (SEM) of (a-b) 304, (c-d) 304L, (e-f) 316 and (g-h) 316L stainless steels in the $Zn_{84}Al_{8.7}Mg_{7.3}$ eutectic molten alloy after 720 hours at isothermal temperature of 400 ºC.

In general, four steels show similar corrosion mechanisms, where the 304L steel presents the highest corrosion resistance. In four cases, uniform and continuous corrosion layers are observed in the interface between both materials. The thickness of these layers are13.7 µm, 4.9 µm, 5.6 µm y 10 µm for 304, 304L, 316 y 316L steels, respectively, where the 304L shows the thinnest layer. On the other hand, some isolated and big intermetallic particles have been also observed in all cases. By EDX analysis, the corrosion layers have been identified as θ-Al_3Fe intermetallic phases and the intermetallic particles as an Al-Zn-Cr-Mg phase in the case of 304 and 316L stainless steels.

Slight differences among the microstructures of $Zn_{84}Al_{8.7}Mg_{7.3}$ molten alloys are observed in four samples. The molten alloy in contact with the 316 steel shows a homogeneous eutectic structure (see Figure 34 (e,f)). It is not worth to mention here that some Zn dendrites were observed in the alloys but the corrosion layers were detected across all the interface between both materials even where these dendrites are not detected. That means the presence of Zn dendrites is not responsible of the observed corrosion products.

Figure 35 shows EDX maps of the interface between the 316L steel and $Zn_{84}Al_{8.7}Mg_{7.3}$ molten alloy. As it has been observed, the formed Al-Fe intermetallic phase acts as inhibition layer

avoiding the diffusion of metal elements to the stainless steel and vice versa. Similar results were obtained for the other three systems with 304, 304L and 316 stainless steels.

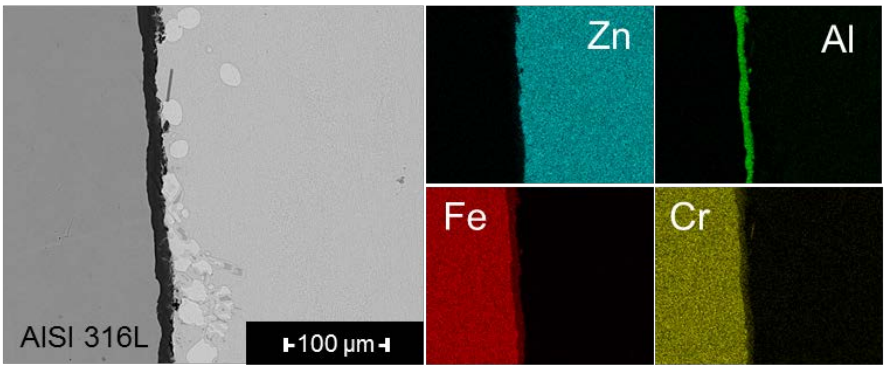

Figure 35. EDX map of the 316L stainless steel in the $Zn_{84}Al_{8.7}Mg_{7.3}$ eutectic alloy after 720 hours at isothermal temperature of 400 ºC.

Compatibility tests with 321, 316Ti and 430 special stainless steels

The interfaces between 316Ti, 321 y 430 steels and $Zn_{84}Al_{8.7}Mg_{7.3}$ eutectic alloys after compatibility tests at 400 ºC for 720 hours are shown in Figure 36. In general, the three stainless steels show different corrosion mechanisms, where the corrosion layer is absent in the case of 316Ti steel while is present in the case of 321 and 430 steels.

On the one hand, the cross-section micrographs of the interface between the 316Ti steel and $Zn_{84}Al_{8.7}Mg_{7.3}$ alloy sample are presented in Figure 36 (a,b). As it can be clearly seen, no corrosion layer is obtained. Very thin separation layer of approximately 1.4 µm is observed in the interface between both materials may be due to the high surface tension of $Zn_{84}Al_{8.7}Mg_{7.3}$ molten alloy to 316Ti stainless steel. On the other hand, corrosion layers were obtained in the case of 321 and 430 steels, where the first one presents the highest corrosion reaction. Figure 36 (c,d) shows cross-section micrographs of the interface between 321 steel and the metal alloy, where a regular and continuous thin layer of 1.14 µm thickness, adjacent and adhered to the steel, and diffusion of intermetallic particles from the interface toward the metal alloy were observed. The particles diffusion reaches approximately 181.8 µm of thickness where the size of particles increases as they move away of the interface. By EDX analysis two intermetallic phases have been identified in the intermetallic particles diffusion. Intermetallic particles of θ-Al_3Fe with needlefish form (in dark-grey) and particles of Al-Zn-Cr intermetallic phase (in light-grey). Moreover, the regular intermetallic layer adjacent to the steel has been identified as Al_2Fe intermetallic phase. The identified phases present low content Ni or/and Cr atoms. In addition, a fissure in the interfaces between the corrosion layer and metal alloy is observed.

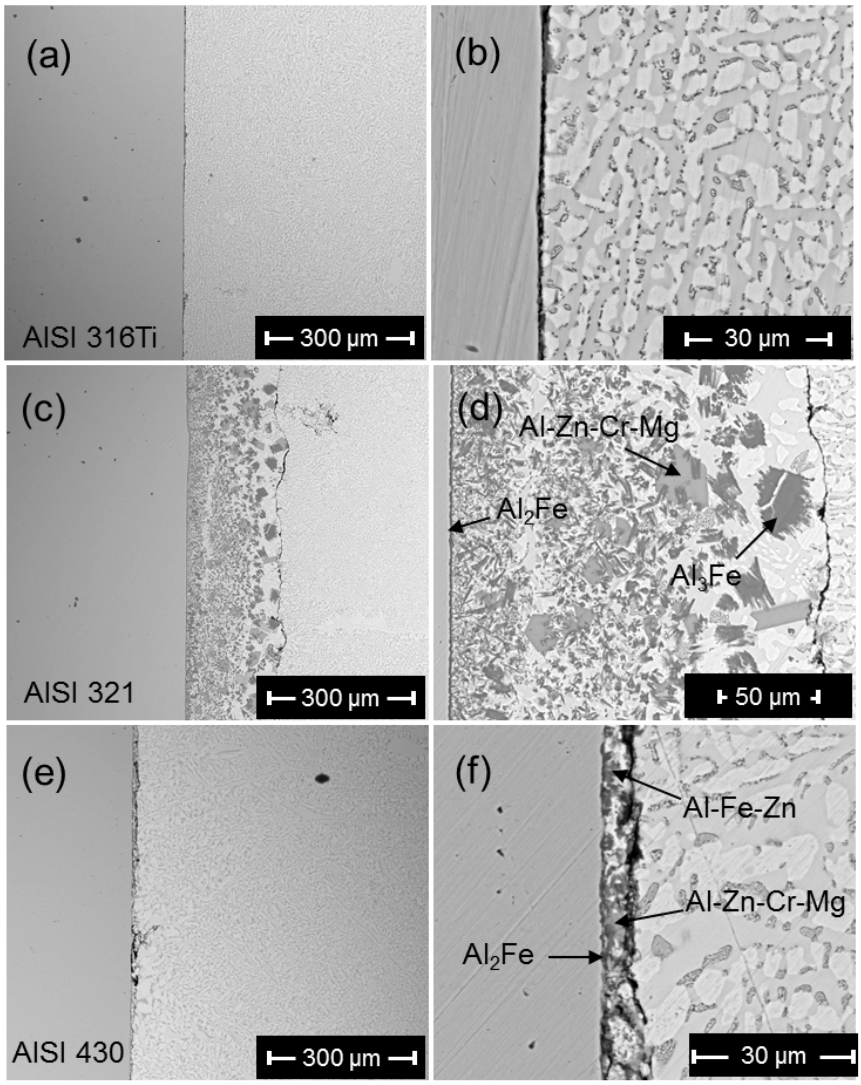

Figure 36. The back scattered-electron cross-section micrograph (SEM) of: (a-b) 316Ti, (c-d) 321, and (e-f) 430 stainless steels in the $Zn_{84}Al_{8.7}Mg_{7.3}$ eutectic alloy after 360 hours at isothermal temperature of 400 ºC.

The 430 steel shows slightly thinner corrosion layer compared to the one observed in 316Ti steel. Cross-section micrographs of the interface between the 430 steel and$Zn_{84}Al_{8.7}Mg_{7.3}$ alloy are shown in Figure 36 (e,f). The corrosion layer is formed by intermetallic particles and a thin continuous intermetallic layer adjacent to the steel of around 9.9 µm. In addition, the corrosion layer presents a fissure in its interface with the metal alloy. By EDX analysis the intermetallic layer adjacent to the steels has been identified as Al_2Fe intermetallic phase. On the other hand, intermetallic particles have been identified as an Al-Zn-Cr-Mg intermetallic phase (in light-grey) and as an Al-Zn-Fe intermetallic phase (in dark-grey).

Summary and discussion

The results of compatibility tests performed in this work are summarised in Table 21, where the identified intermetallic phases, corrosion layer thickness and layers morphology are listed for each alloy combined with the stainless steel proposed as containing material. Firstly, the 304, 304L, 316 and 316L stainless steels have shown a very good compatibility with the $Mg_{70}Zn_{24.9}Al_{5.1}$ eutectic alloy. In these cases, no corrosion reaction has been observed after 720 hours at 400 ºC. Therefore, the four stainless steels may be suitable as containment materials of the $Mg_{70}Zn_{24.9}Al_{5.1}$ PCM for the TES unit construction. Secondly, the good compatibility between 321 and 430 stainless steels and $Zn_{88.7}Al_{11.3}$ eutectic alloy can be also observed, where no corrosion reaction has been observed after 360 hours at 400 ºC. So, the 321 and 430 stainless steels can consider as good candidate materials to contain the $Zn_{88.7}Al_{11.3}$ alloy as PCM in a TES unit. Finally, the compatibility tests between the $Zn_{84}Al_{8.7}Mg_{7.3}$ eutectic alloy and the seven stainless steels demonstrate that the 316Ti stainless steel as the best candidate as containment material for $Zn_{84}Al_{8.7}Mg_{7.3}$. The 316Ti steel shows very high corrosion resistance with $Zn_{84}Al_{8.7}Mg_{7.3}$ alloy after 360 hours at 400 ºC.

The role of the metal alloy chemical composition in corrosion reaction

The formed corrosion layers with $Zn_{88.7}Al_{11.3}$ and $Zn_{84}Al_{8.7}Mg_{7.3}$ metal alloys have been identified as Al-Fe intermetallic phases. As it has been shown in this work these intermetallic layers behave like inhibition layers to Zn, avoiding its diffusion toward the steels and the consequent corrosion reaction between Fe and Zn due to the highest affinity of Al to Fe. This result is in agreement with performed observations in [104-106].

The roles of chemical compositions of metallic alloys can be analysed by comparing the results obtained in contact with the same stainless steel. The Fe is inert to molten Mg below 1000 ºC, according to the Mg-Fe equilibrium phase diagram [107]. So, the Al content is, therefore, the

Metallic alloy	Stainless steel (AISI)	Temperature (ºC)	Immersion time (h)	Corrosion reaction	Corrosion layer morphology	Corrosion layer average thickness (μm)	Particles diffusion average thickness (μm)	Identified phases
$Mg_{70}Zn_{24.9}Al_{5.1}$	304	400	720	No	-	-	-	-
	304L	400	720	No	-	-	-	-
	316	400	720	No	-	-	-	-
	316L	400	720	No	-	-	-	-
$Zn_{88.7}Al_{11.3}$	304	400	720	Yes	Uniform intermetallic layer adhered to steel and intermetallic crystal diffusion toward molten alloy.	3.2	38.4	θ-Al_3Fe
	304L	400	720	Yes	Uniform intermetallic layer adhered to steel and intermetallic crystal diffusion toward molten alloy.	3.3	31.5	θ-Al_3Fe
	316	400	720	Yes	Uniform corrosion layer.	10.3	-	Al_2Fe; Al-Fe-Zn
	316L	400	720	Yes	Uniform intermetallic layer adhered to steel.	2.8	-	Al_2Fe
	316Ti	400	360	Yes	Uniform intermetallic layer adhered to steel and intermetallic crystal diffusion toward molten alloy.	6.8	14.2	θ-Al_3Fe; Al-Fe-Zn
	321	400	360	No	-	-	-	-
	430	400	360	No	-	-	-	-
$Zn_{84}Al_{8.7}Mg_{7.3}$	304	400	720	Yes	Uniform intermetallic layer adhered to steel.	13.7	-	θ-Al_3Fe; Al-Zn-Cr-Mg
	304L	400	720	Yes	Uniform intermetallic layer adhered to steel.	4.9	-	θ-Al_3Fe; Al-Zn-Cr-Mg
	316	400	720	Yes	Uniform intermetallic layer adhered to steel.	5.6	-	θ-Al_3Fe
	316L	400	720	Yes	Uniform intermetallic layer adhered to steel.	10	-	θ-Al_3Fe
	316Ti	400	360	No	-	-	-	-
	321	400	360	Yes	Uniform intermetallic layer adhered to steel and intermetallic crystal diffusion toward molten alloy.	1.1	181.1	Al_2Fe; θ-Al_3Fe; Al-Zn-Cr-Mg
	430	400	360	Yes	Uniform intermetallic layer adhered to steel and intermetallic crystal diffusion toward molten alloy.	0.9	8.9	Al_2Fe; Al-Zn-Cr-Mg; Al-Fe-Zn

Table 21. Summary of compatibility test results: the identified intermetallic phases, corrosion layer thickness and layers morphology.

dominant factor in the baths chemistry. On the other hand, depending on Al and Fe content different intermetallic phases into Al-Fe system will be formed. In this way, if corrosion layers of $Zn_{88.7}Al_{11.3}$ and $Zn_{84}Al_{8.7}Mg_{7.3}$ metal alloys with the same stainless steel are compared and in all cases different intermetallic phases are formed (see Table 21). These results mark the great importance of Al and Fe contents in the interfacial zone for the intermetallic layer formation.

The addition of small amount of Al allows the formation of Al-Fe inhibition layer and reduces the activity of Zn. However, when the amount of Al reaches a critical value the dominant corrosion reaction changes from Fe-Zn to Al-Fe. From this point, the corrosion rates increase when Al content in the molten metal increases. The corrosion rates as a function of Al content is proposed graphically in [104], where Al critical value has been estimated in 0.22 wt%. In other to analyze the Al content influence on corrosion rate, the same growth rates of different Al-Fe intermetallic layer is assumed. Under this assumption, corrosion layers in the $Zn_{88.7}Al_{11.3}$ metal alloy have to be thicker than layers in the $Zn_{84}Al_{8.7}Mg_{7.3}$ bath. In Table 21 can be observed that this trend is true in the half of the cases. The test performed with the 316L, 321 and 430 steels in the $Zn_{88.7}Al_{11.3}$ metal alloy reveal thinner corrosion layers than in the $Zn_{84}Al_{8.7}Mg_{7.3}$ metal alloy, although the highest Al content in the $Zn_{88.7}Al_{11.3}$ alloy. This fact suggests that the Fe concentration in the interfacial reaction zone could have higher influence in the corrosion rate than Al concentration.

The addition of small amount of Al allows the formation of Al-Fe inhibition layer and reduces the activity of Zn. However, when the amount of Al reaches a critical value the dominant corrosion reaction changes from Fe-Zn to Al-Fe. From this point, the corrosion rates increase when Al content in the molten metal increases. The corrosion rates as a function of Al content is proposed graphically in [104], where Al critical value has been estimated in 0.22 wt%. In other to analyze the Al content influence on corrosion rate, the same growth rates of different Al-Fe intermetallic layer is assumed. Under this assumption, corrosion layers in the $Zn_{88.7}Al_{11.3}$ metal alloy have to be thicker than layers in the $Zn_{84}Al_{8.7}Mg_{7.3}$ bath. In Table 21 can be observed that this trend is true in the half of the cases. The test performed with 316L, 321 and 430 steels in the $Zn_{88.7}Al_{11.3}$ metal alloy reveal thinner corrosion layers than in the $Zn_{84}Al_{8.7}Mg_{7.3}$ metal alloy, although the highest Al content in the $Zn_{88.7}Al_{11.3}$ alloy. This fact suggests that the Fe concentration in the interfacial reaction zone could have higher influence in the corrosion rate than Al concentration.

According to Al, Zn and Mg affinities with Fe, Al-Fe intermetallic phase formations are expected in the performed compatibility tests with the $Mg_{70}Zn_{24.9}Al_{5.1}$ metal alloy. However, no corrosion reaction is observed, which indicates the importance of the Mg presence in the corrosion

mechanism of the $Mg_{70}Zn_{24.9}Al_{5.1}$ metal alloy, where Fe is inert to the Mg. The high content of Mg hinders the Al diffusion through the melt.

The control mechanism in the corrosion reaction

The corrosion process in the investigated steel/alloy systems is controlled by the diffusion mechanism. Al-Fe intermetallic layers act as diffusion barrier to Zn, while the Al itself is not diffusing through the layer toward steels [106]. However, the Fe and alloying elements of steels diffused through Al-Fe layers into metal alloy and as consequence, Al-Fe layers move deeper into molten alloy. The Al/Fe reaction rate is much faster than Fe diffusion through the layer, so, the Fe diffusion through the Al-Fe layer into the metal alloy is controlling the corrosion reaction in $Zn_{88.7}Al_{11.3}$ and $Zn_{84}Al_{8.7}Mg_{7.3}$ baths. On the other hand, the Fe diffusion dominance on Al-Fe layer explains the less influence on corrosion rate of Al concentration in the interfacial reaction zone of these alloys.

As it has been discussed above, compatibility tests results obtained in the $Mg_{70}Zn_{24.9}Al_{5.1}$ metal alloy suggests that the high Mg content in this bath hinders Al diffusion through the melt toward steel and the consequent corrosion reaction in the interface. Thus, the corrosion reaction in the $Mg_{70}Zn_{24.9}Al_{5.1}$ eutectic metal alloy is controlled by the Al diffusion through the melt toward the interface.

The role of the stainless steels composition in corrosion reaction

The comparison of intermetallic layers in the same metal alloy but with different stainless steels shows the influence of steel composition in corrosion reaction. Based on constant Al content in the $Zn_{88.7}Al_{11.3}$ metal alloys the same Al-Fe intermetallic phase could be expected with all stainless steels. However, same intermetallic layer is only observed with 304 and 304L steels and with 316 and 316L. In the $Zn_{84}Al_{8.7}Mg_{7.3}$ metal alloy, however, 304, 304L, 316 and 316L steels show same intermetallic layer while 316Ti, 321 and 430 steels shows different layer. These results show that the steels composition have important role in the intermetallic layer formation when Al-Fe is the dominant reaction.

The corrosion resistance of steels in molten metals also depends on the concentration of allowing element (typically Cr and Ni) in steels. According Xu et al. [108] high contents of Cr combined with Ni improve the corrosion resistant of steels in molten Zn. All tested stainless steels in this work have high contents of Cr and Ni, except AISI 430 steel, which does not present Ni in its

chemical composition. The 430 steel does not show higher corrosion reaction than other steels in $Zn_{88.7}Al_{11.3}$ and $Zn_{84}Al_{8.7}Mg_{7.3}$ baths.

On the other hand, other stainless steels present similar Cr and Ni, which do not explain the big differences observed in corrosion reactions with $Zn_{88.7}Al_{11.3}$ and $Zn_{84}Al_{8.7}Mg_{7.3}$ baths. So, a deeper study about the influence of different stainless steel compositions on corrosion process is required to understand the obtained complex results.

Elements diffusion through intermetallic layers

The presence of Al-Fe corrosion layers hindered the diffusion of element through itself toward interfacial reaction zone. However, the partial break down and spallation of the layer after continues exposure times exposed a novel steel surface to react with Al. So, the intermetallic layers with lower tendency to break down and spall after continues exposure times advantage the corrosion resistant of steels.

Steels corrosion in molten metals by means of the dissolution process depends on the amount of dissolved elements in intermetallic layer and their diffusion rate through intermetallic layers toward interfacial reaction zone. At the same time, the morphology and microstructure of layers affect in the diffusion rate, where the concentration gradient is the driving force. However, the diversity and complexity of observed corrosion reactions, in $Zn_{88.7}Al_{11.3}$ and $Zn_{84}Al_{8.7}Mg_{7.3}$ baths, require an extensive study. However, the first general analysis suggests the expected behaviour. The Fe, Cr and Ni concentrations in interfaces decrease as they move away from steels whereas that Al and/or Zn concentrations in interfaces decrease as they move away of the metal alloys This result suggests different solubility and diffusion rate of these elements in the layers.

Others parameter roles in corrosion reactions

Other parameters that can influence in corrosion reactions are adhesion levels between the steels and metal alloys and the concentration of Zn dendrites in the metal alloys. The results analysis during the execution of this study suggests, in some cases, the existence of different adhesion level between steels and metal alloys during the execution of compatibility tests. A poor adhesion between both materials, favored by the high surface tension of the molten metal, will hinder the corrosion reaction. It should be point out this analysis was performed at lab scale. Hence, at larger scale the adhesion level between steels and molten alloys can be different due to the mass and geometry of the TES system.

By the analysis of Al-Fe intermetallic layers in different zones has been observed in some cases that the presence of Zn dendrites cause the break of layers and the existence of corrosion crystal with high content of Zn. Although these results have not been observed in all cases is advisable to avoid the Zn dendrites presence in the microstructure of eutectic alloys due to their fast migration toward the steel surface.

Conclusions

In this work the compatibility of four eutectic metallic alloys as PCM with seven stainless steels as potential containment materials has been tested for latent heat storage application. The aim of this study is to identify the most adequate stainless steel to contain each eutectic metallic alloy in a TES unit. Thereby, the common stainless steels, i.e. 304, 304L, 316 and 316L have not shown any corrosion reaction with the $Mg_{70}Zn_{24.9}Al_{5.1}$ eutectic molten alloy. Moreover, the 430 stainless steel followed 321 steel have been shown the highest corrosion resistance in $Zn_{88.7}Al_{11.3}$ eutectic molten alloy. Finally, the 316Ti stainless steel has been present the best compatibility with $Zn_{84}Al_{8.7}Mg_{7.3}$ eutectic molten alloy. Therefore, based on obtained test results, the indicated stainless steels may be adequate material to contain the $Mg_{70}Zn_{24.9}Al_{5.1}$, $Zn_{88.7}Al_{11.3}$ and $Zn_{84}Al_{8.7}Mg_{7.3}$ as potential PCMs in a TES unit.

Based on corrosion reaction analysis, it can be concluded:

In $Zn_{88.7}Al_{11.3}$ and $Zn_{84}Al_{8.7}Mg_{7.3}$ bath, the Al-Fe intermetallic phases act like inhibition layers to Zn, avoiding the corrosion reaction between Fe and Zn due to the highest affinity of Al. Different Al-Fe intermetallic phases observed with same stainless steel in both baths mark the importance of Al and Fe contents in the interfacial zone for the intermetallic layer formation. The Fe concentration in interfacial reaction zone has higher influence in the corrosion rate than Al concentration. On the other hand, in $Mg_{70}Zn_{24.9}Al_{5.1}$ molten alloy no corrosion reaction was observed due to the Mg hinders the Al diffusion through the melt.

The corrosion process in investigated systems is controlled by the diffusion mechanism. The Fe diffusion through the Al-Fe layer into the molten alloy is controlling the corrosion reaction in $Zn_{88.7}Al_{11.3}$ and $Zn_{84}Al_{8.7}Mg_{7.3}$ baths. The corrosion reaction in the $Mg_{70}Zn_{24.9}Al_{5.1}$ eutectic molten alloy is controlled by the Al diffusion through the melt toward the interface.

Stainless steels compositions show high influence in the corrosion reaction. However, the big differences observed in corrosion reactions with $Zn_{88.7}Al_{11.3}$ and $Zn_{84}Al_{8.7}Mg_{7.3}$ baths in function of their alloying element concentrations has not been explained and a deeper study is required.

The diversity and complexity of observed corrosion reactions, in $Zn_{88.7}Al_{11.3}$ and $Zn_{84}Al_{8.7}Mg_{7.3}$ baths, require an extensive study in order to analyse the steels elements diffusion through intermetallic corrosion layer. However, the first analysis suggests that the Fe, Cr and Ni concentrations in interfaces decrease as they move away from steels whereas that Al and Zn concentrations in interfaces decrease as they move away of molten alloys.

Different adhesion level between steels and molten alloys during the tests have been observed, where a poor adhesion advantages the corrosion resistance. Finally, the observed Zn dendrites migration toward the steel surfaces may lead to possible break of corrosion layers. Consequently, it is advisable to avoid the Zn dendrites presence in the molten alloys.

Finally, compatibility test with different immersion times are under consideration in order to study the evolution of corrosion layer with the time.

5. Collaborations

5.1. Thermodynamic study of the eutectic Mg_{49}-Zn_{51} alloy used for thermal energy storage

Introduction

In this work, the Mg-Zn binary system has been identified of particular interest as it presents an eutectic composition, Mg_{49}-Zn_{51} (mass %), which matches the requirements concerning melting-solidification temperature and storage energy density [44] for direct steam generation in a concentrated solar power plant.

Within this scope, the exhibited solid-solid and solid-liquid phase transitions have been carefully characterized. A detailed thermodynamic study focused on the specific heat of the investigated alloy is also provided. The c_p behaviour, very important in the thermal energy storage frame, is theoretically modeled and experimentally validated by quasi-isothermal Modulated Differential Scanning Calorimetry measurements. Different intermetallic phases of the Mg-Zn binary system have also been successfully described within this approach in the complete temperature range.

Experimental results

Various standard DSC experiments at different heating/cooling rates have been performed. At 5 and 10 K min^{-1} rates two partially overlapped transformation peaks have been found on heating and cooling. At 1 K min^{-1} rate, Figure 37 shows two clear separate transformation peaks on the heating run, which permits to analyze each transformation event separately. According to the Mg-Zn phase diagram [110,111], the first peak, with $T_1^h = 608.3\,\mathrm{K}$ onset temperature and $\Delta H_1^h = 24.8\,\mathrm{J\,g^{-1}}$ enthalpy, corresponds to the eutectoid reaction of the MgZn intermetallic phase (also identified as $Mg_{12}Zn_{13}$ [112] and $Mg_{21}Zn_{25}$ with trigonal structure, space group $R\bar{3}c$ [64]) and Mg. This leads to the formation of the $Mg_{51.04}Zn_{19.80}$ (orthorhombic structure, space group Immm [113]) intermetallic compound. The second peak at $T_2^h = 614.5\,\mathrm{K}$, corresponds to the melting process of the eutectic

alloy with a latent heat of $\Delta H_2^h = 130.2\ \mathrm{J\ g^{-1}}$. Overall, the total enthalpy value of both transformation processes is $\Delta H_T^h = 155.0\ \mathrm{J\ g^{-1}}$, in agreement with reference [44].

On cooling, both peaks are partially overlapped, even at 0.5 K min^{-1} cooling rate. The onset temperature of the solidification process is found at $T_2^c = 606.6\ \mathrm{K}$ while the eutectoid reaction onset temperature cannot be accurately determined. However, $T_1^c = 605.4\ \mathrm{K}$ approximated value is obtained by extrapolation of the DSC peak. Based on the onset temperatures of the melting-solidification process and the eutectoid reaction the thermal hysteresis values are $\Delta T_2 = 7.9\ \mathrm{K}$ and $\Delta T_1 = 2.9\ \mathrm{K}$ respectively. The determination of the individual transformation enthalpies is difficult in this case, but the total value of both processes is $\Delta H_T^c = 153.0\ \mathrm{J\ g^{-1}}$.

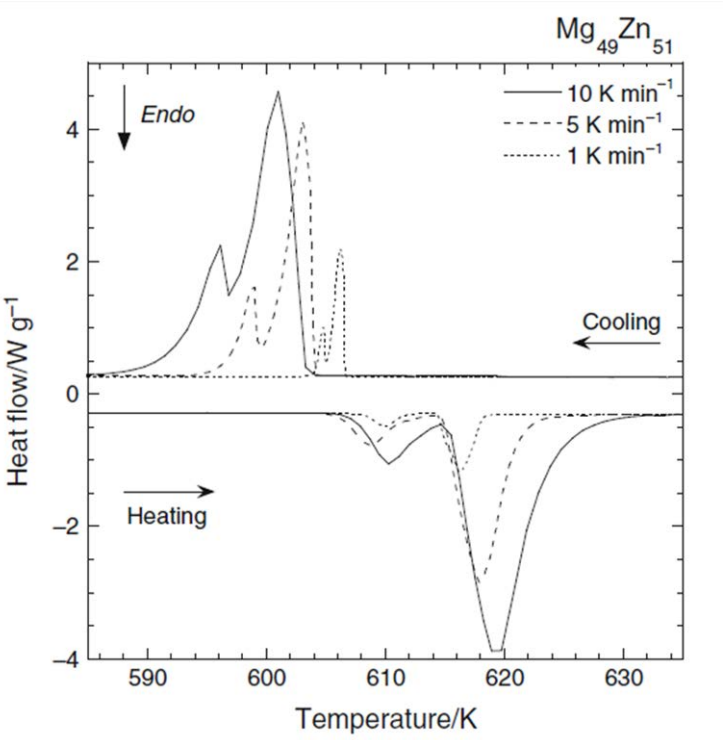

Figure 37. DSC results for the eutectic Mg_{49}-Zn_{51} alloy at 10, 5 and 1 K min^{-1} heating/cooling rates. Exception made for the 1 K min^{-1} heating run, two overlapped transformations peaks have been found in the performed DSC experiments.

When heating at 5 and 10 K min^{-1}, the obtained eutectoid reaction temperatures are $T_1^h = 605.6\ \mathrm{K}$ and $T_1^h = 606.5\ \mathrm{K}$ respectively. The melting temperatures are similar to the value found at 1 K min^{-1}. On cooling, the measured solidification temperatures are $T_2^c = 604.3\ \mathrm{K}$ at 5 K min^{-1} and $T_2^c = 603.6\ \mathrm{K}$ at 10 K min^{-1}. In the three investigated rates no changes on the total enthalpy value have been found.

The differences on the solidification process, shown in Figure 37, which are dependent on the cooling rate, might influence the nucleation process of the alloy. In addition, due to the different thermal hysteresis values, both transformation processes are closer in temperature on the cooling run. As no thermal equilibrium is attained during the measurement, the eutectoid reaction could start before the solidification process is completed. Overall, these phenomena might influence the nucleation process of the solid phases and the subsequent eutectoid reaction on consecutive thermal cycles. As a consequence, different eutectoid reaction behaviour and temperatures can be expected. This may explain the discrepancy on the eutectoid reaction temperatures between the value obtained in this work and the ones given by [111] and [114], $T_1^h = 598.2\text{K}$ and $T_1^h = 594\,\text{K}$ respectively. The small difference of the total enthalpy value measured on heating and cooling, around 1%, which is larger than the experimental error, might be also related to similar mechanisms. Anyway, further investigation is needed to clarify this behaviour.

Theoretical lattice specific heat calculation of the Mg_{49}-Zn_{51} alloy

The thermodynamic functions such as the enthalpy, entropy or Gibbs energy, determine the thermal behaviour of a material. For this reason, when a sensible or latent heat storage device is designed, $H(T), S(T)$ and $G(T)$ are usually required. All these functions can be numerically obtained from the specific heat data. As a consequence, the knowledge of the specific heat of the storage material becomes of great importance. The lattice specific heat of a compound can be determined in the complete temperature range by using a theoretical model based on the addition of the harmonic, electronic and anharmonic contributions. However, due to the lack of complete experimental data about the investigated alloy, the specific heat has to be calculated within an approximated frame.

Harmonic contribution

The harmonic lattice specific heat (C_h), which in general can be assumed to be the specific heat at constant volume (C_v) can be directly obtained from the Debye model by using equation (18). For both metals, Mg and Zn, this model assumes a parabolic distribution of the phonon density of states (DOS) given by equation (19) where ν_D is the Debye´s cut-off frequency:

$$C_h = C_v = 3nk_B\left(\frac{T}{\theta_D}\right)^3 \int_0^{\theta_D/T} \frac{x^4 e^x}{(e^x - 1)^2} dx \tag{18}$$

$$g(\nu) \propto \nu^2 \quad (0 \le \nu \le \nu_D) \tag{19}$$

In equation (18), n is the number of atoms per unit mass, θ_D is the empirical Debye temperature, k_B is the Boltzmann constant and h is the Planck constant. The Debye´s cut-off frequency (ν_D) and the variable (x) of equation (18) are given by equations (20) and (21) respectively.

$$\nu_D = \frac{k_B \theta_D}{h} \tag{20}$$

$$x = \frac{h\nu_D}{k_B T} \tag{21}$$

In order to obtain accurate numerical results, the Debye integral (equation 1) has been expanded by means of a polynomial fitting as a function of the coefficient (θ_D/T) in two separate temperature ranges, as shown in equation (22). Conventionally, the high and low temperature limit between both ranges has been established in $T = (\theta_D/25)$.

$$C_h = C_v = \begin{cases} \sum_{n=0}^{20} a_n \left(\frac{\theta_D}{T}\right)^n & \text{if} \quad T \geq \left(\frac{\theta_D}{25}\right) \\ \frac{b}{\left(\frac{\theta_D}{T}\right)^3} & \text{if} \quad T < \left(\frac{\theta_D}{25}\right) \end{cases} \tag{22}$$

By using this procedure the harmonic specific heat of each individual metallic component of the alloy, Mg and Zn, has been calculated. In the literature different characteristic Debye temperatures (θ_D) of both metals can be found [115-118]. However, the best results are obtained selecting $\theta_D^{Mg} = 318\,\text{K}$ and $\theta_D^{Zn} = 234\,\text{K}$ [34]. The harmonic lattice specific heats averaged by the mass percentage of each component of the alloy, 49% Mg and 51% Zn respectively, are shown in the figure 2 (C_h^{Mg} and C_h^{Zn}). The addition of both contributions as shown in equation (23) gives the total harmonic specific heat of the Mg_{49}-Zn_{51} eutectic alloy (curve 1 in Figure 38).

$$C_h^{alloy} = C_v^{alloy} = 0.49 C_h^{Mg} + 0.51 C_h^{Zn} \tag{23}$$

Electronic contribution

Within the free electron model, which is valid to describe most of the metallic elements, this contribution to the total lattice specific heat is given by equation (24). Except at low temperatures, it is usually very small when compared with the harmonic contribution of the lattice. Its value at room temperature represents around a 0.5% of the total specific heat.

$$C_e = \frac{\pi^2 k_B^2 n}{2\varepsilon_F} T \tag{24}$$

In equation (24) k_B is the Boltzmann constant, n is the number of electrons in the conduction band and ε_F is the Fermi energy.

In the Mg_{49}-Zn_{51} eutectic alloy each metal contributes with 2 electrons to the conduction band. As a consequence, the electron number per unit mass in the conduction band is given by equation (25) as a function of the Avogadro´s number (N_A=6,022x10^{23}) and the atomic mass of each element (A).

$$n = \frac{2N_A}{A} \tag{25}$$

Taking into account that Fermi's energy values are ε_F=7,08 eV for Mg and ε_F=9,47 eV for Zn [119], the electronic contribution to the specific heat of the eutectic alloy as a function of temperature is given by equation (26) in terms of the averaged individual contribution (mass %).

$$C_e^{alloy} = 0{,}49 C_e^{Mg} + 0{,}51 C_e^{Zn} = 0{,}49 \cdot 4{,}11x10^{-5} T + 0{,}51 \cdot 1{,}14x10^{-5} T \tag{26}$$

At room temperature (T=298.15 K), the electronic contribution is $C_e^{alloy} = 0{,}0077\ \mathrm{J\,g^{-1}K^{-1}}$, which represents around 1% of the harmonic lattice contribution to C_p. This is a noticeably high value compared with other metallic elements or alloys. However, this behaviour might be explained by the electronic band structure of the transition metals like Zn which usually leads to high electronic specific heat [115]. The addition of the harmonic and electronic contributions, $C_h^{alloy} + C_e^{alloy}$, leads to the curve 2 of the figure 2. As can be seen, both contributions clearly underestimate the experimental value of the C_p baseline of the eutectic alloy (circled line in figure 2). This difference can be associated to the anharmonic contribution to the total lattice C_p.

Anharmonic contribution

For isotropic materials, it can be shown that the anharmonic contribution is given by equation (27).

$$C_{anh} = C_p - C_v = TV\frac{\alpha^2}{k_T} \tag{27}$$

where T is the absolute temperature, V is the specific volume, α is the volume thermal expansion coefficient and k_T is the isothermal compressibility.

For anisotropic materials this relation can be generalized as a function of the elastic constant tensor (c_{ijkl}), as shown in equation (28).

$$C_{anh} = C_p - C_v = TV \sum_{i,j,k,l=1}^{3} c_{ijkl}\alpha_{ij}\alpha_{kl} \tag{28}$$

Taking into account the symmetry of the crystal, equation (28) can be simplified. However, this procedure implies the knowledge of the elastic constant tensor which is not available for the eutectic Mg_{49}-Zn_{51} alloy. As a consequence, in order to obtain the anharmonic contribution to the lattice specific heat, a phenomenological model is necessary. One alternative is the Nernst-Lindemann semi-empirical relation, shown in equation (29). It is based on Grüneisen equation and it states that the anharmonic contribution is proportional to the product of the absolute temperature and the squared total lattice specific heat (C_p).

$$C_{anh} = C_p - C_v = aTC_p^2 \tag{29}$$

In equation (29), "a" is an empirical parameter, given by equation (30), which depends on the material. It has a nearly constant value over a wide range of temperature.

$$a = \frac{V\alpha^2}{C_p^2 k_T} \tag{30}$$

If any of the expansivity parameters is not known, one alternative is to empirically fit the measured C_p baseline by changing the value of the "a" constant. Using the harmonic specific heat values of the alloy obtained from equation (23), the anharmonic contribution can be calculated in the complete temperature range by solving equation (29) for C_p and selecting empirically $a = 3.4x10^{-4}$ g J^{-1}. It can be noted that the value of this constant is similar to the one found for pure Zn and it is close to the value corresponding to Cu ($3x10^{-4}$ g J^{-1}).

Finally, curve 3 of the Figure 38 shows the theoretical specific heat of the eutectic Mg_{49}-Zn_{51} alloy $\left(C_h^{alloy} + C_e^{alloy} + C_{anh}^{alloy}\right)$ together with the experimental C_p values obtained by modulated DSC (circles in Figure 38). It can be noted that the difference between theoretical and experimental values is lower than 3%.

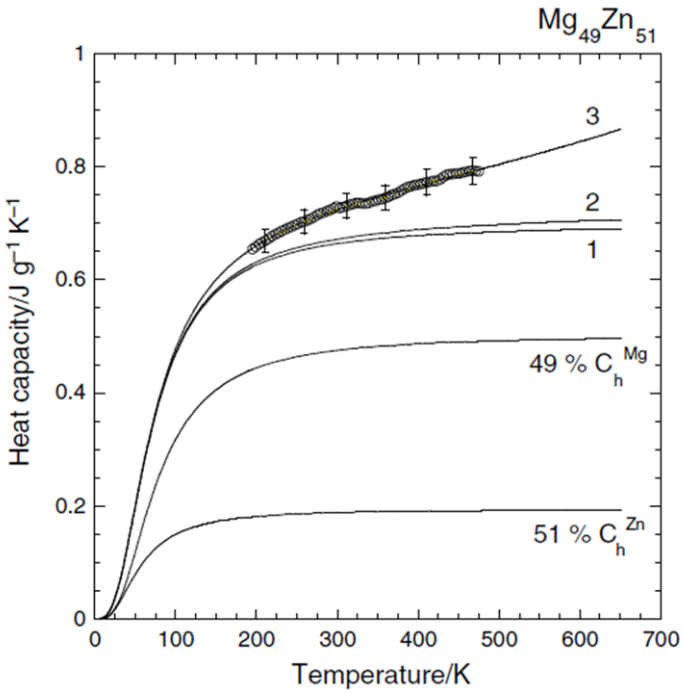

Figure 38. Circles represent the experimental Cp value of the eutectic Mg-%51Zn alloy obtained by modulated Differential Scanning Calorimetry. Curve (1): harmonic specific heat of the alloy; (2) harmonic + electronic specific heat; (3) harmonic + electronic + Nernst-Lindemann anharmonic specific heat.

For comparison, as an example, the experimentally obtained C_p value of the eutectic Mg_{49}-Zn_{51} alloy at room temperature is $C_p^{alloy}(298.15) = 0{,}73\,\mathrm{J\,g^{-1}K^{-1}}$. Calculating the weighted average specific heat at the same temperature from the experimental values of the individual metallic elements $C_p^{Mg}(298.15) = 1.024\,\mathrm{J\,g^{-1}K^{-1}}$ and $C_p^{Zn}(298.15) = 0.388\,\mathrm{J\,g^{-1}K^{-1}}$ [119]), the obtained result is $C_p^{average} = 0.70\,\mathrm{J\,g^{-1}K^{-1}}$. Finally, the C_p value predicted by the thermodynamic model explained above is $C_p^{alloy} = 0.72\,\mathrm{J\,g^{-1}K^{-1}}$. In the three cases the data dispersion is contained within a ±4%.

This theoretical model provides an accurate specific heat baseline in the complete temperature range. Its direct numerical integration allows the calculation of the thermodynamic functions of the eutectic alloy. Within this frame, the transformation thermodynamic functions can also be obtained. The thermodynamic equilibrium temperature of the eutectoid reaction and melting/solidification process can be defined as the average temperature between the heating and cooling transformation events: $T_{eq1} = 606.85\,\mathrm{K}$ and $T_{eq2} = 610.55\,\mathrm{K}$ respectively. Equation (31) gives the entropy change in both cases.

$$\Delta S = \frac{\Delta H}{T_{eq}} \tag{31}$$

The obtained values are $\Delta S_1(T_{eq1}) = 0.04\ \mathrm{J\ g^{-1}K^{-1}}$ and $\Delta S_2(T_{eq2}) = 0.21\ \mathrm{J\ g^{-1}K^{-1}}$ respectively. Finally, the driving force of the melting and solidification process of the alloy can be calculated from equation (15).

$$\Delta G(T) = \left| G_{liquid}(T) - G_{solid}(T) \right| \tag{32}$$

The respective values are $\Delta G_m(T_2^h = 614.5\ \mathrm{K}) \approx \Delta G_s(T_2^c = 606.6\ \mathrm{K}) \approx 0.84\ \mathrm{J\ g^{-1}}$.

Application to other Mg-Zn alloys

This thermodynamic model has also been applied to several Mg-Zn intermetallic compounds. Morishita et al. [120] have reported the specific heat values of the $Mg_{25.55}$-$Zn_{74.45}$, $Mg_{19.86}$-$Zn_{80.14}$, $Mg_{15.66}$-$Zn_{84.34}$ and $Mg_{6.34}$-$Zn_{93.66}$ (mass %) alloys in the 2-700 K temperature range. As indicated in [120], C_p was measured by using the so-called "relaxation technique" for the 2-400 K range and by DSC for the 400-700 K range.

For each alloy, the harmonic and electronic contributions to the total specific heat are directly obtained selecting the individual metal compositions (mass %) on each case. On the other hand, the anharmonic contribution depends on the material. The thermophysical properties that determine the anharmonic contribution associated to different intermetallic compounds might show noticeable changes leading to different C_{anh} values. In this model, this contribution is empirically determined selecting the "a" constant in equation (29) for each different alloy. The selected values have been $a = 2.7x10^{-4}, 2.9x10^{-4}, 2.4x10^{-4}$ and $2.4x10^{-4}\ \mathrm{g\ J^{-1}}$ for $Mg_{25.55}$-$Zn_{74.45}$, $Mg_{19.86}$-$Zn_{80.14}$, $Mg_{15.66}$-$Zn_{84.34}$ and $Mg_{6.34}$-$Zn_{93.66}$ respectively. The comparison between the reported experimental C_p data and the predicted by the model is shown in Figure 39, where a very good agreement is found at low temperatures in all cases. However, the model overestimates the experimental data around 3% in the medium temperature range (100-250 K). This behaviour might be due to the simplicity of the phonon spectrum assumed by the Debye model, used to determine the harmonic contribution. The high temperature range, where the anharmonic contribution is more relevant, is also successfully described.

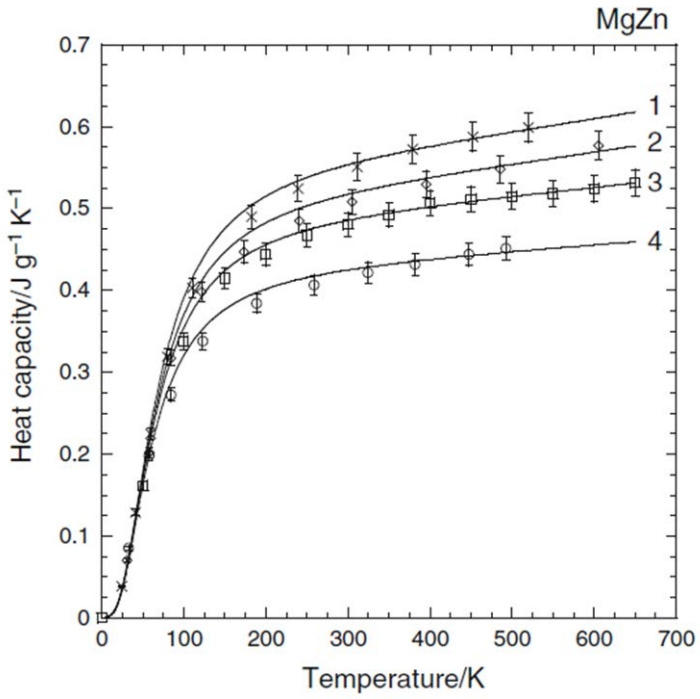

Figure 39. Model predicted (continuous lines) and experimental specific heat data (points) of the different Mg-Zn alloys. Respectively: (1) and (x) $Mg_{25.55}$-$Zn_{74.45}$; (2) and (◊) $Mg_{19.86}$-$Zn_{80.14}$; (3) and (□) $Mg_{15.66}$-$Zn_{84.34}$; (4) and (○) $Mg_{6.34}$-$Zn_{93.66}$.

Conclusions

To conclude, the phase transformation behaviour of the Mg_{49}-Zn_{51} eutectic alloy proposed as phase change material for thermal energy storage has been studied. A simple thermodynamic model has been developed to calculate the lattice specific heat of the eutectic Mg_{49}-Zn_{51} (mass %) alloy and different intermetallic phases of the Mg-Zn binary system in the complete temperature range. In all cases, a very good agreement has been found between the theoretical calculation and the experimental C_p data. However, the knowledge of the phonon spectra or the elastic constants could lead to even more accurate results in the low-intermediate temperature range. This model also allows to calculate the thermodynamic functions of the alloy. Finally, within the thermal energy storage frame where c_p plays a capital role, this theoretical calculation is a powerful predictive tool which can be generalized for other metallic alloys used as storage materials.

5.2. Thermophysical characterization of $Mg_{49}Zn_{51}$ eutectic metal alloy: a phase change material for thermal energy storage in direct steam generation applications

Introduction

This paper is focused on the study of the $Mg_{49}Zn_{51}$ (mass%) metal alloys to be used as a TES system in concentrated solar power (CSP) applications is analysed. From the exergetic point of view, it is desirable that the preheating of the water and superheating of the steam is carried out by sensible heat TES, and that the vaporization of the water is given by latent heat TES. This study is focused on the study of the $Mg_{49}Zn_{51}$ alloys that could be used as a TES system devoted to the vaporization process of the water.

An extensive thermophysical characterization of the $Mg_{49}Zn_{51}$ eutectic metal alloy between room temperature and melting temperature has been performed. The results are compared with some available data in the literature, and founded differences are discussed. A comparison with pure, binary and ternary inorganic salts used as PCM is done highlighting the advantages and disadvantages of the different systems.

This alloy was already proposed as a PCM for heat storage [44-46], and some structural and thermophysical parameters are given in the literature. In particular two melting temperatures of 340 ºC [46] and 343 ºC [44,46] as well as three experimental values of the heat of fusion, 138 kJ/kg [44], 180 kJ/kg [45] and 210 kJ/kg [46] were reported. In addition, a structural study of the eutectic $Mg_{0.72}Zn_{0.28}$ – which corresponds to a 49% wt. of Mg and 51% wt. of Zn– was performed by means of X-Ray and neutron diffraction techniques [121,122].

The $Mg_{49}Zn_{51}$ is presented not only as a candidate for latent heat thermal energy storage for direct steam generation (DSG) in CSP applications but for high pressure and high energy steam processes as well. Reported data are essential for ensuing modelling and experimental reactor studies employing this alloy as a PCM for TES.

Results and discussion

Concerning the synthesis of the alloy, the use of the materials in form of ingots was found to be the best solution in order to get a solid block of the desired eutectic alloy. It was found that among all the parameters, the most critical one is the cooling rate. In addition, it was verified by XRD the absence of oxidation of the alloy after the heat treatment in the furnaces.

Structural analysis

As already pointed out, in this study the Mg rich side eutectic alloy has been chosen with the composition of Mg 49 %wt. and of Zn 51 %wt. due to the appropriate melting temperature for the scope of this paper.

The experimental results show that different phases can be formed depending on the thermal treatment applied. Several experiments with different duration and different heating/cooling rate were performed. Among all the parameters, it has been found that the most critical one is the cooling rate confirming results already reported in literature [123] stating the high sensitivity of this system to the cooling process.

An example of this is given in Figure 40 where the X-ray diffraction patterns of two samples subjected to different cooling rates are shown. For both samples two cycles of melting/solidification up to 500 ºC were carried out. For the sample a) a cooling rate of 0.1 K/min was used while for the sample b) a not controlled cooling obtained by opening the furnace was applied (average cooling rate of approximately 5-10 K/min). The structural analysis shows that the sample a) contains the phases as predicted in the phase diagram ($Mg_{21}Zn_{25}$ + α-Mg). In case of sample b) the phase $Mg_{51}Zn_{20}$ together with traces of α-Mg were detected. It has to be pointed out that $Mg_{51}Zn_{20}$ is a metastable phase at room temperature. Indeed, according to the phase diagram this phase should transform through an eutectoid reaction into $Mg_{21}Zn_{25}$ and α-Mg at 325 ºC. In the experimental conditions applied probably due to kinetic constrains the formation of the expected phases is hindered. This means that for high cooling rates the system has no time to transform from the metastable $Mg_{51}Zn_{20}$ phase into the phases α-Mg and $Mg_{21}Zn_{25}$.

In further experiments, it has been shown that the sample with the metastable $Mg_{51}Zn_{20}$ phase was transformed into the α-Mg and $Mg_{21}Zn_{25}$ phases by keeping the sample at a temperature below the transformation temperature (for instance 250 ºC) for several hours. Gao and Nie [124[123]] found a similar behaviour in a binary mixture of Mg and Zn with 8wt% content of Zn that was subjected to isothermal ageing at 200 ºC. The initial phase $Mg_{51}Zn_{20}$ was transformed into the intermetallic phase $Mg_{21}Zn_{25}$ passing by the transition phase Mg_4Zn_7. It should be noted that in our experiments, under certain conditions, the phase Mg_4Zn_7 was also detected.

On the one hand, the specifications of the conditions for achieving the stable phases are sufficient for the use of this alloy as a PCM for TES applications. On the other hand, in order to

clarify all the behaviours observed a more detailed study focused on material behaviour is advisable and will be the subject of another paper.

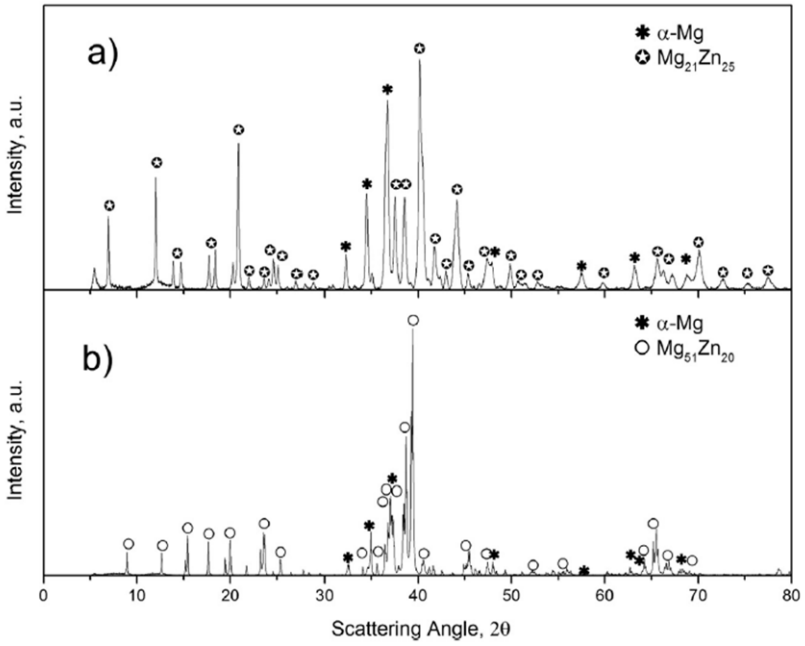

Figure 40. Diffractogram of $Mg_{49}Zn_{51}$ after second heat treatment up to 500 ºC. Sample a) Slow cooling at 0.1 K/min. Sample b) Fast cooling rate in opened furnace.

Melting and solidification enthalpies and phase transition temperatures

In Figure 41 the DSC results of a sample synthesized from ingots are reported. The only phases identified in the starting material were the expected $Mg_{21}Zn_{25}$ and α-Mg. No oxidation was detected from the X-ray analysis. The selected heating/cooling rate was 0.5 K/min.

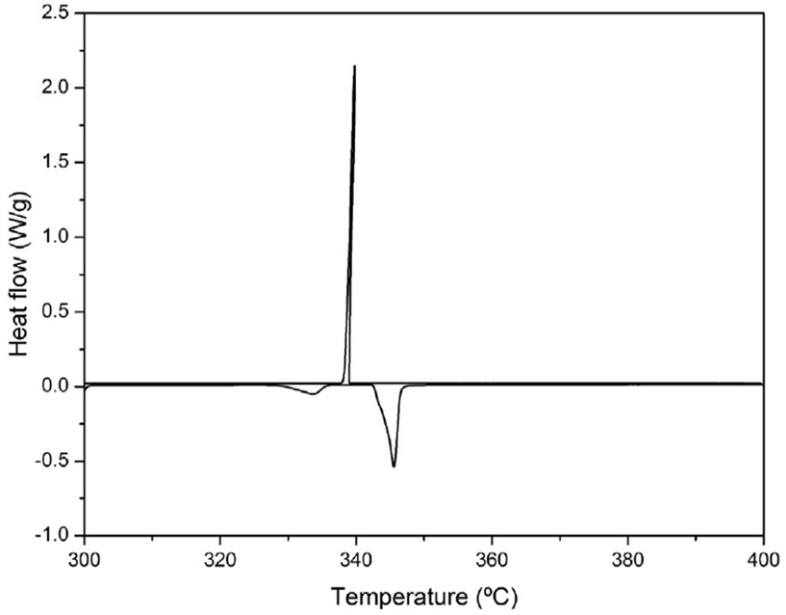

Figure 41. DSC signal for the melting and solidification processes of the eutectic alloy at a heating/cooling rate of 0.5 K/min. Initial phases $Mg_{21}Zn_{25}$ and α-Mg.

As expected the heating curve shows two peaks. The first one corresponds to the eutectoid transformation as already described in the previous paragraph and the second one corresponds to the melting of the material. The enthalpy associated to the first transformation is 27 J/g with an onset temperature of 329 ºC. The enthalpy of the melting is 128 J/g with a melting temperature of 342 ºC. Therefore, the overall energy needed to melt the alloy is 155 J/g.

Upon cooling only one peak is presented in Figure 41. After cooling, the present phase was $Mg_{51}Zn_{20}$. The experimental results show that the enthalpy of solidification and its onset temperature depend on the phase formed upon cooling. In particular, when the formed phase is Mg_4Zn_7 the solidification enthalpy is 153 J/g and the onset temperature is 332 ºC. When the formed phase is $Mg_{51}Zn_{20}$ the solidification enthalpy is 127 J/g and the onset temperature is 337 ºC. In none of the DSC experiment the $Mg_{21}Zn_{25}$ and α-Mg phases were identified after cooling. Figure 42 shows the DSC results of a sample were the phases identified in the starting material were Mg_4Zn_7 and α-Mg. The experiment runs between 200 ºC and 450 ºC at 10 K/min. In the melting there are two peaks as in the previous case (see Figure 42). The melting enthalpy is 156 J/g with an onset temperature of 343 ºC. After the cooling process the initial phases Mg_4Zn_7 and α-Mg are recovered. The solidification enthalpy is 153 J/g and the onset temperature is 333 ºC.

Nucleation problems in addition to size effects may influence the randomly formation of Mg_4Zn_7 or $Mg_{51}Zn_{20}$ phases in the cooling process. This is still an open question which does not interfere with the main objectives of this work because, on the one hand, the melting behaviour of Mg_4Zn_7 phase is like the one of $Mg_{21}Zn_{25}$ and α-Mg phases, and, on the other hand, $Mg_{51}Zn_{20}$ phase transforms into $Mg_{21}Zn_{25}$ and α-Mg phases after ageing at temperatures below the melting temperature.

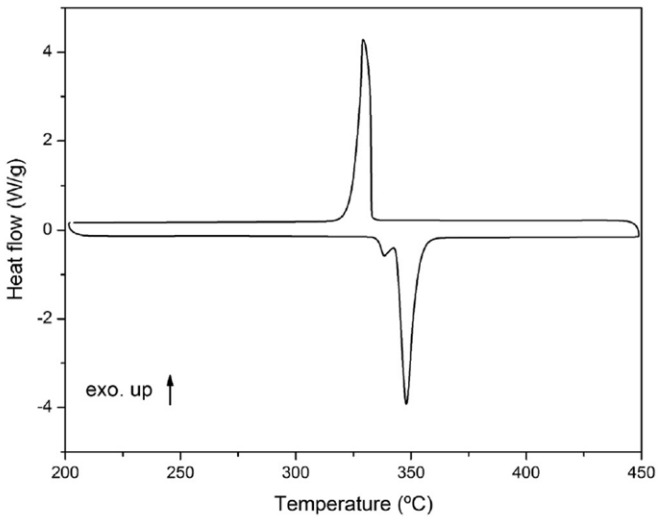

Figure 42. DSC signal for the melting and solidification processes of the eutectic alloy at a heating/cooling rate of 10 K/min. Initial phases Mg_4Zn_7 and α-Mg.

The melting enthalpy value of 155 J/g is between the three different literature values given by the same authors (138 J/g, 180 J/g and 210 J/g) [44-46]. These differences can be attributed to different raw materials, experimental synthesis conditions, calorimeter accuracies, heating and cooling rates as well as to the tracing of the base line (the lattice specific heat). Concerning the onset temperatures the results agree within the reported data in the literature [44-46,112].

Thermal Stability and life-cycle analysis

Life-cycle analysis of the material is crucial for the use of this alloy as a PCM for TES in CSP applications. The estimated life cycles in real applications is around 11000 cycles with only one melting-solidification cycle per day during 30 years. Measurements reproducing real conditions are obviously very long and, in this study, preliminary tests up to 20 cycles between 300 ºC and 400 ºC have been performed employing a heating and cooling rate of 10 K/min.

It has to be pointed out that this cooling rate is much higher than what the alloy would have in a real DSG application. In fact, the use of thousands of tonnes of material, the storage capacity of typically several hours and the fact that the PCM works around its melting temperature ensures that the difference between the melting temperature and the PCM temperature will be of only several degrees and, therefore, cooling rates will be much smaller than those used in calorimetric measurements and the life cycle analysis.

Figure 43 shows the thermogravimetric measurements of twenty melting-solidification cycles. As it can be seen there is no appreciable mass change during the 20 cycles. Additionally, the sample was weighed before and after the experiment by means of an ultra microbalance XP6U (Mettler Toledo) showing a minimal weight increase of 0.04%, which can be attributed to some oxidation produced by the residual contaminated air in the system.

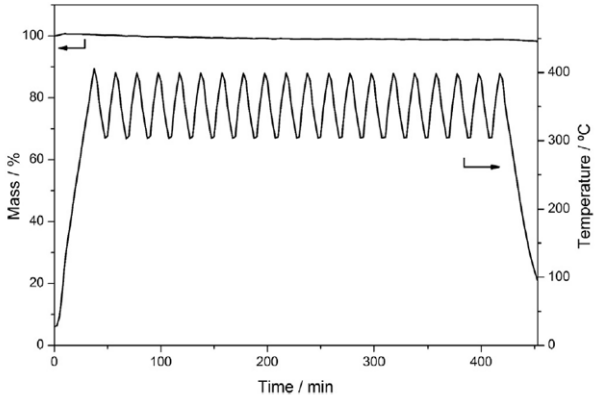

Figure 43. Mass stability of $Mg_{49}Zn_{51}$ as function of melting and solidification cycles.

Longer experiments together with proper analytical and simulation tools that could extrapolate the experimental results to the scale of years to corroborate that this alloy is stable and suitable for TES applications are necessary.

Thermal conductivity

The thermal conductivity is crucial for the possible use of the $Mg_{49}Zn_{51}$ eutectic alloy as TES. The thermal conductivity can be obtained using the equation (17):

$$\lambda = a \cdot \rho \cdot C_p \qquad (17)$$

Where λ is the thermal conductivity in W/m K, a is the thermal diffusivity in m^2/s, ρ is the density in kg/m^3 and C_p is the specific heat capacity in J/g K.

The results of the thermal diffusivity of the eutectic alloy are shown in **Error! Reference source not found.**44 for the two different room temperature phases identified in Figures 41 (a) and (b). The thermal diffusivity of the $Mg_{21}Zn_{25}$ + α-Mg phase shows a slight increase from room temperature up to 200 ºC. Then, it exhibits a very light decrease up to the melting temperature where, in agreement with the first order phase transitions predictions, shows a noticeable decreasing step. It must be noticed that the accuracy of the experimental values decreases around the melting temperature because part of the energy of the laser pulse might be used to melt the sample.

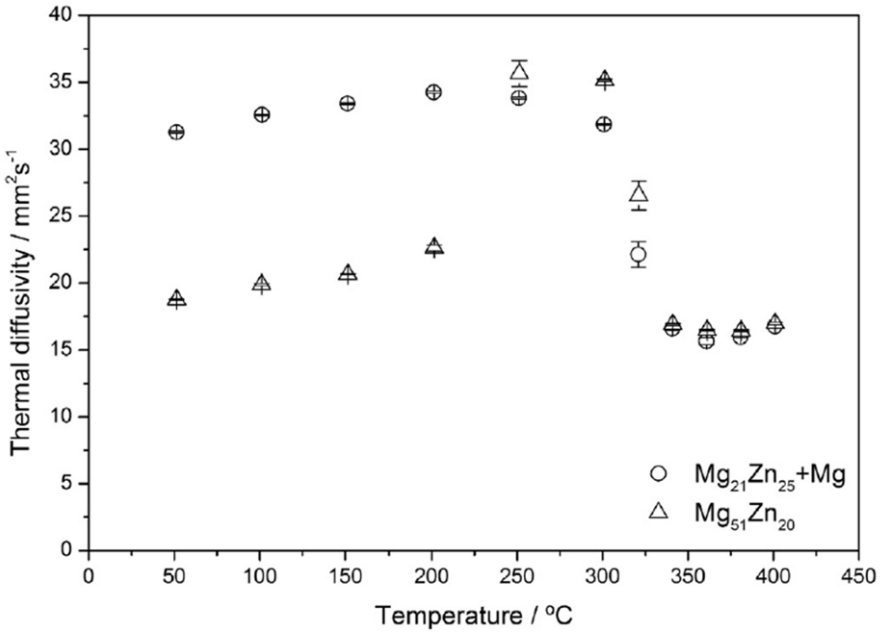

Figure 44. Thermal diffusivity of eutectic alloy Mg-%51Zn. Comparison between phases $Mg_{21}Zn_{25}$ + Mg and $Mg_{51}Zn_{20}$.

The thermal diffusivity of the metastable $Mg_{51}Zn_{20}$ phase shows the same qualitative behaviour than the stable $Mg_{21}Zn_{25}$ + α-Mg phases up to 250 ºC, but the experimental values are much lower (40%). At around 250 ºC the thermal diffusivity increases 40% suggesting the transformation of $Mg_{51}Zn_{20}$ into $Mg_{21}Zn_{25}$ + α-Mg. This fact has been corroborated with experiments performed in a solid block presenting initially the phase $Mg_{51}Zn_{20}$ and being exposed to different thermal treatments of several hours at a temperature below the melting temperature of the eutectic alloy. After the heat treatment the present phases were $Mg_{21}Zn_{25}$ + α-Mg.

The values of the thermal diffusivity of Figure 44 are given in Tables 22 and 23.

Temperature (ºC)	Thermal diffusivity (10^{-6} m^2/s)	Std. Deviation
51.4	31.28	0.08
101.4	32.57	0.04
151.4	33.41	0.05
201.2	34.27	0.08
251	33.84	0.07
300.9	31.85	0.03
320.9	22.13	0.96
340.8	16.6	0.13
360.8	15.65	0.26
380.8	15.97	0.07
400.8	16.76	0.1

Table 22. thermal diffusivity of starting $Mg_{21}Zn_{25}$ + α-Mg phases.

Temperature (ºC)	Thermal diffusivity (10^{-6} m^2/s)	Std. Deviation
51.4	18.76	0.05
101.1	19.89	0.08
151.6	20.65	0.03
201.5	22.63	0.22
251.2	35.67	0.98
301.2	35.17	0.09
321.1	26.54	1.1
341.1	16.9	0.07
361.1	16.48	0.04
381	16.43	0.07
401	16.96	0.11

Table 23. Thermal diffusivity of starting $Mg_{51}Zn_{20}$ phase.

The experimental value of the density at room temperature of the $Mg_{21}Zn_{25}$ + α-Mg phases is 2850 Kgm^{-3} which is far away from the literature estimated value of 4900 Kg/m^3 [44**Error! Reference source not found.**]. A calculus of the theoretical $Mg_{49}Zn_{51}$ eutectic alloy density can be carried out taking into account the theoretical composition of the alloy at the eutectic point (32wt.%

Mg and 68wt.% $Mg_{21}Zn_{25}$) considering the theoretical values for Mg and $Mg_{21}Zn_{25}$, 1738 kg/m^3 and 4240 kg/m^3 [64], respectively. A value of 3440 kg/m^3 is obtained representing the maximum density value of this alloy assuming perfect crystal lattices with no defects.

Preliminary values of dilatation allow to estimate a decrease in the density of a 2.5% from room temperature to 300 °C.

The specific heat capacity was determined using a modulated DSC Q2000 technique. The specific heat curve shows a normal behaviour up to the solid-solid phase transition. The specific heat value passes from 0.73 J/gK at room temperature up to 0.84 J/gK at 300 ºC [125]. This value is 20% lower than that found in the literature (1.04 J/gK) [45]. This literature value seems too high because it would imply an anharmonic contribution to the lattice specific heat of around 20%, which is higher than usual values found in metals or alloys (between 5-10%) [125].

Introducing into the equation (17) the experimental values obtained for the thermal diffusivity, the density and the heat capacity, the thermal conductivity can be obtained.

The thermal conductivity increases from a value of 67 $Wm^{-1}K^{-1,}$ at room temperature, up to 75 $Wm^{-1}K^{-1}$ at 300 ºC. This result is in good agreement with the 80 $Wm^{-1}K^{-1}$ estimated value [44].

Case study: a comparison with molten salts as PCM

In this section a comparative study between the metal alloy described and some selected molten salts intensively studied for latent heat applications [85,126,127] will be performed. In particular, the thermophysical data, the costs together with their possible use for direct steam generation applications will be taken into account.

Table 24 shows, regarding DSG applications, the most important thermophysical properties of pure, binary and ternary inorganic salts as well as those of the $Mg_{49}Zn_{51}$ eutectic metal alloy.

Material	Density (kgm^{-3})	Enthalpy ($kJkg^{-1}$)	Vol. heat storage (MJm^{-3})	Heat capacity ($kJkg^{-1}K^{-1}$)	Thermal diffusivity (mm^2s^{-1})	Thermal conductivity ($Wm^{-1}K^{-1}$)	Melt./Sol. temperature (ºC)	Sat. Vapour Pressure (bar absolute)
$NaNO_3$	2261[b]	172[b]	389	1.1[b]	0.2[a]	0.5[b]	306[b]/n.a.	93
KNO_3	2109[b]	95[b]	200	0.953[b]	0.2[a]	0.5[b]	335[b]/n.a.	137
KNO_3/KCl	2100[b]	74[b]	155	1.21[b]	0.2[a]	0.5[b]	320[b]/n.a.	113
KOH	2040[b]	134[b]	273	1.34[b]	0.2[a]	0.5[b]	360[b]/n.a.	186
$MgCl_2$/ KCl / NaCl	1800[b]	400[b]	720	0.96[b]	n/a	n/a	380[b]/n.a.	above critical point
$Mg_{49}Zn_{51}$	2850	155	442	0.73	33/17	75/-	342/337	150/141

a Indirectly calculated from reported thermal conductivity, heat capacity and density.

b Values from Ref. [85].

Table 24. Comparison of eutectic $Mg_{21}Zn_{25}$ and Mg thermophysical properties with some molten salts.

The $MgCl_2$-KCl-NaCl ternary salt has the highest enthalpy of fusion, but a too-high melting temperature for the application considered. Indeed, this melting temperature is above the critical point of water (374.15 ºC and 221 bar). Not only suitable saturated or superheated vapour turbines have to be used, but also the conduction system (piping) along the solar field has to support those pressures at their related temperatures. These pressures seem to be too high for current DSG technology. To the best of our knowledge, experiments up to 100 bar have been carried out using the parabolic trough technology [128]. It would be a technological challenge to increase the working pressure of parabolic trough pipes.

In the case of power tower technology the implementation of PCM with high melting points would be easier as the total length of piping needed is hundreds times shorter.

In any case, the experience of power tower technology for DSG is limited to some few commercial cases such as PS10 or PS20 where the maximum working pressure is 40 bar.

A similar argument can be followed in the case of KOH salt. The use of KOH and $MgCl_2$-KCl-NaCl salts as PCM for the evaporation process of water in DSG application would be possible in the middle-long term after the explained technological challenges concerning the increase of the performances of the system against temperatures and pressures will be overcome.

The melting enthalpies and melting temperatures of the other three salts in Table 24 are close to that of the $Mg_{49}Zn_{51}$ eutectic alloy. However, the values of the thermal conductivity of the salts are considerably lower than that of the alloy.

Considering a pinch point of 5 ºC, the eutectic metal alloy $Mg_{49}Zn_{51}$ working as PCM for DSG would need saturated steam at minimum 159 bar at 347 ºC to charge it (melting), and it could produce saturated steam at maximum 132 bar at 332 ºC in the discharge process (solidification). Current available steam turbines are within this range of operation. They can support up to 165 bar at 585 ºC of superheated steam, with a power output from 20 MW to more than 250 MW.

It has to be pointed out that, in the present case of the eutectic metal alloy, around 40% of the total energy needed to generate saturated steam is needed for the vaporization process of the water. The rest of the energy should be provided by a sensible source of energy, like for instance concrete [127] or ceramic materials [129].

Finally, the factors to be considered for the possible use of $Mg_{49}Zn_{51}$ eutectic alloy as a candidate compared to molten salts are summarized in the following:

- The thermal diffusivity and thermal conductivity are two orders of magnitude higher than any of the salts of Table 24.

- Modelling of the heat exchanger in the confinement of the TES system tank demonstrates that the cost of the heat exchanger decreases significantly. A prototype laboratory is being built to make experiences with 70 Kg of the eutectic alloy.

- The heat capacity is between 30% and 80% smaller than molten salts. These differences must be taken into account when the system uses both the sensible and phase change heats.

- The energy density of the eutectic alloy, except for the discarded ternary salt, is between 12% and 285% higher than that of the studied molten salts. This means a significant reduction in the size of the holding tank and, therefore, a reduction in cost.

- The price is a factual obstacle for the eutectic $Mg_{49}Zn_{51}$ metal alloy to be used as a PCM in a CSP plant for DSG.

- However, a more in-depth study of simulation as well as the realization of experimental tests in a laboratory-scale reactor is still required in order to be able to know how each of the factors influences the cost of the final TES system.

- Additionally, other application niches must be taken into account. For example in high pressure or high heat energy steam processes used in different industries. If smaller TES systems are required compared to CSP where the cost of the TES material is not the critical parameter, but a small part of the total cost of the system, then this eutectic metal alloy would be competitive with molten salts, especially in those applications where high power is required.

Conclusions

In this paper, a thermophysical characterization of the eutectic metal alloy, $Mg_{49}Zn_{51}$, regarding the most important properties inherent to DSG applications is presented.

A first conclusion is that the phases that the system Mg-Zn shows at room temperature depend on the synthesis settings and subsequent heating and cooling cycles.

The eutectic metal alloy would be suitable as PCM for DSG in either parabolic trough or power tower technologies in CSP plants. For that purpose, some technological challenges have to be overcome, for instance the maximum working pressure of the conduction system of the solar field has to be increased.

On the one hand, the main advantages of the eutectic metal alloy $Mg_{49}Zn_{51}$ are its thermal diffusivity, heat capacity and energy density compared to molten salts. On the other hand, the main drawback is its price. Additional applications of the eutectic alloy as PCM for a TES system are suggested, for instance, in those industrial processes where high pressure or high heat energy steam is needed.

Reported data are essential for modelling studies and for the definition of the experimental conditions of a lab scale heat exchanger that is planned to construct in order to show up the performances of such a TES system under real operation conditions.

5.3. Experiments on a lab scale TES unit using eutectic metal alloy as PCM

Introduction

The behavior of a Mg-51%Zn ($Zn_{72}Mg_{28}$ (at.%)) eutectic metal alloy used as thermal energy storage (TES) material is tested in a laboratory scale TES unit. The TES unit consists of two concentric tubes with the central tube surrounded by 67 kg of the metal alloy and two caps at both ends of the tube through which the heat transfer fluid (HTF) flows. Charging (melting) and discharging (solidification) processes of the eutectic alloy are performed using synthetic oil as the HTF. The experimental results are used to test the validity of the model via simulations performed with a computational fluid dynamics tool.

The results corroborate that phase change materials with high thermal conductivity, such as eutectic metal alloys, are ideal for the evaporation process of water in direct steam generation applications due to the quasi-constant melting and solidification temperatures and to its high heat transfer capacity.

Nomenclature

H	enthalpy function	ρ	density
$\vec{v}$	liquid velocity	β	liquid volume fraction
A_{mush}	mushy zone constant	$\vec{v}_p$	solid velocity
S	source term	κ	thermal conductivity

Prototype and model description

Oil test loop

Although the main proposed application of the studied material is for DSG and therefore water should be used as the HTF, oil has been used instead because of the ease of the installation at the laboratory scale. The oil test loop has 40 kW power provided by low density ($2W/cm^2$) electrical heaters. It has a magnetic circulation pump (Dickow) with a pumping capacity of 25 m^3/h and a 90 kW air fan heat exchanger for cooling process. The piping system is of 2 inches diameter. The design pressure of the installation is 20 bar and the maximum working temperature is limited to 400 ºC due to the use of Syltherm 800 heat transfer fluid (HTF).

The oil flow is measured by an ultrasound flowmeter (UFM 530, Krone). An automatic three-way-valve controls the oil flow directed to the TES unit from 5 ± 0.5 m^3/h to 25 ± 0.1 m^3/h. The rest of the flow is sent to the inlet of the pump by means of a bypass. A second automatic three-way-valve is used to control the temperature of the oil, especially in discharging process when the oil has to be cooled down through the air fan heat exchanger. Flow direction can be modified by means of another two automatic three-way-valves. The charging (melting) is always applied with the oil flow from top to bottom, and the contrary in the discharge (solidification)-from bottom to top-.

TES unit

Prior to the construction of the TES unit, a compatibility study between different container materials (SS304, SS304L, SS316 and SS316L) and the eutectic metal alloy has been performed in order to avoid undesired chemical reactions or progressive degradation of the PCM and construction materials. None of the studied stainless steels has suffered any reaction or corrosion with the eutectic alloy. Therefore, the material construction has been adopted on an economic basis, and SS304 has been finally selected for the construction of all components of the TES unit.

The TES unit consists of two concentric cylinders of one inch diameter for internal pipe and 8 inches diameter for external pipe. In between, 67 kg of Mg-51%Zn eutectic binary alloy have been placed, having thus 2.88 kWh of energy in the phase change. The thermophysical properties of interest for TES applications have been previously determined and studied [71,82].

The design of the unit allows to exchange the eutectic metal alloy by other materials of interest in future studies. For this reason, two caps on top and bottom ends have been placed. Moreover, the TES unit has been designed with the possibility to vary the internal pipe diameter and it allows to study the effect of the top and bottom flanges that enclose the storage material. There is free space on top of the PCM for expansion and volume change of liquid/solid phases of the alloy. This space is filled by Ar gas with an overpressure of 0.5 bars in order to avoid metal oxidation.

The HTF flows through the inner pipe and exchanges the heat with the surrounding metal alloy. In the charging process (melting) the oil enters from the top and exits from the bottom. In the discharging process (solidification) the oil flow is reversed, it enters from the bottom and exits from the top.

In order to register the evolution of the temperature distribution in the total volume of TES unit, seven multipoint sheaths (labeled as 1 to 7 in Figure 45 (a) have been placed in the axial direction with six K-type thermocouples each (labeled as A to F in Figure 45 (a) equidistantly separated in

the radial direction. Additionally, two thermocouples have been placed on top and bottom flange connections in order to determine inlet temperature in both charging and discharging processes. Sheath 7 has been placed on top of the free surface of the PCM. The rest of sheaths have been dipped into the metal.

With the aim of reducing thermal losses a rock wool blanket of 0.12 m thickness has been employed to cover the entire unit. In some critical zones a second insulation layer of the rock wool blanket has been applied in order to minimize thermal losses. Figure 45 (b) shows a picture of the TES unit before covering it with the insulation material.

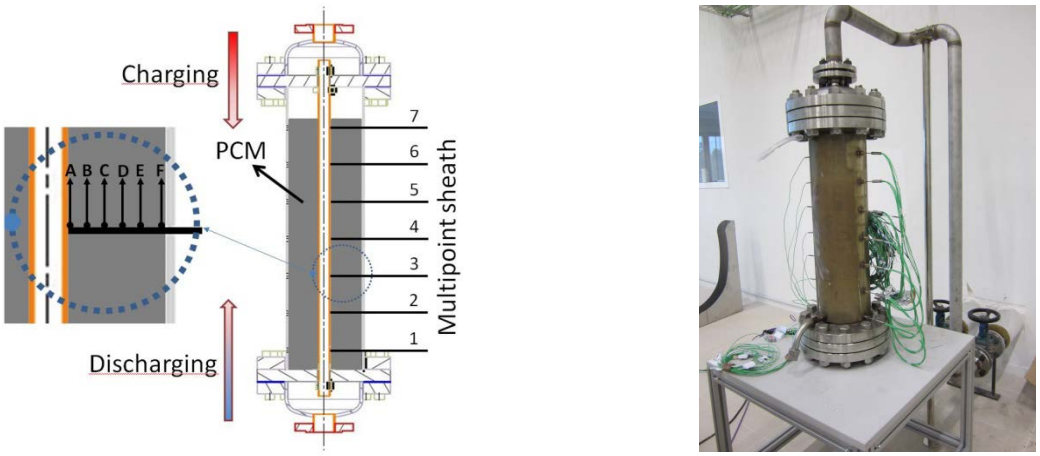

Figure 45. (a) Scheme of the TES unit with sheath and thermocouple distribution; (b) Picture of the TES unit.

Model description

From the mathematical point of view, the phase change is a transient, nonlinear and, regarding the solid-liquid interface, a “moving boundary” problem. Due to this complexity, analytical solutions are only possible for simple and highly symmetric systems. In general, an approached frame is necessary in order to obtain accurate enough solutions for real application latent heat storage devices. Within this frame, fixed grid methods are the most accepted alternative as they provide high accuracy and do not require any tracking of the liquid/solid moving interface.

The solid/liquid fraction of the PCM can be determined by means of different approaches such as enthalpy methods and temperature based equivalent heat capacity methods. The first alternative is the most widely used one [130-132] and has been validated in a wide variety of metallurgical problems such as melting/solidification of pure metals and alloys, casting processes and others [133].

In this model two separate zones are identified. On the one hand, the PCM (Mg-Zn eutectic alloy) where the heat transfer mechanisms will be dominated by conduction both, in the solid and liquid phases due to their high thermal conductivity. For this zone, the energy equation solved in this method is:

$$\frac{\partial(\rho H)}{\partial t} + \nabla \cdot (\rho \vec{v} H) = \nabla \cdot (\kappa \nabla T) + S \tag{18}$$

where H is the enthalpy function, ρ the density of the PCM, $\vec{v}$ the velocity of the liquid and S a source term given in equation (19).

$$S = \frac{(1-\beta)^2}{(\beta^3 + \varepsilon)} A_{mush} (\vec{v} - \vec{v}_p) \tag{19}$$

where β is the liquid volume fraction, ε is a small number fixed to 0.001 to prevent division by zero, A_{mush} is the mushy zone constant and $\vec{v}_p$ is the solid velocity due to the pulling velocity of solidified material out of the domain, zero in our simulations.

The mushy zone constant (A_{mush}) represents the amplitude of the damping between both phases [134,135], modeled as a porous zone. High values imply steeper transition of the velocity from the liquid to the solid values. However, even for isothermal transformations like eutectic phase changes, this value cannot be very large as it might cause the solution to oscillate. In our case a value of A_{mush}=100000 has led to satisfactory values.

On the other hand, the calculation of the liquid fraction (β) in this method is based on the porous media formulation of the melting process. In particular, the porosity value ranges from ε=0 to ε=1 from the solid to liquid phase, which leads to a liquid fraction ranging from β=0 to β=1, respectively. For intermediate values, taking into account the eutectic and hence isothermal transition behavior of the modeled PCM, an iterative process between the energy equation and the liquid fraction described in [136] has been used.

In the HTF zone the governing heat transfer mechanisms will correspond to convective processes. In this case, a standard k-ε Reynolds Average Navier Stokes model [137,138] has been used in order to model the fluid dynamics. The main assumptions of the model are the following:

- Isotropic and homogeneous phase change material.
- Incompressible and Newtonian fluids.

- Constant heat transfer fluid inlet temperature and velocity.
- 2-D axisymmetric model.
- No viscous dissipation.

The complete calculation has been performed by using Ansys Fluent® commercial computational fluid dynamics (CFD) software.

Results and Discussion

Melting and solidification of metal PCM

As one of the goals of this work is to study how the eutectic alloy behaves in melting and solidification processes, as an example Figure 46 shows the temperature profile of the six thermocouples of sheath 4. Prior to the beginning of the experiment the system was equilibrated to around 305 ºC. Then, for the melting test, the oil inlet temperature has been set to 381 ºC with an oil velocity of 1 m/s. For the solidification test, the HTF inlet temperature has been set to 306 ºC with same oil velocity. In the heating, three different regions can be easily distinguished:

- The first one corresponds to the preheating of the solid alloy where the temperature of the alloy is gradually increased up to the melting point.
- The second one corresponds mainly to the melting process that occurs at a temperature of 342 ºC. This temperature agrees with the values obtained in previous calorimetric experiments [71, 82].
- The last one is the superheating of the liquid melt to the set value of 381 ºC. It has to be stressed that during the melting, there is some preheating and superheating of the alloy as well.

In the cooling process a similar behavior is observed:

- First, the cooling of the liquid melt.
- Then the solidification at a quasi-constant temperature.
- Finally the cooling of the solid phase up to the inlet HTF temperature.

In the heating process, it is considered that the melting starts when the first thermocouple (always A) reaches the melting point. The melting process ends when last thermocouple (always F)

overpasses the melting point. For consistency, the inflection point of the temperature curve has been taken. Similar criterion has been used for the cooling process.

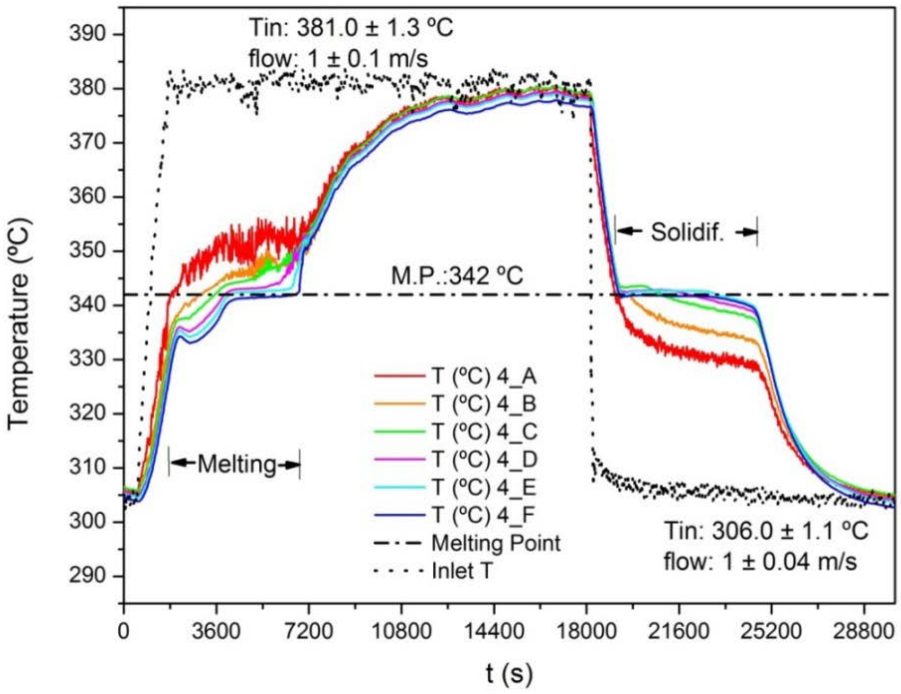

Figure 46. Temperature evolution of thermocouples of sheath 4 in melting and solidification processes.

Once the melting process starts, the heating rate of all thermocouples is drastically reduced. The temperature profile of thermocouple 4A is flattened and remains at quasi-constant temperature above the melting point and below the set value until all PCM at that level is melted. After the melting, the heating rate speeds up again until it approaches the set value. During the melting, the temperature difference between 4A and melting point is $\Delta T < 10$ºC. This is the one needed to ensure the heat transfer to the surrounding external region. This fact shows the good ability of this material as a high thermal conductive material for TES applications.

When the melting starts in the region close to the internal tube, the external thermocouples decreases even more drastically their heating rate due to the fact that all the energy provided by the internal tube is used to melt the surrounding alloy and some of the energy is used to continue with the preheating of the metallic parts of the container. Moreover, as the melting front goes forward, a liquid layer having half thermal conductivity than that of the solid material is formed which limits the heat transfer compared to solid phase. In this sense, at the beginning of the melting process, a small temperature decrease of external thermocouples is observed which might be attributed to thermal inertia of the system.

As the melting front advances to the outer region, the external thermocouples increase their temperature until the melting point, where they remain at constant temperature until the corresponding region is melted.

Concerning the cooling process, the solidification temperature is the same as for the melting, 342 ºC. There is no subcooling effect as it has been previously observed in calorimetric experiments [71,82]. The reason might be the sample mass influence on the thermal response of the material [139,140].

The melting time of the PCM at the position of sheath 4 is 81 minutes, while the solidification time is 90 minutes, being the temperature difference between inlet temperature and melting point ΔT=39 ºC and ΔT=36 ºC for melting and solidification tests, respectively.

Figure 47 shows the temperature evolution of external thermocouples (F) of sheaths 1 to 6 in the melting and solidification processes. Sheath 7 is not represented because its values are influenced by the fact of not being dipped into the metal and being in contact with the Ar atmosphere. From the melting curves it can be seen that the melting front advances from top to bottom. On the other hand, the solidification advances in both directions, from top to bottom and vice versa, being the central part (sheaths 3, 4 and 5) the last one to solidify. The total melting and solidification times are given in Table 25.

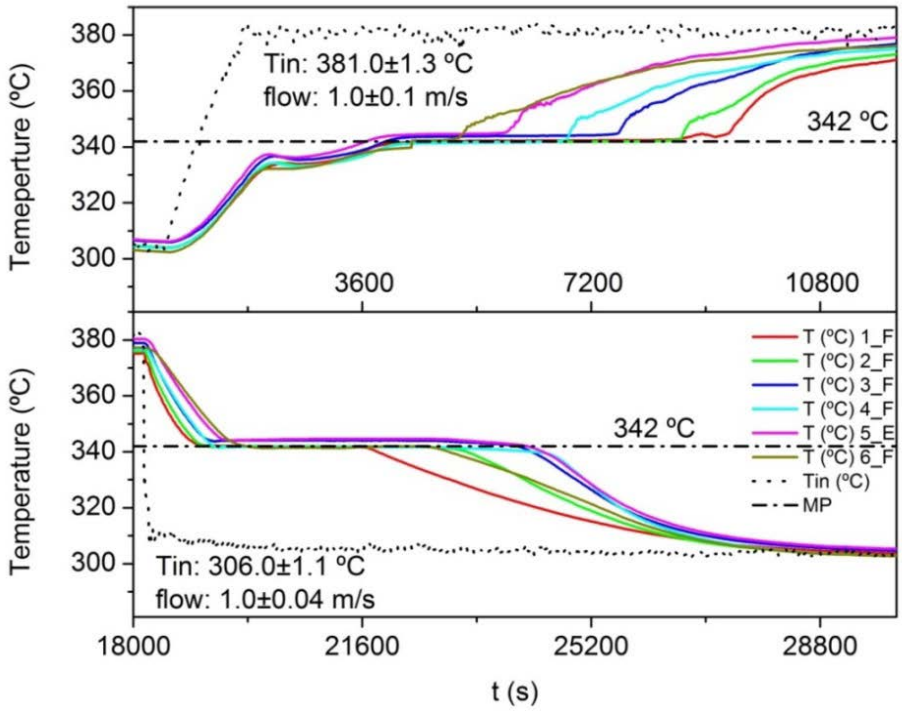

Figure 47. Temperature evolution of thermocouples F of all sheaths in melting and solidification processes.

The total melting time needed to melt all the PCM is 120 minutes while for the solidification it is 90 minutes. Therefore, around 25 % less time is needed to solidify than to melt. This gap together with the difference on the melting and solidification front advances might be attributed to several factors. Among them, the principal ones are the convection of the liquid melt, the insulation in the bottom part of the unit and the design of the device.

Sheath	1	2	3	4	5	6
Melting time (s)	7270	6510	5860	4870	4200	3400
Solidification time (s)	2710	4150	4830	5420	4940	3360

Table 25. Melting and solidification times as function of sheath position.

Together with the convection on the liquid melt, once the alloy is melted close to the internal tube it will move upwards due to the density difference between both solid and liquid phases.

The unit has been fixed on a table with a rock wool blanket of 0.12 m thickness in between both table and bottom flange. It serves as insulation material which has been compressed due to the weight of the unit, and therefore its insulation capacity is expected to be reduced. As a result, the total time for melting is increased and the total time of solidification is reduced.

Concerning the design of the unit, the two caps configuration might contribute to a lower melting rate, especially in the bottom part of the unit where there is direct contact between bottom cap flanges and PCM. In the top part of the unit, Ar gas is in between PCM and top flanges and cap which might be also a reason for the asymmetry of the solidification front.

Model validation

The explained model has been applied to the particular measurement shown in section 3.1 under the mentioned operation conditions. The obtained results are shown in Figure 48, where the experimental temperature profiles of sheath 3, chosen as an example, are compared with the results of the modeling.

As can be seen, a good fitting is obtained both, in charge and discharge runs. A and B thermocouples show good agreement with the experimental temperatures. The radial temperature distribution between the thermocouples is also correctly calculated. However, some differences are found. At the beginning of the melting process, the temperature decrease shown by thermocouples C, D, F and E is more pronounced in the experimental data than in the calculated temperatures. As

said before, this behavior could be related to the thermal inertia of the experimental TES unit, which might be underestimated in the calculation.

The overall melting/solidification times are successfully determined from the calculation, within a maximum difference of around 10%. The analysis of the data leads to an overall estimated value of the heat transfer coefficient of around h=700 W/m^{2}K.

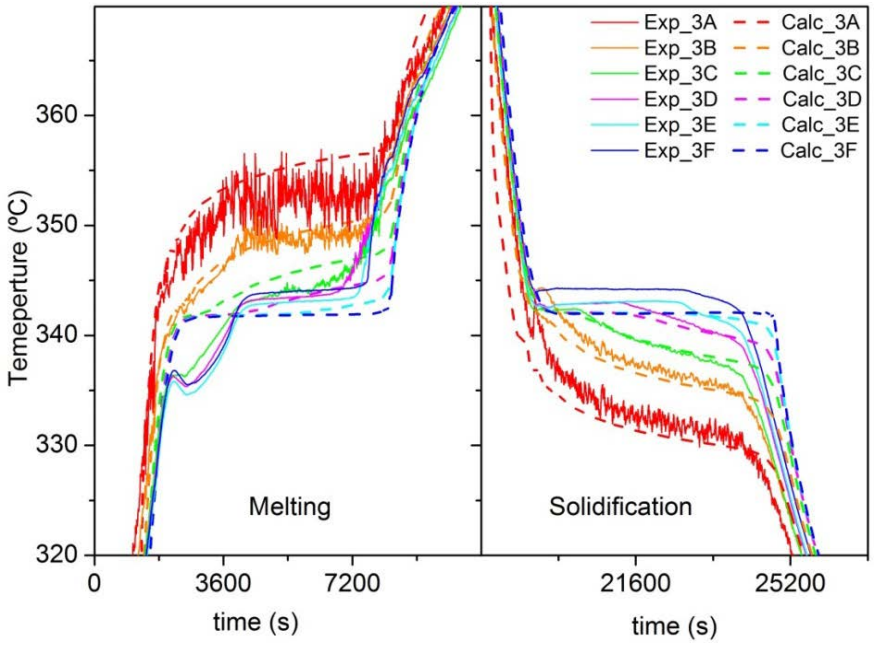

Figure 48. Charge/discharge (left/right respectively) temperature behaviour of the investigated case. Continuous lines correspond to the experimental data. Discontinuous lines represent the calculated radial temperature distribution.

Impact of the thermal conductivity on the TES unit

As mentioned before, one of the major benefits of metal alloys used for latent heat storage is their high thermal conductivity. The influence of this parameter on the storage behavior and operation is determinant in order to obtain a fast thermal response unit able to operate at high power values. In this frame, the large thermal conductivity of the proposed material, eutectic Mg-Zn alloy, could imply important advantages in current CSP technologies. However, even in the case of large thermal conductivity materials, the overall heat transfer is determined by conduction/convection mechanisms that need to be modeled in order to determine a realistic influence of the thermal conductivity on the storage system. In this section, a simplified storage unit of the presented design in section 2.2 has been modeled. A simple shell and tube configuration with no caps and no free volume for PCM expansion has been considered. Different thermal conductivity values have been assumed in order to determine its influence on the overall storage device. The rest of the PCM

properties have been assumed invariant for all simulations. Concerning the operating parameters of the HTF, the inlet temperature has been set to 400 ºC with a velocity of 3 m/s.

As a result, Figure 49 shows the melting time (charging process) as a function of the assumed different thermal conductivities. From Figure 49, it can be clearly seen that around k=20 W/mK there is a conductivity threshold. Under the mentioned HTF conditions, larger conductivity value materials do not represent a big benefit in the storage behavior, as the heat transfer is limited by the HTF convection mechanisms. On the other hand, lower thermal conductivity materials lead to a fast increase of the melting time of the PCM. In this case, the thermal conductivity of the storage material is the limiting issue of the heat transfer. In any case, the competition between convective and conductive mechanisms is the key issue in order to establish this threshold value of thermal conductivity. In Figure 49, an empirical double exponential function has been used in order to fit the data obtained from the calculation with very good agreement.

In our case, the proposed eutectic Mg-Zn alloy presents a thermal conductivity high enough in both, solid (k=75 W/mK) and liquid (k=35 W/mK) phases [82] which guarantees, under the mentioned fluid parameters, that the heat transfer limitation is related to the HTF convection.

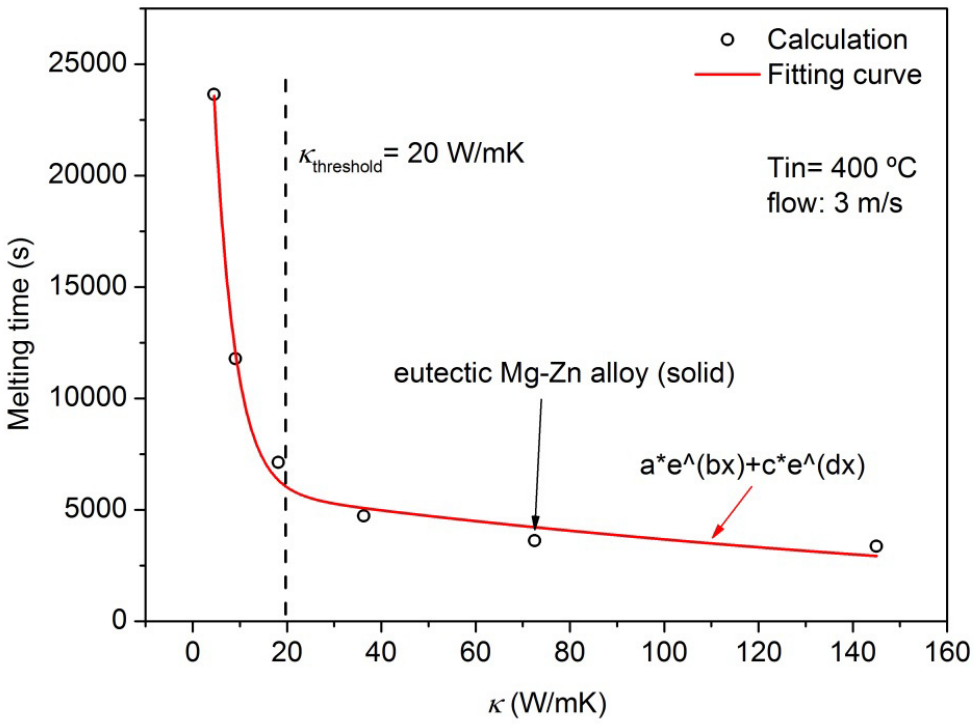

Figure 49. Influence of the thermal conductivity of the PCM in the investigated storage design. The melting time is plotted as a function of the thermal conductivity value.

Advantages of Mg-51%Zn as TES

The main advantages of the Mg-51%Zn system arising from the present study are its high thermal conductivity and the quasi constant melting and solidification temperatures.

On the one hand, in the present study, the high thermal conductivity of the eutectic alloy is not the limiting factor for heat transfer, but the heat transfer of the liquid oil inside the pipe. In this regard, if a two-phase fluid is used instead of oil, the system would be charged and discharged faster since the heat transfer of a two-phase fluid (liquid-vapor or vapor-liquid phase changes) is higher. Therefore, experiments such as the one presented by Adinberg et al. [141] would highlight even better the good properties of the metal PCM.

On the other hand, as the melting and solidification temperatures are equal, the differences between charging and discharging HTF conditions are minimized. Concerning direct steam generation application, taking 5 ºC as the temperature difference needed for charging and discharging with respect to melting/solidification temperature, the conditions of the saturated steam needed for charging would be 159 bar at 347 ºC [82] and the produced saturated steam in the discharge process would be 140 bar at 337 ºC. As suggested in [82], the use of this eutectic metal alloy would imply a technological challenge for parabolic trough technology with the need of developing high pressure parabolic trough pipes and corresponding connections. Concerning power tower technology, the challenge would be focused on the development of high pressure central receivers. Apart from CSP applications, this PCM is also proposed as TES material for high pressure or high heat energy steam demanding processes. Nonetheless, due to its high thermal conductivity it could be used for high power heat demanding processes as well.

Conclusions

The potential use of eutectic metal alloys as latent heat thermal energy storage has been experimentally investigated by means of heating and cooling tests around the melting point of the phase change material.

There is no subcooling effect as in previous mg scale calorimetric experiments. Melting and solidification temperatures are equal to 342 ºC. Melting and solidification fronts are different due to the combination of different factors such as the used experimental conditions, the design of the prototype, the insulation as well as convection of the liquid melt.

The experimental results have been used to validate a model that has been developed by means of CFD simulations. In addition, with current presented configuration, the limiting factor of the heat transfer comes from the liquid oil inside the pipe and not from the thermal conductivity of the metal PCM. The use of a two-phase fluid as the HTF would highlight even more the properties of the alloy and would allow to study the limitations concerning heat transfer of proposed metal PCM.

6. Summary and final conclusions

6.1. Summary

In this thesis Mg-Zn-Al binary and ternary alloys have been proposed as latent heat storage materials for solar power generation plants. For this proposed, after the synthesis process of the alloys, the structural characterization and thermophysical properties determination, as well as, the long term thermal stability and compatibility tests with container materials have been carried out.

Due to the extension of this work a summary of results prior to the conclusions is presented in this chapter. In this regard, in order to clarify their exposure, the obtained results are summarized in the Table 26. On the other hand, due to the extension thereof, they have been divided on function of the analyzed property.

Metal alloys	Structural analisis	Melting point		Heat of fusion	Density	Specific heat	Thermal conductivity		Thermal cycling test		Compatibility test
	Stability	(ºC)		(kJ/kg)	(kg/m^3)	(kJ/kg·K)	(W/m·K)		Cycle nº	RPD of enthalpy	
		Theo.	Exp.			Solid	Solid	Liquid		(%)	Compatible material
$Mg_{72}Zn_{28}$ eu.	metast.	340	342	155	2850	0.73-0.84	67-75	-	700	-0.4	304/304L/316/316L
$Mg_{71}Zn_{28.9}Al_{0.1}$	stable	341	343	153	3000	0.70-0.77	57-64	27-28	-	-	-
$Mg_{70}Zn_{24.9}Al_{5.1}$ eu.	stable	338	340	157	2820	0.72-0.79	47-60	35-38	700	1.4	304/304L/316/316L
$Mg_{70}Zn_{24.4}Al_{5.6}$	stable	340	341	157	2790	0.73-0.79	41-53	26-28	-	-	-
$Zn_{84}Al_{8.7}Mg_{7.6}$ eu.	stable	346	344	132	6546	0.46-0.53	70-67	42-52	100	-1.9	316Ti
$Zn_{88.7}Al_{11.3}$ eu.	stable	381	382	118	6752	0.45-0.54	134-120	50-61	100	1.3	321/430
$Zn_{92.2}Mg_{7.8}$ eu.	metast.	364	371	106	6763	0.47-0.52	88-83	34-40	100	-19.8	-

Table 26. Summary of the obtained experimental results in this work (low accuracy quantitative values).

6.1.1. Analysis of synthesis protocol:

The results of XRPD, SEM and calorimetric analysis (DSC) such as: The expected phase's identification by XRPD, the structural homogeneity and eutectic morphology observation by SEM and the observations of narrow eutectic transition peaks, the expected reaction sequences by calorimetric (DSC) analysis ensure the correct eutectic composition of the alloys samples. Based on these results, the synthesis protocol can is considered validate.

6.1.2. Microstructure analysis:

The $Mg_{71}Zn_{28.9}Al_{0.1}$ (quasi-peritectic), $Mg_{70}Zn_{24.9}Al_{5.1}$ (eutectic) and $Mg_{70}Zn_{24.4}Al_{5.6}$ (quasi-peritectic) alloys, with melting temperatures around 340 ºC, have shown high structural stabilities in comparison to the binary $Mg_{72}Zn_{28}$ eutectic alloy, which showed a random formation of stable ($Mg_{21}Zn_{25}$) and metastable (Mg_7Zn_3) phases, depending of the solidification rate. The metastable behaviour of the $Mg_{72}Zn_{28}$ alloy showed the influence on some thermophysical properties such as in the thermal diffusivity and conductivity, where the metastable phase presented 40% lower diffusivity and conductivity values than the stable phase (see section (5.2)). In the section (4.1.1) it has been demonstrated that the addition of a small amount of Al, even 0.1% (at.%), leads to stabilise the system forming stable $Mg_{21}Zn_{25}$ intermetallic phase and Mg solid solution at room temperature independently of the cooling rate. On the other hand, the metastability observed by XRD in the $Zn_{92.2}Mg_{7.8}$ eutectic alloy (see section (4.1.2)) does not affect to its thermophysical properties.

The cubic $Mg_{32}(Al,Zn)_{49}$ intermetallic phase has not been observed under 0.1 and 10 K/min cooling rates in the $Mg_{70}Zn_{24.9}Al_{5.1}$ and $Mg_{70}Zn_{24.4}Al_{5.6}$ alloys as was expected according to the Mg-Zn-Al phase diagram (section (4.1.1)). The Al amount associated to the $Mg_{32}(Al,Zn)_{49}$ phase was mainly dissolved in the $Mg_{21}Zn_{25}$ phase, increasing the Al solubility of these phase. This effect caused the increasing of the lattice parameters of $Mg_{21}Zn_{25}$ phase, the loss of periodicity in its crystalline cells and as a consequence, the reduction of their thermal conductivities.

Finally, the lattice parameters analysis performed in the section (4.1.2) signalizes the $Zn_{88.7}Al_{11.3}$ eutectic alloy as the most perfect crystalline eutectic microstructure, where, its Al and Zn solid solutions show very high purity.

6.1.3. Thermophysical properties analysis:

The alloys cover approximately a range of meting temperatures from 340 to 380 ºC, where $Mg_{72}Zn_{28}$, $Mg_{71}Zn_{28.9}Al_{0.1}$, $Mg_{70}Zn_{24.9}Al_{5.1}$ and $Mg_{70}Zn_{24.4}Al_{5.6}$ melt ~340 ºC, $Zn_{84}Al_{8.7}Mg_{7.6}$ at ~345 ºC, $Zn_{88.7}Al_{11.3}$ at ~370 ºC and $Zn_{92.2}Mg_{7.8}$ at ~380 ºC. Similar heat of fusions between 106 and 157 J/g have been shown, where, $Mg_{72}Zn_{28}$, $Mg_{71}Zn_{28.9}Al_{0.1}$, $Mg_{70}Zn_{24.9}Al_{5.1}$ and $Mg_{70}Zn_{24.4}Al_{5.6}$ have ~155 J/g enthalpy, $Zn_{84}Al_{8.7}Mg_{7.6}$ has ~130 J/g, $Zn_{88.7}Al_{11.3}$ has ~120 J/g and $Zn_{92.2}Mg_{7.8}$ has ~105 J/g. On the other hand, the $Mg_{72}Zn_{28}$ alloy due to its metastable nature can randomly present a solidification enthalpy of ~155 J/g and ~130 J/g at 332 and 337 ºC, respectively (section (5.2)).

Small thermal hysteresis between 5 and 13 ºC have been observed. It believe that the observed hysteresis are associated to the small amounts of samples (milligrams) used in calorimetric analysis as it has been demonstrated by means of the thermal behaviour analysis of the $Mg_{72}Zn_{28}$ alloy in a lab-scale TES unit (section (5.3)).

The density of alloys are around approximately 2800 kg/m^3 for the Mg-rich $Mg_{72}Zn_{28}$, $Mg_{71}Zn_{28.9}Al_{0.1}$, $Mg_{70}Zn_{24.9}Al_{5.1}$ and $Mg_{70}Zn_{24.4}Al_{5.6}$ alloys and around 6700 kg/m^3 for the Zn-rich $Zn_{84}Al_{8.7}Mg_{7.6}$, $Zn_{88.7}Al_{11.3}$ and $Zn_{92.2}Mg_{7.8}$. alloys. The high density of Zn-rich alloys, which is two or three times higher than those inorganic salts, leads to similar energy densities of salts in spite of the lower heats of fusion.

Relevant agreements between experimentally measured and quasi-empirically calculated specific heats have been observed, which validates the developed thermodynamic model for metal specific heat calculations presented in the section 5.1.

In the solid phase the specific heat increases approximately from 0.7 to 0.8 J/g·K in the Mg-rich $Mg_{72}Zn_{28}$, $Mg_{71}Zn_{28.9}Al_{0.1}$, $Mg_{70}Zn_{24.9}Al_{5.1}$ and $Mg_{70}Zn_{24.4}Al_{5.6}$ alloys and from 0.45 to 0.55 J/g·K in the Zn-rich $Zn_{84}Al_{8.7}Mg_{7.6}$, $Zn_{88.7}Al_{11.3}$ and $Zn_{92.2}Mg_{7.8}$ alloys. The differences among the obtained results are mainly based on the specific heat contribution of individual metals (1.023, 0.897 and 0.39 J/g·K for Mg, Al and Zn, respectively). In this way, the $Mg_{72}Zn_{28}$ alloy with the highest Mg content presents the highest specific heat, whereas, the $Zn_{92.2}Mg_{7.8}$ alloy with the highest Zn content displays the lowest value. The alloys show lower specific heats than convectional inorganic salts, however, it is not a driving thermophysical parameter in the latent heat storage.

In the solid phase the thermal conductivity slightly increases with temperature in the $Mg_{72}Zn_{28}$, $Mg_{71}Zn_{28.9}Al_{0.1}$, $Mg_{70}Zn_{24.9}Al_{5.1}$ and $Mg_{70}Zn_{24.4}Al_{5.6}$ alloys while decreases in the $Zn_{84}Al_{8.7}Mg_{7.6}$, $Zn_{88.7}Al_{11.3}$ and $Zn_{92.2}Mg_{7.8}$ alloys. After the melting process they decrease around to the half and increase with temperature in all cases.

Thermal conductivities of investigated alloys are shown large differences in their values, which, close to the melting process cover a range from 53 to 120 W/m·K in the solid phase and from 26 to 50 W/m·K in the liquid phase. These values are above of the thermal conductivity threshold of 20 W/m·K calculated in the section (5.3).

The thermal conductivities are between two and three orders higher than those of the inorganic salts. Considering the use of the studied metal alloys as storage media in a TES system,

the mentioned fact can highly decrease the heat exchanger size and, consequently, its cost. At the same time, the highest conductivities of the alloys drive to higher power ratios for a given heat exchanger.

The periodicity of the crystalline phases in each alloys has a big influence in the thermal conductivity. In this way, due to the high amount of Al dissolved in the $Mg_{21}Zn_{25}$ phase of the $Mg_{70}Zn_{24.4}Al_{5.6}$ alloy, this presents at room temperature the lowest thermal conductivity of 41 W/m·K (see Table 26) although based on the individual metal thermal conductivity contribution (237, 156 and 116 W/m·K for Al, Mg and Zn, respectively), the highest thermal conductivity of 141 W/m·K was expected for this composition. On the other hand, due to the high purity and periodicity of its Al and Zn solid solutions, $Zn_{88.7}Al_{11.3}$ is the unique alloy that presents at room temperature same experimentally measured and theoretically approximated thermal conductivities of 134 W/m·K value in both cases. Finally, the extreme sensibility of the thermal conductivity with respect to crystalline structure periodicity, it can be observed by comparison of Mg-rich alloys conductivity results. In these alloys, a small variation of 0.1%, 4% and 4.4% (wt.%) of Al content in the $Mg_{71}Zn_{28.9}Al_{0.1}$ $Mg_{70}Zn_{24.9}Al_{5.1}$ and $Mg_{70}Zn_{24.4}Al_{5.6}$ alloys, respectively, lead to a substantial conductivity reduction of 15%, 30% and 39% respect to $Mg_{72}Zn_{28}$ alloy due to the Al impurity role in $Mg_{21}Zn_{25}$ and Mg phases of these three alloys (see Table 26).

Based on the results of thermophysical properties analysis, the $Mg_{70}Zn_{24.9}Al_{5.1}$ alloy is distinguished among the Mg-rich alloys, as potential PCM of ~340 ºC transition temperature due to its stable transition process and its eutectic nature. Among Zn-rich eutectic alloys, the $Zn_{84}Al_{8.7}Mg_{7.6}$, $Zn_{88.7}Al_{11.3}$ and $Zn_{92.2}Mg_{7.8}$ alloys are identified as potential PCMs for ~345 ºC, ~370 ºC and ~380 ºC transition temperatures, respectively. Between the $Mg_{70}Zn_{24.9}Al_{5.1}$ and $Zn_{84}Al_{8.7}Mg_{7.6}$ alloy, which show similar fusion temperatures of 340 and 344 ºC, respectively, it has to be noted the highest density of the $Zn_{84}Al_{8.7}Mg_{7.6}$ alloy due to its high Zn content.

6.1.4. Long term thermal stability analysis:

The $Mg_{72}Zn_{28}$, $Mg_{70}Zn_{24.9}Al_{5.1}$, $Zn_{84}Al_{8.7}Mg_{7.3}$ and $Zn_{88.7}Al_{11.3}$ alloys have shown good thermal stability after performed thermal cycling tests. Regarding the $Zn_{92.2}Mg_{7.8}$ alloy, a substantial enthalpy reduction of 19.8% after 100 cycles, accompanied with a progressive formation of a peak before the eutectic solidification peak has been observed. This behaviour may be caused the formation of the metastable $MgZn_2$ phase in this composition. Further investigations are needed in order to confirm this hypothesis. Finally, the evaluation in an insulated pilot scale TES unit is considered necessary.

6.1.5. Compatibility analysis:

Based on compatibility test results the 304, 304L, 316 and 316L stainless steels have been identified as potential containments materials for the $Mg_{70}Zn_{24.9}Al_{5.1}$ alloy, the 430 and 321 steels for the $Zn_{88.7}Al_{11.3}$ alloy and 316Ti stainless steel for the $Zn_{84}Al_{8.7}Mg_{7.3}$ alloy.

On the other hand, the corrosion behaviours of stainless steels in molten alloys have been discussed, where the influence of the molten alloys and stainless steels chemical composition in corrosion reaction have been analyzed, as well as, the control mechanism on corrosion reactions and the element diffusion through the corrosion layers.

6.1.6. Applicability analysis:

The investigated alloys are proposed as alternative of inorganic salts as potential PCMs for TES system in solar power generation plants. The analysed properties such as high conductivity, no thermal hysteresis, good thermal stability and low corrosiveness showed to be promising and overcome the currently investigated salts limitations.

However, the highest cost of metals is their main limitation in order to consider them as a real alternative in commercial solar TES systems, where tones of material are necessary. This drawback should be evaluated in the frame of the TES system, considering also the cost of the heat exchanger. Therefore, a detailed economic study of a TES system using metal alloys is necessary in order to evaluate its economic viability.

Even tough, the real advantage of metal alloys lays on their high thermal conductivity, compared with other materials already used as PCMs. This characteristic allows reaching high power ratios, which can be an important parameter in solar plants to provide protection against thermal shocks or to reduce the impact of solar fluctuations or star-up times.

Regarding on this new application proposed for solar power plants it can be highlight that currently CIC energiGUNE is conducting a project in collaboration with a private solar engineering company. The project consists of the design and testing in a real plant of a short time response TES unit based on one of the alloys analysed in this thesis. The main objective of the project is to evaluate the technical and economical viability for its deployment in currently operational plants.

On the other hand, TES systems using metal PCMs are also proposed for those industrial processes with high levels of waste heat and where short time on charging and discharging processes could be a must. In this regard, a detailed study of industrial sectors potentially interested on this technology should be performed.

6.2. Final conclusions

The $Mg_{70}Zn_{24.9}Al_{5.1}$, $Zn_{84}Al_{8.7}Mg_{7.3}$ and $Zn_{88.7}Al_{11.3}$ eutectic alloys with fusion temperatures of 340, 344 and 371 ºC, respectively, present the highest potentiality to be used as high temperature phase change materials in solar generation powers plants. These alloys have shown; adequate structural and thermophysical properties, long thermal stability and low reactivity with evaluated stainless steels.

Among the advantages of these alloys, it must be emphasized:

(1) The good compatibility of the $Mg_{70}Zn_{24.9}Al_{5.1}$ alloy with commonly used containments materials due to lack of affinity of the Mg with the Fe, in where, the Mg prevents the diffusion of the Al and Zn to the interface due its high concentration and bigger size.

(2) The high density of the $Zn_{84}Al_{8.7}Mg_{7.3}$ alloy, as well as, its potentiality as 350 ºC PCM, in where, the finding a salt for this transition temperature is extremely difficult due to that all the possible candidates are mixtures of corrosive chlorides and fluorides.

(3) The high thermal conductivity of the $Zn_{88.7}Al_{11.3}$ alloys due to the high purity of its Al/Zn phases, its good thermal stability without enthalpy reduction after 100 cycles, as well as, the high density of this Zn-rich alloy.

With respect to others investigated eutectic and quasi-peritectic alloys can be highlighted the following conclusions:

(1) In the $Mg_{72}Zn_{28}$ alloy good compatibility with commonly used steels as containments materials is expected due to its high Mg concentration. This observation points the $Mg_{72}Zn_{28}$ alloy as high potential PCM, where, the addition of small amount of Al would avoid its metastable behaviour.

(2) The lack of thermal stability observed by thermal cycling test in the $Zn_{92.2}Mg_{7.8}$ alloy must be deeply studied due to the potentiality of this alloy as 380 ºC PCM (see section (4.1.2)). On the other hand, based on the performed compatibility analysis, stainless steel corrosion in $Zn_{92.2}Mg_{7.8}$ bath is expected due to the reaction of the Zn with the Fe. In this context and based on Wang et al. [104] research the Al addition between 0.12-0.22% (wt. %) is proposed in order to form Al-Fe inhibition corrosion layer.

(3) The $Mg_{71}Zn_{28.9}Al_{0.1}$ and $Mg_{70}Zn_{24.4}Al_{5.6}$ alloys are not seriously considered as potential PCMs due to that their quasi-peritectic natures. Their study has shown the influence of chemical composition on the thermophysical properties where the high influence of the microstructure on the thermal conductivity has been shown. However, these alloys long term thermal stability analysis is proposed in order to evaluate the thermal cycling behaviour of non-eutectic alloys.

From the results, long term thermal behaviour analysis in pilot scale TES unit is considered adequate, in order to guarantee the adequacy of these alloys as PCMs, which might represent a breakthrough concept regarding current storage technologies.

7. Ongoing work

7.1. Thermal expansion analysis of Investigated alloys

Introduction

Thermal expansion analysis is performed in order to determine the mechanical stress on the TES unit during the charging and discharging processes.

The alloy samples measured by dilatometry techniques were $Mg_{71}Zn_{28.9}Al_{0.1}$, $Zn_{84}Al_{8.7}Mg_{7.6}$, $Zn_{88.7}Al_{11.3}$, $Zn_{92.2}Mg_{7.8}$ (eutectic alloys) and $Mg_{70}Zn_{24.9}Al_{5.1}$, $Mg_{70}Zn_{24.4}Al_{5.6}$ (quasi-peritectic alloys), and the linear coefficient of thermal expansion (CTE) was calculated as it has been explained in sections (2.4) and (3.4.4).

Preliminary results

Figures 50 and 51 show the curves of the LCTE in the solid phase as a function of the temperature.

In particular, Figure 50 presents the obtained LCTE curves of $Mg_{71}Zn_{28.9}Al_{0.1}$, $Mg_{70}Zn_{24.9}Al_{5.1}$ and $Mg_{70}Zn_{24.4}Al_{5.6}$ alloys, which show a quasi-constant behaviour in the temperature range from 100 to 270 ºC. This indicates that the microstructures of the studied alloys are at thermodynamic equilibrium with near-zero thermal strain. As it can be seen, the CTE values decrease with increasing Al proportion in the alloys. These results are related to the lower CTE value of Al ($23.6 \cdot 10^{-6}$ ºC^{-1}) in comparison to the ones of Mg ($25.2 \cdot 10^{-6}$ ºC^{-1}) and Zn ($39.7 \cdot 10^{-6}$ ºC^{-1}).

The results of $Zn_{84}Al_{8.7}Mg_{7.6}$, $Zn_{88.7}Al_{11.3}$ and $Zn_{92.2}Mg_{7.8}$ eutectic alloys are shown in Figure 51. The LCTE are constant in the complete temperature range except between 260 ºC and 285 ºC in the $Zn_{84}Al_{8.7}Mg_{7.6}$ and $Zn_{88.7}Al_{11.3}$ alloys, which present maximum values of $57 \cdot 10^{-6}$ ºC^{-1} and $87 \cdot 10^{-6}$ ºC^{-1} at 269 ºC and 275 ºC, respectively . These changes in their LCTE values are due to the presence of Al (α) + Zn(η) → ZnAl(β) eutectoid reaction observed by calorimetric analysis (see section (4.1.2), Figure 23).

The average LCTE values of investigated alloys are around $26 \cdot 10^{-6}$ ºC^{-1}, $24 \cdot 10^{-6}$ ºC^{-1} $22 \cdot 10^{-6}$ ºC^{-1}, $24.3 \cdot 10^{-6}$ ºC^{-1}, $17.3 \cdot 10^{-6}$ ºC^{-1} and $27.4 \cdot 10^{-6}$ ºC^{-1} for $Mg_{71}Zn_{28.9}Al_{0.1}$, $Mg_{70}Zn_{24.9}Al_{5.1}$, $Mg_{70}Zn_{24.4}Al_{5.6}$, $Zn_{84}Al_{8.7}Mg_{7.6}$, $Zn_{88.7}Al_{11.3}$ and $Zn_{92.2}Al_{7.8}$ alloys, respectively. These values are slightly higher than the ones of the common stainless steel used in the construction of the storage unit (around 17.3 10^{-6} ºC^{-1}).

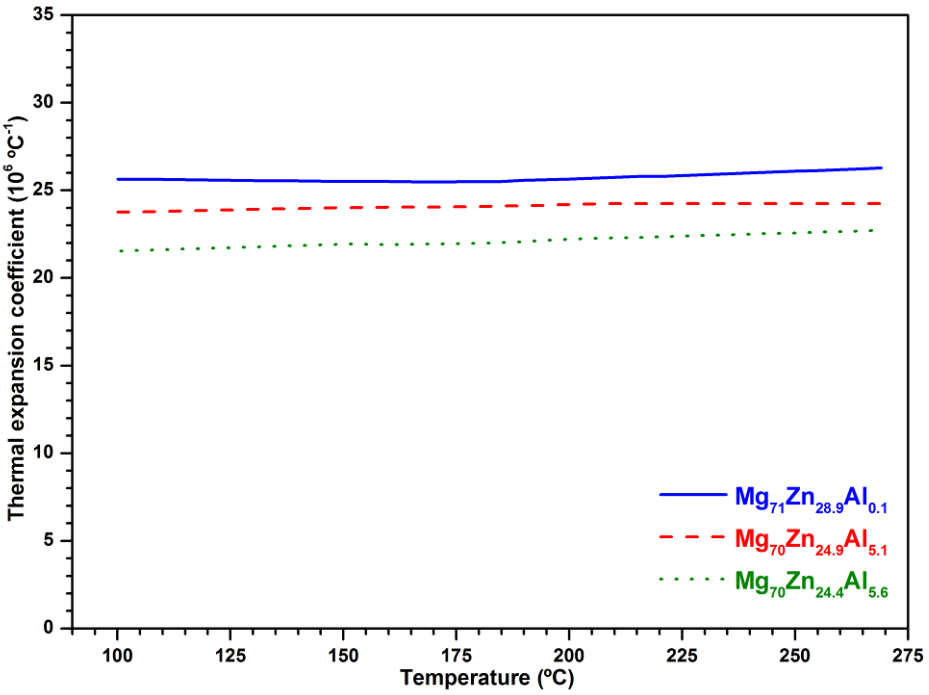

Figure 50. The temperature dependence of the thermal expansion coefficients of $Mg_{71}Zn_{28.9}Al_{0.1}$, $Mg_{70}Zn_{24.9}Al_{5.1}$ and $Mg_{70}Zn_{24.4}Al_{5.6}$ metal alloys.

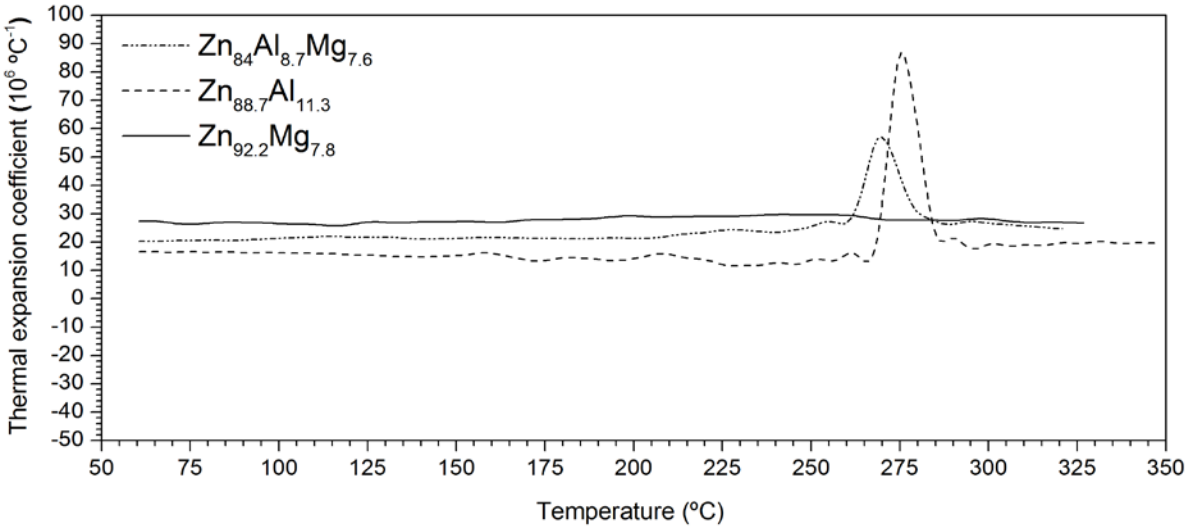

Figure 51. The linear thermal expansion coefficient values in solid state of the $Zn_{84}Al_{8.7}Mg_{7.6}$, $Zn_{88.7}Al_{11.3}$ and $Zn_{92.2}Mg_{7.8}$ eutectic alloys.

Future work

The results obtained are currently under study and researchers are preparing a journal publication including more detailed analysis.

7.2. Compatibility test: analysis of elements diffusion through corrosion layers

Introduction

As it has been discussed in the section (4.3.1) the stainless steels corrosion mechanism in $Zn_{88.7}Al_{11.3}$ and $Zn_{84}Al_{8.7}Mg_{7.3}$ molten metals depends on stainless steel elements dissolution on the corrosion layers and on their diffusion thought them toward interfacial reaction zone.

Therefore, in order to gain a greater understanding and knowledge of the observed corrosion mechanism, it is necessary to perform a more extensive analysis of the following factors:

- Dissolved amount of elements on the corrosion layers.
- The concentration profile of elements thought the corrosion layers.
- The morphology and microstructure of intermetallic corrosion layers.

This analysis is currently on going, therefore only partial and preliminary results are presented bellow.

Preliminary results

Dissolved amount of elements on the corrosion layers

Regarding θ-Al_3Fe and Al_2Fe intermetallic layers present similar element concentration after corrosion tests during 720 hours as Table 27 shown. In this way, θ-Al_3Fe intermetallic layer presents an average concentration of 5.4% Zn, 4.2% Cr and 1.6% Ni (at.%), where as, Al_2Fe layer show 3.2 % Zn, 8.0 % Cr and 2.8 % Ni average concentration. These results show the different solubility of these elements in θ-Al_3Fe and Al_2Fe intermetallic phases.

Corrosion layer	Metallic alloy	Stainless steel	Immersion time (h)	Fe	Cr	Ni	Al	Zn
θ-Al_3Fe	$Zn_{88.7}Al_{11.3}$	304	720	21.91	4.26	1.32	64.38	4.06
θ-Al_3Fe	$Zn_{88.7}Al_{11.3}$	304L	720	21.12	4.23	1.23	65.18	5.97
θ-Al_3Fe	$Zn_{84}Al_{8.7}Mg_{7.3}$	304	720	19.46	4.34	1.62	69.01	5.56
θ-Al_3Fe	$Zn_{84}Al_{8.7}Mg_{7.3}$	316	720	18.23	3.30	2.15	70.48	5.84
θ-Al_3Fe	$Zn_{84}Al_{8.7}Mg_{7.3}$	316L	720	17.56	4.79	1.69	64.15	4.83
Al_2Fe	$Zn_{88.7}Al_{11.3}$	316L	720	25.93	7.76	3.65	50.71	3.42
Al_2Fe	$Zn_{88.7}Al_{11.3}$	316	720	29.77	8.33	2.00	55.51	2.89

Table 27. Element concentration on θ-Al_3Fe and Al_2Fe corrosion layers after 720 hours immersion time for the compatibility test of $Zn_{88.7}Al_{11.3}$ and $Zn_{84}Al_{8.7}Mg_{7.3}$ alloys with tested stainless steels.

The concentration profile of elements thought the corrosion layers

As it has been indicated in the section (4.3.1.) the concentration of Fe, Cr and Ni (steel elements) along the steel/alloy interface decreases as they move away of steels and the concentration of Al and Zn (molten alloy elements) as they move away of molten alloys. This behaviour of the concentration profile of the elements is the expected one and is fulfilled in any of observed Al-Fe intermetallic phases. However, when Al-Zn-Cr-Mg particles are present in the corrosion layer, the Cr concentration profile shows an anomaly.

The Figure 52 shows SEM images of two corrosion tests, in which Al-Zn-Cr-Mg particles have been identified. These particles diffusion toward molten metal can be observed in the Figure 52 together the presence of different Al-Fe layers adjacent to the steels.

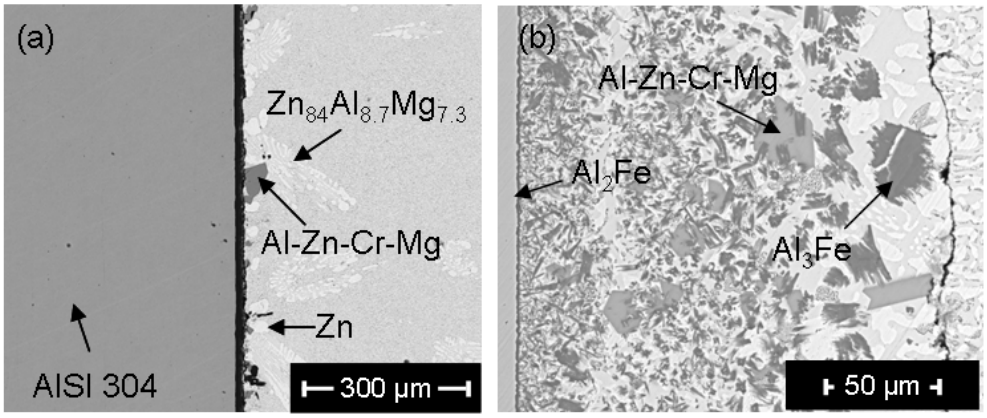

Figure 52. The back scattered-electron cross-section micrograph (SEM) of: (a) 304 steel and (b) 321 in contact with $Zn_{84}Al_{8.7}Mg_{7.3}$ alloy after corrosion tests at 400 ºC for 720 and 360 hours, respectively.

However, in both cases the Al-Zn-Cr-Mg particles have higher Cr content than Al-Fe layers adherent to the steels as is shown in Table 28. In this way, the $Zn_{84}Al_{8.7}Mg_{7.3}$/304 sample shows a increasing of Cr content from 4.34% to 8.15% and in the case of $Zn_{84}Al_{8.7}Mg_{7.3}$/321 sample from 5.74% to 8.21%.

Metallic alloy	Stainless steel	Time (h)	Identificated phases	Fe	Cr	Ni	Al	Zn	Mg
$Zn_{84}Al_{8.7}Mg_{7.3}$	304	720	θ-Al_3Fe layer	19.46	4.34	1.62	69.01	5.56	traces
			Al-Zn-Cr-Mg part	0.49	8.15	traces	45.97	39.99	5.4
	321	360	Al_2Fe layer	25.46	5.74	1.9	59.07	5.24	0.62
			θ-Al_3Fe part	18.84	0.42	1.73	70.59	2.8	traces
			Al-Zn-Cr-Mg part	0.48	8.21	0.10	46.64	37.27	6.48

Table 28. The intermetallic layers and particles element concentration (at%) of 304 and 321 stainless steels in the $Zn_{84}Al_{8.7}Mg_{7.3}$ bath after immersion times of 720 and 360 hours, respectively, at 400 ºC isothermal temperature.

In addition, other anomaly can be observed in the Cr content of θ-Al_3Fe particles of $Zn_{84}Al_{8.7}Mg_{7.3}$/321 sample: The particles have a Cr content of 0.42%, which is much lower than the observed average value for this phase (4.2%).

These observations suggest the following hypotheses:

- The low Cr content on θ-Al_3Fe particles of $Zn_{84}Al_{8.7}Mg_{7.3}$/321 sample suggests the preferential dissolution of Cr in Al-Zn-Cr-Mg particles, when both particles, θ-Al_3Fe and Al-Zn-Cr-Mg, are formed at the same time during the corrosion reaction.

- The formation of Al-Zn-Cr-Mg particles before Al-Fe layers formation.

Similar Cr behaviour has been observed by W.J. Wang et al. [106] by means of corrosion test between liquid Zn and 316 stainless steels after 3 and 5 days. In these specimens, the corrosion layer that formed on the surface of the 316 steel showed a increasing Cr and Ni concentrations from the inner to outermost layer, which was attributed to a lower dissolution rate of Cr from the steel to the layer than its diffusion rate through it.

Future work

As mentioned in the introduction, further analysis of the obtained results are needed in order to increase the understanding of observed corrosion mechanisms, which will be published in a new scientific paper.

7.3. Other eutectic metal alloy identification as potential PCMs

Introduction

In this research work the $Al_{56-60}Mg_{32-39}Zn_{5-8}$ (E2), $Al_{59-62}Mg_{38-41}$ (e4) and $Mg_{69}Al_{31}$ (e7) (at.%) eutectic alloys from Mg-Al-Zn system, as well as, the $Mg_{66-68}Al_{30-32}Cu_{1.7-2.5}$ (E9) (at.%) eutectic alloy from Mg-Al-Cu system had been also selected to be investigated as potential high temperature PCMs. The potentiality of these alloys is based on availability and low cost of these metals, on their high heat of fusion above 200 J/g [22] and on their melting temperatures range between 425 and 450ºC.

The Figures 53 and 54 show Mg-Al-Zn and Mg-Al-Cu liquid projections, where, the alloys are pointed as E2, e4, e7 in Figure 53 and as E9 in Figure 54. At same time, the e4 and e7 binary alloys are also shown by the Al-Mg binary phase diagram in the Figure 55.

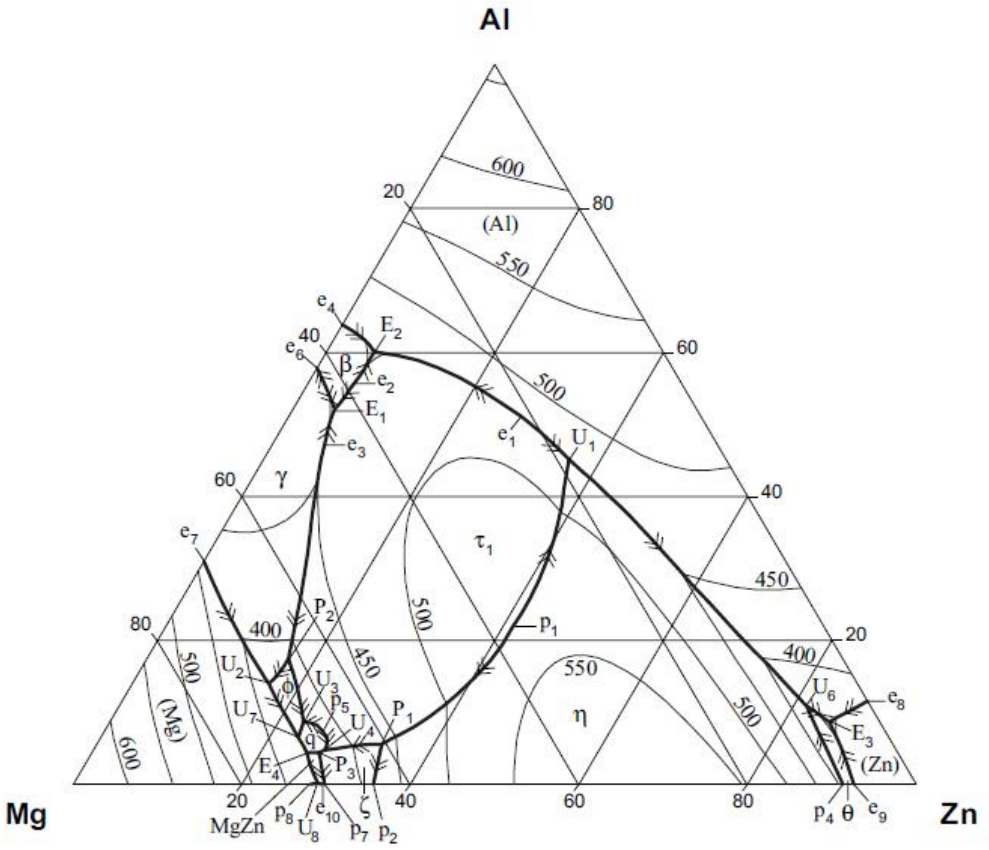

Figure 53. Mg-Al-Zn liquid projection (at.%) shows E2, e4 and e7 eutectic alloys [142].

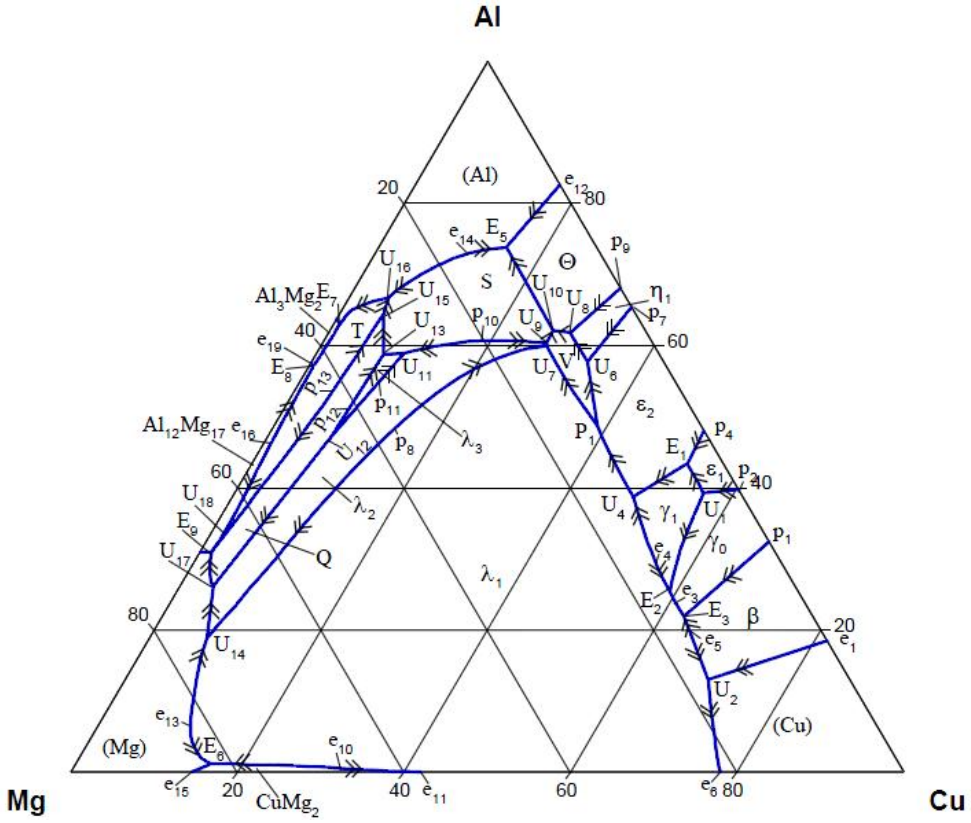

Figure 54. Mg-Al-Cu liquid projection (at.%) shows E9 eutectic alloy [143].

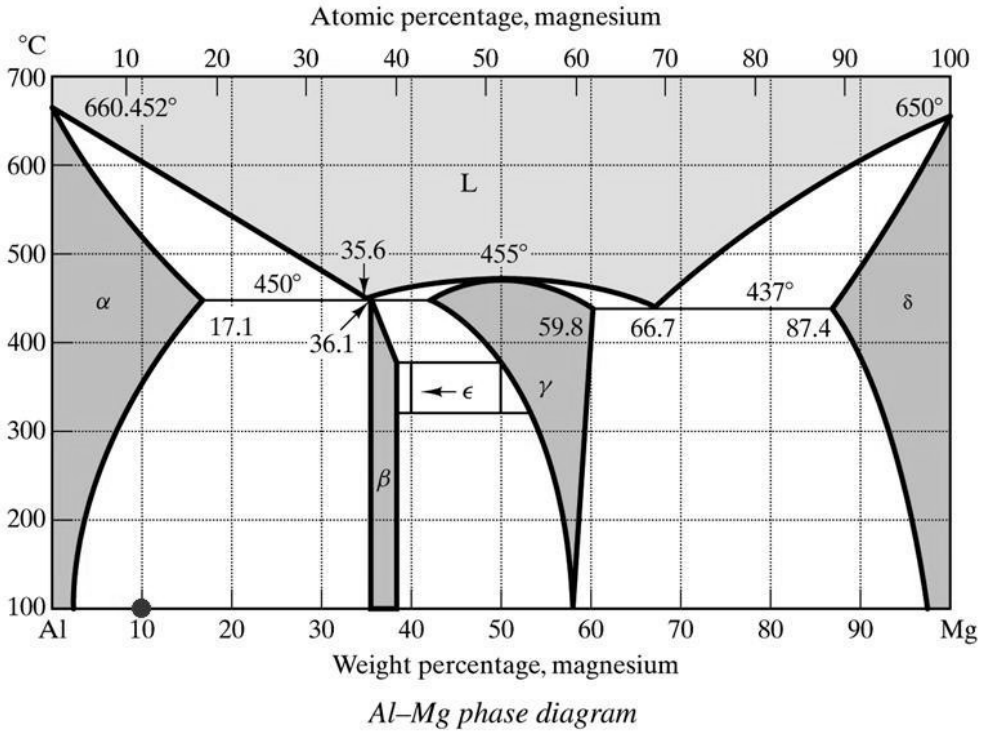

Figure 55. Al-Mg phase diagram shows e4 and e7 eutectic alloys, where, e4 composition is indicated as Al-35.6%Mg (wt.%) and e7 composition as Mg-33.3%Al (wt.%) [144].

Table 29 shows the reactions of the selected alloys, theoretical melting temperatures and their approximated compositions.

Type	Alloy	Eutectic reaction	T(ºC)	Composition (at.%)				Ref.
				Al	Mg	Zn	Cu	
E2	$Al_{556-60}Mg_{32-39}Zn_{5-8}$	(Al) + β + $\tau_1 \leftrightarrow$ L	447	56 - 60	32 - 39	5 - 8	-	[142]
e4	$Al_{59-62}Mg_{38-41}$	(Al) + β $\leftrightarrow$ L	450	62	38	-	-	[144]
e7	$Mg_{69}Al_{31}$	(Mg) + γ $\leftrightarrow$ L	437	31	69	-	-	[144]
E9	$Mg_{66-68}Al_{30-32}Cu_{1.7-2.5}$	(Mg) + Q + $Al_{12}Mg_{17} \leftrightarrow$ L	424.9	30 - 32	66 - 68	-	1.7 - 2.5	[143]

Table 29. The alloys eutectic reactions, theoretical melting temperatures from [142-144] references and approximated compositions are shown.

In this frame, the research of these alloys is in its initial state, i.e., (a) the correct eutectic composition of alloys must be determined and (b) the adequate synthesis protocol of alloys must be defined.

Eutectic composition determination

Several chemical compositions of the proposed alloys reported by other authors are shown in Table 30. As it can be seem for E2, E9 and e4 alloys several compositions have been found. Therefore, given the variety of proposed compositions it is necessary to determine the correct eutectic one. The compositions synthesized in this research are marked in boldface.

Type	Alloy	Composition (at.%)				T_m (ºC)	ΔH (J/g)	Ref.
		Al	Mg	Zn	Cu			
E2	**E2-1**	**59.882**	**32.258**	**7.859**		453.97	-	[53]
	E2-2	**56.1**	**39.2**	**4.7**	-		-	[66]
	E2-3	**60.3**	**34.6**	**5.1**	-		-	[66]
	E2-4	60.1	34.3	5.6		447	-	[142]
	E2-5	58.34	38.69	2.47		443	310	[22]
	E2-6	59.9	37.6	2.5		450.3	329.1	[22]
e4	**e4-1**	**62.01**	**37.99**	-	-	450	-	[144]
	e4-2	58.76	41.24	-	-	497	285	[22]
e7	**e7-1**	**31.06**	**68.94**	-	-	437	-	[144]
E9	**E9-1**	**31.04**	**67.21**	-	**1.75**	424.9	-	[143]
	E9-2	31.10	67.20	-	1.70	424.9	-	[143]
	E9-3	30.00	67.54	-	2.46	425	-	[143]
	E9-4	30.87	66.92	-	2.21	424	-	[143]
	E9-5	31.06	67.15	-	1.79	426	-	[143]
	E9-6	31.12	67.17	-	1.71	425	-	[143]
	E9-7	30.79	67.17	-	2.04	427	-	[143]

Table 30. Reported compositions, melting temperatures and enthalpies for the proposed alloys are listed. (The synthesized compositions are marked in boldface).

Synthesis protocol determination

For the sample alloying, the synthesis process which explained in chapter 3 has been followed. However, due to their different compositions, the synthesis process temperatures and times must be again determined for each new eutectic alloy. For this propose, based on the primary element melting points (650, 660, 420 and 1084.62 ºC for Mg, Al, Zn and Cu, respectively) and the alloys eutectic phase transition temperatures, different alloying conditions have been tested as is shown in Table 31.

Experimental results

The tested synthesis conditions for each selected alloy, as well as, the calorimetric analysis (DSC) results for each sample are listed in Table 31. In general, all samples shows good agreement between experimental and theoretical melting temperatures. The comparison among the melting point and enthalpies values of the samples with same composition shows similar melting temperatures and a little difference in their enthalpies values. Respect to the synthesis of E9 alloy, the total oxidation of 1, 2 and 3 samples of E9-1 composition have been observed after their synthesis process. Consequently, no adequate synthesis conditions were found for the E9 alloy.

Type	Alloy	Sample	Melting conditions		Nº alloying	DSC		
			T(ºC)	Time (h)		T_m (ºC)	ΔH(J/g)	Compositon
E2	E2-1	1	450	12	2	449.62	10.86	non-eutectic
(447ºC)	($Al_{59.9}Mg_{32.3}Zn_{7.8}$)	2	**450**	**4**	**5**	448.39	267.7	non-eutectic
		3	450	6	6	447.99	259.6	non-eutectic
		4	660 / 500	0.5 / 1.5	First / 2	448.39	242.1	non-eutectic
	E2-2	1	**500**	**4**	**3**	448.79	271.0	non-eutectic
	($Al_{56.1}Mg_{39.2}Zn_{4.7}$)	2	660 / 500	0.5 / 1.5	First / 2	449.69	231.8	non-eutectic
	E2-3	1	500	4	3	447.72	268.6	non-eutectic
	($Al_{60.3}Mg_{34.6}Zn_{5.1}$)	2	500	4	4	448.08	206.0	non-eutectic
		3	**660 / 500**	**0.5 / 1.5**	**First / 2**	**448.00**	**257.3**	**eutectic**
e4	e4-1	**1**	**650 / 490**	**0.75 / 2**	**First / 4**	**451.05**	**291.7**	**eutectic**
(450ºC)	($Al_{62}Mg_{38}$)	2	650 / 490	0.75 / 4	first / 3	450.77	274.2	eutectic
		3	660	0.5	1	451.39	284.2	eutectic
		4	660	1.5	1	450.56	283.0	eutectic
e7	e7-1	1	700	2	3	421.23	176.1	non-eutectic
(437ºC)	($Mg_{69}Al_{31}$)	**2**	**650 / 490**	**0.75 / 2**	**First / 4**	**437.94**	**241.5**	**eutectic**
		3	650 / 490	0.75 / 4	First / 3	424.79	250.3	eutectic
E9	E9-1	1	650	10	1			
(424.9ºC)	($Mg_{67.4}Al_{30.8}Cu_{1.8}$)	2	650	10	1		-	
		3	650	10	1			

Table 31. The tested synthesis conditions for each selected alloy and their calorimetric analysis (DSC) results are listed. (The synthesis conditions that have shown the more promising calorimetric curves are marked in boldface).

Taking into account, the obtained calorimetric curves in each case (based line, enthalpy value and melting/solidification peaks) the more promising synthesis conditions, as well as, the more promising samples have been determined (boldface letters in Table 31) for the E2, e4 and e7 alloys. The Figure 56 shows DSC curves of these samples (E2-3_3, e4-1_1 and e7-1_2).

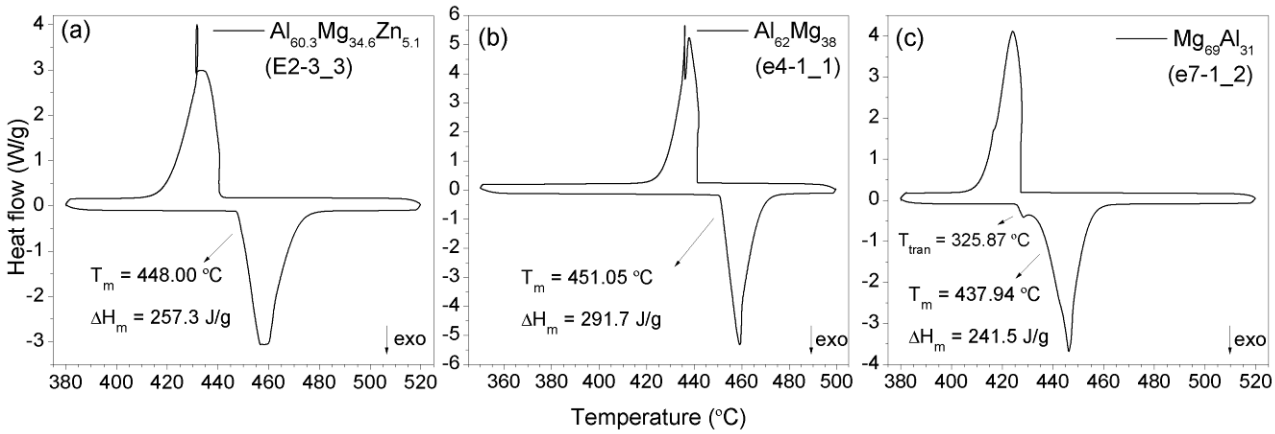

Figure 56. The $Al_{60.3}Mg_{34.6}Zn_{5.1}$ (a), $Al_{62}Mg_{38}$ (b) and $Mg_{69}Al_{31}$ (c) alloys DSC curves.

The based lines and transitions peaks of curves indicate that the sample compositions are close to eutectic ones. On the other hand, the secondary peak observed at 325.87 ºC in Figure 56 (c) suggest metastability behaviour in the $Mg_{69}Al_{31}$ (e7-1) alloy due to no solid → solid reaction is predicted by it phase diagram (Figure 55). The alloys present 448.00, 451.05 and 437.94ºC melting temperatures and 257.3, 291.7 and 241.5 J/g enthalpies in E2-3_3, e4-1_1 and e7-1_2 samples, respectively. The melting temperatures of alloys are in agreement with theoretically calculated ones of 447, 450 and 437 ºC, respectively [142,144]. On the other hand, the enthalpy values of E2-3 (257.3 J/g) and e4-1 (291.7 J/g) alloys are in the order of 310, 329.1 and 285 J/g enthalpies of E2-5, E2-6 and e4-7 composition (Table 30) reported by [22].

Conclusions and future work

The $Al_{56\text{-}60}Mg_{32\text{-}39}Zn_{5\text{-}8}$ (E2), $Al_{59\text{-}62}Mg_{38\text{-}41}$ (e4), $Mg_{69}Al_{31}$ (e7) and $Mg_{66\text{-}68}Al_{30\text{-}32}Cu_{1.7\text{-}2.5}$ (E9) eutectic alloy had been selected to be investigated as potential high temperature PCMs. As first step of this study their eutectic composition and synthesis protocol determination have been carried out. Based on this study the following conclusions are obtained:

The more promising synthesis conditions for E2, e4 and e7 alloys have been determined. However, in order to determine the optimal synthesis protocol deeper analysis is required. On the other hand, no adequate synthesis conditions have been found for the E9 alloy.

The $Al_{60.3}Mg_{34.6}Zn_{5.1}$ (E2-3), $Al_{62}Mg_{38}$ (e4-1) and $Mg_{69}Al_{31}$ (e7-1) alloys, with melting temperatures between 425-450ºC and enthalpies between 240-300 J/g may present correct eutectic compositions. The structural characterization of these alloys must be performed in order to ensure this assumption.

After determining the correct composition, their complete characterization of these alloys (thermophysical properties, thermal stability and compatibility) should be carried out in order to evaluate their potentiality as high temperature PCMs.

7.4. Crystal growth analysis of kinetic $Zn_{88.7}Al_{11.3}$ alloy by infrared thermography

Introduction

The crystallization process has a strong influence on the final material microstructure and as a consequence, on its properties. Therefore, solidification processes on different materials have been intensely studied since decades. One of the basic problems that researchers must face is related with the crystal growth kinetic during the solidification, which can be controlled by any of following three factors: species diffusion in the melt (either long- or short-range), flow of latent heat away from the growing crystal surface and reactions at the crystal-melt interface.

In order to determine which process controls the solidification mechanism in a given system, the crystal morphology and the crystal growth kinetic as a function of the undercooling are usually analyzed. For this propose the time-laps photography and cinematography methods are the most widely using techniques [144,145].

However, by this techniques the temperature in the bulk of specimens can be only provide, which can lead to an error when differs from the temperature of crystal-melt interface. If in a interface-controlled growth the rate of production of latent heat is faster than the rate of removal, the interface temperature will increase and the growth rate will slow down up to the point where the latent heat can be removed at the same heat it is produced. This phenomenon leads to a discrepancy between the bulk and interface temperatures, where, the interface temperature is higher than bulk one. Therefore, the knowledge of the crystal-melt interface temperature is essential when the temperature dependence of experimentally determined growth rate is discussed.

In this research work experimental analysis of crystal growth in undercooled eutectic metal alloy by using microscopic infrared thermography instead of optical microscopy is carried out. Infrared camera can provide thermal images at high scan speed (> 1600 Hz), allowing the determining of temperature at any point of the interface at any time. The spacial resolution of infrared images is around 20 mm, which it is lower than that of the optical microscopy images due to the wavelength of infrared radiation limitation. In this way, optical microscopy provides a better view of the crystal morphology, whereas the infrared thermography is better technique when the temperature dependence of crystal growth rates is analyzed and when the specimens are not transparent to visible light.

This part of the thesis was developed during a three months research stay at I2M – CNRS, University of Bordeaux (France), from March to July 2015.

The theory of interface-controlled crystal growth

Rate equation

For eutectic alloys, at constant solidification temperature the interface reaction controls the crystal growth kinetic process [146]. Assuming a lamellar eutectic alloy with α and β phase, during solidification process the α and β phases grow side by side in a cooperative manner. The α phase rejects *B* atoms and the β phase rejects *A* atoms, however, the *B* atoms rejected by the α phase are needed for the growth of the β phase, and vice versa. In this way, as Figure 57 shown the *A* and *B* solutes diffuse along the solid-liquid interface from one phase to the other (diffusion coupling). This rearrangement processes controls the growing process and therefore, reaction in the crystal-melt interface controls the crystal growth kinetic in eutectic systems. The rearrangement frequency is independent of the interface position and therefore independent of the time.

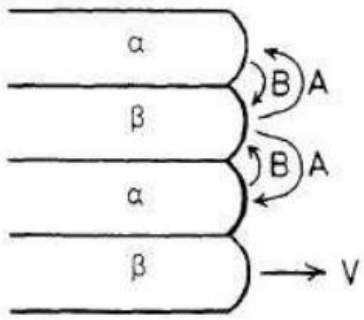

Figure 57. The A and B solutes interdiffusion in the crystal-melt interface of a lamellar eutectic composition during its growing [147].

On the other hand, it is assumed that the rearrangement process involves a diffusive jump (diffusion-limited kinetics). According to reaction-rate theory it is assumed when an atom or molecular group diffuse from melt to crystal that must pass through an activated state or activation threshold to decay into the crystalline state. This activation threshold is built up by the energy potential of the surrounding atoms and it assumed as the energy barrier for atomic diffusion [147].

In this way, the interface-controlled growth theory considers for the crystal rate determination the difference between the rates at which atoms or molecules group attach from the liquid to the solid (r_s) and the rates at which atoms or molecules detach from the crystal surface (r_l) as is shown in equation (20):

$$v = a_0 f\left(r_l - r_s\right) = a_0 fv' \exp\left(-\frac{\Delta G_{ls}}{RT}\right)\left[1 - EXP\left(-\frac{\Delta G_{ls}}{RT}\right)\right] = V_0\left[1 - \exp\left(-\frac{\Delta G}{RT}\right)\right] \quad (20)$$

where a_0 is the interatomic spacing, f is the fraction of interface sites that are active growth sites, and v' is atomic vibration or thermal frequency of single atoms in the liquid state. ΔG_{ls} is the free energy difference between the liquid and solid phases whereas ΔG_a is activation energy for atomic jumps or the free energy difference between the liquid and activated state. Finally, R is the universal gas constant and T is the temperature.

At constant pressure:

$$\Delta G_{ls} = \Delta H_{ls} - \Delta S_{ls} T \quad (21)$$

$$\Delta G_a = \Delta H_a - \Delta S_a T \quad (22)$$

H and S correspond to the enthalpy and entropy. Usually the free energy difference between liquid and solid phases is not known. So, by assuming that the enthalpy and entropy differences are not sensitive functions of the temperature, ΔG_{ls} may be approximated by:

$$\Delta G_{ls} = \Delta H_{ls} \Delta T \Big/ T_m \quad (23)$$

ΔH_{ls} is the latent heat of fusion, $\Delta T = T_m - T$ is the undercooling and T_m is the liquidus temperature.

The early models for the crystal growth rate are those of Wilson in 1900 and Frenkel in 1930, in which the factor v_o in equation (20) is related to atomic diffusivity $D \sim exp(-\Delta Ha/RT)$. The modern form of the Wilson-Frenkel model is [146]:

$$v = \frac{6a_0 D(T)}{l^2} f \exp\left(-\frac{\Delta S_a}{R}\right)\left[1 - \exp\left(-\frac{\Delta G_{ls}}{RT}\right)\right] \quad (24)$$

Where l is the diffusion jump distance.

The diffusion coefficient can be expressed by the Stokes-Einstein relation:

$$D(T) = \frac{k_B T}{3\pi\eta(T) a_0} \quad (25)$$

Where k_B is the Boltzman constant and η is the viscosity of the melt.

By the substitution of equation (25) in (24) the expressions for interface-controlled crystal growth limited by the atoms or molecules diffusion (diffusion-limited kinetics) is obtained.

$$\nu = \frac{2k_B T}{l^2 \pi \eta(T)} f \exp\left(-\frac{\Delta S_a}{R}\right)\left[1-\exp\left(-\frac{\Delta G_{ls}}{RT}\right)\right] \tag{26}$$

In diffusion limited growth kinetic as it is shown in Figure 58 the crystal growth rate increases as undercooling degrees increases up to reach a maximum, and then slows down with the increasing of undercooling. The diffusion is thermally activated process and, therefore, the lower the temperature the lower the rate of species diffusion thought up to the liquid mobility is suppressed.

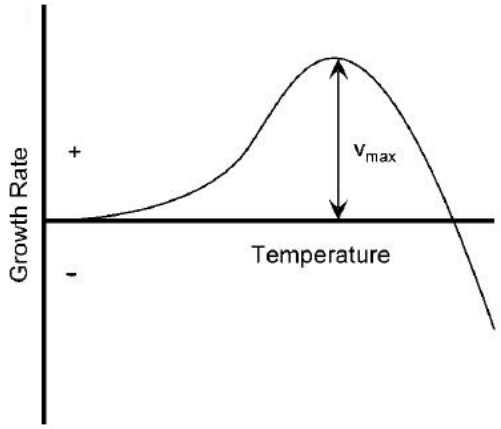

Figure 58. Growth rate versus undercooling for diffusion-limited kinetic [148].

Mechanism of interface-controlled growth

In an interface-controlled growth, the mechanism of grow can be continuous or lateral. The continuous growth mechanism happens when the atoms or molecules can attach to the growing crystal surface at any site (rough surfaces). In this case, the interface spread perpendicular of itself and uniformly. The lateral growth mechanism occurs when the surface of a crystal is essentially atomically flat (smooth surfaces). The growing happen by lateral migration of growth layers of one-molecule thicknesses, which are found at specific points of the growing crystal surface. In this case, the atoms or molecules can only attach to the edges of these layers in growth. In this case, the interface spread laterally of itself and non-uniformly. The lateral growth mechanism can be divided in two idealized types: surface-nucleation and screw dislocation as Figure 59 shown. In the surface-nucleation mechanism, each layer is initiated by one or more one-molecule-thick nuclei, the formation of which obeys the classical laws of nucleation kinetics. In such case, the density of growth sites is provided by the nucleation process. However, defects in the crystal structure can help to form new layers, so that a nucleation process is not necessary for growth (Figure 59 (a)). In

the screw dislocation the emergence of a dislocation in the crystal surface drives a permanent step that twists on itself creating a spiral ramp. This spiral ramp maintains the edge of the layer and therefore, the crystal growth [149] (Figure59 (b)).

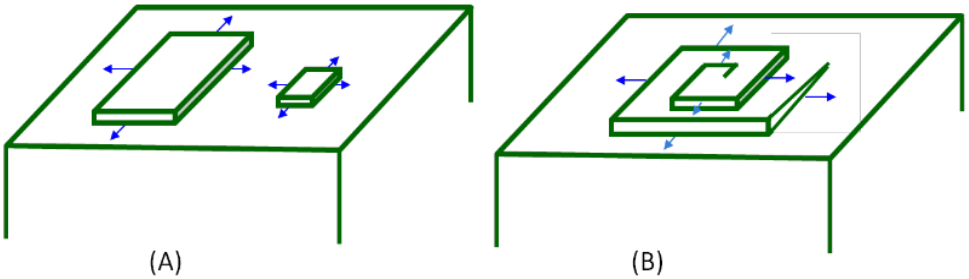

Figure 59. Schematic representation of (a) surface nucleation and (b) screw dislocation [149].

A way to know which type of growth mechanism occurs in a given system is analysis the dependence of *f* (fraction of interface sites that are active growth sites) with temperature from the equation (26).

In this way, the equation (b) can be re-written as:

$$kf = \frac{v\eta(T)}{\left(2k_B T/\pi\right)\left[1-\exp\left(-\frac{\Delta H_{ls}\Delta T}{RT_m T}\right)\right]} \tag{27}$$

Where

$$k = \frac{1}{l^2}\exp\left(-\frac{\Delta S_a}{R}\right) \tag{28}$$

By assuming that the entropy difference, *ΔSa*, and the diffusion jump distance, *l*, are not sensitive functions of the temperature, the pre-factor *k* can be considered as a constant and equation (27) can be used to analyze the temperature dependence of *f*. In this way, for continuous growth *f* is generally assumed to be independent of the temperature and large. In surface-nucleation mechanism the density of active growth sites *f* depends on the density of growth sites provided by the nucleation process or by defects in the crystal structure. Finally, the screw dislocation mechanism the fraction *f* is proportional to the undercooling [146].

Other proposed way to analysis the *f* dependence with temperature is by the expression of reduced growth rate (v_r) [150]:

$$v_r = \frac{v\eta(T)}{\left[1-\exp\left(-\frac{\Delta H_{ls}\Delta T}{RT_m T}\right)\right]} = \frac{k_B T}{3\pi a_0^2} f \tag{29}$$

Where:

$$v = f\frac{k_B T}{3\pi a_0^2 \eta(T)}\left[1-\exp\left(-\frac{\Delta H_{ls}\Delta T}{RT_m T}\right)\right] \tag{30}$$

In this case for continuous mechanism the plot v_r versus T should be straight lines with zero slopes. In surface nucleation mechanism is expected the approximately exponential increasing of v_r with T. Finally, for screw dislocation mechanism the plots of v_r versus T should be straight lines with positive slopes.

Experimental

By infrared thermography is analyzed the crystal growth kinetic in an undercooled eutectic metal alloy. The crystallization at constant bulk temperature happened spontaneously and the growth of the solid phase is observed using infrared camera at several undercooled temperatures. The recorder thermal images allow determining:

(a) The position of crystallization front at any time.

(b) The velocity of advancement of the front at any point and time.

(c) And the temperature at the points of the interface at any time.

By means of this information the control process of crystal growth kinetic is determined as it will explain later.

Material

The investigated material is the $Zn_{88.7}Al_{11.3}$ (at.%) (95%Zn-5%Al (mass%)) binary eutectic metallic alloy. This eutectic alloy is formed by Zn (hexagonal closed-packet (hcp) structure, $P6_3/mmc$ space group) solid solution and Al (face-centred cubic (fcc) structure, space group Fm-3m) solid solution as primary phases. The $Zn_{88.7}Al_{11.3}$ alloy corresponds to crystallized lamellar microstructure as is shown in the Figure 60. Its theoretical melting temperature is 380 ºC and the experimental melting/solidification temperatures are ~382 and ~376 ºC, respectively, with a heat of fusion of ~119 J/g (for more detail see chapter (4.1.2)).

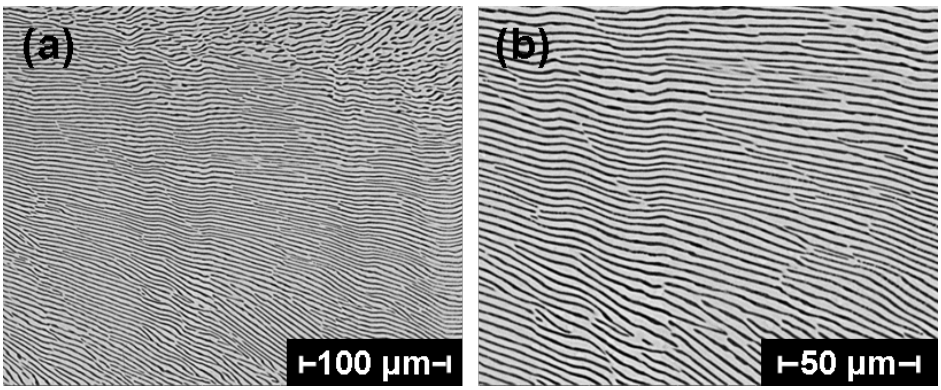

Figure 60. SEM images of the $Zn_{88.7}Al_{11.3}$ lamellar eutectic alloy at 10 K/min cooling rate at 800X (100 µm) and 1500X (50 µm) magnifications.

Experimental setup

A schematic picture of the experiment set-up is show in the Figure 61. The main elements of the set-up are an infrared camera a heating/cooling system for temperature control. The heating/cooling system is compound by a micro-furnace, heating control system and cooling pump for temperature regulation. The micro-furnace includes thermal resistances on the bottom, an alumina insulation cavity in the middle and a graphite crucible inside of the alumina cavity. The alumina cavity in equipped with thermocouples for temperature control. The infrared camera (FLIR SC7000, detection window: 1.5-5 µm) is equipped with an optical microscope G1 (F/2) objective (provider by FLIR). The highest spatial resolution reachable is about 20 µm. Digital full frame rate of the camera ranges from 170 Hz to 380 Hz, and up to 11 kHz-32 kHz with windowing. The sep-up is mounted on a vibration free solid support. The heating system allows working temperature from ambient to 1000 ºC.

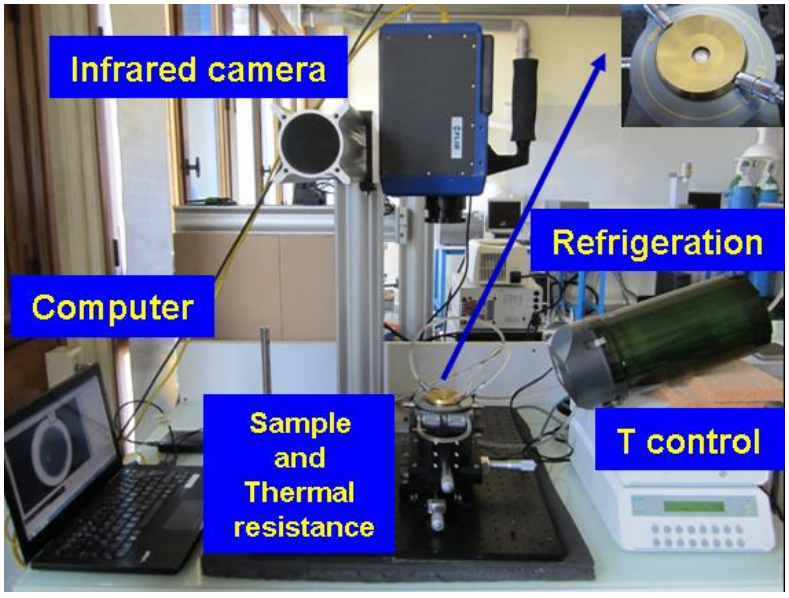

Figure 61. Picture of experimental setup.

Experimental procedure

A disc form metal alloy sample is placed in graphite crucible inside the micro-furnace. The sample is heated between 10 and 60 °C above its melting temperature and is maintained in liquid phase for 10 or 15 min. Then, the heating/cooling system is used to reach the selected working temperature (T_0), which is below the melting point. T_0 is maintained constant thereafter. Subsequently, the crystallization is spontaneously initiated by itself and the thermal behaviour of the sample during crystallization is observed by the infrared camera. Simultaneously, the temperature of the alumina cavity is measured by the thermocouples. This procedure is repeated several times with the same sample in order to recorder by infrared camera the crystallization process at different undercooling ($\Delta T = T_m - T_0$) temperatures.

The infrared camera does not provide direct measurements of temperature, therefore, a calibration is necessary to transform electrical signal (DL = Digital Level) values into temperature data. For this propose, the sample is placed in the experimental setup and reach thermal equilibrium, a series of images are recorded by infrared camera and the temperature of the sample is measured by the thermocouples. This procedure is repeated for different working temperatures for melt and solid sample. The calibration curve is obtained by representing the space-time average DL-values in a series of infrared images against sample temperature.

In order to analysis the crystal growth kinetic of the $Zn_{88.7}Al_{11.3}$ eutectic alloy a disc form sample (called nº 8) with 10 mm of diameter and 0.70 mm average thickness was measured. The sample weight was 281.92 mg and its surface was rough (no polished). On the other hand, in order to determine the optimal the sample thickness several specimens with different thickness between 0.71 and 0.60 mm were subjected to shorter testing.

8.2.3.4. Data processing to determine the crystal growth velocity from the infrared images

At each T_0 working temperature (measured by thermocouples placed in the alumina cavity) the raw DL images are recorded by infrared camera while the crystallization process takes place. The images are recorded at 25, 50 and 100 Hz depending of ΔT value. As an example, the Figure 62 shows 100 Hz DL maps (300x 250 pixels) obtained at different times (1, 3, 6 and 11 seconds) during the experiment at 2 ºC of ΔT. The white line corresponds to solid-liquid interface, which moves to the left as the solidification process occurs. Thus the solid phase is to the right of solid-liquid interface, while the liquid phase is to the left of it.

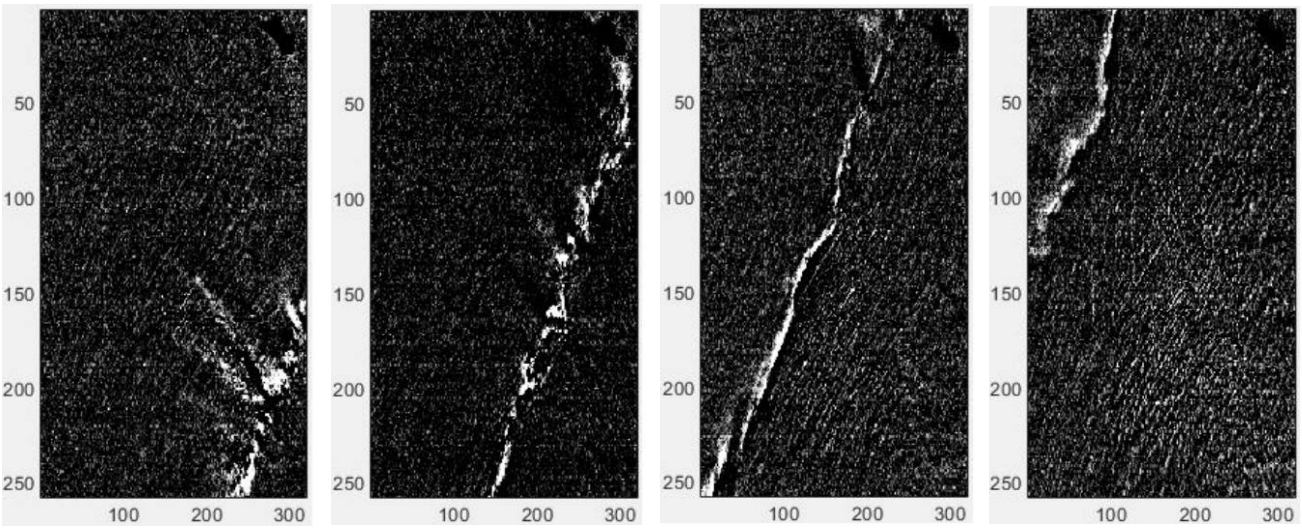

Figure 62. Snapshots of infrared images recorded over time at 1, 3, 6 and 11 seconds, respectively, for the $Zn_{88.7}Al_{11.3}$ alloy at undercooled temperature of 2 ºC. The white line corresponds to solid-liquid front. The solid phase is to the right size of the solid-liquid interface and the liquid phase in the left size.

By calibration curve DL data are transformed in temperature values. At any time, the maximum temperature values are observed in the crystallization front, where, latent heat release happens. In this way, by the maximum temperature identification in each interface row, the interface position *s(x,y,z)* is determined for each sampling time. The graphical representation of *s(x,y,z)* is used to determine the trajectories and the velocity of the interface points as well as the temperature profile along these trajectories. For this procedure, a limited number of crystallization front points are selected. This procedure is carried out for all tested undercoolling temperatures.

To determine the crystal growth velocity for each undercolling temperature the distance traveled by selected front points is calculated as a function of time, *d(t)*, where, the velocity of the points is determined by the time derivation of *d(t)* function. In this way, if the crystal growth is controlled by species diffusion in the melt, *d(t)* is proportional to the square root of time. However, if the crystal growth is controlled by the reactions at the crystal-melt interface or by flow of latent heat away from the growing crystal surface, *d(t)* is a linear function of time, where, the velocity is given by the slope of *d(t)*.

Preliminary results and future work

In order to record the crystallization process in adequate conditions, e.i., in a isothermal step of cooling protocols and not in a cooling ramp and due to the spontaneous and fast crystallization of metal alloys numerous cooling protocols were tested for each undercooling temperature (ΔT), as well as, numerous heating protocols to the melting temperature determination. At the same time,

due to the fast crystallization process only low subcooling temperatures from 1 ºC to 15 ºC with 1 ºC of step were recorded. In this way, for nº 8 sample with 0.70 mm of thickness from 15 ºC of subcooling temperature the crystallization happened in the cooling ramps (at no constant temperatures) in any of tested protocols. On the other hand, thickness analysis suggested a minimum value needed of 0.70 mm in order to observe the crystallization process in isothermal step of cooling ramp. This observation suggests that samples larger thicknesses might allow measurements at subcooling temperatures higher than 15 ºC.

Currently the calibration curve and the DL data treatment are in process. Therefore, only the results visually observed during the experimental measurements are described bellow.

The visual analysis of recorded videos shows the expected behaviour in performed tests, where, the increasing of growth rate was observed as undercooling increases. On the other hand, in order to analysis the reproducibility of the results the same sample nº 8 was analyzed twice using the same protocol and the same subcooling temperature. The results for lowest undercolling temperatures of 1 and 2 ºC showed relevant differences in the visually estimated crystallization times. This phenomenon may be caused by the presence of different of nucleation sites. It has to be underlined that this visual analysis can lead to an error and therefore, DL data treatment must be performed in order to confirm these preliminary hypothesis and observations.

References

[1] Report of International Energy Agency (IEA) “Work Energy Investment Outlook 2014”. IEA Publications, (2014) Paris.

[2] Departamento de Asuntos Económicos y Sociales, División de Población de “Situación demográfica en el mundo, 2014”. Naciones Unidas (UN), (2014) New York.

[3] Report of International Energy Agency (IEA) “Work Energy Investment Outlook 2015”. IEA publications, (2015) Paris.

[4] Report of Organization for Economic Co-operation and Develepment (OECD) “Perspectivas ambientales de la OCDE hacía 2050: consecuencias de la inacción”. OECD, (2012) ISBN 978-92-64-122161.

[5] Report of World Energy Council (WEC) “2015 Energy Trilemma Index: Benchmarking the sustainability of national energy systems”. WEC, (2015) London.

[6] Special report of Working Group III of International Panel of Climate Change (IPCC) “Renewable energy sources and climate change mitigation”. IPCC, (2012).

[7] Special report of International Energy Agency (IEA) “Energy and Climate Change: World Energy Outlook Special Report”. IEA publications, (2015) Paris.

[8] Report of International Energy Agency (IEA) “Work Energy Investment Outlook 2010”. IEA publications, (2010) Paris.

[9] A. Gil, M. Medrano, I. Martorell, A. Lázaro, P. Dolado, B. Zalba and L. F. Cabeza, “State of the art on high temperature thermal energy storage for power generation. Part 1-Concepts, materials and modellization”. Renewable and Sustainable Energy Reviews 14 (2010) 31–55.

[10] M. Kenisarin and K. Mahkamov, “Solar energy storage using phase change materials”. Renewable and Sustainable Energy Reviews, 11 (2007) 1913–1965.

[11] K. Nithyanandam and R. Pitchumani, “Cost and performance analysis of concentrating solar power systems with integrated latent thermal energy storage”. Energy, 64 (2014) 793-810.

[12] V. Gnaneswar Gude, “Energy storage for desalination processes powered by renewable energy and waste heat sources”. Applied Energy, 137 (2015) 877–898.

[13] V. Gadhamshetty, V. Gnaneswar Gude and N. Nirmalakhandan, “Thermal energy storage system for energy conservation and water desalination in power plants”. Energy, 66 (2014) 938-949.

[14] N. R. Jankowski and F. P. McCluskey, “A review of phase change materials for vehicle component thermal buffering”. Applied Energy, 113 (2014) 1525–1561.

[15] F. Kuznik, D. David, K. Johannes and J-J. Roux, “A review on phase change materials integrated in building walls”. Renewable and Sustainable Energy Reviews 15 (2011) 379–391.

[16] N. Soares, J.J. Costa, A.R. Gaspar and P. Santos, “Review of passive PCM latent heat thermal energy storage systems towards buildings’ energy efficiency”. Energy and Buildings 59 (2013) 82–103.

[17] A. Sharma V.V. Tyagi, C.R. Chen and D. Buddhi, “Review on thermal energy storage with phase change materials and applications”. Renewable and Sustainable Energy Reviews 13 (2009) 318-345.

[18] X. Wang, E. Lu, W. Lin and C. Wang, “Micromechanism of heat storage in a binary system of two kinds of polyalcohols as a solid–solid phase change material”. Energy Conversion and Management, 41 (2000) 135–144.

[19] Q. Cao and P. Liu, “Hyperbranched polyurethane as novel solid–solid phase change material for thermal energy storage”. European Polymer Journal, 42 (2006) 2931–2939.

[20] A. Sari, H. Sarı and A. Önal, “Thermal properties and thermal reliability of eutectic mixtures of some fatty acids as latent heat storage materials”. Energy Conversion and Management 45 (2004) 365-376.

[21] M. M. Farid A.M. Khudhair, S.A.K. Razack and S. Al-Hallaj, “A review on phase change energy storage: materials and applications”. Energy Conversion and Management 45 (2004) 1597-1615.

[22] M. Liu, W. Saman and F. Bruno, “Review on storage materials and thermal performance enhancement techniques for high temperature change thermal storage systems”. Renewable and sustainable Energy Reviews 16 (2012) 2118-2132.

[23] A. H. Abedin and M. A. Rosen, “A Critical Review of Thermochemical Energy Storage Systems”. The Open Renewable Energy Journal, 4 (2011) 42-46.

[24] M. Medrano A. Gil, I. Martorell, X. Potau, L. F. Cabeza, “State of the art on high-temperature thermal energy storage for power generation. Part 2—Case studies”. Renewable and Sustainable Energy Reviews, 14 (2010) 56–72.

[25] T. Wang, D. Mantha and R. G. Reddy, “Novel low melting point quaternary eutectic system for solar thermal energy storage”. Applied Energy, 102 (2013) 1422–1429.

[26] F. Roget, C. Favotto and J. Rogez, “Study of the KNO_3–$LiNO_3$ and KNO_3–$NaNO_3$–$LiNO_3$ eutectics as phase change materials for thermal storage in a low-temperature solar power plant”. Solar Energy, 95 (2013) 155–169.

[27] M. M. Kenisarin, “Thermophysical properties of some organic phase change materials for latent heat storage. A review”. Solar Energy, 107 (2014) 553–575.

[28] B. Zalba, J.M. Marín, L. F. Cabeza and H. Mehling, “Review on thermal energy storage with phase change: materials, heat transfer analysis and applications”. Applied Thermal Engineering, 23 (2003) 251-283.

[29] R. V. Seeniraj and N. Lakshmi Narasimhan, ”Performance enhancement of a solar dynamic LHTS module having both fins and multiple PCMs”. Solar Energy, 82 (2008) 535-542.

[30] T. Nomura, N. Okinaka and T. Akiyama, “Waste heat transportation system, using phase change materials (PCM) from steelworks to chemical plant”. Resources, Conservation and Recycling, 54 (2010) 1000-1006.

[31] D. Laing, C. Bahl, T. Bauer, D. Lehmann and W-D. Steinmann, “Thermal energy storage for direct steam generation”. Solar Energy, 85 (2011) 627-633.

[32] G. C. Glatzmaier, J. Gomez, J. Ortega, A. Starace and C.Turchi, “High temperature phase change materials for thermal energy storage applications”. SolarPACES, (2011) Granada, Almeria.

[33] X. Wei, M.Song, W. Wang, J. Ding and J. Yang, “Design and thermal properties of a novel ternary chloride eutectics for high-temperature solar energy storage”. Applied Energy, 156 (2015) 306–310.

[34] N. Gokon, S. Nakamura, T. Yamaguchi and T. Kodama, “Cyclic properties of thermal storage/discharge for Al-Si alloy in vacuum for solar thermochemical fuel production”, Energy Procedia, 69 (2015) 1759 – 1769.

[35] G. Nardin, A.Meneghetti, F. Dal Magro and N. Benedetti, “PCM-based energy recovery from electric arc furnaces”, Applied Energy, 136 (2014) 947 – 955.

[36] R. Bayon E. Rojas, L. Valenzuela, E. Zarza and J. León, “Analysis of the experimental behaviour of a 100 kWth latent heat storage system for direct steam generation in solar thermal power plants”. Applied Thermal Engineering, 30 (2010) 2643 - 2651.

[37] N. Gokon, S-i Inutab, S. Yamashitab, T. Hatamachic and T. Kodamac, “Double-walled reformer tubes using high-temperature thermal storage of molten-salt/MgO composite for solar cavity-type reformer”. International Journal of Hydrogen Energy, 34 (2009) 7143 – 7154.

[38] M. Jonshon, J. Vogel, M. Hempel, A. Dengel, M. Seitz and B. Hachmann, “High temperature latent heat thermal energy storage integration in a co-gen plant”. Energy Procedia, 73 (2015) 281 – 288.

[39] D. J. Malan, R.T. Dobson and F. Dinter, “Solar thermal energy storage in power generation using phase change material with heat pipes and fins to enhance heat transfer”. Energy Procedia, 69 (2015) 925 – 936.

[40] M. M. Kenisarin, “High-temperature phase change materials for thermal energy storage”. Renewable and Sustainable Energy Reviews, 14 (2010) 955-970.

[41] J. Yagi and T. Akiyama, ”Storage of thermal energy for effective use of waste heat from industries”. Journal of Materials Processing Technology, 48 (1995) 793-804.

[42] S. Khare, M. Dell’Amico, C. Knight and S. McGarry, ”Selection of materials fro high temperature latent heat energy storage”. Solar Energy Materials & Solar Cells, 107 (2012) 20-27.

[43] A. Hoshi, D. R. Mills, A. Bittar and T. S. Saitoh, ”Screening of high melting point phase change materials (PCM) in solar thermal concentrating technology based on CLFR”. Solar Energy, 79 (2005) 332-339.

[44] C.E. Birchenall and A. F. Riechman, “Heat storage in eutectic alloys” Metallurgical Transactions A-physical Metallurgy and Materials Science, 11(1980) 1415–1420.

[45] C.E. Birchenall, “NASA Reports: Heat Storage in Alloy Transformations”., NASA CR-159787; 1980.

[46] D.Farkas and C.E. Birchenall, “New Eutectic Alloys and Their Heats of Transformation”. Metallurgical transformation A, 16A (1985) 323–328.

[47] Z. Wang, H. Wang, X. Li, D. Wang, Q. Zhang and G. Chen, Zhifeng Ren “Aluminum and silicon based phase change materials for high capacity thermal energy storage”. Applied Thermal Engineering, 89 (2015) 204-208.

[48] R. Fukahori, T. Nomura, C. Zhu, N. Sheng, N. Okinaka and T. Akiyama, “Thermal analysis of Al–Si alloys as high-temperature phase-change material and their corrosion properties with ceramic materials”. Applied Energy, 163 (2016) 1–8.

[49] J. Q. Sun, R.Y. Zhang, Z.P. Liu and G.H. Lu, “Thermal Reliability Test of Al-34%Mg-6%Zn Alloy as Latent Heat Storage Material and Corrosion of Metal with Respect to Thermal Cycling”, Energy Conversion and Management, 48 (2007) 619–624.

[50] N. Maruoka, K. Sato, J-i. Yagi and T. Akiyama, “Development of PCM for recovering high temperature waste heat and utilization for producing hydrogen by reforming reaction of methane”, ISIJ International, 42 (2002) 215–219.

[51] G. Zhang, J. Li, Y. Chen, H. Xiang, B. Mad, Z. Xu and X. Mad, “Encapsulation of copper-based phase change materials for high temperature thermal energy storage”, Solar Energy Materials & Solar Cells, 128 (2014) 131–137.

[52] H. Sugo, E. Kisi and D. Cuskelly, “Miscibility gap alloy with inverse microstructure and high thermal conductivity for high energy density thermal storage applications”, Applied Thermal Engineering, 51 (2013) 1345-1350.

[53] http://www.crct.polymtl.ca/factsage/fs_polythermal_proj.php.

[54] MTDATA, Phase Diagram Software from the National Physical Laboratory “Calculated Al-Zn phase diagram”. http://resource.npl.co.uk/mtdata/phdiagrams/alzn.htm.

[55] MTDATA, Phase Diagram Software from the National Physical Laboratory “Calculated Mg-Zn phase diagram”. http://resource.npl.co.uk/mtdata/phdiagrams/mgzn.htm.

[56] A. M. Gasanaliev and B Yu Gamataeva, “Heat-accumulating properties of Melts”. Russian Chemical Reviews. 69 (2000) 179 – 186.

[57] V. Esteve “El método Rietveld”. Publicacions de la Universitat Jaume, (2006).

[58] M. Jankula, P. Šín, R. Podoba and J. Ondruška, “Typical problems in push-rod dilatometry analysis”. Material Technology_Anyagtechnológia, 65 (2013) 11-14.

[59] Y. Naofumi, A. Remiand and O. Masahiro, “A calibration method for measuring thermal expansions with a push-rod dilatometer measurement”. Science and Technology 12 (2001) 2121-2129.

[60] T. Roisnel and J. Rodríguez-Carvajal, “WinPLOTR: a Windows tool for powder diffraction patterns analysis”. Materials Science Forum, Proceedings of the Seventh European Powder Diffraction Conference (EPDIC 7), 378 (2000) 118-123.

[61] J. Rodriguez-Carvajal and T. Roisnel, “FullProf.98 and WinPLOTR New Windows 99/NT Applications for Diffraction”. Commission For Powder Diffraction, International Union for Crystallography, 20 (1998) 35-36.

[62] J. Blumm, A. Lindemann and S. Min, “Thermal characterization of liquids and pastes using the flash technique”. Thermochimica Acta, 455 (2007) 26–29.

[63] S. Min, J. Blumm and A. Lindemann, “A new laser flash system for measurement of the thermophysical properties”. Thermochimica Acta, 455 (2007) 46–49.

[64] R. Cêrný and G. Renaudin, The intermetallic compound $Mg_{21}Zn_{25}$”, Acta Crystallographica Section C, 58 (2002) 154-155.

[65] M. E. Straumanis, “The precision determination of lattice constants by the powder and rotating crystal methods and applications”, Journal of Applied Physics 20 (1949) 726-734.

[66] H. Liang, S.-L. Chen, and Y.A. Chang, “A thermodynamic description of the Al-Mg-Zn system”, Metallurgical and Materials Transactions, 28 (1997) 1725-1734.

[67] G. Bergman, J.L.T. Waugh and L. Pauling, “The crystal structure of the metallic phase $Mg_{32}(Al, Zn)_{49}$”. Acta Crystalographica, 10 (1957) 254-259.

[68] W. Sun, F.J. Lincoln, K. Sugiyama and K. Hiraga, “Structure refinement of (Al, Zn)$_{49}$Mg$_{32}$-type phases by single-crystal X-ray diffraction”. Materials Science and Engineering, 294-296 (2000) 327-330.

[69] A. Smontara, I. Smiljanića, A. Bilušića, Z. Jagličić, M. Klanjšek, S. Roitsch, J. Dolinšek and M. Feuerbacher, “Electrical, magnetic, thermal and thermoelectric properties of the “Bergman phase” Mg$_{32}$ (Al, Zn)$_{49}$ Complex Metallic Alloy”, Journal of Alloys and Compounds, 430 (2007) 29–38.

[70] Y. P. Ren, G. W. Qin, W. L. Pei, S. Li, Y. Guo and H.D. Zhao, “Phase equilibria of Mg-rich corner in Mg-Zn-Al ternary system at 300 °C”, Transactions of Nonferrous Metals Society of China, 22 (2012) 241-245.

[71] J. Rodríguez-Aseguinolaza, P. Blanco-Rodríguez, E. Risueño, M. J. Tello and S. Doppiu, “Thermodynamic study of the eutectic Mg49–Zn51 alloy used for thermal energy storage”, Journal of Thermal Analysis and Calorimetry, 117 (2014) 93-99.

[72] D. G. McCartney, J. D. Hunt and R. M. Jordan, “The structure expected in a simple ternary eutectic system: Part I. Theory”, Metallurgical Transactions A, 11 (1980) 1243-1249.

[73] D. G. McCartney, J. D. Hunt and R. M. Jordan, “The structure expected in a simple ternary eutectic system: Part II. The Al-Ag-Cu ternary System”, Metallurgical Transactions A, 11 (1980) 1251-1257.

[74] C. Morando, O. Garbellini and H. Palacio, “Estructuras de solidificación esperadas en sistemas eutécticos ternarios simples”. Anales Afa, 17 (2005) 234-239.

[75] Y.P. Ren, G.W. Qin, W.L. Pei, Y. Guo, H.D. Zhao, H.X. Li, M. Jiang and S.M. Hao, “The α-Mg solvus and isothermal section of Mg-rich corner in the Mg–Zn–Al ternary system at 320 ◦C”, Journal of Alloys and Compounds, 481 (2009) 176–181.

[76] R.H. Kane, B.C. Giessen and N.J. Grant, “New metastable phases in binary tin alloy systems”, Acta Metallurgica, 14-5 (1966) 605–609.

[77] J.H. Perepezcko and D.H. Rasmussen, In Proceedings of the International Conference on Solidification and casting of metals, 1 (1977) 169.

[78] O. Ast, M. Perez and S. Carlet, “Paul alloys density measurements using gas pycnometer: First results”. Journal of Alloys and Compounds, 444–445 (2007) 226-229.

[79] J.B. Clark, L. Zabdyr and Z. Moser, “Phase diagrams of binary magnesium alloys”. Alloys Phase Diagram ASM International, 3 (1988) 1113.

[80] V. Raghavan, “Al-Mg-Zn (Aluminum-Magnesium-Zinc)”, Journal of phase equilibria and diffusion, 28-2 (2007) 203-208.

[81] P. Liang, T. Tarfa, J.A. Robinson, S. Wagner, P. Ochin, M.G. Harmelin, H.J. Seifert, H.L. Lukas and F. Aldinger, “Experimental investigation and thermodynamic calculation of the Al-Mg-Zn System”, Thermochimica Acta, 314 (1998) 87-110.

[82] P. Blanco-Rodríguez, J. Rodríguez-Aseguinolaza, E. Risueño and M. Tello, “Thermophysical characterization of Mg-51%Zn eutectic metal alloy: A phase change material for thermal energy storage in direct steam generation applications”, Energy 72 (2014) 414-420 [Corrigendum: Energy 75 (2014) 630].

[83] M. V. Akdepniz and J. V. Wood, “Microstructures and phase selection in rapidly solidified Zn-Mg alloys”, Journal of Material Science, 31 (1996), 545-550.

[84] E. Risueño, A. Faik, J. Rodríguez-Aseguinolaza, P. Blanco-Rodríguez, A. Gil, M. J. Tello and B. D’Aguanno, “Mg-Zn-Al eutectic alloys as phase change material for latent heat thermal energy storage”. Energy Procedia, 69 (2015) 1006-1013.

[85] H. Michels and R. Pitz-Paal, “Cascade latent heat storage for parabolic trough solar power plants”. Solar Energy, 81 (2007) 829-837.

[86] S. Jegadheeswaran and S.D. Pohekar, “Performance Enhancement in Latent Heat Thermal Storage System: A review”, Renewable and Sustainable Energy Reviews, 13 (2009) 2225–2244.

[87] J.M. Khodadadi, L. Fan and H. Babaei, ” Thermal conductivity enhancement of nanostructure-based colloidal suspensions utilized as phase change materials for thermal energy storage: A review”. Renewable and Sustainable Energy Reviews, 24 (2013) 418–444.

[88] S. Pincemin, R. Olives, X. Py and M. Christ, “Highly conductive composites made of phase change materials and graphite for thermal storage”. Solar Energy Materials & Solar Cells, 92 (2008) 603–613.

[89] Z. Huang, X. Gao, T. Xu, Y. Fang and Z. Zhang, “Thermal property measurement and heat storage analysis of $LiNO_3$/KCl – expanded graphite composite phase change material”. Applied Energy, 115 (2014) 265–271.

[90] H. Tian, W. Wang, J. Ding, X. Wei, M. Song and J. Yang, “Thermal conductivities and characteristics of ternary eutectic chloride/expanded graphite thermal energy storage composites”. Applied Energy, 148 (2015) 87–92.

[91] M. K. Rathod and J. Banerjee, “Thermal stability phase change materials used in latent heat energy storage systems: A review”. Renewable and Sustainable Energy Reviews, 18 (2013) 246-258.

[92] A. Sari and A. Karaipekli, “Preparation, thermal properties and thermal reliability of palmitic acid/expanded graphite composite as form-stable PCM for thermal energy storage”. Solar Energy Materials & Solar Cells, 93 (2009) 571-576.

[93] A. Sari, “Eutectic mixture of some fatty acids for latent heat storage: Thermal properties and thermal reliability with respect to thermal cycling”. Energy Conversion and Management, 47 (2006) 1207-1221.

[94] A.A. El-Sebaii, S. Al-Heniti, F. Al-Agel, A.A. Al-Ghamdi and F. Al-Marzouki, “One thousand thermal cycles magnesium chloride hexahydrate as a promising PCM for indoor solar cooking”. Energy Conversion and Management, 52 (2011) 1771-1777.

[95] V.V. Tyagi and D. Buddhi, “Thermal cycle testing of calcium chloride hexahydrate as a possible PCM for latent heat storage”. Solar Energy Materials & Solar Cells, 92 (2008) 891-899.

[96] A. Sharma, S.D. Sharma and D. Buddhi, “Accelerated thermal cycle test of acetamide, stearic acid and paraffin wax for solar thermal latent heat storage applications”. Energy Conversion and Management, 43 (2002) 1923-1930.

[97] A. Sari, “Thermal reliability test of some fatty acids as PCMs used for solar thermal latent heat storage applications”. Energy Conversion and Management, 44 (2003) 2277-2287.

[98] A. Shukla, D. Buddhi and R.L. Sawhney, ”Thermal cycling test of few selected inorganic and organic phase change materials”. Renewable energy, 33 (2008) 2606-2614.

[99] S. D. Sharma, D. Buddhi and R.L. Sawhney, “Accelerated thermal cycle test of latent heat-storage materials”. Solar Energy, 66 (1999) 483-490.

[100] B. C. Shin and S. D. Kim, “Ternary carbonate eutectic (lithium, sodium and potassium carbonates) for latent heat storage medium”. Solar Energy Materials 21 (1990) 81-90.

[101] S. Kuravi, J. Trahan, D.Y. Goswami, M.M. Rahman and E.K. Stefanakos, ”Thermal energy storage technologies and systems for concentrating solar power plants”. Progress in Energy and Combustion Science, 39 (2013) 285-319.

[102] T. E. Alam, J.S. Dhau, D.Y. Goswami, E. Stefanakos “Macroencapsulation and characterization of phase change materials for latent heat thermal energy storage systems”. Applied Energy 154 (2015) 92-101.

[103] M. Liu, J.C. Gomez, C.S. Turchi, N.H.S. Tay, W. Saman and F. Bruno, “Determination of thermo-physical properties and stability testing of high-temperature phase-change materials as CSP applications”. Solar Energy Materials & Solar Cells, 139 (2015) 81-87.

[104] X. Liu, E. Barbero, J. Xu, M. Burris, K-M Chang and V. Sikka, ”Liquid metal corrosion of 316L, Fe_3AI, and FeCrSi in molten Zn-Al baths”. Metallurgical and Material Transactions A, 36 (2005) 2049-2058.

[105] N. -Y. Tang, ”Characteristics of continuous-galvanizing baths”. Metallurgical and Material Transactions B, 30 (1999) 144-148.

[106] W.J. Wang, J.P. Lin, Y.L. Wang and G.L. Chen, “The corrosion of intermetallic alloys in liquid zinc”. Journal of Alloys and Compounds, 428 (2007) 237–243.

[107] F. Czerwinski, “Magnesium alloys - properties in solid and liquid states”. InTech, (2014) ISBN 978-953-51-1728-5, DOI: 10.5772/58293.

[108] J. Xu, M.A. Bright, X. Liu, E. Barbero, “Liquid metal corrosion of 316L stainless steel, 410 stainless steel, and 1015 carbon steel in a molten zinc bath” Metallurgical and Material Transactions, A 38 (2007) 2727-2736.

[109] J. B. Clark, L. Zabdyr, Z. Mose, In: Massalki TB, ed. Binary alloy phase diagram, Materials Park (OH): ASM; 1990. p. 2571.

[110] R. Agarwal, S.G. Fries, H.L. Lukas, G. Petzow, F. Sommer, T.G. Chart, Effenberg G. Z. Met. Kd 1992;83(4):216-23

[111] P. Ghosh, M. Mezbahul-Islam and M. Medraj, “Critical assessment and thermodynamic modeling of Mg–Zn, Mg–Sn, Sn–Zn and Mg–Sn–Zn systems”. Calphad, 36 (2012) 28–43.

[112] J.B. Clark and F.N. Rhines, “Central region of the magnesium–zinc phase diagram”. Journal of Metals, 9 (1957) 425–430.

[113] I. Higashi, N. Shiotani, M. Uda, T. Mizoguchi and H. Katoh, “The crystal structure of $Mg_{51}Zn_{20}$”. Journal of Solid State Chemistry, 36 (1981) 225-233.

[114] E.S.R. Gopal, “Specific Heats at Low Temperatures”, London: Heywood Books/Plenum Press; 1966.

[115] N.W. Ashcroft and N.D. Mermin, “Solid state physics”. Fort Worth (TX): Harcourt Brace College Publishers; 1976.

[116] C. Kittel and H. Kroemer, “Thermal Physics”. Freeman WH (Ed.); 1980.

[117] T.H.K. Barron and G.K. White, “Heat Capacity and Thermal Expansion at Low Temperatures”. New York (NY): Kluwer / Plenum Press; 1999.

[118] D. R. Lide (Ed.). CRC Handbook of Chemistry and Physics, 86th ed. Taylor & Francis; 2006.

[119] M. Morishita, H. Yamamoto, S. Shikada, M. Kusumoto and Y Matsumoto, “Thermodynamics of the formation of magnesium-zinc intermetallic compounds in the temperature range from absolute zero to high temperature”. Acta Materialia, 54 (2006) 3151-3159.

[120] D. Laing, T. Bauer, D. Lehmann and C. Bahl, “Development of a thermal energy storage system for parabolic trough power plants with direct steam generation”. Journal of Solar Energy Engineering-transactions of the Asme, 132(2) (2010) 021011-1 - 021011-8.

[121] D. Laing, C. Bahl, T. Bauer, D. Lehmann, and W. D. Steinmann, “Thermal energy storage for direct steam generation”. Solar Energy, 85(4) (2011) 627–633.

[122] http://www.psa.es/webesp/instalaciones/parabolicos.php, 2013.

[123] X. Gao and J. F. Nie, “Structure and thermal stability of primary intermetallic particles in an Mg-Zn casting alloy”. Scripta Materialia, 57(7) (2007) 655–658.

[124] P. Andonov and P. Chieux, “Structural study of eutectic $Mg_{0.72}Zn_{0.28}$ alloy I. Local order in the amorphous and liquid states comparison with the crystalline phase $Mg_{51}Zn_{20}$”. Journal of Non-crystalline Solids, 93 (1987) 331–349.

[125] P. Andonov and P. Chieux, “Structural study of eutectic $Mg_{0.72}Zn_{0.28}$ alloy II. Crystallization processes in the amorphous, liquid and undercooled states of the eutectic alloy $Mg_{0.72}Zn_{0.28}$”. Journal of Non-crystalline Solids, 108 (1989) 58–74.

[126] L. Lutterotti, R. Ceccato, R. Dal Maschio, and E. Pagani, “Quantitative analysis of silicate glass in ceramic materials by the rietveld method”. Materials Science Forum, 278-281 (1998) 87-92.

[127] W. Xiang, L. Hong-mei, L. Xin-lin, L. Li, and Z. Yu-feng “Effect of cooling rate and composition on microstructures and properties of Zn-Mg alloys”. Transactions of Nonferrous Metals Society of China, 17 (2007) 120-125.

[128] X. Py, N. Calvet, R. Olives, A. Meffre, P. Echegut, C. Bessada, E. Veron, and S. Ory, “Recycled material for sensible heat based thermal energy storage to be used in concentrated solar thermal power plants”. Journal of Solar Energy Engineering-transactions of the Asme, 133 (2011) 031008.

[129] C.R. Swaminathan and V.R. Voller, “A general enthalpy method for modeling solidification processes” Metallurgical Transactions B, 23B (1991) 1992-651.

[130] C.R. Swaminathan and V.R. Voller, “Towards a general numerical scheme for solidification systems”. International Journal of Heat and Mass Transfer, 40 (1997) 2859-2868.

[131] V. R. Voller. "Modeling solidification processes". Technical report. Mathematical Modeling of Metals Processing Operations Conference, Palm Desert, CA American Metallurgical Society. (1987)

[132] F. Agyenim, N. Hewitt, P. Eames and M. Smyth, “A review of materials, heat transfer and phase change problem formulation for latent heat thermal energy storage systems (LHTESS)”. Renewable and Sustainable Energy Reviews, 14 (2010) 615–628.

[133] A.B. Crowley and J.R. Ockendon. “Modelling mushy regions”. Applied Scientific Research, 44 (1987) 1-7.

[134] V. R. Voller, A. D. Brent and C. Prakash, “Modelling the mushy region in a binary alloy” Applied Mathematical Modelling, 14 (1990) 320-326.

[135] V. R. Voller and C. Prakash, "A fixed-grid numerical modeling methodology for convection-diffusion mushy region phase-change problems". International Journal of Heat and Mass Transfer, 30 (1987) 1709–1720.

[136] B.E. Launder and D.B. Spalding, “Lectures in mathematical models of turbulence”. Academic Press, (1972) London (England).

[137] B.E. Launder and D.B. Spalding, “The numerical computation of turbulent flows”. Computer Methods in Applied Mechanics and Engineering, 3 (1974) 269-289.

[138] A. Solé, L. Miró, C. Barreneche, I. Martorell, and L. F. Cabeza, “Review of the T-history method to determine thermophysical properties of phase change materials (PCM)” . Renewable & Sustainable Energy Reviews, 26 (2013) 425–436.

[139] E. Günther, S. Hiebler, H. Mehling, and R. Redlich, “Enthalpy of phase change materials as a function of temperature: required accuracy and suitable measurement methods”. International Journal of Thermophysics, 30 (2009) 1257–1269.

[140] R. Adinberg, D. Zvegilsky, and M. Epstein, “Heat transfer efficient thermal energy storage for steam generation”. Energy Conversion and Management, 51 (2010) 9–15.

[141] D. Petrov, A. Watson, J. Gröbner, P. Rogl, J-C. Tedenac, M. Bulanova, V. Turkevich and H. L. Lukas, “Al-Mg-Zn (Aluminium – Magnesium – Zinc)”. Materials Science International Team (MSIT), 11A3 (2005) 119-209.

[142] G. Effenberg, A. Prince, O. Bieloborodova, L. Gulay, F. H. Hayes, M. G. Harmelin, H. L. Lukas and T. Yanson, “Aluminium - Copper – Magnesium”. Materials Science International Team (MSIT), IV/11A2 4 (2003) 1-41.

[143] www.al-chemist.info/node/161.

[144] S. Verma and P.J. Shlichta, "Imaging techniques for mapping solution parameters, growth rate, and surface features during the growth of crystals from solution", Progress in Crystal Growth and Characterization of Materials, 54 (1-2) (2008) 1-120.

[145] W.R. Wilcox and P.J. Shlichta, "A survey of movies on crystal growth", Journal of Crystal Growth, 15 (1972) 61-72.

[146] A. Godin, M. Duquesne, E. Palomo del Barrio and J. Morikawa, “Analysis of crystal growth kinetics in undercooled melts by infrared thermography”. Quantitative InfraRed Thermography Journal, 12(2) (2015) 237-251.

[147] http://www.slideshare.net/kkh007/eutectic-solidification

[148] K.A. Jackson, "Kinetics processes. Crystal Growth, Diffusion, and Phase Transitions in Materials", Wiley-VCH Verlag GmbH & Co. KGaA, Weinheim, 2004.

[149] M.C. Merino Casals “Diagramas y transformaciones de fase. 6. Solidificación”. Reduca (Recursos Educativos) Serie Química de Materiales, 4 (3) (2012) 211-284.

[150] R.J. Kirkpatrick, “Cristal growth from the melt: A review”. American Mineralogist, 60, (1975) 798-814.